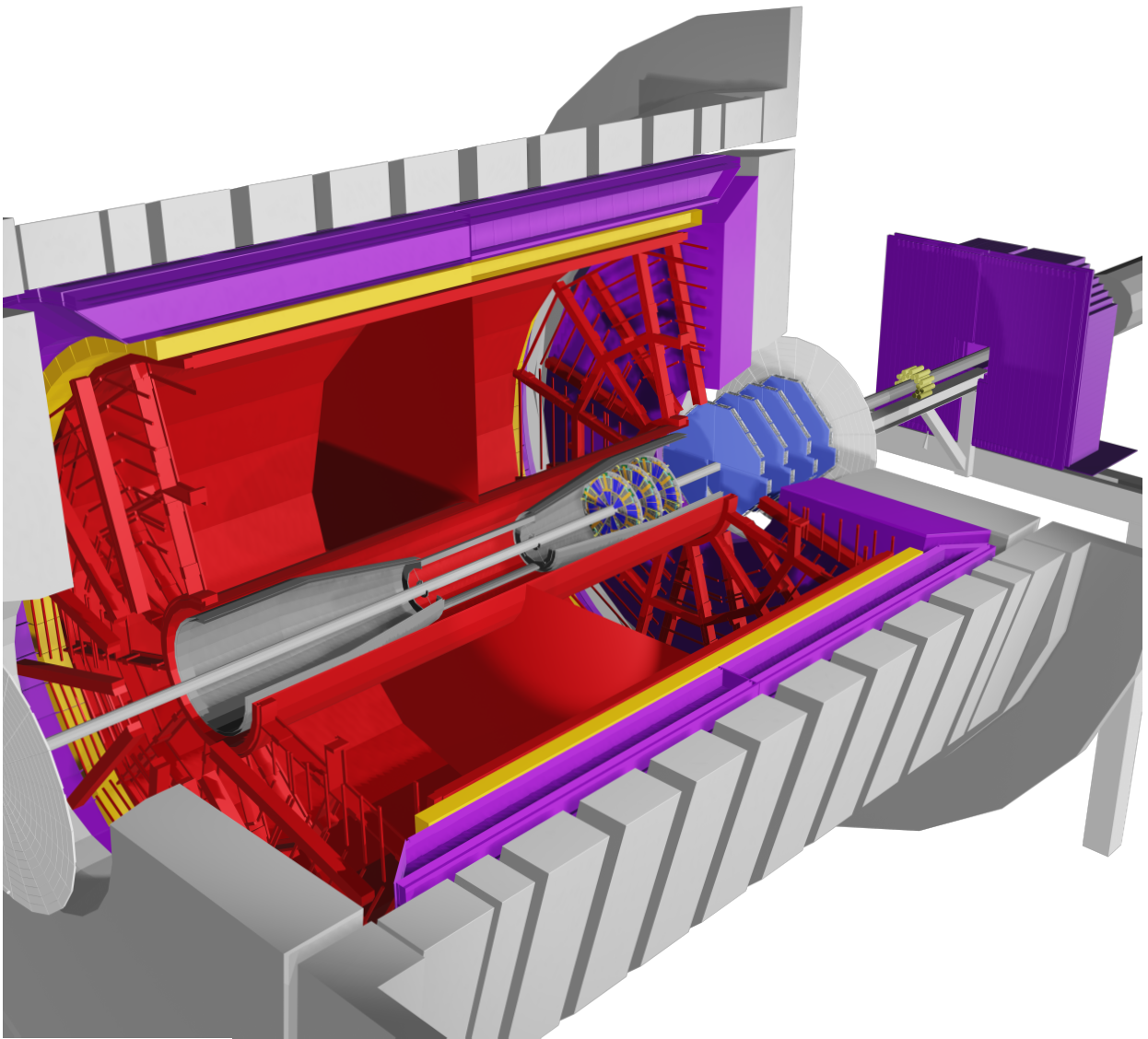


The STAR Beam Use Request for Run-21, Run-22 and data taking in 2023-25

The STAR Collaboration



1 Executive Summary

2 This Beam Use Request outlines the physics programs that compels the STAR collaboration
3 to request data taking during the years 2021-2025.

4 STAR's **highest scientific priorities** for Run-21 and Run-22 are to complete the NSAC-
5 endorsed second phase of the Beam Energy Scan (BES-II) program, and initiate the "must-
6 do" Cold QCD forward physics program enabled by the newly completed suite of forward
7 detectors via the collection of transversely polarized p+p data at 510 GeV. From 2023-25
8 we will use a combination of soft and hard probes to explore the microstructure of the QGP
9 and continue the forward physics program via the collection of high statistics Au+Au, p+Au
10 and p+p data at $\sqrt{s_{NN}} = 200$ GeV.

11 The BES-II program has so far been very successful. As shown in Table 1, we have
12 recorded collisions at $\sqrt{s_{NN}} = 9.2-27$ GeV in collider mode, and $\sqrt{s_{NN}} = 3-7.7$ GeV in fixed
13 target (FXT) mode. We expect to complete data collection at $\sqrt{s_{NN}} = 9.2$ GeV by the end
14 of Run-20b. In Run-21, as shown in Table 2, our number one priority is to complete the
15 BES-II by recording 100 M good events at $\sqrt{s_{NN}} = 7.7$ GeV.

Table 1: Summary of all BES-II and FXT Au+Au beam energies, equivalent chemical potential, event statistics, run times, and date collected.

| Beam Energy (GeV/nucleon) | $\sqrt{s_{NN}}$ (GeV) | μ_B (MeV) | Run Time | Number Events Requested (Recorded) | Date Collected |
|------------------------------|--------------------------|------------------|--------------|---------------------------------------|---------------------|
| 13.5 | 27 | 156 | 24 days | (560 M) | Run-18 |
| 9.8 | 19.6 | 206 | 36 days | 400 M (582 M) | Run-19 |
| 7.3 | 14.6 | 262 | 60 days | 300 M (324 M) | Run-19 |
| 5.75 | 11.5 | 316 | 54 days | 230 M (235 M) | Run-20 |
| 4.59 | 9.2 | 373 | in progress | 160 M ¹ | Run20+20b |
| 31.2 | 7.7 (FXT) | 420 | 0.5+1.1 days | 100 M (50 M+112 M) | Run-19+20 |
| 9.8 | 4.5 (FXT) | 589 | 0.9 days | 100 M (108 M) | Run-20 |
| 7.3 | 3.9 (FXT) | 633 | 1.1 days | 100 M (117 M) | Run-20 |
| 19.5 | 6.2 (FXT) | 487 | 1.4 days | 100 M (118 M) | Run-20 |
| 13.5 | 5.2 (FXT) | 541 | 1.0 day | 100 M (103 M) | Run-20 |
| 5.75 | 3.5 (FXT) | 666 | 0.9 days | 100 M (116 M) | Run-20 |
| 4.59 | 3.2 (FXT) | 699 | 2.0 days | 100 M (200 M) | Run-19 |
| 3.85 | 3.0 (FXT) | 721 | 4.6 days | 100 M (259 M) | Run-18 |
| 3.85 | 7.7 | 420 | 11-20 weeks | 100 M | Run-21 ² |

¹ Run-20b is still in progress at the time of submission of this BUR, we expect to reach our goals

² Data not yet collected, Run-21 forms part of this year's BUR.

16 Based on guidance from the Collider-Accelerator Department (C-AD) and past experience
17 we expect that the bulk of Run-21 will be devoted to Au+Au collisions at $\sqrt{s_{NN}} = 7.7$ GeV,

Table 2: Proposed Run-21 assuming 24 -28 cryo-weeks, including an initial one week of cool-down, one week for CeC ,and a one week set-up time for each collider energy and 0.5 days for each FXT energy.

| Single-Beam Energy (GeV/nucleon) | $\sqrt{s_{NN}}$ (GeV) | Run Time | Species | Events (MinBias) | Priority |
|----------------------------------|-----------------------|-------------|---------|--------------------------|----------|
| 3.85 | 7.7 | 11-20 weeks | Au+Au | 100 M | 1 |
| 3.85 | 3 (FXT) | 3 days | Au+Au | 300 M | 2 |
| 44.5 | 9.2 (FXT) | 0.5 days | Au+Au | 50 M | 2 |
| 70 | 11.5 (FXT) | 0.5 days | Au+Au | 50 M | 2 |
| 100 | 13.7 (FXT) | 0.5 days | Au+Au | 50 M | 2 |
| 100 | 200 | 1 week | O+O | 400 M 200 M (central) | 3 |
| 8.35 | 17.1 | 2.5 weeks | Au+Au | 250 M | 3 |
| 3.85 | 3 (FXT) | 3 weeks | Au+Au | 2 B | 3 |

18 the lowest collider energy of the program. Collection of these events is our highest priority.
19 However, if we assume optimistic, but not overly so, rates and up-times, and 28 cryo-weeks,
20 we project that the opportunity to collect of other exciting datasets will arise.

21 The *second highest priority* for Run-21 identified by the STAR collaboration is four short
22 FXT runs; the collection of 300 M good events at $\sqrt{s_{NN}} = 3$ GeV and 50 M good events
23 at each of three higher beam energies ($\sqrt{s_{NN}} = 9.2, 11.5, \text{ and } 13.7$ GeV). In the second
24 highest priority block shown in Table 2, the 3 GeV FXT system is listed first for reasons
25 of logistics. It is recognized that the opportunity to address the topics listed as second and
26 third priorities will be contingent on the performance of the 7.7 GeV collider run. Should
27 it become evident early on in that run (in the first 4-8 weeks or so), that performance is
28 exceeding the conservative projections and that time will be available at the end of run 21,
29 then it would be beneficial to take three days to complete the 3 GeV FXT run. This system
30 uses the same single beam energy (3.85 GeV) as the 7.7 GeV collider program, so there would
31 be no time lost transitioning and acquiring these data early in the run would give sufficient
32 time to analyze the results of the ExpressStream production to investigate the acceptance
33 and background for the search of the double- Λ hypernucleus and determine the statistics
34 necessary to pursue this physics topic (currently estimated to be three weeks). 300 M events
35 at 3 GeV with the enhanced iTPC and eTOF coverage gives access to the proton higher
36 moments, precision ϕ , hypernuclei, and dilepton measurements. The higher $\sqrt{s_{NN}}$ FXT data
37 combined with the collider data at the same energy will provide full proton rapidity coverage
38 allowing us to probe in detail the mechanisms of stopping at play in heavy-ion collisions. We
39 estimate the total run time required to collect all these datasets is 6 days.

40 The STAR collaboration also finds important scientific opportunities are presented by
41 the collection of our *third highest priority* datasets:

- 42 • O+O data at $\sqrt{s_{\text{NN}}} = 200$ GeV, in the context of understanding the early-time condi-
43 tions of small systems. These data would allow for a direct comparison with a similarly
44 proposed higher-energy O+O run at the LHC, and further motivate the case for a small
45 system scan complementary to ongoing efforts by the NA61/SHINE collaboration at
46 SPS energies, and other proposed light-ion species at the LHC.
- 47 • A sixth collider beam energy at $\sqrt{s_{\text{NN}}} = 17.1$ GeV. These data will provide for a finer
48 scan in a range where the energy dependence of the net-proton kurtosis and neutron
49 density fluctuations appear to undergo a sudden change.
- 50 • 2 B good events at $\sqrt{s_{\text{NN}}} = 3$ GeV in FXT mode. These enhanced statistics make
51 possible the measurements of mid-rapidity proton 5-th/6-th order moments/cumulants,
52 the system size dependence of ϕ meson production and the double- Λ hypernuclei.

53 The sequence with which we collect these datasets is currently somewhat fluid and are
54 listed in the order of the requested run time; we do not want to take partial datasets. We
55 expect to refine the ordering of our goals as Run-21 progresses. Collection of these data
56 during future RHIC running periods is also of interest to the collaboration.

57 For Run-22, as shown in Table 3, we propose **a dedicated 20 cryo-week transversely**
58 **polarized p+p run at $\sqrt{s} = 510$ GeV**. This run will take full advantage of STAR's new
59 forward detection capabilities, consisting of a Forward Calorimeter System (FCS) and a
60 Forward Tracking System (FTS) located between $2.5 < \eta < 4$, and further capitalizes on the
61 recent BES-II detector upgrades.

62 These data will enable STAR to explore, with unprecedented precision, forward jet
63 physics that probe both the high-x (largely valence quark) and low-x (primarily gluon)
64 partonic regimes.

Table 3: Proposed Run-22 assuming 20 cryo-weeks, including an initial one week of cool-down and a two weeks set-up time.

| \sqrt{s} (GeV) | Species | Polarization | Run Time | Sampled Luminosity | Priority |
|---------------------|---------|--------------|----------|-----------------------|----------|
| 510 | p+p | Transverse | 16 weeks | 400 pb ⁻¹ | 1 |

65 Looking further out, the STAR collaboration has determined that there is a compelling
66 scientific program enabled by the first opportunity to capitalize on the combination of the
67 BES-II and Forward Upgrades in the data collected from Au+Au, p+Au, and p+p collisions
68 at $\sqrt{s_{\text{NN}}} = 200$ GeV as outlined in Table 4.

69 Significantly increased luminosities, the extended acceptance at mid-rapidity due to the
70 iTPC, improved event plane and triggering capabilities of the EPD, and the ability to probe
71 the previously inaccessible forward region are all exploited in our Hot QCD program, that
72 informs on the microstructure of the QGP, and our Cold QCD program that will utilize
73 transverse polarization that sets the stage for related future measurements at the EIC.

Table 4: Proposed Run-23 - Run-25 assuming 24 (28) cryo-weeks of running every year, and 6 weeks set-up time to switch species in 2024. Sampled luminosities assume a "take all" triggers.

| $\sqrt{s_{\text{NN}}}$ (GeV) | Species | Number Events/ Sampled Luminosity | Date |
|---------------------------------|---------|--------------------------------------|------|
| 200 | Au+Au | 10B / 38 nb ⁻¹ | 2023 |
| 200 | p+p | 235 pb ⁻¹ | 2024 |
| 200 | p+Au | 1.3 pb ⁻¹ | 2024 |
| 200 | Au+Au | 10B / 52 nb ⁻¹ | 2025 |

74 Contents

| | | |
|-----|--|-----------|
| 75 | 1 Highlights from the STAR Program | 1 |
| 76 | 1.1 Highlights from the Heavy Ion Program | 1 |
| 77 | 1.1.1 Heavy-Ion Jet Measurements | 1 |
| 78 | 1.1.2 Bulk Correlations | 5 |
| 79 | 1.1.3 Light Flavor Spectra and Ultra-peripheral Collisions | 12 |
| 80 | 1.1.4 Heavy-Flavor | 16 |
| 81 | 1.2 CME Search and Isobar Run | 22 |
| 82 | 1.2.1 Introduction | 22 |
| 83 | 1.2.2 Modality of Isobar Running at RHIC | 22 |
| 84 | 1.2.3 Blinding of Data Sets and Preparation for Analyses | 23 |
| 85 | 1.2.4 Methods for the Isobar Blind Analyses | 24 |
| 86 | 1.2.5 Observables for Isobar Blind Analyses | 25 |
| 87 | 1.2.6 Prospect of CME search beyond isobar-era | 29 |
| 88 | 1.3 Highlights from the Spin and Cold QCD Program | 31 |
| 89 | 1.3.1 Introduction | 31 |
| 90 | 1.3.2 Longitudinal program | 32 |
| 91 | 1.3.3 Transverse program | 34 |
| 92 | 1.3.4 Unpolarized Results | 36 |
| 93 | 1.4 Run-20 Performance | 39 |
| 94 | 2 Proposed Program - Hot QCD in Run-21, 23, and 25 | 43 |
| 95 | 2.1 Beam Request for Run-21 | 43 |
| 96 | 2.1.1 Completion of the BES-II Program | 43 |
| 97 | 2.1.2 Au+Au Collisions in FXT Mode at $\sqrt{s_{NN}} = 3.0$ GeV - I: 300 million | |
| 98 | goal | 44 |
| 99 | 2.1.3 Au+Au Collisions in FXT Mode at $\sqrt{s_{NN}} = 9.2, 11.5,$ and 13.7 GeV . | 48 |
| 100 | 2.2 Further Opportunities in Run-21 | 49 |
| 101 | 2.2.1 Small System Run: O+O at $\sqrt{s_{NN}} = 200$ GeV | 49 |
| 102 | 2.2.2 Au+Au Collisions at $\sqrt{s_{NN}} = 17.1$ GeV | 58 |
| 103 | 2.2.3 Au+Au Collisions in FXT Mode at $\sqrt{s_{NN}} = 3.0$ GeV - II: 2 Billion Goal | 62 |
| 104 | 2.3 Future Possibilities | 63 |
| 105 | 2.3.1 Exploring the Nuclear Equation-of-State (EoS) with Heavy Ion Collisions | 63 |
| 106 | 2.4 Exploring the Microstructure of the QGP (Run-23 and Run-25 Au+Au) . . | 65 |
| 107 | 2.4.1 Correlation Measurements Utilizing Extended Acceptance | 67 |
| 108 | 2.4.2 Correlation Measurements Utilizing the Enhanced Statistics | 72 |
| 109 | 2.4.3 Electromagnetic Probes | 74 |
| 110 | 2.4.4 Deconfinement and Thermalization With Charmonia Measurements . | 78 |
| 111 | 2.4.5 Jet Probes | 81 |

| | | | |
|-----|----------|---|------------|
| 112 | 3 | Cold QCD Physics with $p^\uparrow p^\uparrow$ and $p^\uparrow + A$ Collisions at 510 and 200 GeV | 87 |
| 113 | 3.1 | Run-22 Request for $p^\uparrow p^\uparrow$ Collisions at 510 GeV | 88 |
| 114 | 3.1.1 | Inclusive transverse spin asymmetries at forward rapidities | 88 |
| 115 | 3.1.2 | Sivers and Efremov-Teryaev-Qiu-Sterman Function | 90 |
| 116 | 3.1.3 | Transversity, Collins Function and Interference Fragmentation Function | 92 |
| 117 | 3.1.4 | Spatial Imaging of the Nucleon | 97 |
| 118 | 3.2 | Run-24 Request for Polarized p+p and p+A Collisions at 200 GeV | 100 |
| 119 | 3.2.1 | Spin Physics with Polarized p+p and p+Au Collisions at 200 GeV . . | 100 |
| 120 | 3.2.2 | Physics Opportunities with Unpolarized proton-Nucleus Collisions . . | 105 |
| 121 | 4 | Detector Updates, Operations, and Opportunities | 119 |
| 122 | 4.1 | Status and Performance of the eTOF | 119 |
| 123 | 4.2 | Forward Upgrade | 120 |
| 124 | 4.2.1 | Status | 121 |
| 125 | 4.2.2 | Forward Calorimetry System | 121 |
| 126 | 4.2.3 | Forward Silicon Tracking | 122 |
| 127 | 4.2.4 | sTGC Tracking | 123 |
| 128 | 4.2.5 | Software | 123 |

1 Highlights from the STAR Program

1.1 Highlights from the Heavy Ion Program

1.1.1 Heavy-Ion Jet Measurements

Jet quenching, the modification of parton showers due to interactions in the QGP, is manifest in several distinct ways: energy transport to large angles, observable via jet energy loss and large-angle energy recovery; multiple-soft and single-hard coherent scatterings off of plasma constituents, observable via jet deflection or acoplanarity; and the modification of jet substructure. This broad spectrum of phenomena provides unique and incisive probes of the microscopic structure of the QGP. It also provides a robust experimental program, in which different observables with different systematic sensitivity probe the same underlying physics, providing stronger constraints on theoretical models of jet quenching than single measurements. STAR has a comprehensive jet quenching program which covers the full spectrum of these phenomena, using hadrons, direct photons, and reconstructed jets as probes.

STAR has led the development of essential analysis techniques for the challenging task of measuring reconstructed jet observables in heavy-ion collisions at RHIC. These include a data-driven Mixed-Event technique to measure uncorrelated jet background for semi-inclusive observables [1], enabling unbiased jet measurements over a broad phase space in heavy-ion collisions, notably low jet p_T (~ 10 GeV/ c) and large jet resolution parameter ($R \sim 0.5$); and sub-jet observables that are robust to the underlying event and yet sensitive to the jet splitting kinematics, applying them as a tool to access the resolution scale in jet-medium interactions [2].

Jet quenching measurements have traditionally utilized p+p collisions to provide an unmodified reference, and p +A collisions to measure initial state effects that may mask signals of quenching in the final state. More recently it has become evident that small systems themselves exhibit QGP-like flow signatures for event selection corresponding to high Event Activity (EA), and an urgent question in the field is whether evidence can likewise be found for jet quenching in such systems. The STAR jet quenching program therefore includes measurements in (unpolarized) p+p and p +Au collisions, as well as Au+Au collisions.

In this section we present recent highlights of the STAR jet quenching program. The STAR papers published in this area in the past year can be found in Refs. [3–7].

Inclusive and semi-inclusive jet yield suppression: Inclusive jet yield suppression is a hallmark of jet quenching in heavy-ion collisions. STAR has recently reported the first measurement at RHIC of inclusive charged-particle jet distributions in central and peripheral Au+Au collisions at $\sqrt{s_{NN}} = 200$ GeV [7], together with measurements of their yield suppression, R_{AA} (normalized by the yield in p+p collisions calculated by PYTHIA tuned to other STAR data [8]) and R_{CP} . Figure 1 shows the extracted R_{CP} compared to a similar measurement by ALICE, and to charged-hadron R_{CP} measured at both colliders. A striking similarity is seen between the two inclusive jet measurements, and between the two

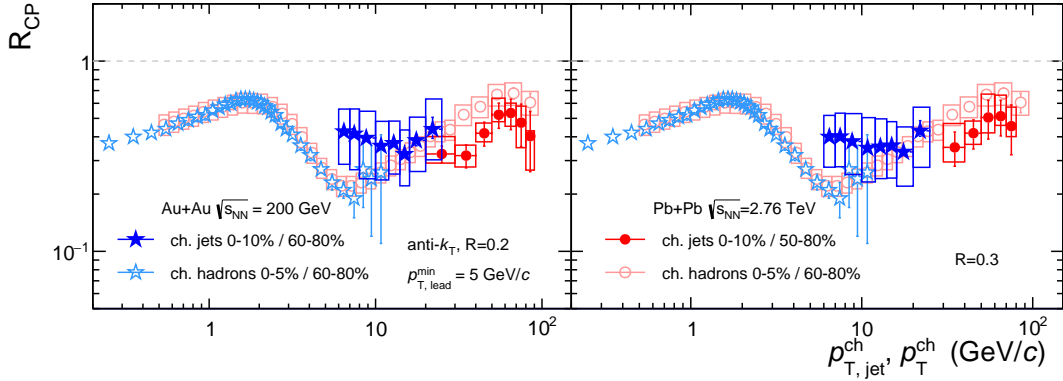


Figure 1: Measurement of R_{CP} as a function of $p_{T,jet}^{ch}$ for charged-particle jets (anti- k_T , $R = 0.2$ and 0.3) measured by STAR (blue points) [7], compared to charged-jet R_{CP} at the LHC and to inclusive hadron R_{CP} at RHIC and the LHC. Note the different centrality selections.

168 inclusive hadron measurements. The p_T -dependence of R_{CP} is stronger for hadrons in the
 169 region of overlap. While there remain differences in centrality selection between the datasets,
 170 this is the most direct comparison to date of reconstructed jet measurements at RHIC and
 171 the LHC.

172 This paper also reported the ratio of jet yields in central and peripheral Au+Au collisions
 173 for $R = 0.2$ and 0.4 , which is a probe of jet shape and its in-medium modification. Consis-
 174 tency to theoretical calculations is found within uncertainties. However, the calculations
 175 exhibit significant spread in the jet shape ratio, presenting an opportunity for more precise
 176 measurements to discriminate between them. A measurement of the inclusive jet yield in
 177 Au+Au collisions including both charged and neutral particle constituents using the much
 178 larger data set recorded in 2014, corresponding to 9.9 nb^{-1} [9] is underway. STAR also has
 179 full jet measurements in p+p collisions for use for the R_{AA} normalization.

180 A recent STAR measurement, likewise using the 9.9 nb^{-1} 2014 dataset, extends the semi-
 181 inclusive measurement of charged jets (anti- k_T , $R = 0.2$ and 0.5) recoiling from a high- E_T
 182 photon trigger to photon triggers in the range $15 < E_T^{trig} < 20 \text{ GeV}$ [10]. Currently, the
 183 recoil jet yield suppression for 0–15% Au+Au collisions (I_{AA}) is determined by comparison to
 184 the yield in p+p collisions calculated using PYTHIA-6 (STAR tune [8]) and PYTHIA-8 [11].
 185 Significant yield suppression in central Au+Au collisions is observed for $R = 0.2$, with less
 186 suppression for $R = 0.5$. Theoretical calculations predict a stronger dependence of I_{AA} on
 187 $p_{T,jet}^{ch}$ for $R = 0.5$ than observed. A measurement of this observable in p+p collisions is in
 188 progress, to provide a data reference rather than PYTHIA calculations for I_{AA} .

189 Jet yield suppression is an indirect measurement of energy loss, because it convolutes
 190 out-of-cone energy loss with the shape of the jet spectrum – a fixed energy loss generates
 191 greater suppression for a steeper spectrum. Since the jet spectrum shape depends strongly on
 192 the choice of observable (inclusive, semi-inclusive) and collision energy, direct comparison of
 193 different jet quenching measurements requires this effect to be taken into account. Figure 2

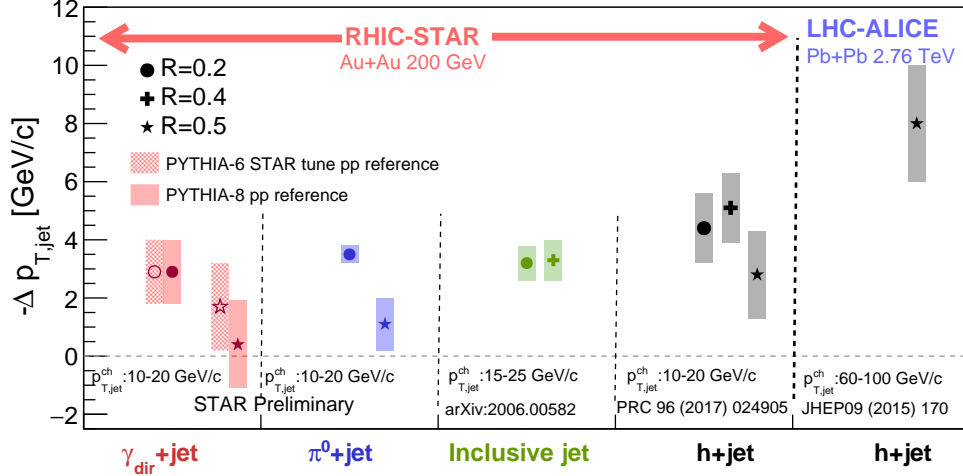


Figure 2: Out-of-cone jet energy loss derived from jet yield suppression measurements in A+A collisions (see text) for $\gamma_{dir}+jet$, π^0+jet , inclusive jet, and h+jet measurements at RHIC, and h+jet measurements at the LHC [9, 10]. Note the different $p_{T,jet}$ ranges.

194 shows the $p_{T,jet}$ shift needed between jet spectra measured in a reference system (p+p or
 195 peripheral A+A collisions) and in central A+A collisions, for several jet yield suppression
 196 measurements at RHIC and the LHC [9, 10]. The absolute magnitude of medium-induced
 197 jet energy loss is similar for several different observables at RHIC, and is smaller than the
 198 LHC measurement. Note that the $p_{T,jet}^{ch}$ range is significantly higher for the LHC h+jet
 199 measurement, so that the *relative* energy loss is smaller than at RHIC.

200 This is a first look at comparing medium-induced out-of-cone radiation at RHIC and the
 201 LHC. Clearly, as the measured $p_{T,jet}$ range at RHIC moves up and that at the LHC moves
 202 down in upcoming measurements, more precise comparisons can be made. Nevertheless,
 203 Fig. 2 already provides significant constraints on jet quenching calculations that seek to
 204 model RHIC and LHC measurements in a unified way.

205 **Jet-structure modifications:** The Fragmentation Function (FF), normalized per jet,
 206 provides information of the longitudinal momentum fraction ($z = p_{T,trk} \cos(\Delta r)/p_{T,jet}$) of
 207 charged particles projected along the jet axis. While FF have been measured previously at
 208 the LHC [12, 13], STAR has utilized the semi-inclusive approach to measure the FF of charged
 209 jets for the first time at RHIC [14]. The Mixed-Event approach developed in [1] is extended
 210 for the FF measurement, and utilized for the correction of uncorrelated jet contributions.
 211 The fully corrected FF are shown in Fig. 3 for jets of varying $p_{T,jet}^{ch}$ for mid-peripheral 40-60%
 212 collisions compared to PYTHIA-8 predictions shown by the dashed curved. The FF shape in
 213 data is reproduced by PYTHIA-8 in these peripheral collisions. Measurements are ongoing
 214 to extend to central collisions where one expects a larger path length for the recoil jet and
 215 enhanced medium effects.

216 Another observable of the jet transverse profile is the differential jet shape, measured in

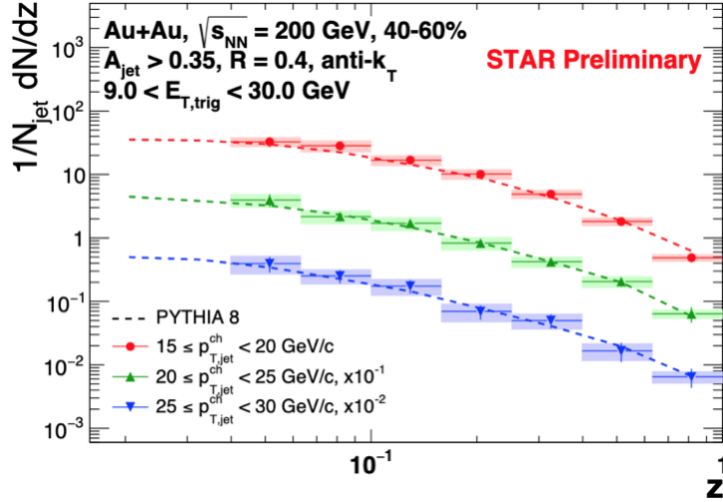


Figure 3: Fragmentation functions for recoil charged-particle jets of varying $p_{\text{jet},T}^{\text{ch}}$ with trigger $9.0 < E_T < 30.0$ GeV in 40–60% peripheral events compared to PYTHIA-8 simulations in the dashed curves.

217 radial annuli around the jet axis ($\rho(\Delta r)$). Utilizing the hard-core jet selection [15] which
 218 provides a pure sample of hard-scattered jets with a high constituent threshold, the fully
 219 corrected ρ as a function of Δr (distance between the constituent tracks and the jet axis)
 220 of leading jet with $20 < p_{T,\text{jet}} < 40$ GeV/c for central (0–10%) and mid-central (20–50%)
 221 events are calculated. To probe possible in-medium modification of the jet structure and
 222 its dependence on the path length in medium, this observable is also differentially measured
 223 based on the jet’s orientation with respect to the event plane for 20–50% mid-central colli-
 224 sions, as shown in Fig 4. High- $p_{T,\text{trk}}$ particles are found closer to the jet core, whilst softer
 225 constituents are more evenly distributed around the jet. In comparing the soft particle pro-
 226 duction for in-plane vs. out-of-plane jets one finds subtle hints of path-length dependence.

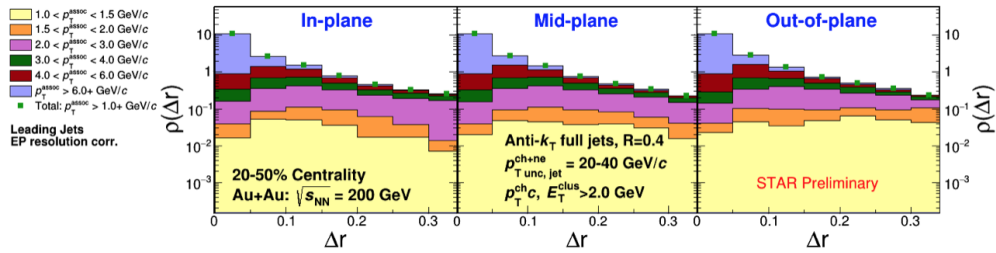


Figure 4: Differential measurement of the leading jet ($20 < p_{T,\text{jet}} < 40$ GeV/c) shapes in 20–50% central Au+Au collisions shown for different jet azimuthal angles with respect to the event-plane angle. The $p_{T,\text{trk}}$ -dependence of the associated tracks are shown in the different stacked histograms. Results are corrected for event-plane resolution effects.

228 **Jets in p+Au collisions:** STAR has searched for jet-medium interactions in p+Au colli-
 229 sions by looking at potential modifications of semi-inclusive charged-particle jet yields and
 230 jet substructure observables such as the jet mass and SoftDrop groomed jet mass. p+Au col-
 231 lisions are classified as low or high event-activity (EA) according to the particle multiplicity
 232 in the Au-going direction as measured by the BBC-East detectors.

233 The charged-particle jet spectra, normalized per HT trigger (uncorrected for detector
 234 effects) are shown on the left of Fig. 5 where the open (full) markers correspond to low (high)
 EA. The different colored markers represent the azimuthal separation between the trigger and

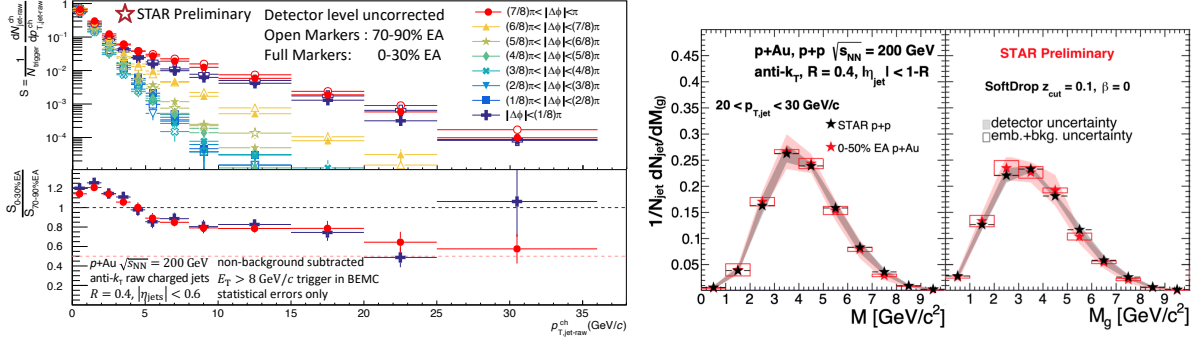


Figure 5: Left: Semi-inclusive charged jet spectra in p+Au collisions for high and low event-activity (EA) events, the ratio is shown in the bottom panel. Right: Fully corrected (groomed) jet-mass distributions in p+Au with high EA and p+p collisions.

235 the recoil jet. We see for jet with $p_{T, \text{jet-raw}} > 10$ GeV/c, a significant suppression in high to
 236 low EA events for both the trigger-side and recoil-side spectra. These suppression ratios are
 237 qualitatively different from jet suppression in Au+Au collisions, where the recoil jets traverse
 238 more QGP on average and are suppressed compared to the trigger-side. In investigating if
 239 this suppression is a result of modification of jet structure, STAR also measured the fully
 240 corrected jet-mass and groomed jet-mass distributions, normalized per jet, on the right of
 241 Fig. 5. The distribution in high EA p+Au collisions is comparable to that in p+p collisions
 242 within the systematic uncertainties, and this leads to the conclusion that CNM effects do not
 243 significantly affect the jet substructure. The jet mass measurements in p+Au will be followed
 244 in a more differential fashion by studying finer EA classes and rapidity selections which can
 245 isolate jets originating from the Au vs p side. Both of these measurements from STAR point
 246 to lack of jet modification from nuclear effects and also to a more fundamental selection bias
 247 when identifying classes of high vs low activity events in asymmetric collisions.

249 1.1.2 Bulk Correlations

250 Over the past years, the STAR collaboration has performed a series of correlation measure-
 251 ments directed towards a comprehensive understanding of the QCD phase diagram and the
 252 bulk properties of the QGP phase. Here we highlight the most recent STAR results on bulk
 253 correlations, which are expected to shed light on the QCD phase diagram as well as on the
 254 transport properties of the QGP.

255 **Net-proton number fluctuations and the QCD critical point:** One of the main
 256 goals of the STAR Beam Energy Scan (BES) program is to search for possible signatures
 257 of the QCD critical point (CP) by scanning the temperature (T) and the baryonic chemical
 258 potential (μ_B) plane by varying the collision energy. When the system produced in the heavy
 259 ion collisions approaches the CP, the correlation length diverges. Higher order cumulants
 260 of conserved net-particle multiplicity distributions are sensitive to such correlation lengths
 261 as the divergence of correlation length leads to enhanced fluctuations in the net-particle
 multiplicity distributions.

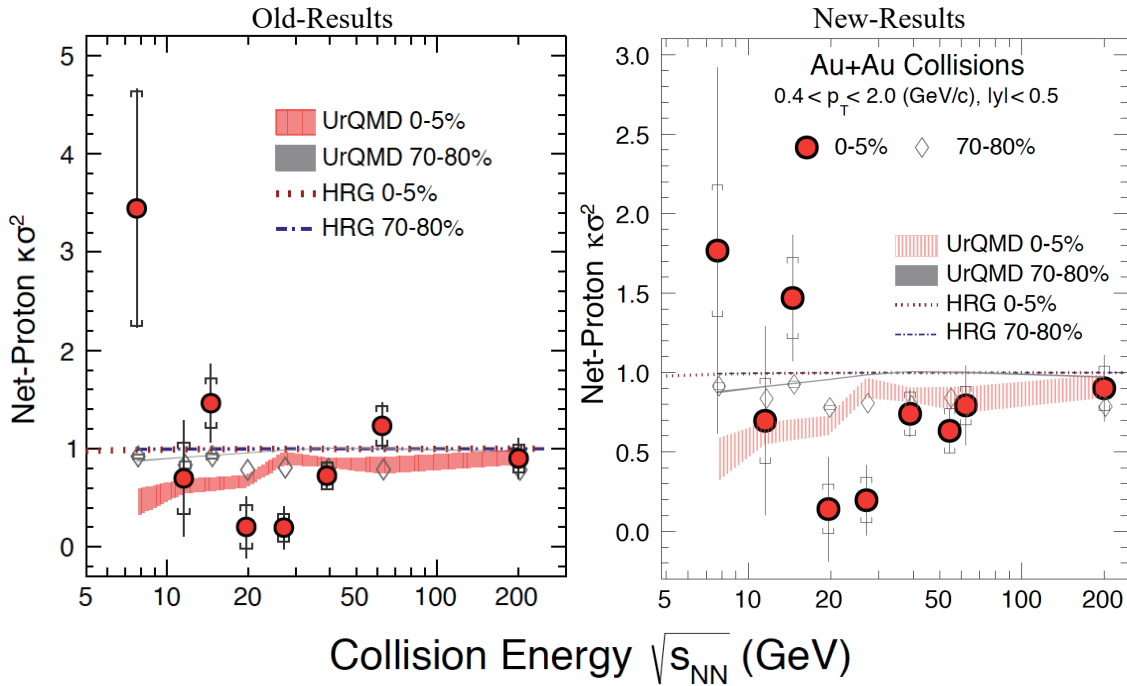


Figure 6: $\kappa\sigma^2$ as a function of collision energy for net-proton distributions measured in central (0-5%) and peripheral (70-80%) Au+Au collisions within $0.4 < p_T$ (GeV/c) < 2.0 and $|y| < 0.5$. The error bars and caps show statistical and systematic uncertainties, respectively. The dashed and dash-dotted lines correspond to results from a hadron resonance gas (HRG) model. The shaded bands are the results of a transport model calculation (UrQMD). The model calculations utilize the experimental acceptance and incorporate conservation laws for strong interactions, but do not include the dynamics of phase transition or critical point. **The new results are obtained after removing the spoiled events, the largest changes are seen in central Au+Au collisions at 7.7 and 62.4 GeV.**

262
 263
 264

The ratios of the cumulants of identified net-particle multiplicity distributions, such as net-protons, have been predicted to be ideal observables sensitive to the onset of the QCD

265 phase transition and the location of the CP. A non-monotonic variation of these ratio of
 266 cumulants, such as C_4/C_2 ($=\kappa\sigma^2$), as a function of collision energy has been proposed to be
 267 an experimental signature of the CP. Taking the ratios of cumulants has advantages as it
 268 cancels the volume fluctuations to first order. Further, these ratios of cumulants are related
 269 to the ratio of baryon-number susceptibilities at a given T and μ_B . Near the critical point,
 270 QCD-based calculations predict the net-baryon number distributions to be non-Gaussian
 271 and susceptibilities to diverge, causing these ratios to have non-monotonic variation as a
 272 function of collision energy. However, the finite-size and finite-time effects in heavy-ion
 273 collisions limit the growth of correlation length, and hence it could restrict the values of $\kappa\sigma^2$
 274 from its divergence as a function of collision energy.

275 Figure 6 shows the collision energy variation of net-proton $\kappa\sigma^2$ for central and peripheral
 276 Au+Au collisions within the acceptance of $0.4 < p_T < 2.0$ GeV and $|y| < 0.5$. In central
 277 collisions, a non-monotonic variation with beam energy is observed for $\kappa\sigma^2$ with a significance
 278 of 3.0σ . In contrast, monotonic behavior with beam energy is observed for the statistical
 279 hadron gas (HRG) model, and for a nuclear transport UrQMD model without a critical
 280 point, and experimentally in peripheral collisions.

281 High statistics data from the ongoing BES-II program can provide precision measure-
 282 ments at higher μ_B region in the QCD phase diagram. In addition, due to the iTPC [16]
 283 and eTOF [17] upgrades, a differential measurement in $|y| < 1.5$ and $p_T > 0.15$ GeV/c will be
 284 explored. The study of acceptance dependence of net-proton $\kappa\sigma^2$ and other cumulants ra-
 285 tios are important to understand critical fluctuation. Furthermore, the forward Event-Plan
 286 Detector (EPDs) [18] can also be used to determine the centrality selection in heavy-ion
 287 collisions for this measurement.

288 **Global polarization measurements at 27 GeV:** In heavy-ion collisions, many theoret-
 289 ical models propose that the large angular momentum in the collisions of two nuclei [19–21]
 290 can be transferred to the microscopic constituent of the created matter. Consequently, the
 291 spin of the produced quarks and gluons might be polarized along the direction of the global
 292 angular momentum due to spin-orbit coupling. The direction of the global angular momen-
 293 tum is perpendicular to the reaction plane, as defined by the incoming beam and the impact
 294 parameter vector. This direction can be determined from directed flow measurements of the
 295 spectators. STAR observed significant non-zero polarization of hyperons [20] with increasing
 296 strength with decreasing collision energy (from 200 to 7.7 GeV).

297 We recently report more differential measurements using our newly installed EPDs in
 298 Au+Au collisions at 27 GeV as functions of the hyperon’s transverse momentum, and pseudo-
 299 rapidity. In Fig. 7 left panel we observe that the polarization does not show a strong
 300 dependence on p_T , albeit large uncertainties. There are several expectations on the p_T
 301 dependence on the polarization. If global polarization is generated by the vorticity of the
 302 initial state that does not have a strong p_T dependence then the result is compatible with
 303 expectations. Alternatively, at lower p_T , due to the smearing effect caused by scattering at
 304 later stages of the collisions, we might expect a decrease of the polarization. In addition,
 305 one might expect a decrease in the polarization at higher p_T due to the expected larger

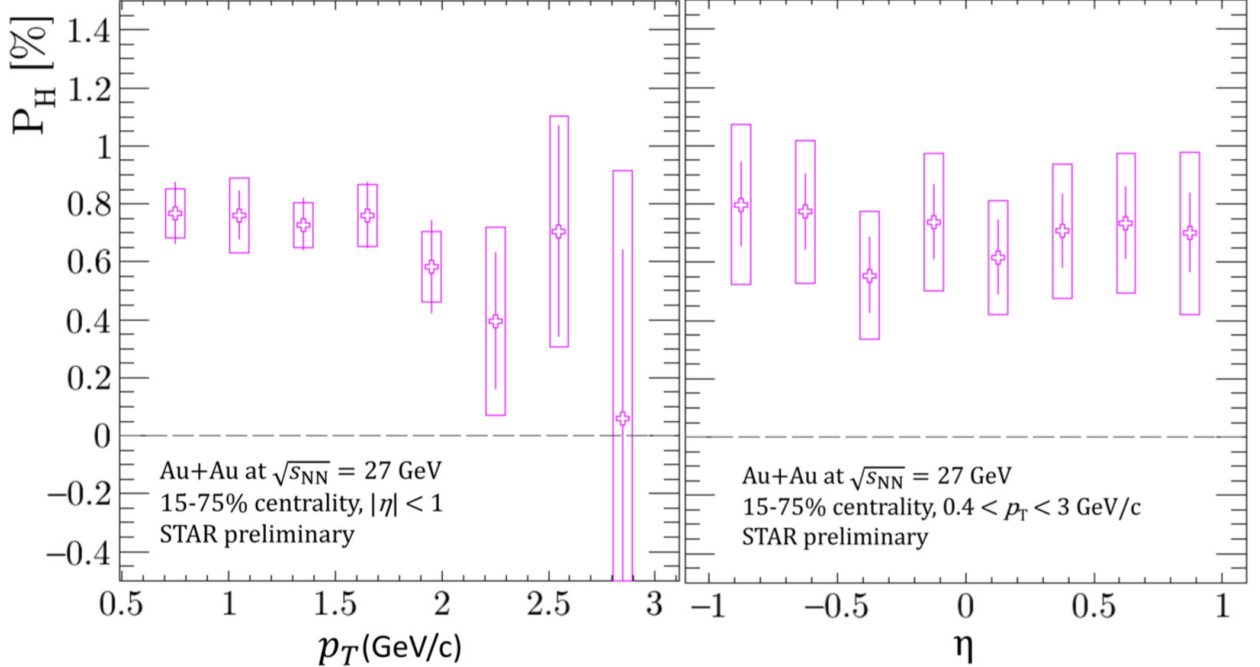


Figure 7: The global polarization measurements as a function of p_T and η in 15-75% central Au+Au collisions at $\sqrt{s_{NN}} = 27$ GeV. The figure is taken from Ref [22].

306 contribution from jet fragmentation. Fig 7 right panel shows the pseudo-rapidity dependence
 307 of the polarization measurement, no η -dependence of the polarization is observed within
 308 uncertainties. The vorticity is expected to decrease at larger rapidity, but might also have a
 309 local minimum at $\eta=0$ due to complex shear flow structure [21, 23, 24] however, this might
 310 be difficult to observe within STAR's acceptance. This preliminary observation of no p_T or η
 311 dependence of the polarization is consistent with our previous measurements at 200 GeV [19].
 312 STAR plans to perform the same measurement with an extended pseudo-rapidity coverage
 313 using the iTPC detector upgrade and with higher statistics BES-II data set enabling higher
 314 a precision result.

315 **Global spin alignment of K^{*0} and ϕ :** Unlike the self-analyzing (anti) Λ , the polarization
 316 of vector mesons such as $\phi(1020)$ and $K^{*0}(892)$ cannot be directly measured since vector
 317 mesons mainly decay through the strong interaction in which parity is conserved. The spin
 318 alignment of vector mesons can be given by a 3×3 spin density matrix with unit trace [25].
 319 The spin density matrix diagonal elements ρ_{nn} , $n=0,1$ and -1 , represent the probabilities
 320 for the spin component along the quantization axes. When there is no spin alignment this
 321 means that all three spin states (ρ_{nn}) have equal probability to be occupied meaning $\rho_{nn} =$
 322 $1/3$. Out of the three diagonal elements, only the $n=0$ case is independent of the other two.
 323 Consequently, it is intriguing to experimentally investigate the ρ_{00} of vector mesons.

324 Figure 8 shows the centrality dependence of ρ_{00} for both vector meson species for Au
 325 + Au collisions at 200 GeV. The ϕ -meson results are presented for transverse momentum

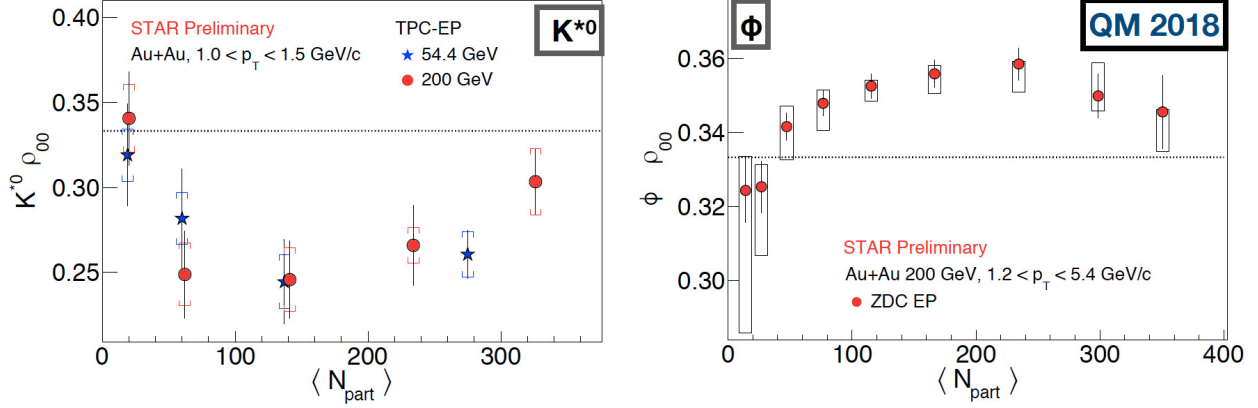


Figure 8: The spin alignment ρ_{00} measurements of vector mesons K^{*0} and ϕ as a function of N_{part} for the indicated p_T range of the Au+Au collisions at 200 and 54.4 GeV. The figure is taken from Ref [26].

326 $1.2 < p_T < 5.4$ GeV/c, and ρ_{00} for this species is significantly above 1/3 for mid-central
 327 collisions, indicating finite global spin alignment. The K^{*0} -meson results are presented for
 328 transverse momentum $1.0 < p_T < 1.5$ GeV/c, and the magnitude of ρ_{00} for this particle
 329 species is observed to be significantly less than 1/3 for mid-central collisions.

330 The distinction between the global spin alignment for K^{*0} and ϕ may be assigned to
 331 different in-medium interactions due to the difference in the lifetime (ϕ -meson is 10 times
 332 larger than K^{*0} -mesons), and/or a different response to the vector meson field. These global
 333 spin alignment results are expected to shed light on the possible vector meson fields [27, 28].
 334 Such investigations are extremely important since vector meson fields are a crucial part of
 335 the nuclear force that binds nucleons to atomic nuclei and are also central in describing
 336 properties of nuclear structure and nuclear matter.

337 **Nuclear deformation measurements:** Deformation is a fundamental property of atomic
 338 nuclei that reflects the correlated nature of the dynamics of nucleons within the quantum
 339 many-body system. The majority of atomic nuclei possess an intrinsic deformation, most of
 340 which is an axial quadrupole, or ellipsoidal, deformation.

341 Prior relativistic heavy-ion collision measurements from STAR reported strong signatures
 342 of nuclear deformation using detailed comparisons between Au+Au collisions and U+U col-
 343 lisions [29]. These measurements suggest that U+U collisions being much more deformed
 344 in their ground state. Consequently, we can say that these detailed comparisons between
 345 Au+Au and U+U collisions enabled us to examine the geometry of the colliding nuclei.

346 The study of mean transverse momentum dependence of the elliptic and triangular flow
 347 harmonics in Au+Au and U+U collisions are recently proposed by theory calculations [31]
 348 that are more sensitive to the deformation of the colliding nuclei.

349 Figure 9 shows the scaled mean p_T dependence of v_2 and v_3 for the central Au+Au and
 350 U+U collisions. STAR preliminary data show a clear positive correlation for v_2 and v_3 in
 351 Au+Au collisions that is in agreement with the v_3 from U+U collisions. In contrast, a
 352 nontrivial negative correlation is observed in v_2 as a function of scaled mean p_T in U+U

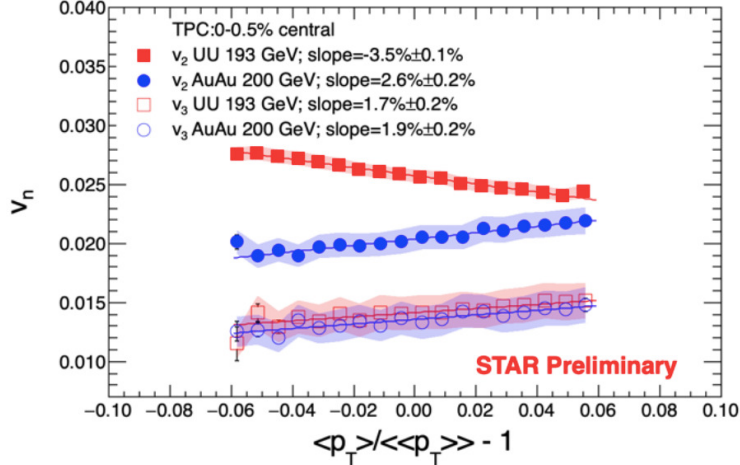


Figure 9: The scaled mean p_T dependence of the elliptic and triangular flow harmonics for 0-0.5% central Au+Au and U+U collisions. The figure is taken from Ref [30].

353 collisions. Also these preliminary results are consistent with the theoretical expectation for
 354 a deformed U nuclei [31].

355 **Flow correlations and fluctuations measurements:** Flow harmonics (v_n) calculated
 356 from the Fourier expansion of the particle azimuthal distributions are commonly employed
 357 to quantify the azimuthal anisotropy of particle emission relative to the collision symmetry
 358 planes. While the lower-order Fourier coefficients (v_2 and v_3) are more directly related to the
 359 corresponding eccentricities of the initial state, the higher-order flow harmonics ($v_{n>3}$) can
 360 be induced by a non-linear (mode-coupled) response to its lower-order harmonics and also
 361 with a linear response to the same-order anisotropy. These higher-order flow harmonics and
 362 their linear and mode-coupled contributions can be used to constrain the initial conditions
 363 and the transport properties of the medium in the theoretical calculations.

364 The v_2 and v_3 harmonics are sensitive to the respective influence of the initial-state
 365 eccentricity and the final-state viscous attenuation, which have proven difficult to disentangle.
 366 The mode-coupled coefficients show characteristically different dependencies on the viscous
 367 attenuation and the initial-state eccentricity [32]. Therefore, they can be used in conjunction
 368 with measurements for the v_2 and v_3 harmonics to leverage additional unique constraints for
 369 initial-state models, as well as reliable extraction of transport coefficient.

370 Figure 10 shows the mode-coupled response coefficients, $\chi_{4,22}$ and $\chi_{5,23}$, with a weak
 371 centrality dependence, akin to the patterns observed for similar measurements at the LHC
 372 for Pb+Pb collisions at 2.76 TeV [34]. These patterns suggest that the mode-coupled response
 373 coefficients are dominated by initial-state eccentricity couplings which is known from models
 374 to have a weak dependence on beam energy. The correlations of the event plane angles, $\rho_{4,22}$
 375 and $\rho_{5,23}$ show a strong centrality dependence that agrees well with the LHC measurements
 376 for Pb+Pb collisions at 2.76 TeV. The predictions from viscous hydrodynamic models [35,
 377 36] give a good qualitative description of the mode-coupled response coefficients and the

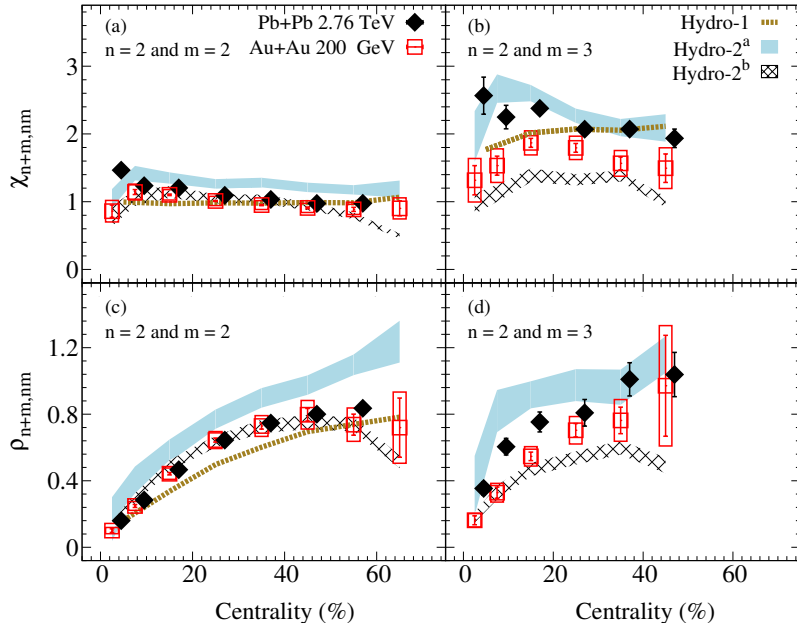


Figure 10: Results as a function of centrality for Au+Au collisions at 200 GeV [33]. Panels (a) and (b) shows the mode-coupled response coefficients, and panels (c) and (d) show the correlations of event plane angles. The closed-symbols represents similar LHC measurements [34]. The shaded bands indicate hydrodynamic model predictions Hydro-1 [35], Hydro-2^a and Hydro-2^b [36].

378 correlation of event plane angles.

379 **Small system measurements:** The comparisons of theoretical models to the flow har-
 380 monics, v_n , continue to be an essential avenue to evaluate the transport properties of partonic
 381 matter produced in large to moderate-sized collision systems [37–39]. For the small collision-
 382 systems formed in p/d/³He+Au and p+Pb collisions, collective flow might not develop due
 383 to the presence of large gradients in the energy-momentum tensor that could trigger non-
 384 hydrodynamic modes [40, 41]. Certainly, the most important question that divided our field
 385 is whether an alternative initial-state-driven mechanism [42] dominates over hydrodynamic
 386 expansion for these collision systems.

387 Current measurements for p/d/³He+Au collisions, which supplement earlier measure-
 388 ments at both RHIC [43] and the LHC [44] aim to address the respective influence of collision-
 389 system size and its subnucleonic fluctuations, and viscous attenuation on the measured v_n .

390 Figure 11 shows the $v_2(p_T)$ and $v_3(p_T)$ values for p/d/³He+Au collisions at 200 GeV
 391 before and after non-flow subtraction, compared for all three subtraction techniques. The
 392 presented results show non-flow contributions which are system-dependent, but the non-
 393 flow subtracted v_2 (top panels) and v_3 (bottom panels) are method-independent within the
 394 uncertainties.

395 These STAR measurements with non-flow subtracted show that for the comparable
 396 charged-hadron multiplicity (N_{ch}) events v_2 and v_3 , values are independent of collision sys-

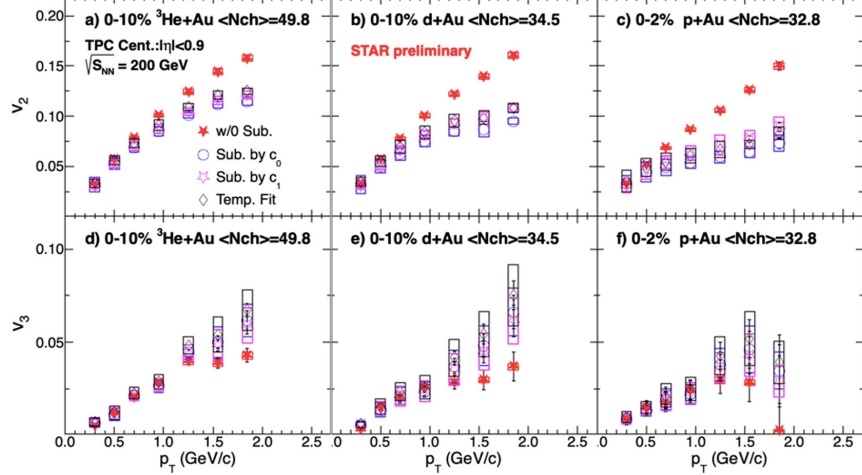


Figure 11: Comparison of the $v_{2,3}(p_T)$ values for p/d/ ^3He +Au collisions at 200 GeV, before and after non-flow subtraction. The figure is taken from Ref [45].

397 tem. These observations are compatible with the significant influence of the subnucleonic
 398 fluctuations-driven eccentricities, $\epsilon_{2,3}$, in a system whose size is primarily determined by
 399 N_{ch} . However, they are incompatible with the notion of shape engineering in p/d/ ^3He +Au
 400 collisions.

401 1.1.3 Light Flavor Spectra and Ultra-peripheral Collisions

402 The Light Flavor Spectra and Ultra-peripheral Collisions (LFSUPC) physics working group
 403 is responsible for the measurements of calibrated production yields and spectra in inclusive
 404 ion-ion collisions, ultra-peripheral collisions, and exclusive p+p collisions.

405 In ion-ion collisions, analysis efforts can be grouped based on the methodology and physics
 406 issues. The general categories include light charge hadrons (π , K , p), strange hadrons (ϕ ,
 407 Λ , Ξ , Ω), light nuclei (d, t, ^3He , ^4He), and hyper-nuclei ($^3_\Lambda H$ and $^4_\Lambda H$). Examples of recent
 408 results from light nuclei and hyper-nuclei are shown in other sections (see sections 2.2.3 and
 409 2.2.2). Here some recent results will be presented from the light charged hadron and strange
 410 hadron analyses.

411 **Light hadron production:** Light charged hadron spectra and yields are measured using
 412 particle identification through dE/dx in the TPC, $1/\beta$ in the time-of-flight detectors and
 413 careful study of the acceptance and efficiency of the detectors. These studies are particularly
 414 useful in defining the basic thermal properties (T and μ_B) of the system. Previous studies
 415 of the light charged hadrons from BES-I measured the spectra and yields at midrapidity.
 416 The newest results now include rapidity dependence which allows for a better understanding
 417 of baryon stopping, which is key to the dependence of μ_B with $\sqrt{s_{NN}}$. New preliminary π ,
 418 K, and p transverse mass spectra are shown as a function of rapidity in Fig. 12 for Au+Au
 419 collisions at $\sqrt{s_{NN}} = 27$ GeV. Additional pre-preliminary results have been produced from
 420 fast offline pre-calibration quality assurance productions from the other BES-II collider and

421 fixed-target energies.

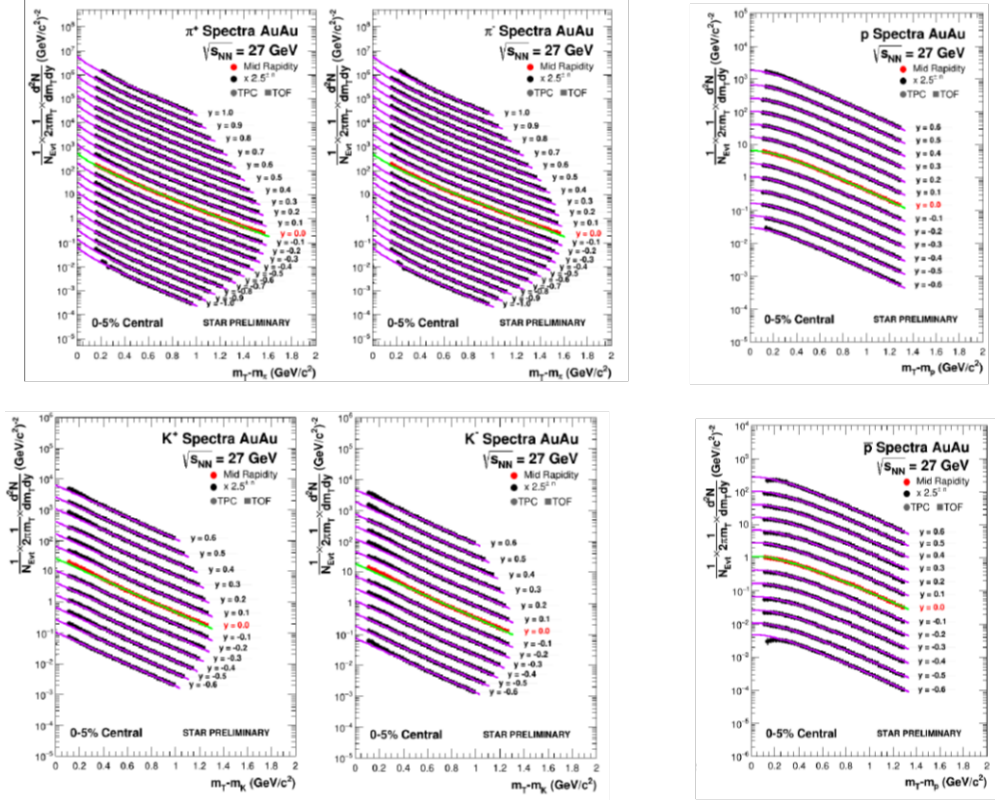


Figure 12: Transverse mass spectra for pions, Kaons, and protons from Au+Au collisions at $\sqrt{s_{NN}} = 27$ GeV as a function of rapidity.

422 **Strange hadron production:** Strange hadron spectra and yields are measured by deter-
 423 mining the invariant mass from the charged daughters from weak decays of neutral strange
 424 hadrons. These studies define the role of the strange quark in the thermodynamic evolution
 425 of the system. STAR has recently implemented a new V^0 finding routine called *KFparticle*
 426 which increases the sensitivity of our strange hadron studies. The highlights of recent
 427 measurements have come from the newest fixed-target data. The fixed-target energy range
 428 covers the production threshold energies for Ξ^- (3.247 GeV), Ω^- (4.09 GeV), Ξ^+ , Ξ^- (4.52
 429 GeV), and Ω^+ , Ω^- (5.22 GeV). Figure 13 shows the invariant mass plots for measurements
 430 of Λ 's, Ξ 's, and Ω 's for fixed-target Au+Au at $\sqrt{s_{NN}}$ of 3.0 and 7.2 GeV. Additional pre-
 431 preliminary measurements have been made at other collider and fixed-target energies. In
 432 addition, studies of the production of the ϕ meson have been made at 3.0 and 7.2 GeV.

433 **Central exclusive production:** Central exclusive production is measured in p+p colli-
 434 sions using the very forward roman pot detectors to identify the the two colliding protons
 435 and the TPC to measure the products. Figure 14 shows the invariant mass of pion pairs

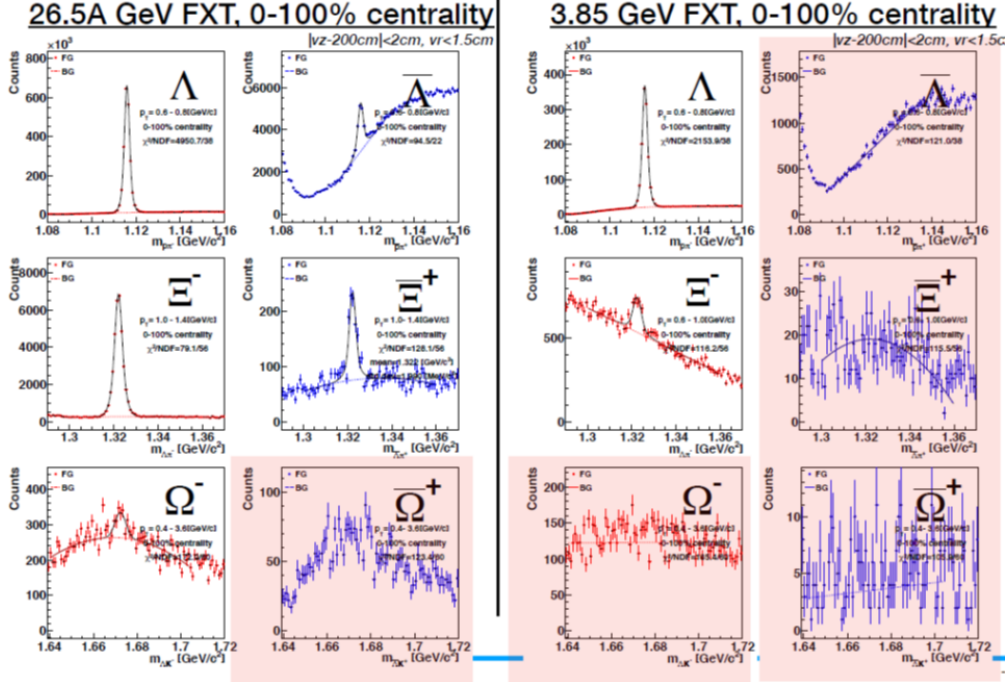


Figure 13: Invariant mass plots for measurements of Λ 's, Ξ 's, and Ω 's for fixed-target Au+Au collisions at $\sqrt{s_{NN}}$ of 3.0 and 7.2 GeV (single beam energies of 3.85 and 26.5 GeV respectively).

436 in exclusive p+p events at 200 GeV. These are the first measurements at this energy and
 437 show significant peaks in the invariant mass spectra that were not predicted by the models.
 438 Similar results are available for kaon and proton pairs.

439 **Electromagnetic probes:** Electromagnetic radiation from high-energy heavy-ion colli-
 440 sions provides rich information about the properties of the produced medium. Dileptons
 441 directly probe the in-medium electromagnetic correlator of hadronic currents [46, 47]. Dy-
 442 namical information on in-medium spectral functions encodes not only changes in degrees
 443 of freedom, chiral symmetry restoration [48–50], and transport properties of medium like
 444 the electrical conductivity [51, 52], but also the life time and average temperature of the
 445 interacting fireball [53], and the emission history and origin of the radiation [54–57].

446 STAR reported measurement of thermal dilepton radiation ranging from $\sqrt{s_{NN}} = 200$
 447 GeV down to 19.6 GeV [58–61]. A significant excess in the low-mass region when compared
 448 to the known hadronic sources has been observed. It was shown that the predictions of
 449 hadronic manybody theory for a melting ρ meson, coupled with QGP emission utilizing
 450 a modern lattice QCD-based equation of state [51, 62], yield a quantitative description of
 451 dilepton spectra in heavy-ion collisions [58, 61]. This is demonstrated in Fig. 15 (left panel).
 452 Moreover, it has been shown that the integrated low-mass excess radiation provides a direct
 453 measure of the total fireball lifetime [60]. Secondary vertex rejection employing information
 454 provided by the Heavy Flavor Tracker installed for Run-14 and Run-16 will enable unique

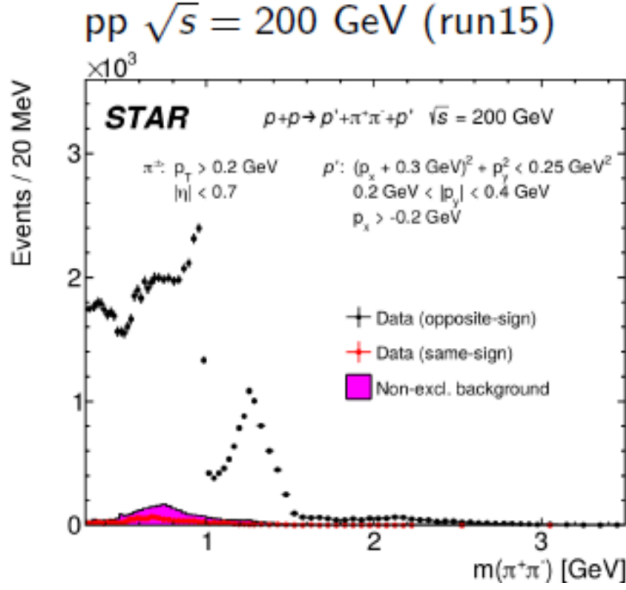


Figure 14: Invariant mass spectra for pion pairs from exclusive p+p events at 200 GeV.

455 temperature measurements of the QGP.

456 The low-mass line shape will provide a critical test of the ρ -melting scenario (which is
 457 consistent with expectations of chiral symmetry restoration) at vanishing baryon chemical
 458 potential. A precision measurement at top RHIC energy will provide additional constraints
 459 that can be directly tested against the lattice QCD predictions and will be put in focus via
 460 the additional data collected in 2023-2025 (see section 2.4.3).

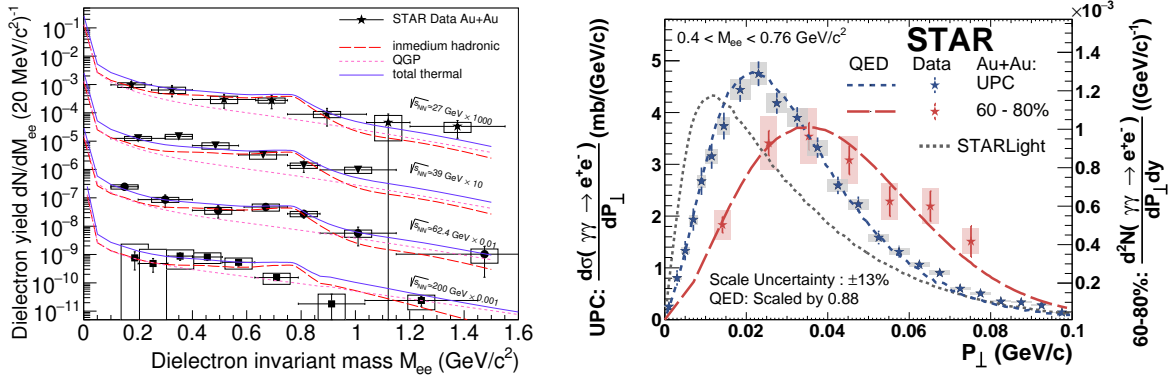


Figure 15: Left: Acceptance-corrected dielectron excess mass spectra, normalized by dN_{ch}/dy , for Au+Au collisions at $\sqrt{s_{NN}} = 27, 39, 62.4, 200$ GeV. Right: Comparison of the P_T distribution in 60–80% central Au+Au collisions with that in UPCs [63].

461 Dileptons generated by the intense electromagnetic fields accompanying the relativistic
 462 heavy nuclei at large impact parameters [64], in ultra-peripheral collisions (UPC) where
 463 there is no nuclear overlap has recently become experimentally accessible, offering several
 464 opportunities. According to the equivalent photon approximation (EPA), the electromag-

465 netic field generated by an ultra-relativistic nucleus can be viewed as a spectrum of quasi-real
 466 photons coherently emitted by the entire nucleus and the dilepton production process can be
 467 represented as $\gamma + \gamma \rightarrow l^+ + l^-$. Recently, the STAR and ATLAS collaborations made mea-
 468 surements of dileptons at small impact parameters with nuclear overlap, and found that the
 469 electromagnetic production of dileptons can also occur in hadronic collisions. Furthermore,
 470 a significant P_{\perp} broadening as shown in Fig. 15 (right panel) effect for lepton pairs produced
 471 by the two photon scattering process has been observed in hadronic collisions compared to
 472 measurements in UPC and to EPA calculations. Precision measurements will provide an im-
 473 portant constraints for quantitative theoretical analyses of magnitude and duration of initial
 474 magnetic fields. It was perceived that photons participating in such collisions are quasi-real
 475 with transverse-momentum $k_t \simeq 1/R$ (30 MeV/c) reflecting the virtuality and uncertainty
 476 principle of their origin. This led to the implementation in many EPA models that the initial
 477 transverse momentum of the dilepton pairs does not depend on impact parameter and the
 478 transverse space coordinates where the pair are created are randomly distributed due to the
 479 same principles. Our new measurements of centrality dependence and azimuthal distribu-
 480 tions have shown that the photons behave like real photons in all observables and the renewed
 481 models and theories have demonstrated that correction to the real photon approximation is
 482 suppressed at the order of $1/\gamma^2$ even to the pair's transverse momentum distribution. The
 483 discovery of the Breit-Wheeler process and the utilization of linearly polarized photons in
 484 UPC are conceptually and experimentally highly nontrivial. With future high statistics data
 485 with larger TPC acceptance in UPC, we can explore the phase space of photon collisions
 486 in transverse momentum, rapidity and momentum-space-spin correlations in extreme QED
 487 field [65,66] (see section 2.4.3).

488 1.1.4 Heavy-Flavor

489 The production of heavy-flavor (HF) quarks proceeds predominately via the hard scatterings
 490 of partons in $p(A)+p(A)$ collisions. This fact gives rise of the utility of heavy-flavor hadron
 491 measurements in heavy-ion experiments since they are produced independently of the QCD
 492 medium and probe it's properties by scattering with the medium constituents. Topics of
 493 medium-induced parton energy loss, QGP transport properties, hadronization mechanisms,
 494 and quarkonia melting are some of the pivotal studies that have emerged within the HF
 495 category. Besides the highlights discussed in detail below, the following measurements have
 496 been recently published: First Measurement of Λ_c Baryon Production in Au+Au Collisions
 497 at $\sqrt{s_{NN}} = 200$ GeV [67]; Measurement of inclusive J/ψ suppression in Au+Au collisions at
 498 $\sqrt{s_{NN}}=200$ GeV through the dimuon channel at STAR [68]; First Observation of the Directed
 499 Flow of D^0 and \bar{D}^0 in Au+Au Collisions at $\sqrt{s_{NN}} = 200$ GeV [69].

500 **Charm coalescence:** Recent measurements of D^0 [70] and D^+ meson yields (shown at
 501 Hard Probes 2020) as a function of transverse momentum (p_T) in heavy-ion collisions show a
 502 significantly suppressed spectrum with respect to $p + p$ collisions. The two mechanisms that
 503 predominately produce suppressed meson distributions are parton energy loss in the QGP
 504 and different hadronization schemes. The latter is nicely illustrated via the measurement of

505 the Λ_c^+/D^0 yield ratio [67], which is significantly enhanced with respect to the expectation
 506 in $p + p$ collisions and is attributed to baryon production via coalescence hadronization.
 507 Recently, STAR has measured the ratio of D_s^+/D^0 yields in heavy-ion collisions, which
 508 is important as it probes charm hadronization and strangeness enhancement mechanisms.
 509 Utilizing the excellent pointing resolution resolution of the Heavy Flavor Tracker (HFT), the
 510 D_s is measured in 2014 and 2016 data via topological reconstruction using a multi-variate
 511 analysis (MVA). The final results of D_s^+ yield with respect to D^0 were reported in the 2019
 512 Quark Matter conference, and are shown in Figure 16. The ratios for 0-10% (blue points)
 513 and 10-40% (red points) centrality regions are consistent within experimental uncertainties.
 514 Also shown in the left panel are the ratios averaged over $p+p/e+p/e+e$ collisions, PYTHIA,
 515 and a model calculation (TAMU) including coalescence hadronization for 10-40% centrality.
 516 The D_s yield is significantly enhanced in Au+Au collisions with respect to that of elementary
 517 $p+p/e+p/e+e$ collisions. Shown in the right panel are model calculations including sequential
 518 (solid lines) and simultaneous (dashed lines) coalescence for both Au+Au collisions at RHIC
 519 and Pb+Pb collisions at LHC energies. The ALICE data, also shown in the right panel,
 520 are consistent within uncertainties with the STAR data. The model including sequential
 521 coalescence is able to best capture the trends in the data.

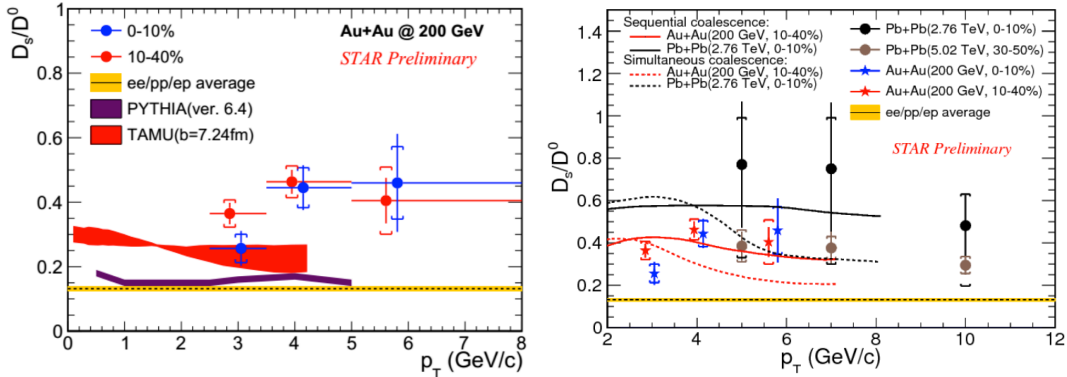


Figure 16: Left: STAR measurement of the D_s/D^0 ratio in 0-10% (blue circles) and 10-40% (red circles) centrality Au+Au collisions as a function of $D_s p_T$. The yellow shaded band shows the average from $p + p/e + p/e + e$ collisions. The purple and red shaded bands show the expectations from PYTHIA and TAMU model calculations, respectively. Right: STAR D_s/D^0 ratio measurements compared to model calculations including sequential (solid lines) and simultaneous coalescence (dotted lines) hadronization, and data from the ALICE measurements (blue and brown circles) and the respective model calculations at LHC energies.

522 **Mass dependence of partonic energy loss:** The mass dependence of parton energy
 523 loss has been probed in heavy-ion collisions with the measurements of light- and heavy-flavor
 524 hadron nuclear modifications factors (R_{AA}). At high p_T , where mass effects are predicted
 525 to significantly modify the quark energy loss from gluon radiation in the QGP, the values
 526 of light-flavor and charm hadron R_{AA} are measured to be degenerate, and can be explained

527 by mechanisms that are not related to parton energy loss (e.g, see [71]). In that respect
 528 systematic comparisons of both bottom and charm hadron nuclear modification factors are
 529 predicted to be a clean probe of the mass dependence of parton energy loss by several model
 530 calculations [72–75]. However, from an experimental point of view measuring bottom hadrons
 531 have been difficult at RHIC due to the low bottom quark production cross-section, and have
 532 only been accessible via the measurement of displaced electrons or charmed hadrons. STAR
 533 has now reported at the 2019 Quark Matter conference an updated measurement of single
 534 electrons from bottom semileptonic decays utilizing both 2014 and 2016 data sets. The
 535 contribution of bottom- and charm-decayed electrons, and backgrounds, are topologically
 536 separated using the three-dimensional distance-of-closest approach (DCA) utilizing the HFT
 537 detector. In contrast to previous measurements utilizing the transverse dimension DCA
 538 (DCA_{xy}), the 3D DCA is able to separate charm- and bottom-decay electrons with greater
 539 significance since the longitudinal and transverse DCA have similar resolution. The updated
 540 STAR measurement also includes an improved electron identification selection, which is based
 541 off a projective likelihood MVA. The improvement in the mis-identified hadron fraction is a
 542 factor of two when compared to traditional cut-based particle identification. The results of
 543 bottom- and charm-decayed electron R_{AA} are shown in Figure 17 in the top panel, and their
 544 ratio in the bottom panel. A constant fit to the double ratio is used to quantify the enhanced
 545 $b \rightarrow e R_{AA}$ and is measured to be $1.92 \pm 0.25(\text{stat.}) \pm 0.21(\text{syst.})$. Shown in the bottom panel as
 546 the hashed blue curve is a null hypothesis where we assume equal values of R_{AA} for charm and
 547 bottom hadrons and then fold the distributions to the decay-electron, and subsequently take
 548 a double ratio. Performing this exercise shows the effects from different production spectra,
 549 fragmentation, and decay phase-space of charm and bottom hadrons, and it is clearly seen
 550 these effects have a small impact on the double ratio. The double ratios of $b \rightarrow e$ to $c \rightarrow e$
 551 R_{CP} are also measured and a similar constant fit as in the R_{AA} case is performed and found
 552 to be $1.68 \pm 0.15(\text{stat.}) \pm 0.12(\text{syst.})$ and $1.38 \pm 0.08(\text{stat.}) \pm 0.03(\text{syst.})$ for the ratios of $R_{CP}(0-$
 553 $20\%/40-80\%)$ and $R_{CP}(0-20\%/20-40\%)$, respectively. We additionally compare the data to
 554 a modified Langevin transport model (DUKE) [73] which includes the mass dependence
 555 of parton energy loss, and within uncertainties the data and model are consistent in both
 556 the absolute R_{AA} data and the double ratios of R_{AA} and R_{CP} . Combining the agreement
 557 between model and experiment, and the quality of the data, these observations represent,
 558 for the first time, evidence of mass-ordering of parton energy loss in heavy-ion collisions.

559 **Charm and bottom flow:** Measurements of heavy-flavor flow are also essential to under-
 560 standing the QGP properties as particle flow and yield provide a test-bed for model calcula-
 561 tions to simultaneously describe the data. It has already been established by STAR [76] in
 562 200 GeV Au+Au collisions that D^0 hadrons have a significant elliptic flow that is compara-
 563 ble to light-flavor hadrons after taking into account particle mass and number of constituent
 564 quarks. Measurements of heavy-flavor hadron flow at lower collision energies have been ex-
 565 plored via the measurements of single electron elliptic flow in the 2017 and 2018 data sets,
 566 and was reported at the 2020 Hard Probes conference. Previous STAR measurements of
 567 heavy-flavor electron v_2 in 62.4 and 39 GeV Au+Au collisions [77] were statistically limited

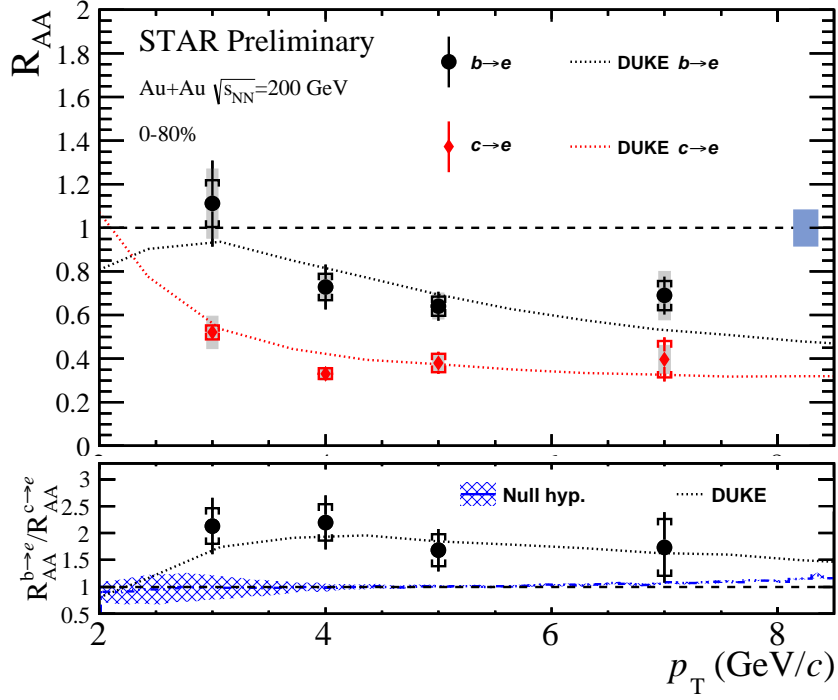


Figure 17: Top: Data for bottom- (blue stars) and charm-decay (red diamonds) electron R_{AA} as a function of electron p_T . The DUKE model calculation are shown as the respectively colored dotted lines. Bottom: The double ratio of bottom to charm R_{AA} , and the null hypothesis (explained in the text) shown as the blue shaded band and DUKE calculation as the dotted line.

568 and within experimental uncertainties consistent with zero. The data collected during Run-
569 17 and Run-18 at $\sqrt{s_{NN}}$ 54.4 and 27 GeV Au+Au collisions, respectively, are more than
570 an order of magnitude larger in statistics and allow for a more precise measurement. The
571 heavy-flavor decay electron v_2 is extracted from the inclusive electron v_2 by correcting for
572 electron v_2 from hadron and photon decays. The data are shown in Figure 18 for both 54.4
573 and 27 GeV Au+Au collisions, and compared to previously published STAR data in 200
574 GeV Au+Au collisions [77]. The 54.4 GeV data show a significant v_2 that is comparable to
575 200 GeV Au+Au collisions, indicating heavy-flavor hadrons gain significant collective flow
576 in the produced medium in 54.4 GeV Au+Au collisions. The data at 27 GeV indicate a hint
577 of non-zero v_2 , but still have considerable uncertainties due to a lower signal-to-background
578 ratio.

579 STAR has also recently reported at the 2019 Quark Matter conference charm-decayed
580 electron v_1 and v_2 , and bottom-decay electron v_2 in 200 GeV Au+Au collisions utilizing
581 the HFT to isolate charm- or bottom-decayed electrons, respectively. The measurement of
582 charm-decayed electron v_1 and v_2 was compared to previous STAR data of D^0 mesons, and
583 show consistency between the two measurements. In the former case the measured slope
584 of the charm-decayed electron v_1 versus rapidity corroborated the recently measured large

585 negative v_1 slope by STAR [69], and with an improved significance of 5σ . The bottom-decay
 586 electron v_2 was measured to have a non-zero v_2 with a significance of about 3.4σ , and is
 587 consistent in magnitude with expectations from the DUKE model [73]. This is the first
 588 significant measurement of bottom hadron v_2 at RHIC.

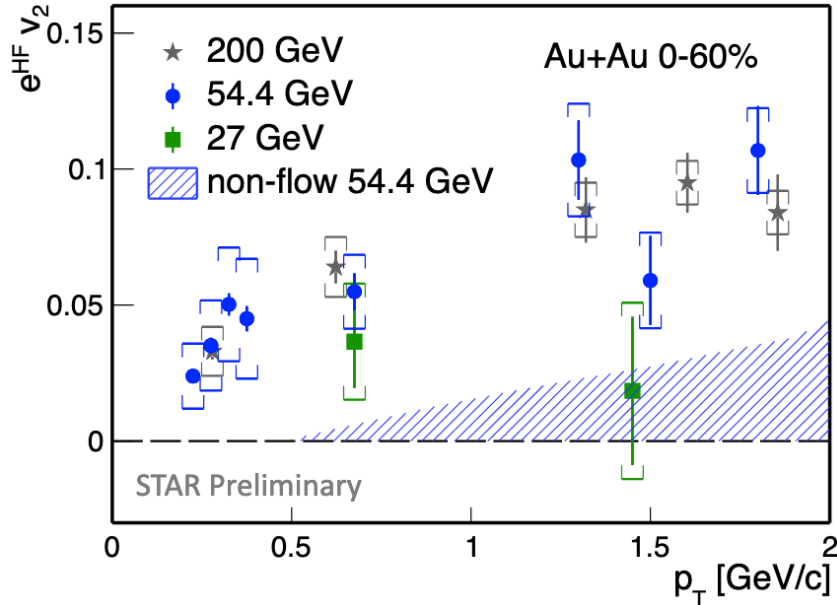


Figure 18: Heavy-flavor electron v_2 as a function of electron p_T in 54.4 (blue circles) and 27 (green squares) GeV Au+Au collisions. The STAR published data at 200 GeV are also shown as the gray stars. The shaded blue histogram shows the estimated non-flow contribution in the 54.4 GeV data.

589 Recent measurements of quarkonia have opened up new ways to probe production mech-
 590 anisms by measuring their distributions with jets. It has been observed that there is no
 591 simultaneous description of models to the J/ψ spectra and polarization data. It has also
 592 been shown that measurements of quarkonia fragmentation functions in jets can have good
 593 discriminating power between different models. Recently reported at the 2020 Hard Probes
 594 conference, was the measurement of J/ψ mesons within jets as a function of the J/ψ p_T
 595 fraction ($z = p_T(J/\psi)/p_T(jet)$). The results are shown in Figure 19 for a given set of jet
 596 reconstruction requirements, and unfolded to account for detector smearing. The depen-
 597 dence on cone size was also investigated and the data showed as the cone sized is increased
 598 the z distribution became more populated at lower values. Compared with the data in the
 599 same plot is the expectation of PYTHIA simulations (shown as the gray shaded histogram).
 600 The data show a clear discrepancy with PYTHIA, suggesting J/ψ mesons are not produced
 601 mostly in isolation. This new measurement is expected to provide valuable input to the
 602 theory community.

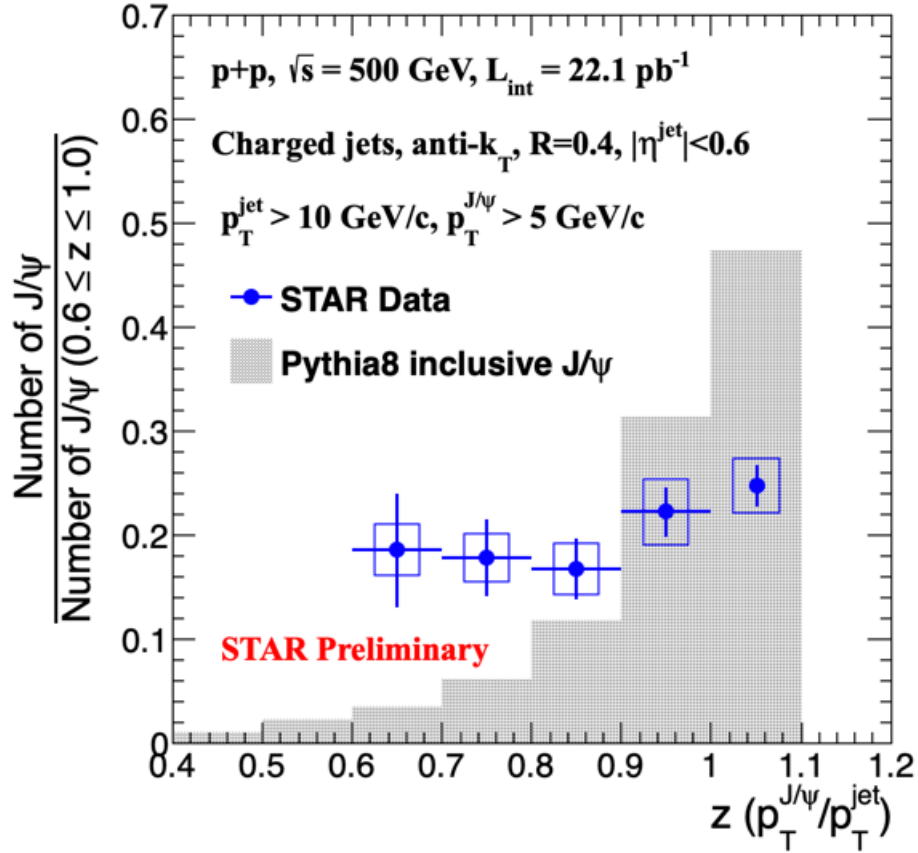


Figure 19: J/ψ momentum fraction in jets in 500 GeV $p+p$ data for a given set of jet reconstruction parameters listed. Also shown is the expectation from PYTHIA simulation as the gray histogram.

603 1.2 CME Search and Isobar Run

604 1.2.1 Introduction

605 Finding a conclusive experimental signature of the Chiral Magnetic Effect (CME) has be-
 606 come one of the major scientific goals of the heavy-ion physics program at the Relativistic
 607 Heavy Ion Collider (RHIC). The existence of CME will be a leap towards an understanding
 608 of the QCD vacuum, establishing a picture of the formation of deconfined medium where
 609 chiral symmetry is restored and will also provide unique evidence of the strongest known
 610 electromagnetic fields created in relativistic heavy-ion collisions [78, 79]. The impact of such
 611 a discovery goes beyond the community of heavy-ion collisions and will possibly be a mile-
 612 stone in physics. Also, as it turns out, the remaining few years of RHIC run and analysis
 613 of already collected data probably provides the last chance for dedicated CME searches in
 614 heavy-ion collisions in the foreseeable future. Over the past years significant efforts from
 615 STAR as well as other collaborations have been dedicated towards developing new meth-
 616 ods and observables to isolate the possible CME-driven signal and non-CME background
 617 contributions in the measurements of charge separation across the reaction plane. Many
 618 clever ideas have been proposed and applied to existing data. The general consensus is
 619 that measurement from the isobar collisions, Ruthenium+Ruthenium (Ru+Ru) that has
 620 10 – 18% higher B-field than Zirconium+Zirconium (Zr+Zr), provides the best solution to
 621 this problem. During the time when this beam user request document is being written, the
 622 analysts from the STAR collaboration are about to start the final step of the (three-step)
 623 blind analysis of the isobar data that we discuss at length in the following section.

624 1.2.2 Modality of Isobar Running at RHIC

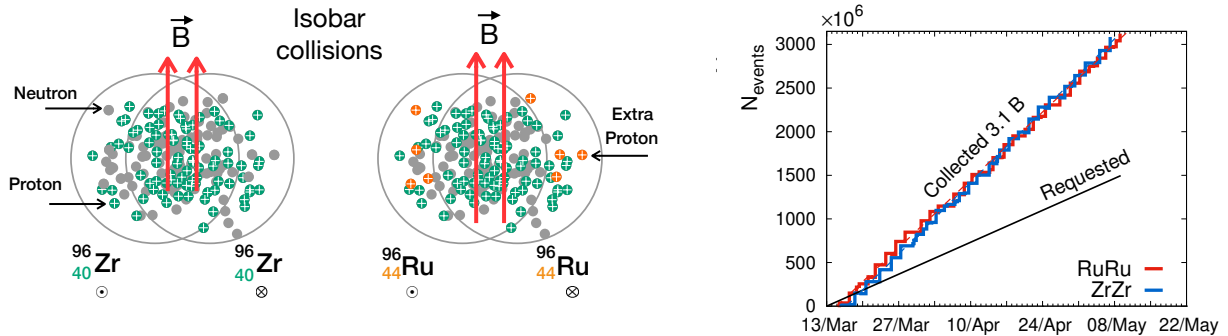


Figure 20: Left: Cartoon of the isobar collisions, about 10 – 18% stronger B-field is expected in Ru+Ru collisions as compared to Zr+Zr collisions due to four extra protons in each Ru nucleus. Right: Summary of the data collected for isobar collisions during Run 18 – almost a factor of two more events were collected than the request 1.5 Billion events over the course of 3.5 weeks.

625 The idea of colliding isobar, particularly Ru+Ru and Zr+Zr to make a decisive test of

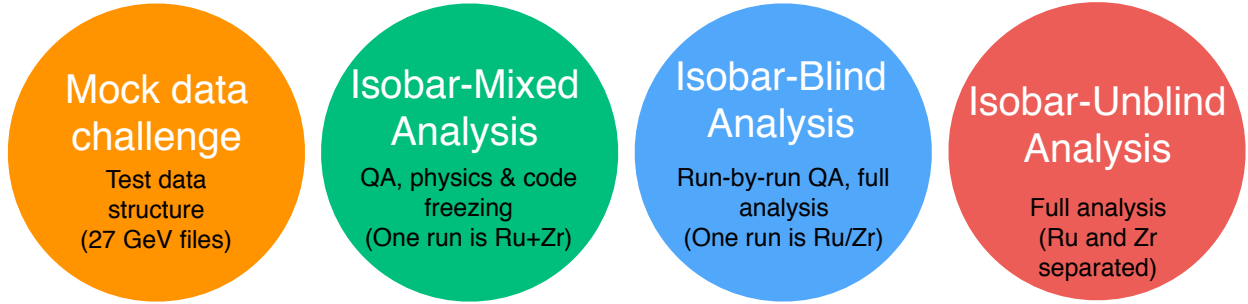


Figure 21: Cartoon showing steps of analysis consisting of the mock-data challenge and the three-step isobar blind analysis. This cartoon is based on the procedure for the blind analysis of isobar data that have been outlined in Ref [85]. During the time when this document is being written STAR collaboration has finished the mock-data challenge and two other steps and about to begin the final step of isobar-unblind analysis (shown in red).

626 CME was proposed by Voloshin in Ref [80], the same paper which also proposed to use
 627 Uranium collisions to disentangle signal and background of CME. The possible difference in
 628 the signals relies on the 10–18% higher B-field in Ru+Ru compared to Zr+Zr [81] in contrast
 629 to about 4% difference in flow driven background [36]. Such estimates are sensitive to details
 630 of shapes, charge distribution and neutron skin thickness of the two isobar nuclei [81–83].
 631 In the 2017-18 RHIC beam user request [84] STAR collaboration therefore proposed to
 632 collect data for two 3.5 week runs in the year 2018. The projection was based on the
 633 prospect of achieving five-sigma significance in a scenario where the measurement of $\Delta\gamma$
 634 has 80% non-CME background. This, however, relies on the assumption that the systematic
 635 uncertainty of the measurements is only a few percent and is much smaller than the statistical
 636 uncertainty. This started a large scale collaboration wide effort in synergy with the RHIC
 637 collider accelerator department to plan for the isobar running in the year 2018. Based on the
 638 studies of previous years of data from $Au + Au$ and $U + U$ collisions several major sources of
 639 systematics in the measurement of $\Delta\gamma$ were identified. The major sources include: run-to-run
 640 variation of detector response due to loss of acceptance, change in efficiency and variation in
 641 luminosity that affects the number of reconstructed tracks in the Time Projection Chamber.
 642 This eventually leads to uncorrectable systematic uncertainties in $\Delta\gamma$, the main observable
 643 to measure charge separation across event plane. In order to minimize such systematics the
 644 proposal were to: 1) switch species in RHIC between stores and, 2) keep long stores to level
 645 the luminosity aiming for specific rates in the coincidence measurements of beam fragments
 646 by the STAR zero-degree calorimeters. The aim was to maintain exact balance of run and
 647 detector conditions for the two species so that observations in the two systems are equally
 648 affected and can later on be largely eliminated in the ratios of observables.

649 1.2.3 Blinding of Data Sets and Preparation for Analyses

650 The procedure to blind isobar data was already in place well ahead of the actual data
 651 taking to limit the access of the data to the analysts. With the successful conclusion of

652 the isobar run in the year 2018 STAR experiment collected more than 3 billion events for
653 each isobar species. The next step was to develop the plans for a blind analysis, the main
654 idea behind which is to eliminate possible unconscious biases. A total of five institutional
655 groups are set up to perform the analysis of the data. The analysts from each group will
656 focus on a specific analysis described in the following section although in many cases there
657 are substantial overlap in some analyses that will help cross check the results. An important
658 part of the blind analysis is the blinding of the isobar species during the analysis. The details
659 of the blinding of the the blinding procedure and data structure is decided by members of
660 an analysis blinding committee (ABC) who are not part of the team of analysts and will
661 work in close collaboration with STAR experts who are part of the production team. The
662 idea is to provide the analysts the access to data in files where species-specific information
663 are disguised or removed before the final step of unblinding. A careful consideration is taken
664 by the ABC to make sure only the essential information to do the analysis-specific quality
665 assurance of the data is available to the analysts. Some of the quality assurance, calibration
666 and centrality determination work that require species information are done only by STAR
667 experts who are not a part of the analysis team. Above all, the main goal of the committee
668 is to make sure that under no circumstances, physics analysts can access un-blinded data
669 and jeopardize the blind analysis. For example, all the data sets are produced with pseudo-
670 run-number that cannot be used by the analysts to retrieve the exact species information.

671 **1.2.4 Methods for the Isobar Blind Analyses**

672 The detailed procedure for the blind analyses of isobar data have been outlined in Ref [85].
673 Figure.21 is a cartoon that summarizes the mock-data challenge and three steps of blind
674 analysis.

675 In the zeroth step shown in the extreme left of Fig.21 (by orange circle) is the mock-
676 data challenge and not considered as a step of the isobar data analysis but a crucial step
677 to familiarize the analysts with the technicalities of the data structures that have been
678 specifically designed for blind analysis.

679 The first step shown in Fig.21 (by green circle) as the "isobar-mixed analysis" or "mixed-
680 blind analysis" is truly the first step of blind analysis. This is also the most challenging
681 steps from the point of view of the analysts. In this step the analysts are provided with data
682 sample where each run comprises of events that are mixed samples from two species. In this
683 step the analysts perform the full quality assurance (QA) and physics analysis of the data,
684 document every details of steps of the procedure and freeze the codes. After the completion
685 of this step, no changes to the analysis code is permissible. Also, no changes in the analysis
686 procedure is allowed. The only permissible change in the following step is to reject bad runs
687 or pile-up events. However, in order to avoid unconscious bias in analysis, such rejection
688 cannot be done arbitrarily. Instead, an automated algorithm for bad run rejection must be
689 developed in this step and corresponding codes have also to be frozen. The stability of the
690 automated QA algorithm is tested with some of the existing data sets of Au+Au and U+U
691 collisions.

692 The second step shown in Fig.21 (by blue circle) is referred to as the "isobar-blind analy-

693 sis" or "unmixed-blind analysis". For this the analysts are provided with files each of which
694 contain data from a single species that is either Ru or Zr. From this step on-wards, the
695 analysts are allowed to run their previously frozen codes. The main purpose of this step is
696 to perform run-by-run QA of the data sample. However, there are two conditions: the files
697 contain limited number of events that cannot lead to any statistically significant result and
698 the species information is not revealed. Although a pseudo-run-number is used for each file,
699 the time ordering is preserved with a unique mapping that is unknown to the analysts. It
700 is important to maintain the time ordering to identify time-dependent changes in detectors
701 and run conditions as a part of the run-by-run quality assurance. With this limited data
702 sample, the analysts need to run the frozen automated algorithm to identify bad runs. A
703 similar automated algorithm is also used for identifying and rejecting bad runs. After this
704 step no more changes are allowed in terms of QA.

705 The final step of isobar blind analysis shown by red circle in Fig.21 is referred to as
706 "isobar-unblind" analysis. In this step, the species information will be revealed and the
707 physics results will be produced by the analysts using the previously frozen codes. The
708 finding from this step will be directly submitted for publication without alteration. If a
709 mistake is found in the analysis code, the erroneous results will also accompany the corrected
710 results.

711 1.2.5 Observables for Isobar Blind Analyses

712 Isobar blind analysis will specifically focus on the following observables. The general strategy
713 is to compare two isobar species to search for a significant difference in whatever observable
714 used. The following sections describe these procedures in brief with comments on the outlook
715 for isobar blind analysis: 1) measurement of higher order harmonics of γ -correlator, 2) ex-
716 ploiting the relative charge separation across participant and spectator planes, 3) differential
717 measurements of $\Delta\gamma$ to identify and quantify backgrounds, 4) the use of R-observable to mea-
718 sure charge separation. The first three approaches are based on aforementioned three-particle
719 correlator and the last employ slightly different approaches to quantify charge separation.
720 There is also another analysis which will be performed using the signed balance function but
721 will not be part of the blind analysis.

722 **Mixed harmonics measurements with second and third order event planes** In
723 order to proceed in this section, it is better to rewrite the conventional γ -correlator by a
724 more general notation as $\gamma_{112} = \langle \cos(\phi_a^\alpha + \phi_b^\beta - 2\Psi_2) \rangle$. The idea is to measure charge sep-
725 arations across the third harmonic event plane by constructing a new correlator $\Delta\gamma_{123} =$
726 $\gamma_{123}(OS) - \gamma_{123}(SS)$, where $\gamma_{123} = \langle \cos(\phi_a^\alpha + 2\phi_b^\beta - 3\Psi_3) \rangle$ that was introduced by CMS
727 collaboration in Ref [87]. Since the Ψ_3 plane is random and not correlated to B-field di-
728 rection (see Fig.22), γ_{123} is purely driven by non-CME background, the contribution of
729 which should go as v_3/N . This is very useful to contrast signal and background sce-
730 nario by comparing the measurements in two isobaric collision systems. Since Ru+Ru has
731 larger B-field than Zr+Zr but have comparable background, the case for CME would be
732 as follows: $(\Delta\gamma_{112}/v_2)^{\text{Ru+Ru}}/(\Delta\gamma_{112}/v_2)^{\text{Zr+Zr}} > 1$ and $(\Delta\gamma_{112}/v_2)^{\text{Ru+Ru}}/(\Delta\gamma_{112}/v_2)^{\text{Zr+Zr}} >$

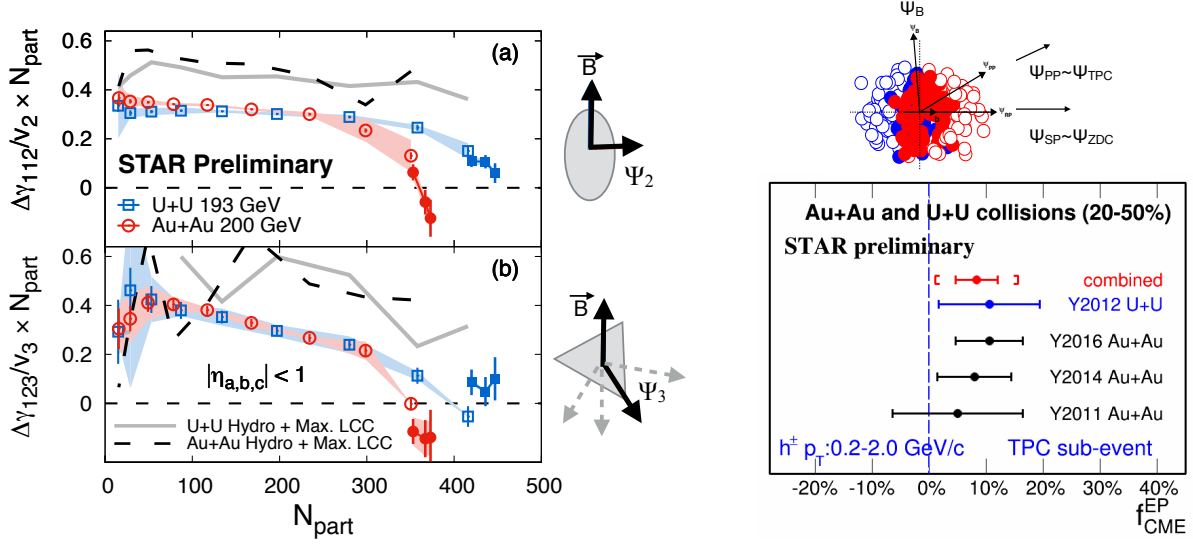


Figure 22: (Left) Measurement of charge separation along second and third order event planes in Au+Au and U+U collisions. (Right) Fraction of possible CME signal in the measurement of $\Delta\gamma$ with respect to spectator and participant planes [86].

733 $(\Delta\gamma_{123}/v_3)^{Ru+Ru}/(\Delta\gamma_{123}/v_3)^{Zr+Zr}$. Fig.22 (left) shows the measurement of these observables
 734 in U+U and Au+Au collisions. Within the uncertainties of the measurements, no significant
 735 difference in the trend of $\Delta\gamma_{112}/v_2$ and $\Delta\gamma_{123}/v_3$ is observed for the two collision systems
 736 except for the very central events. Predictions from hydrodynamic model calculations with
 737 maximum possible strength of local charge conservation [36] is shown on the same plot.
 738 Overall observation indicates the backgrounds dominate the measurements and a similar
 739 analysis of the isobar data is highly anticipated.

740 **Charge separation along participant and spectator planes** This analysis makes use
 741 of the fact that B-field driven signal is more correlated to spectator plane in contrast to
 742 flow-driven background which is maximum along the participant plane. The idea was first
 743 introduced in Ref [88] and later on followed up in Ref [89]. It requires measurement of $\Delta\gamma$
 744 with respect to the plane of produced particles, a proxy for participant plane as well as
 745 with respect to the plane of spectators. In STAR, the two measurements can be done by
 746 using Ψ_2 from TPC and Ψ_1 from ZDC, respectively. The approach is based on three main
 747 assumptions: 1) measured $\Delta\gamma$ has contribution from signal and background, which can be
 748 decomposed as $\Delta\gamma = \Delta\gamma^{bkg} + \Delta\gamma^{sig}$, 2) the background contribution to $\Delta\gamma$ should follow
 749 the scaling $\Delta\gamma^{bkg}(TPC)/\Delta\gamma^{bkg}(ZDC) = v_2(TPC)/v_2(ZDC)$ and, 3) the signal contribution to
 750 $\Delta\gamma$ should follow the scaling $\Delta\gamma^{sig}(TPC)/\Delta\gamma^{sig}(ZDC) = v_2(ZDC)/v_2(TPC)$. The first two have
 751 been known to be working assumptions, widely used for a long time and can be used to test
 752 the case of CME [89] if $(\Delta\gamma/v_2)(ZDC)/(\Delta\gamma/v_2)(TPC) > 1$. The validity of the last one was
 753 studied and demonstrated in Ref [88]. Using all three equations one can extract [86] the
 754 fraction of possible CME signal $f_{CME} = \Delta\gamma^{sig}/\Delta\gamma$ in a fully data-driven way as shown in

755 Fig.22(right). This analysis will be done with the isobar data and the case for CME will be
 756 $f_{\text{CME}}^{\text{Ru+Ru}} > f_{\text{CME}}^{\text{Zr+Zr}} > 0$.

757 **Differential measurements of $\Delta\gamma$ to identify and quantify background** *Invariant*
 758 *mass dependence of charge separation:* Differential measurements of $\Delta\gamma$ with invariant mass
 759 and relative pseudorapidity provide interesting prospects to identify and quantify the sources
 760 of flow and non-flow driven backgrounds. The idea to use invariant mass is simple and was
 761 first introduced in Ref [90]. Resonances are widely identified by observing structures in the
 762 invariant mass spectra of the decay daughters. Consider a pair of opposite sign pions for
 763 example, it is known that a large fraction of them come from the neutral resonances that
 764 show up in the invariant mass spectrum of $m_{\text{inv}}(\pi^+ + \pi^-)$. If we restrict the analysis to
 765 pairs of pions, differential measurements of $\Delta\gamma$ with $m_{\text{inv}}(\pi^+ + \pi^-)$ should also show similar
 766 peak like structures if background from neutral resonances dominate the charge separation.
 767 Indeed similar peak structures are observed and a careful analysis is performed by STAR
 768 collaboration to extract the possible fraction of CME signals from measurements [91]. This
 769 analysis relies on the assumption that CME signals do not show peak like structures in
 770 $m_{\text{inv}}(\pi^+ + \pi^-)$ and also requires an assumption of m_{inv} dependence of the CME signal,
 771 therefore calls for more theoretical inputs in this direction.

772 *Relative pseudorapidity dependence:* The relative pseudorapidity dependence of azimuthal
 773 correlations are widely studied to identify sources of long-range components that are domi-
 774 nated by early time dynamics as compared to late time correlations that are prevented by
 775 causality to appear as short-range correlations. The same can be extended to charge depen-
 776 dent correlations which provide the impetus to explore the dependence of $\Delta\gamma$ on the pseudo-
 777 rapidity gap between the charge carrying particles $\Delta\eta_{ab} = |\eta_a - \eta_b|$ in $\langle \cos(\phi_a^\alpha + \phi_b^\beta - 2\Psi_{RP}) \rangle$.
 778 Such measurements have been performed in STAR with Au+Au and U+U data. It turns
 779 out that the possible sources of short-range correlations due to photon conversion to $e^+ - e^-$,
 780 HBT and Coulomb effects can be identified and described as Gaussian peaks at small $\Delta\eta_{ab}$,
 781 the width and magnitude of which strongly depend on centrality and system size. Going to
 782 more peripheral centrality bins, it becomes harder and harder to identify such components
 783 as they overlap with sources of di-jets fragmentation that dominates both same-sign and
 784 opposite sign correlations. An effort to decompose different components of $\Delta\gamma$ via study of
 785 $\Delta\eta_{ab}$ can be challenging although a clear sign of different sources of correlations are visible in
 786 change of shape of individual same-sign and opposite sign measurements of γ -correlator [92].

787 In any case, these differential measurements of $\Delta\gamma$ in isobar collisions provide the prospect
 788 to extract the $m_{\text{inv}}(\pi^+ + \pi^-)$ and $\Delta\eta$ dependence of CME signals that will provide much
 789 deeper insights on the origin of the effect. Comparing the differential measurements in
 790 Ru+Ru and Zr+Zr it will be possible to extract the invariant mass and the relative pseu-
 791 dorapidity distribution of the CME signal that will provide deeper insight into the origin of
 792 the phenomenon.

793 **Alternate measure: The novel R-observable** The R -observable is actually a distri-
 794 bution, introduced in Ref [95], and defined as the ratio of two distribution functions of

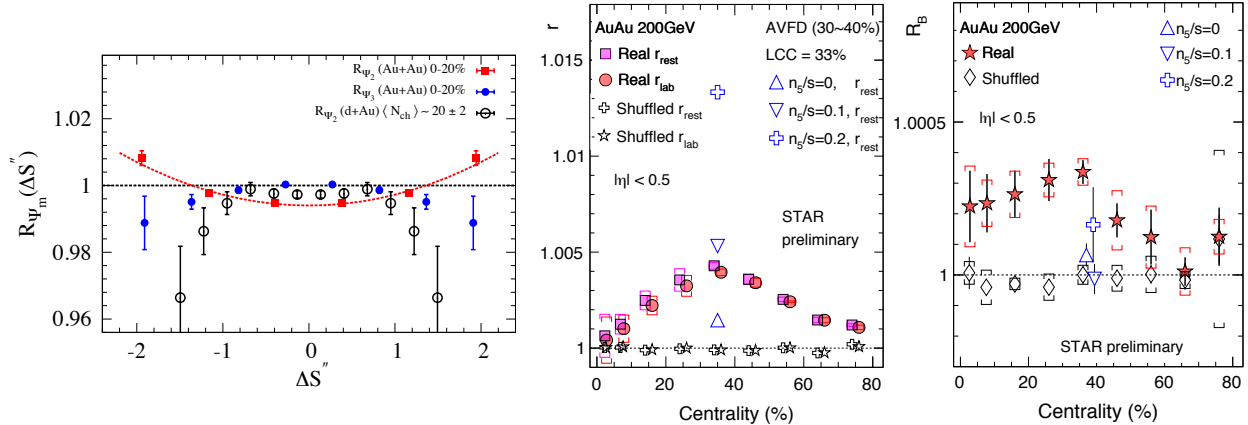


Figure 23: (Left) The R-observable shown for different collision systems, concave shape is consistent with CME expectation [93]. (Right) The two main quantities r and R_B derived from signed balance function, deviation from unity is consistent with CME expectation [94].

795 the quantity ΔS parallel and perpendicular to B-field direction defined as $R_{\Psi_m}(\Delta S) =$
796 $C_{\Psi_m}(\Delta S)/C_{\Psi_m}^\perp(\Delta S)$. Here ΔS measures the difference in the dipole moment of the positive
797 and negative charge in an event (see Ref [95] for details). The shape of $R_{\Psi_2}(\Delta S)$ will be
798 sensitive to CME as well as non-CME background, whereas $R_{\Psi_3}(\Delta S)$ is purely driven by
799 non-CME background and serves as a baseline. Model calculations have established several
800 unique features of this observable: 1) presence of CME signal will lead to a concave shape of
801 the $R_{\Psi_2}(\Delta S)$, 2) increasing strength of CME signal will increase the concavity of $R_{\Psi_2}(\Delta S)$,
802 3) in presence of CME, the concavity of $R_{\Psi_2}(\Delta S)$ will be larger than that of $R_{\Psi_3}(\Delta S)$. The
803 measurement of R_{Ψ_m} is shown in Fig.23. The quantity $\Delta S''$ shown is a slight variant of (ΔS)
804 that incorporates correction for particle number fluctuations and event plane resolution. The
805 observation of Fig.23 indicates more concave shape for R_{Ψ_2} compared to R_{Ψ_3} in Au+Au
806 whereas flat or convex shapes for p/d+Au indicates that the measurements are consistent
807 with expectations of CME [93]. For isobar collisions, the case of CME will be confirmed if:
808 1) a concave shape is observed for the ratio of the observables $R_{\Psi_2}(\Delta S)^{Ru+Ru}/R_{\Psi_2}(\Delta S)^{Zr+Zr}$
809 and 2) the concavity should be weaker for $R_{\Psi_3}(\Delta S)^{Ru+Ru}/R_{\Psi_3}(\Delta S)^{Zr+Zr}$.

810 **Alternate measure: The signed Balance function** A very recently proposed observ-
811 able to search for CME is the signed balance function (SBF) [96]. The idea is to account
812 for the ordering of the momentum of charged pairs measured by the width of SBF that is
813 expected to be different for out-of-plane as compared to in-plane measurement captured in
814 the ratio r_{lab} . In addition, one can also account for the boost due to collective expansion
815 of the system that forces all pairs to move in the same direction and measure the ratio in
816 pair rest frame r_{rest} . In presence of CME, the individual ratios as well as the double ratio
817 $R_B = r_{rest}/r_{lab}$ is expected to be greater than unity. The preliminary measurements shown
818 in Fig.23 (right) from STAR in Au+Au 200 GeV seem to be consistent with CME expect-
819 ation. This observable will be studied with the isobar data in STAR but not as a part of

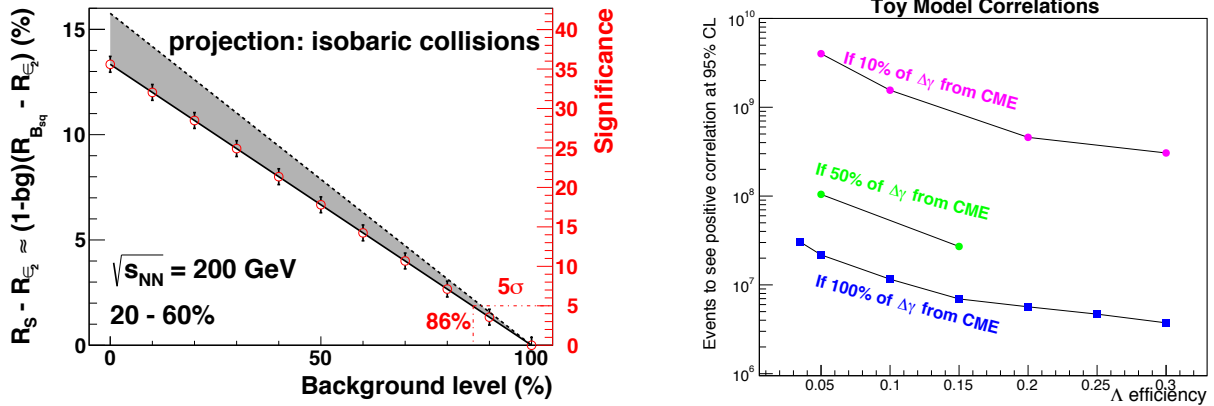


Figure 24: (Left) Projection plot taken from a previous beam user request document [84] indicating the anticipated significance in the measurement of charge separation as a function of the CME signal fraction prepared using 2.5 B simulated events. (Right) Estimation of the number of events required to see positive correlation between net Λ helicity with out-of-plane charge separation sensitive to local parity violation at 95% confidence level, plotted against the efficiency of $\Lambda(\bar{\Lambda})$ reconstruction (see [97] for details).

820 the blind analysis and the CME expectation will be: 1) $r(\text{Ru} + \text{Ru}) > r(\text{Zr} + \text{Zr})$, and 2)
 821 $R_B(\text{Ru} + \text{Ru}) > R_B(\text{Zr} + \text{Zr})$.

822 1.2.6 Prospect of CME search beyond isobar-era

823 It is important to discuss the strategy for CME search beyond the isobar-era. It is true that
 824 such strategy needs to be planned based on the outcome of the isobar program. We would
 825 like to get started by considering two possible scenarios at the top RHIC energy: 1) isobar
 826 program results in a significance of 3σ and below, 2) isobar program results in a significance
 827 of 3σ and above.

828 In the first scenario one can infer from the projection plot of fig.24(left) that the upper
 829 limit of the fraction of CME signal should be less than or equal to 8%. Question is under such
 830 a scenario can STAR perform a follow up measurement to achieve a decisive 5σ significance
 831 and establish a conclusive evidence of CME? It turns out such a measurement is possible
 832 even with a single Au+Au 200 GeV data set during the year 2023 running of STAR concur-
 833 rently with sPHENIX. Current analysis of aforementioned CME signal in Au+Au 200 GeV
 834 extraction using elliptic flow and charge separation with respect to spectator and participant
 835 planes yields 4% statistical uncertainty with 2.4 B events ($2 - 3\sigma$ significance). In order to
 836 get 5σ significance with the same analysis one needs to have statistical uncertainty of order
 837 1.6% which would require about $(4/1.6)^2 \times 2.4 = 15$ Billion events. Therefore, as per the
 838 previous estimates of anticipated 10 Billion events that can be collected by STAR during
 839 the 2023 year, one can achieve about 4σ significance on the upper limit of possible CME
 840 signal fraction in the measurement of charge separation. This estimate does not account
 841 for two important facts that can lead to higher significance and a decisive measurement of

842 CME. The first one is that the magnitude of projected B-field on reaction plane is higher
 843 in Au+Au collisions as compared to isobar collisions. The second one is that iTPC upgrade
 844 enhances the charge particle multiplicity by 50% and therefore triplets($\sim dN/d\eta^3$) (pairs
 845 $\sim dN/d\eta^2$) statistics by a factor of 3.4 (2.3). So the final conclusion is that even if isobar
 846 program results in a 3σ measurement running STAR in the year 2023 will result in a $> 4\sigma$
 847 measurement. This conclusion assumes that the systematic uncertainty can be controlled to
 848 be smaller than the statistical uncertainty, i.e. below 2%.

849 For the second scenario ($> 3\sigma$ measurement from isobar program) we will also be able
 850 to establish an upper limit of the fraction of CME signal. For example, in fig.24(left) we see
 851 that 5σ significance will establish 13% CME signal and a discovery of the CME phenomenon
 852 in heavy ion collisions. The impact of such a discovery will set a milestone in physics.
 853 Running STAR in the year 2023 concurrently with sPHENIX would be essential to perform
 854 dedicated precision measurements to further investigate and characterize the phenomena.
 855 In this context STAR collaboration has stated a new analysis to understand the origin of
 856 parity violation in hot QCD by measuring the correlation of net- Λ helicity with charge
 857 separation across reaction plane [97]. The difference between the number of positive and
 858 negative helicity $\Lambda(\bar{\Lambda})$ $N_L^\Lambda - N_R^\Lambda$ should be associated with net-chirality, i.e. the difference
 859 between right and left handed quarks, in a given event. Since net chirality in the event also
 860 drives out-of-plane charge separation (a_1) in the presence of B-field, one expects a correlation
 861 between a_1 and $N_L^\Lambda - N_R^\Lambda$ as a results of local parity violation. Currently available data sets
 862 do not allow us to perform a significant measurement for this observable. Using a toy model
 863 simulation, shown in fig.24(right), we estimate the number of event required to see non-
 864 zero correlations between a_1 and $N_L^\Lambda - N_R^\Lambda$ at the 95% confidence level as a function of
 865 the efficiency of $\Lambda(\bar{\Lambda})$ reconstruction. Different curves correspond to different magnitudes
 866 of CME fraction in the measurement of γ -correlator. With about 10 B Au+Au 200 GeV
 867 events in run 2023 it will be possible to perform a significant measurement to study this
 868 phenomenon.

869 Regardless of the outcome of the measurements with the isobar program, that will be
 870 performed at the top RHIC energy, one question will remain. What happens at lower collision
 871 energy? In this context a new idea has emerged. The newly installed event-plane detector
 872 (EPD) upgrade provides a new capability at STAR towards CME search at lower collision
 873 energy and for the Beam Energy Scan phase-II program [18]. The idea is simple, at lower
 874 energies EPD acceptance ($2.1 < |\eta| < 5.1$) falls in the region of beam rapidity (Y_{beam}) and
 875 can measure the plane of strong directed flow (Ψ_1) of spectator protons, beam fragments
 876 and stopped protons, therefore strongly correlated to the B-field direction (See fig25). The
 877 next step is to measure $\Delta\gamma$ with respect to Ψ_1 and compare it with the measurement of
 878 $\Delta\gamma$ along Ψ_2 planes from outer regions of EPD and TPC at mid-rapidity that are weakly
 879 correlated to the B-field directions. A test of CME scenario will be to see if large difference
 880 is observed in the measurements. First preliminary measurements from STAR as shown in
 881 Fig 25 is dominated by uncertainty but seems to show a lot of prospects for the CME search
 882 at lower energies. With higher statistics data from the BES-II program (7.7-19.6 GeV) and
 883 STAR fixed target run more precise measurement is possible.

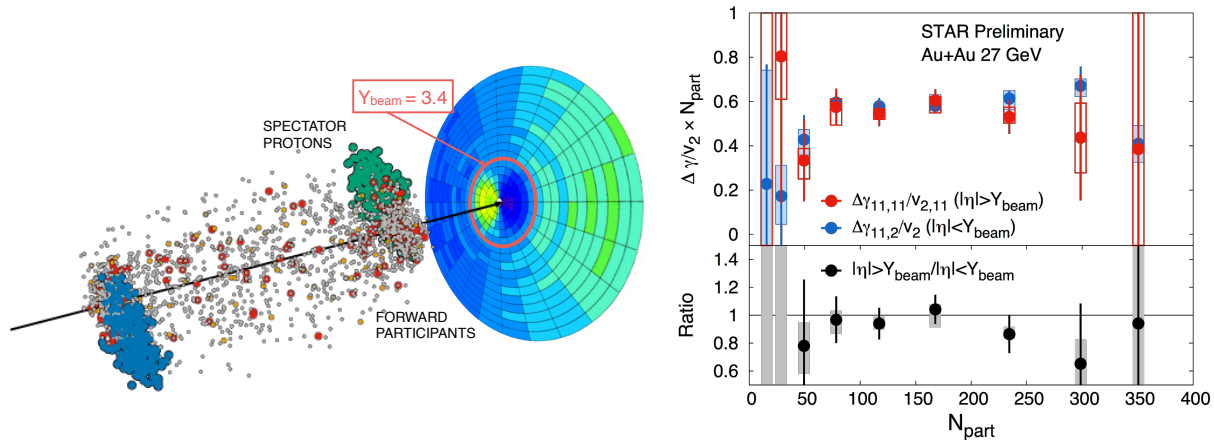


Figure 25: Prospect of precision CME search with the BES-II data. (Left) Single simulated UrQMD event and EPD detector acceptance that covers beam rapidity and detects both forward participants and spectators in 27 GeV Au+Au collisions that have large directed flow which changes sign at $\eta = Y_{\text{beam}} = 3.4$. (Right) γ -correlators scaled by v_2 across different event-planes and double ratio of spectators/participant event planes which should be unity for no-CME scenario.

1.3 Highlights from the Spin and Cold QCD Program

1.3.1 Introduction

The goal of the STAR Cold QCD program is to probe the spin and flavor structure of the proton and understand the role of spin in Quantum Chromodynamics, exploiting the unique capability of RHIC to provide longitudinally and transversely polarized p+p and p+A collisions at multiple energies. Measurements with longitudinal beam polarizations have given new insights into the helicity structure of the proton, while measurements with transverse polarizations have provided new ways to probe polarized parton distribution functions (PDFs) in the collinear and transverse momentum dependent frameworks. Additionally, cross-section measurements in unpolarized p+p collisions provide valuable information to constrain collinear and transverse momentum dependent unpolarized PDFs. This program is complemented by studies of polarized p+p elastic scattering and central exclusive production, in which a far-forward proton is detected intact.

Since 2009, RHIC STAR has completed several highly successful polarized p+p runs both at $\sqrt{s} = 200$ GeV and $\sqrt{s} = 500/510$ GeV. Moreover, p+Au and p+Al datasets with a transversely polarized proton beam have been recorded in 2015 at $\sqrt{s} = 200$ to address important physics problems, including the ridge phenomenon and the possible onset of gluon saturation effects. Table 5 summarizes the STAR sampled luminosity and the luminosity averaged beam polarization as measured by the hydrogen jet (H-jet) polarimeter.

Table 5: Summary of polarized p+p and p+A running periods at RHIC since 2009, including center-of-mass energy, STAR’s integrated luminosity and the average beam polarization for blue (B) and yellow (Y) beams from the H-jet polarimeter.

| Year | System | \sqrt{s} (GeV) | Recorded Lumi. (pb^{-1}) | Polarization | B/Y $\langle P \rangle$ (%) |
|------|--------------|------------------|-------------------------------------|--------------|-----------------------------|
| 2009 | pp | 200 | 25 | Longitudinal | 55/55 |
| 2009 | pp | 500 | 10 | Longitudinal | 39/39 |
| 2011 | pp | 500 | 12 | Longitudinal | 48/48 |
| 2011 | pp | 500 | 25 | Transverse | 48/48 |
| 2012 | pp | 200 | 22 | Transverse | 61/56 |
| 2012 | pp | 510 | 82 | Longitudinal | 50/53 |
| 2013 | pp | 510 | 300 | Longitudinal | 51/52 |
| 2015 | pp | 200 | 52 | Transverse | 53/57 |
| 2015 | pp | 200 | 52 | Longitudinal | 53/57 |
| 2015 | $p\text{Au}$ | 200 | 0.45 | Transverse | 60/– |
| 2015 | $p\text{Al}$ | 200 | 1 | Transverse | 54/– |
| 2017 | pp | 510 | 320 | Transverse | 55/55 |

904 1.3.2 Longitudinal program

905 Since last year’s PAC meeting, the STAR spin and cold QCD physics working group has
906 released preliminary results focused on double-spin asymmetries A_{LL} of inclusive jet [98] and
907 dijet [99] production in longitudinally polarized p+p collisions at a center-of-mass energy
908 $\sqrt{s} = 200$ GeV based on the 2015 data set. These analyses are aimed at providing additional
909 constraints to the gluon helicity distribution $\Delta G(x, Q^2)$, especially for the medium gluon
910 momentum fractions in the range from $x \simeq 0.05$ to $x \simeq 0.5$. Figures 26 and 27 show the
911 preliminary results of inclusive jet A_{LL} together with the 2009 data results of Ref. [100] and
912 dijet A_{LL} together with the 2009 results from [101], respectively. Expected A_{LL} values for
913 the DSSV14 [102] and NNPDF-pol1.1 [103] parton distributions are also presented. The
914 results are in good agreement with previous measurements at $\sqrt{s} = 200$ GeV and with the
915 theoretical evaluations of prior world data. They have better precision and thus provide
916 further evidence that $\Delta G(x, Q^2)$ is positive for $x > 0.05$.

917 The results for the inclusive jet and dijet A_{LL} based on the 2012 $\sqrt{s} = 510$ GeV longi-
918 tudinally polarized p+p data, which enabled exploration of $\Delta G(x, Q^2)$ down to $x \simeq 0.015$,
919 were discussed in the previous PAC report and have since been published in Physical Review
920 D [104].

921

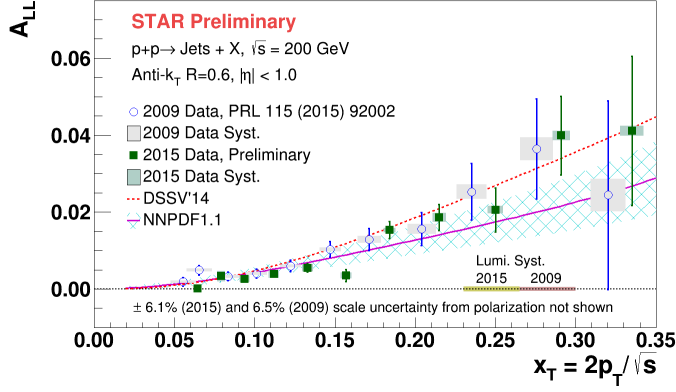


Figure 26: A_{LL} for inclusive jets with $|\eta| < 1.0$ versus x_T . The filled points show 2015 preliminary results [98], whereas the open points show the 2009 data of Ref. [100]. The bars show the size of the statistical uncertainties, whereas the boxes indicate the size of systematic uncertainties. The curves show the expected A_{LL} values for the DSSV14 [102] and NNPDF-pol1.1 [103] parton distributions.

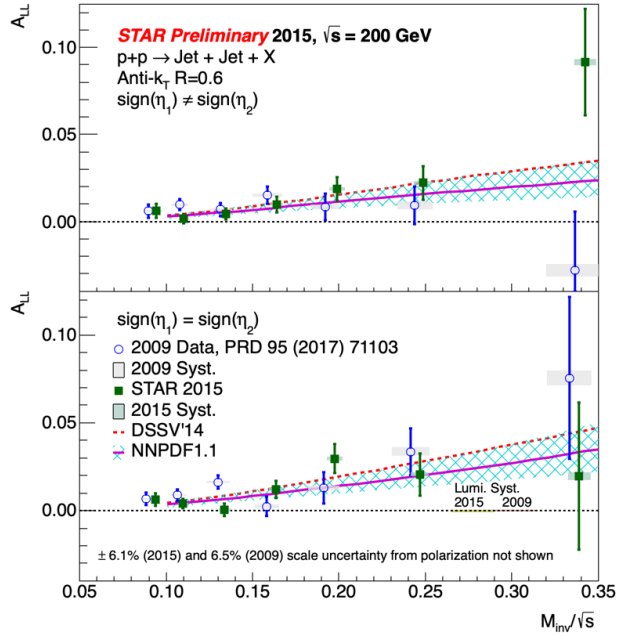


Figure 27: A_{LL} as a function of the parton-level invariant mass for dijets with the opposite-sign (top) and same-sign (bottom) event topologies. The filled points show 2015 preliminary results [99], whereas the open points show the 2009 data of Ref. [101]. The bars show the size of the statistical uncertainties, whereas the boxes indicate the size of systematic uncertainties. The curves show the expected A_{LL} values for the DSSV14 [102] and NNPDF-pol1.1 [103] parton distributions.

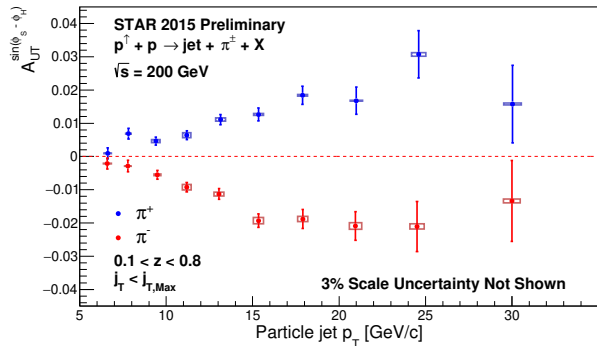


Figure 28: Preliminary results for the Collins asymmetry plotted for identified π^+ (blue) and π^- (red) particles as a function of jet p_T for jets that scatter forward to polarized beam ($x_F > 0$) [105]. The full range of both z and j_T are integrated over.

922 1.3.3 Transverse program

923 There have been several new STAR preliminary results on transverse spin physics released
 924 since the last PAC meeting. Highlights include the Collins asymmetry for charged pions
 925 inside a jet [105] and the dijet Sivvers asymmetry [106] in $\sqrt{s} = 200$ GeV p+p collisions.
 926 Moreover, the final publications of the transverse single spin asymmetries (TSSA) for neutral
 927 pions produced at forward rapidity in $\sqrt{s} = 200$ GeV for p+p, p+Au and p+Al [107], and
 928 500 GeV p+p [108] collisions are in God Parent Committees.

929 The Collins asymmetry in p+p collisions combines the collinear quark transversity in the
 930 proton with the transverse momentum dependent Collins fragmentation function [109–111],
 931 and thus provides a cleaner probe of the Collins fragmentation function than that in semi-
 932 inclusive deep inelastic scattering (SIDIS) and enables tests of evolution, universality and
 933 factorization breaking in the TMD formalism. Figure 28 shows the preliminary Collins
 934 asymmetries for charged pions inside jets that scatter forward ($x_F > 0$) to the polarized
 935 beam from 2015. The measured asymmetries are consistent with previous measurements
 936 from 2012 [112], but have 30% smaller statistical uncertainty.

937 The Sivvers effect describes the correlation of the parton transverse momentum with the
 938 transverse spin of the nucleon. Figure 29 shows the first observation of non-zero Sivvers
 939 asymmetries in dijet production of transversely polarized proton collisions using the STAR
 940 2012+2015 polarized p+p data. Compared to the previous 2006 result [113], fully recon-
 941 structed jets are analyzed with 33 times more statistics. Charge-tagging methods are em-
 942 ployed in order to separate the u and d quark signals. With detailed simulation, the individual
 943 parton spin-dependent $\langle k_T \rangle$ are extracted for u , d and $gluon + sea$ quarks, and indicates that
 944 $\langle k_T^u \rangle \approx 32$ MeV/ c , $\langle k_T^d \rangle \approx -67$ MeV/ c and $\langle k_T^{g+sea} \rangle \approx 0$ MeV/ c .

945 The transverse single spin asymmetry (TSSA) for forward neutral pions produced in
 946 polarized proton collisions with protons (p+p), with aluminum nuclei (p+Al) and with gold
 947 nuclei (p+Au) at $\sqrt{s} = 200$ GeV from FMS data are also measured using the data taken in
 948 2015. The preliminary results for (p+p) and (p+Au) have been released [107], and the final
 949 publication is soon to be submitted to Physical Review D. Measured asymmetries presented
 950 in Fig. 30 are found to rise with transverse momentum at $x_F < 0.5$, while they flatten or
 951 fall at larger x_F . The results are consistent with a weak nuclear A dependence. Moreover,
 952 a further observation is that the TSSA is significantly larger for isolated π^0 s than for non-

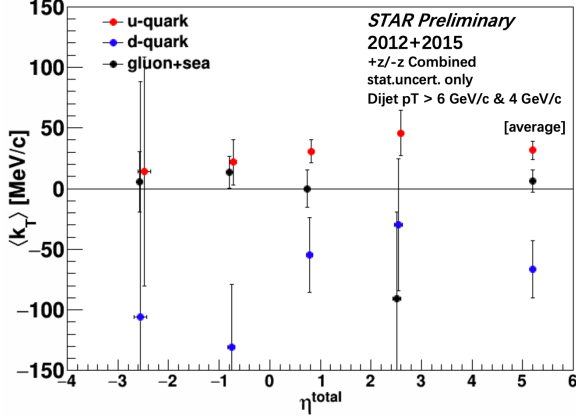


Figure 29: Preliminary results for the spin-dependent k_T values for u , d and $gluon + sea$ from the dijet Sivers measurement as a function of the sum of dijet pseudorapidities $\eta_1 + \eta_2 \sim \ln(\frac{x_1}{x_2})$ [106].

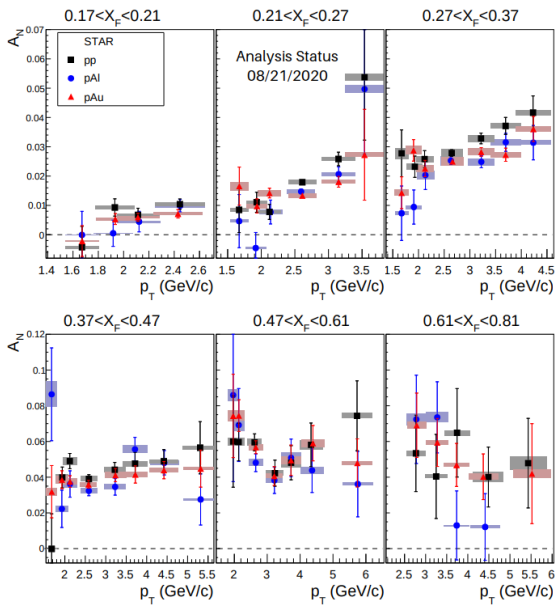


Figure 30: Transverse single spin asymmetry for forward π^0 production as a function of transverse momentum for six Feynman x_T regions. Results for three collisions systems are shown, black squares for p+p, blue circles for p+Al and red triangles for p+Au collisions. The statistical uncertainties are shown with vertical error bars and the filled boxes indicate the horizontal and vertical systematic uncertainties. Analysis status on 08/21/2020. Preliminary results available in Ref. [107].

953 isolated π^0 s, which are accompanied by additional jet-like fragments.

954 The transverse single-spin asymmetry of neutral pions at $\sqrt{s} = 200$ GeV and 500 GeV
 955 from FMS data are compared in Fig. 31. The 200 GeV data are from 2015, while the 500
 956 GeV data are from 2011. The theoretical calculations presented in the plot are based on
 957 the Transverse Momentum Dependent (TMD) and collinear twist-3 functions from a recent
 958 global analysis [114], which also includes previous forward π^0 and charged hadron TSSA data
 959 from RHIC in the fit. The theoretical calculation differs from our measurement and only
 960 provides a reasonable description of the non-isolated π^0 in the low- x_F region. A continu-
 961 ous increase of the TSSA with Feynman-x indicates the independence on the center-of-mass
 962 energy. Pions with no nearby particles, which may not arise from conventional jet fragmen-
 963 tation, tend to have a higher TSSA than non-isolated pions, which suggests that a different
 964 mechanism other than the Sivers or Collins effects is required to explain these results.

965

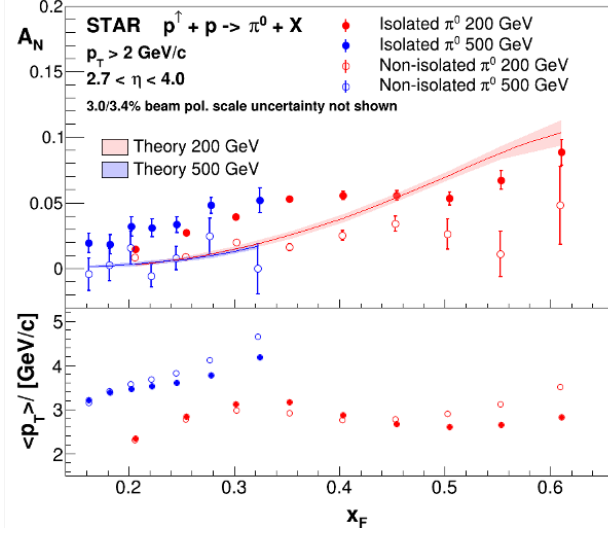


Figure 31: Preliminary results for the transverse single-spin asymmetry as function of Feynman- x for the isolated and non-isolated π^0 in transversely polarized proton-proton collisions at 200 and 500 GeV [108]. Theory curves based on a recent global fit [114] are also shown. The average transverse momentum of the π^0 for each x_F bin is shown in the lower panel.

966 1.3.4 Unpolarized Results

967 The azimuthal correlation of forward di-pions produced in p+p and p+Au collisions provides
 968 an essential tool to access the underlying gluon dynamics in the nonlinear evolution region.
 969 π^0 measured in the FMS in the pseudorapidity region $2.5 < \eta < 4.0$ probe low momentum
 970 fraction partons down to $x \approx 0.001$ at $\sqrt{s} = 200$ GeV, which are dominated by gluons. 2015
 971 p+Au collisions have a unique opportunity to study this phenomenon with much higher
 972 luminosities and smaller background than 2008 d+Au [115]. Figure 32 shows the status
 973 of di-pion correlation measurement from Run15 p+p and p+Au collisions. The away-side
 974 peak is suppressed in high activity p+Au collisions compared with p+p. This effect is more
 975 significant when the more central part of the nucleus is probed (with higher multiplicity as
 976 indicated by BBCE). Further analysis to characterize the p_T dependence and compare with
 977 theoretical expectations is ongoing.

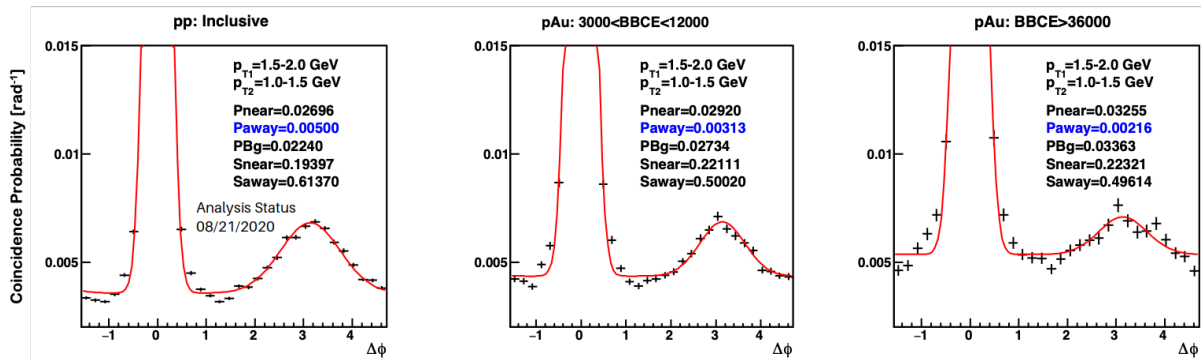


Figure 32: Coincidence probability as a function of azimuthal angle difference between two forward neutral pions in p+p, compared to low- and high-activity p+Au collisions. Analysis status on 08/21/2020.

978 The STAR measurement of the unpolarized cross-section ratio of the W^+ and W^- bosons

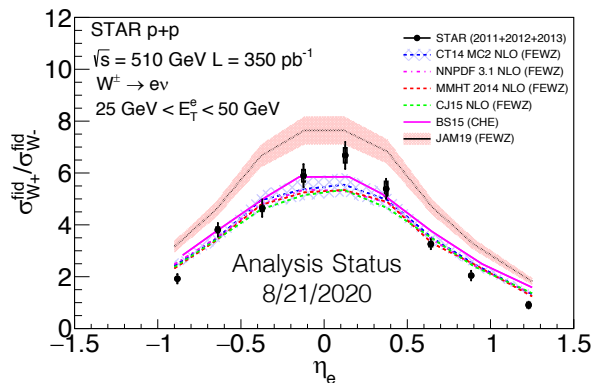


Figure 33: W^+ and W^- cross-section ratio as a function of lepton pseudorapidity for the combined 2011, 2012, and 2013 datasets. The central values correspond to the mean value of η_e distribution for that bin. The error bars represent the statistical uncertainty, whereas the rectangular boxes represent the systematic uncertainty for the respective data point. These measurements are compared to various theory frameworks, which use several different PDF inputs. Analysis status on 08/21/2020. Preliminary results available in Ref. [116].

979 from the STAR 2011 to 2013 data at $\sqrt{s} = 500/510$ GeV has released preliminary results [116]
 980 and is soon to be submitted to Physical Review D. Figure 33 shows the ratio plotted as a
 981 function of lepton pseudorapidity. This unique measurement is sensitive to the unpolarized
 982 \bar{d}/\bar{u} quark distribution and will provide insights into unpolarized light quark distributions
 983 $\bar{d}(x)$ and $\bar{u}(x)$ at $x > 0.05$. The measurement at STAR is complementary to the Drell-Yan
 984 results from NuSea [117] and SeaQuest [118], covering the overlapping x region of about
 985 $0.1 - 0.3$ at higher $Q^2 = M_W^2$.

986 Differential cross sections of Z^0 -boson production as function of transverse momentum
 987 are valuable input to global fits of TMD parton distribution functions, and STAR kinematics
 988 ($0.1 < x < 0.3$) are complementary to LHC and Tevatron data. Figure 34 shows preliminary
 989 results from 2011-2013 data with an integrated luminosity of 350 pb^{-1} [119]. Data on disk
 990 from 2017 comprise about the same luminosity, and preliminary results are expected soon
 991 along with transverse single-spin asymmetries. While the measurement of Z^0 -bosons is an
 992 experimentally very clean observable, it requires a good understanding of the calorimeter
 993 performance. These will inform the on-going background studies of the measurements of
 994 Sivers asymmetries for W -bosons, which are also expected very soon.

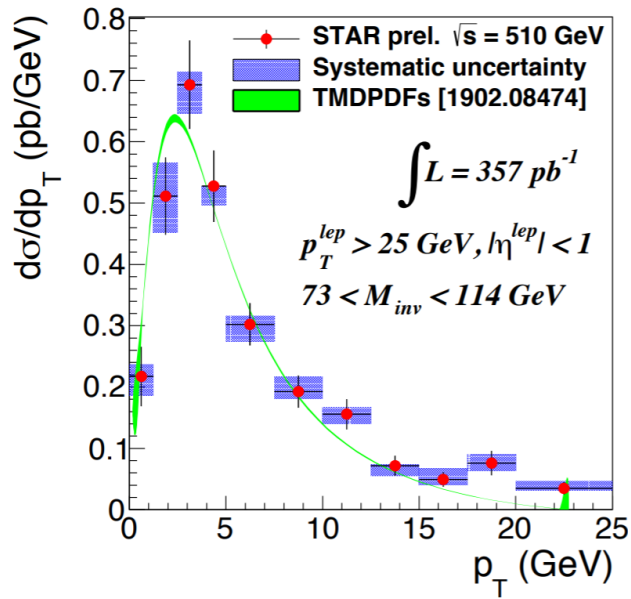


Figure 34: Preliminary results for the differential cross-section of Z^0 -bosons as function of transverse momentum p_T [119] and comparison with theory predictions based on calculations developed in [120]. Results are based on data from 2011-2013.

1.4 Run-20 Performance

In this section, we will review the BES-II collider and fixed-target performance to date. Careful study of these performance metrics will be used to make projections about the required time to complete the 7.7 GeV collider system in run 21.

The BES-II collider program performance is over-viewed in table 6. The 27 GeV system, which was run in 2018, was not officially part of the BES-II physics program, however it is close enough in energy to help provide some performance evaluation. The most important lines in the table from the point of view of performance evaluation are the *good event rate*, which is a measure of the useful luminosity, and the *data hours per day*. In general, we had seen improvements over the luminosities recorded in 2010/2011 of a factor of three to four. For the 27 GeV system, which was run in 2018 we saw the good event rate rise to 620 Hz, which implies a luminosity increase of factor of 3.3 over the 2011 performance.

The 19.6 GeV system was completed in 2019. For this system, the good event rate rose from 100 Hz in 2011 to 400 Hz in 2019 for a factor of 4.0 increase. We should note that it took 5.1 calendar weeks to complete the energy, however during the running period for the 19.6 GeV system, the facility was dedicating two twelve hour shifts per week to LEReC development. Correcting the 5.1 calendar weeks by 6/7 means that 4.4 beam weeks were used to complete this energy which should be compared to the 4.5 weeks which was requested in the STAR BUR for 2019. Historically, it has been shown that the luminosities scale with γ^2 above injection energy (9.8 GeV) and with γ^3 below injection energy. Scaling the 27 GeV performance would have predicted a good event rate of 330 Hz at 19.6 GeV. One should also note that the number of events recorded exceeded the required number significantly. Overall, the performance for the 19.6 GeV system significantly exceeded expectations.

The 14.6 GeV system was completed in 2019. This energy had been run previously in 2014, however the STAR good event rate was unusually low at that time so comparing the 23 Hz rate from 2014 to the 170 Hz rate in 2019 is not a good metric for performance. It required 8.6 calendar weeks to complete the required number of events, however during the running of the 14.6 GeV system, 40% of the beam time was used for LEReC development. Scaling the 8.6 calendar weeks by 60% yields effectively 5.1 weeks of beam time which favorably compares with the 5.5 weeks estimated in the BUR for 2019. Using the performance at 19.6 GeV (good event rate of 400 Hz), and the γ^3 scaling, we would have expected a good event rate at 14.6 GeV of 165 Hz. This compares well the the 170 Hz rate which was achieved for this energy. Performance at this energy slightly exceeded expectations.

The 11.5 GeV system was completed in 2020. The good event rate rose from 30 Hz in 2010 to 80 Hz in 2020 for a factor of 2.67 increase. It took 8.9 calendar weeks achieve the required event statistics. In the BUR for 2020 a range from 7.5 (optimistic) to 10 (pessimistic) was proposed. The actual time required fell in the middle of the expected range. Scaling the good event rate from 14.6 GeV by γ^3 predicted that the good event rate for 11.5 GeV would be 83 Hz, which compares favorably with the 80 Hz actually achieved for the run. Overall, performance at this energy met expectations.

The 9.2 GeV system will be completed in 2020 and is far enough along that we can project to completion. This energy was not run during BES-I, so there is not a historical

1037 comparison. Scaling the good event rate from 11.5 GeV by γ^3 predicts that we should have
1038 seen a good event rate of 38 Hz. Prior to the shutdown of the laboratory in March, we had
1039 achieved an average good event rate of 38 Hz and we had been averaging 16 hours of data
1040 taking per day, however the challenges of running in the summer have reduced the average
1041 number of hours of data taking to 13 and the average good event rate to 33. It is projected
1042 that this system will take 14.0 weeks to achieve the required event statistics, which is at the
1043 high end of the range that was included in the BUR for 2020.

1044 Quality assurance studies of the BES-II and FXT data indicate that roughly 98% of the
1045 data recorded will ultimately be used in physics analyses. The quality assurance takes place
1046 on multiple levels. At the time of data acquisition, online performance plots are reviewed
1047 as each run starts by the shift crew member. There are two levels of online plots; the first
1048 use the raw detector specific data to overview the performance of all systems; the second
1049 level does event-by-events tracking and vertex reconstruction using the High Level Trigger
1050 (HLT) computer farm to generate event level performance plots and to tag the good Au+Au
1051 collision events. The next level of quality assurance uses a FastOffline production of a small
1052 percentage of all recorded events. The plots generated by this review take place on a daily
1053 basis a provide the opportunity for corrections to any issues that might arise. A third level
1054 of quality assurance takes place in a weekly QA meeting which reviews the overlap between
1055 the events flagged as good from the HLT system, a significant fraction of which are recorded
1056 and available to preliminary offline physics analysis, and the events identified as good using
1057 the FastOffline processed data, which utilizes a more sophisticated tracking algorithm. The
1058 overlap of good events has been at the 98% level for all BES-II collider and FXT systems.
1059 The QA meeting also reviews preliminary physics working group quality assurance analysis
1060 of the FastOffline data sets. The final level of quality assurance comes from preliminary
1061 physics analyses using the FastOffline and the ExpressStream data sets. This multi-level to
1062 quality assurance guarantees that the data will meet the needs of the physics analyses for
1063 the BES-II science program.

1064 The relevant data sets recorded in 2018 have been fully calibrated and produced. These
1065 data sets are the 27 GeV collider system and the 3.0 and 7.2 GeV FXT data sets. Preliminary
1066 results for all of the key physics analyses have been performed and highlights of these new
1067 results are reviewed in the previous section of this document. The 2019 data sets have
1068 required extensive calibrations of the new detector systems, the iTPC and the eTOF. The
1069 large volume of cosmic ray data that were recorded have been used to do the fine spatial
1070 alignment of the new iTPC modules. New methods needed to be developed to calibrate
1071 the precise start timing for each event, which is needed to get the correct reconstruction of
1072 the z -location of the hits in the TPC to account for the long bunches used to maximize the
1073 luminosity for BES-II and the FXT programs. The complete set of calibrations for the first
1074 collider energy from 2019, the 19.6 GeV system, have been completed and a test production
1075 using these calibrations has been generated and are undergoing quality control.

1076 As several of the physics opportunities discussed in the following sub-sections utilize fixed-
1077 target systems, it is best to review the performance in this mode of operation. An overview of
1078 the performance for all fixed-target energies is shown in table 7. The first fixed-target physics

Table 6: Achieved and projected experiment performance criteria for the BES-II collider program.

| | | | | | | | |
|--|-------|-------------|------------|------------|------|-------------|-------------|
| Collision Energy (GeV) | 7.7 | 9.2 | 11.5 | 14.6 | 17.1 | 19.6 | 27 |
| Performance in BES-I | 2010 | NA | 2010 | 2014 | NA | 2011 | 2011 |
| Good Events (M) | 4.3 | NA | 11.7 | 12.6 | NA | 36 | 70 |
| Days running | 19 | NA | 10 | 21 | NA | 9 | 8 |
| Data Hours per day | 11 | NA | 12 | 10 | NA | 9 | 10 |
| Fill Length (min) | 10 | NA | 20 | 60 | NA | 30 | 60 |
| Good Event Rate (Hz) | 7 | NA | 30 | 23 | NA | 100 | 190 |
| Max DAQ Rate (Hz) | 80 | NA | 140 | 1000 | NA | 500 | 1200 |
| Performance in BES-II (achieved) | 2021 | 2020 | 2020 | 2019 | 2021 | 2019 | 2018 |
| Required Number of Events | 100 | 160 | 230 | 300 | 250 | 400 | NA |
| Achieved Number of Events | 2.9 | 160 | 235 | 324 | TBD | 582 | 560 |
| fill length (min) | 20-45 | 45 | 25 | 45 | 50 | 60 | 120 |
| Good Event Rate (Hz) | 16-24 | 33 | 80 | 170 | 265 | 400 | 620 |
| Max DAQ rate (Hz) | 400 | 700 | 550 | 800 | 1300 | 1800 | 2200 |
| Data Hours per day | 12-15 | 13 | 13 | 9 | 15 | 10 | 9 |
| Projected number of weeks | 11-20 | 8.5-14 | 7.6-10 | 5.5 | 2.5 | 4.5 | NA |
| weeks to reach goals | TBD | 14.0 | 8.9 | 8.6 | TBD | 5.1 | 4.0 |

1079 run was in 2018 using a 3.85 GeV beam. A total of three and half days was spent on this
 1080 system; first developing the conduct of operation and then recording a robust data sample.
 1081 The lowest energy beam was selected for this first run in 2018 because at that time the
 1082 iTPC and eTOF upgrades were not yet available; the lowest beam energy means the lowest
 1083 center-of-mass boost, which meant that we could still complete the physics program even
 1084 without the detector upgrades. Additionally in 2018, fixed-target data were recorded with
 1085 a single beam energy of 26.5 GeV. Obviously, at such a high energy the detector upgrades
 1086 would be essential for the mid-rapidity physics program. However, the 26.5 GeV beam
 1087 was not requested by STAR; this beam was being using by the Coherent Electron Cooling
 1088 program, and STAR was simply taking these data parasitically. This parasitic data taking
 1089 gave us further opportunities to refine the fixed-target conduct of operations, which gave us
 1090 confidence going forward that we could average 100 M good events per day in fixed-target
 1091 mode. This is limited by the STAR data acquisition system and not by RHIC.

1092 In 2019, eTOF detector upgrade system suffered damage at the start of the 14.6 GeV
 1093 collider system. This meant that it would be unavailable for any fixed-target energies taken
 1094 that year. It was felt that the physics program could still be achieved using the 4.59 GeV
 1095 beam, but that for all higher energies the loss of the eTOF system would compromise the
 1096 physics, so only modest samples at 5.75 and 31.2 GeV were taken.

1097 The eTOF detector was repaired for 2020, and relatively early in the run it was decided
 1098 to spend one week cycling through the seven remaining fixed-target energies. Roughly one

1099 day was spent at each energy. The conclusion from this series of fixed target energies is
 1100 that the collider and the experiment can quickly and efficiently set up and run fixed-target
 1101 systems. STAR can efficiently trigger on good fixed-target events with roughly 80-90% of
 1102 triggers passing the HLTgood test. The operators monitor the STAR event rate to keep the
 1103 current on target at a level to keep the STAR DAQ system running at full capacity and
 1104 minimizing the pile-up of multiple collisions in the target. Stores last for many hours (8-24
 1105 hours) and refill and realignment are fast and efficient.

1106 Preliminary physics results from the 3.0 and 7.2 GeV data sets recorded in 2018 are
 1107 available and highlights have been shown the the previous sections. Internal preliminary
 1108 physics analyses of the ExpressStream and FastOffline data sets have been performed and
 1109 these confirm the quality of the data taken.

Table 7: Event statistics (in millions) needed in the fixed-target part of the BES-II program for various observables, and the total number of events acquired (those events taken in 2018 did not include the iTPC or eTOF detectors; those taken in 2019 did not include the eTOF).

| $\sqrt{s_{NN}}$ (GeV) | 3.0 | 3.2 | 3.5 | 3.9 | 4.5 | 5.2 | 6.2 | 7.2 | 7.7 |
|-----------------------|------|------|------|------|------|------|------|------|------|
| Beam Energy | 3.85 | 4.59 | 5.75 | 7.3 | 9.8 | 13.5 | 19.5 | 26.5 | 31.2 |
| μ_B (MeV) | 721 | 699 | 666 | 633 | 589 | 541 | 487 | 443 | 420 |
| Rapidity y_{CM} | 1.06 | 1.13 | 1.25 | 1.37 | 1.52 | 1.68 | 1.87 | 2.02 | 2.10 |
| Observables | | | | | | | | | |
| Elliptic Flow | 300 | 150 | 80 | 40 | 20 | 40 | 60 | 70 | 80 |
| CME | 70 | 60 | 50 | 50 | 50 | 70 | 80 | 90 | 100 |
| Directed Flow | 20 | 30 | 35 | 45 | 50 | 60 | 70 | 80 | 90 |
| Femtoscopy | 60 | 50 | 40 | 50 | 65 | 70 | 80 | 90 | 100 |
| Kurtosis | 36 | 50 | 75 | 125 | 200 | 400 | 950 | NA | NA |
| Strange hadrons | 300 | 100 | 60 | 40 | 25 | 30 | 50 | 75 | 100 |
| Hypertritons | 200 | 100 | 80 | 50 | 50 | 60 | 70 | 85 | 100 |
| Event Totals | | | | | | | | | |
| Good events (2018) | 258 | | | | | | | 158 | |
| Good events (2019) | 3.7 | 200 | 53 | | | | | | 50 |
| Good events (2020) | | | 116 | 117 | 108 | 103 | 118 | TBD | 112 |

1110 2 Proposed Program - Hot QCD in Run-21, 23, and 25

1111 2.1 Beam Request for Run-21

1112 2.1.1 Completion of the BES-II Program

1113 The highest priority for Run-21 is the completion of the proposed BES-II program. At
1114 this time, the only system that remains to be taken is the 7.7 GeV collider data set. This
1115 energy is extremely important for several reasons. First, theoretical calculations suggest
1116 that the highest baryon density is achieved in collisions at this energy; second, several of the
1117 BES-I experimental signatures which have been put forth to be sensitive to the presence of
1118 deconfined matter either lose significance or are no longer present at this energy; third, the
1119 BES-I data showed enhanced fluctuations at this energy; finally, this energy provides the
1120 best acceptance overlap with the fixed-target program. Although the 7.7 GeV collider data
1121 set is extremely important from the point of view of the science, it is also technically the
1122 most challenging data set. The technical challenge of achieving a viable collision rate at this
1123 energy was the motivation to develop the Low Energy RHIC electron Cooling (LEReC) and
1124 is the reason that this energy has been left to the final year of the program.

1125 The specific physics goals (are required statistics) include: measurement of the elliptic
1126 flow of the phi meson for which the the constituent quark scaling was suggested to break
1127 down in the lowest energy BES-I data (80 M events required); measurement of the correlators
1128 associated with the charge separation induced by the chiral magnetic effect which were seen
1129 to collapse at the lowest BES-I energies (50 M events required); differential measurements of
1130 the directed flow of protons which was seen to show evidence of a softening of the equation of
1131 state in the lowest BES-I data (20 M events required); Azimuthal femtoscopy measurements
1132 of protons to study the tilt angle of the source (35 M events required); measurement of the
1133 net-proton kurtosis which showed significant enhanced fluctuations at 7.7 GeV in the BES-I
1134 data (70 M events required); measurements of the di-lepton invariant mass distributions to
1135 determine in the excess in the low mass region is proportional to the total baryon density
1136 (100 M events required); and the global lambda polarization to determine the magnetic field
1137 significance (50 M events required). These analyses are being pursued at all of the BES-II
1138 collider energies; for several of the physics measurements, the 7.7 GeV energy is expected to
1139 be either the most significant or the most challenging.

1140 The 7.7 GeV collider system provides the essential bridge between the collider and fixed-
1141 target energy scans. Although in later sections we detail a request to acquire fixed-target
1142 data at higher overlap energies, there is the largest region of common coverage at this energy.
1143 This will provide critical cross checks between the different modes.

1144 Although the 7.7 GeV collider system is the most technically challenging system of the
1145 suite of BES-II and FXT energies, one can use the performances which have already been
1146 achieved during the BES-II program to help develop projections for the 7.7 GeV collider
1147 energy. These BES-II performance trends have been detailed in 6. In 2010, STAR achieved
1148 a good event rate of 7 Hz; a factor of three improvement would result in a 21 Hz rate. Scaling
1149 the performance at 9.2 GeV by γ^3 would predict a good event rate of 19.3 Hz. We project the

1150 good event rate to fall between 16 and 24 Hz. We project the range of hours of data taking
 1151 per day to fall between 12 and 15. These numbers suggest a range in the expected number
 1152 of weeks to reach the goals from 11 to 20 weeks. We should note that CAD has provided
 1153 projections which suggest that it will take 28 weeks to reach the goals. Our projections are
 1154 more optimistic. Although we recognize that it is likely that running the 7.7 system will
 1155 require all the available beam time in 2021, the optimistic range of our predictions suggests
 1156 that we should prepare for success and we have therefore considered and prioritized other
 1157 programs which could be run in 2021 if time were to be available.

1158 **2.1.2 Au+Au Collisions in FXT Mode at $\sqrt{s_{\text{NN}}} = 3.0$ GeV - I: 300 million goal**

1159 QCD matter at high baryon chemical potential region contains a wealth of unexplored physics
 1160 and is one the central focus of current and future heavy-ion collision programs in few GeV
 1161 energy range around the world. RHIC has been able to deliver beams with the energy as
 1162 low as 3.85 GeV per nucleon. Utilizing the gold fixed target (FXT) installed in the STAR
 1163 experiment, we were able to record collision events at the center-of-mass-energy as low as
 1164 $\sqrt{s_{\text{NN}}} = 3.0$ GeV, which corresponds to baryon chemical potential of $\mu_B \sim 720$ MeV in
 1165 central collisions. STAR detector configuration (including the iTPC and eTOF) has the
 1166 full midrapidity coverage ($|y| < 0.5$) at this energy and enables us to carry a systematic
 1167 investigation of the dynamics of the QCD matter created in these collisions at $\sqrt{s_{\text{NN}}}$ from
 1168 3.0 up to 200 GeV.

1169 At such a high μ_B region and moderate temperatures, baryon dynamics become important
 1170 or even dominant in understanding the QCD matter properties. Strange quarks, due to their
 1171 heavier masses, play an important role in study the high net-baryon density QCD matter.
 1172 The combination of increased sensitivity of strange quarks with the existing high baryon
 1173 density in low energy heavy-ion collisions offers a unique condition to create various light
 1174 hypernuclei, which enables us to study *e.g.* the hyperon-nucleon (Y - N) interactions, which
 1175 have potential implications for the inner structure of compact stars in nuclear astrophysics.

1176 STAR has collected ~ 250 million FXT Au+Au events at $\sqrt{s_{\text{NN}}} = 3.0$ GeV in 2018
 1177 before iTPC and eTOF were installed.. We propose to collect a minimum of 300 million
 1178 events with the extended phase-space coverage enabled by iTPC and eTOF for the following
 1179 measurements:

- 1180 • high moments of proton multiplicity distributions covering the same midrapidity ac-
 1181 ceptance $|y| < 0.5$, $0.4 < p_T < 2.0$ GeV/ c , comparable to that with the BES-I and BES-II
 1182 measurements in collider mode.
- 1183 • precision ϕ meson production at midrapidity to test the validity of Canonical Ensemble
 1184 (CE) for strangeness production at high baryon density region.
- 1185 • systematic measurements of lifetime, binding energy, production yield, collective flow
 1186 of light hypernuclei (${}^3_{\Lambda}\text{H}$, ${}^4_{\Lambda}\text{H}$, ${}^5_{\Lambda}\text{He}$ etc.).
- 1187 • measurement of low- and intermediate-mass dileptons to extract fireball lifetime, its
 1188 average temperature and to access the microscopic properties of matter. This would

1189
1190

be the first measurement of electromagnetic radiation at this energy which will guide the future high μ_B facilities at FAIR, NICA.

1191
1192

With additional beam time allowed, we would like to further collect up to 2 billion Au+Au FXT events at $\sqrt{s_{NN}} = 3.0$ GeV which will be elaborated in the next section.

1193
1194
1195
1196

One feature we would like to point out is that the single beam energy for FXT collisions at $\sqrt{s_{NN}} = 3.0$ GeV is 3.85 GeV per nucleon, the same beam energy to be used for colliding to collect the major 7.7 GeV collision dataset in year 2021. This leads to a negligible transition time for operation between $\sqrt{s_{NN}} = 7.7$ GeV collider mode and $\sqrt{s_{NN}} = 3.0$ GeV FXT mode.

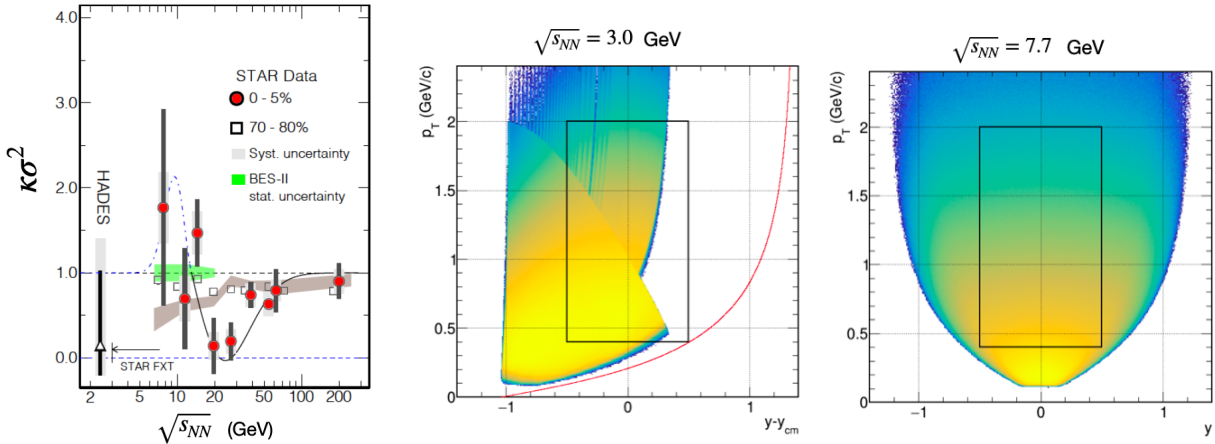


Figure 35: (Left) The net-proton $\kappa\sigma^2$ in most central (0-5%) and peripheral (70-80%) Au+Au collisions as a function of collision energy. (Middle/Right) Proton acceptance plot p_T vs. y in the center-of-mass frame at $\sqrt{s_{NN}} = 3.0$ GeV (FXT data from 2018) and 7.7 GeV (collider data from 2010), respectively. The red curve in the middle panel indicates the acceptance boundary with iTPC and eTOF.

1197
1198
1199
1200
1201
1202
1203
1204
1205
1206
1207
1208
1209
1210

High moments of proton multiplicity distributions A non-monotonic behavior of net-proton high moments $\kappa\sigma^2$ as a function of collision energy has been suggested to be an evidence of the existence of QCD critical point [121, 122]. Figure 35 (left panel) shows the final STAR measurement from the BES-I data as a function of energy exhibiting a suggestive non-monotonic behavior [123, 124]. A complete picture of the non-monotonic behavior requires measurements at collision energies below the lowest collider mode energy (7.7 GeV) by utilizing the FXT mode collisions. STAR detector configuration has the best midrapidity coverage for fixed target collisions at the lowest collision energy $\sqrt{s_{NN}} = 3.0$ GeV. Figure 35 middle and right panels show the proton acceptance with TPC and barrel TOF in 2018 FXT data at 3.0 GeV and 2010 collider data at 7.7 GeV, respectively. In the 2018 FXT data, to ensure $> 95\%$ purity of the proton sample, one needs to utilize the barrel TOF for high momentum particle identification. With this requirement, the proton acceptance in 2018 covers full negative rapidity region ($-0.5 < y < 0$, $0.4 < p_T < 2.0$ GeV/c), while missing a considerable acceptance in the positive rapidity region. A new run, with eTOF and iTPC,

1211 would allow for phase space coverage comparable to the one in collider mode (indicated by the
 1212 box in the middle panel). The estimated acceptance boundary for protons is indicated by the
 1213 red line shown in Fig. 35 middle panel. We can therefore cover the full midrapidity $|y| < 0.5$
 1214 region from $0.4 < p_T < 2.0$ GeV/c which will be the same as these measurements conducted
 1215 in collider mode data, shown in the right panel. This would allow to perform a systematic
 1216 scan of the net-proton high moments analysis within the same mid-rapidity acceptance across
 1217 the collision energy from 3.0 up to 200 GeV. In the meantime, the increased rapidity coverage
 1218 will also enable us to investigate the rapidity-window (Δy) dependence of these fluctuations,
 1219 which will offer us deep understanding on the physics origin through the development of
 1220 these fluctuations vs. Δy [125].

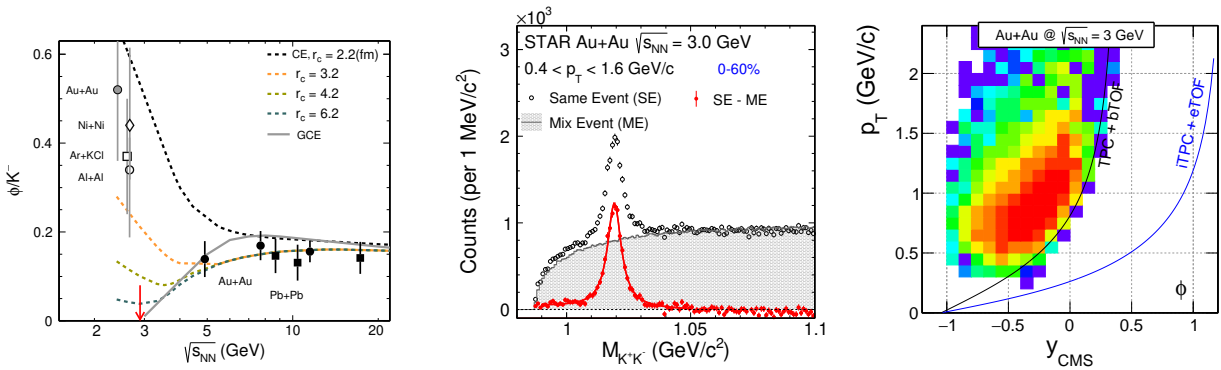


Figure 36: (Left) ϕ/K^- ratio as a function of collision energy from several heavy-ion experiments in comparison to thermal model calculations assuming strangeness following GCE and CE with different canonical radius. (Middle) Invariant mass distributions of K^+K^- pairs and the ϕ meson signal in 2018 FXT data at $\sqrt{s_{NN}}=3.0$ GeV. (Right) Reconstructed ϕ meson candidate phase space distributions using 2018 FXT data taken at $\sqrt{s_{NN}}=3.0$ GeV. The black line shows the boundary of combining the TPC and barrel TOF detector for kaon identification. The blue line indicates the anticipated boundary extended by iTPC and eTOF for kaon identification in the proposed 2021 FXT run at $\sqrt{s_{NN}}=3.0$ GeV.

1221 **ϕ meson production** Yields of strange hadron produced in relativistic heavy-ion col-
 1222 lisions from RHIC BES-I energies up to the LHC energy ($\sqrt{s_{NN}}=7.7-5500$ GeV) can be
 1223 well described by thermal model with Grand Canonical Ensemble (GCE) in which strange
 1224 quark number is conserved on average [126–129]. It has been argued that at low energy
 1225 heavy-ion collisions when the fireball created in these collisions becomes small enough the
 1226 GCE for strange quarks will break down. Strangeness needs to be conserved on the event-
 1227 by-event basis, therefore only Canonical Ensemble (CE) is applicable to strange hadron
 1228 production [127, 129]. Strange hadrons with finite strangeness number (e.g. K , Λ etc.) will
 1229 suffer from a suppression due to the strangeness number conservation, often characterized
 1230 by a canonical radius (r_c) for strange quark profile in comparison to the regular radius (r)
 1231 for light quarks [130, 131]. The ϕ meson is the lightest bound state of s and \bar{s} quarks with
 1232 zero net-strangeness number. Its production yield, on the contrary, will not suffer from the

1233 canonical suppression. Therefore CE models predict the ϕ/K^- ratio will show an enhance-
1234 ment in very low energy heavy-ion collisions while GCE models calculate the ϕ/K^- ratio will
1235 gradually drop to zero at the ϕ production threshold in pp collisions. ($\sqrt{s_{\text{NN}}} = 2.89$ GeV).

1236 Experimentally, the measured ϕ/K^- values stay around 0.15 at $\sqrt{s_{\text{NN}}} > 5$ GeV up to
1237 the LHC energy. At collision energies below the ϕ production threshold in pp collisions,
1238 measurements from HADES and FOPI suggest an enhancement compared to those at high
1239 energies, consistent with the CE description for strange quarks at such low energies within
1240 appreciable uncertainties [132, 133]. High precision measurement of the ϕ/K^- at such low
1241 energies will be of great interest to systematic investigate the ϕ meson and strangeness
1242 production mechanism in heavy-ion collisions.

1243 We have performed such a measurement using the FXT data at $\sqrt{s_{\text{NN}}} = 3$ GeV taken
1244 in 2018. Fig. 36 middle panel shows the reconstructed K^+K^- invariant mass distributions
1245 in 0-60% centrality. The shaded histogram shows the K^+K^- pair distributions from the
1246 mixed-event technique while normalized at the mass region above the ϕ meson signal. The
1247 red data points show the mixed-event background subtracted distributions and the ϕ meson
1248 signal obtained in this data is about 60σ . The right panel shows the ϕ meson acceptance
1249 coverage in center-of-mass frame. Due to the small production yield of kaons, one needs to
1250 rely on clean particle identification using TOF detector to obtain a control background in
1251 the ϕ meson reconstruction. The black curve indicates the single track acceptance boundary
1252 from TPC and barrel TOF in 2018 year run. One can see the ϕ meson p_T acceptance at
1253 midrapidity is limited at ~ 0.6 - 0.8 GeV/ c . This covers roughly only 40% of the ϕ meson yield
1254 in the full p_T region, leading to a considerable amount of systematic uncertainty due to the
1255 p_T extrapolation. The blue curve in the same panel indicates the anticipated single track
1256 boundary with iTPC and eTOF. The p_T lower limit can be extended down to ~ 0.2 GeV/ c ,
1257 yielding a p_T coverage of $\sim 90\%$ of total dN/dy at midrapidity. This will greatly reduce the
1258 systematic uncertainty in the total ϕ meson yield measurement.

1259 We therefore request to take the FXT data at $\sqrt{s_{\text{NN}}} = 3$ GeV with iTPC and eTOF
1260 detectors in RHIC 2021 year run. A roughly similar amount of statistics (300 million) will
1261 allow us to perform the measurement of ϕ/K^- ratio with high precision both statistically
1262 and systematically.

1263 **Hypernuclei production** Hypernuclei are those nuclei with one or more nucleons re-
1264 placed with hyperons (typically Λ s). The study of hypernuclei lifetime, binding energy and
1265 their production mechanism offer insights to the understanding of hyperon-nucleon ($Y-N$)
1266 interactions. The $Y-N$ interactions could have significant implications to our understanding
1267 of the internal structure of compact stars in nuclear astrophysics.

1268 Heavy-ion collisions have shown great potential in studying the light hypernuclei proper-
1269 ties and their production mechanism. There have been unprecedented measurements from
1270 RHIC and LHC on both the lifetime and binding energy (anti-)hypertriton (${}^3_{\Lambda}\text{H}$ and ${}^3_{\Lambda}\overline{\text{H}}$). At
1271 low energy heavy-ion collisions, due to the high baryon density and high strangeness popu-
1272 lation, statistical hadronization thermal model predicts a significant enhancement of various
1273 light hypernuclei production yield, shown in Fig. 37 left panel [134]. The STAR FXT energy

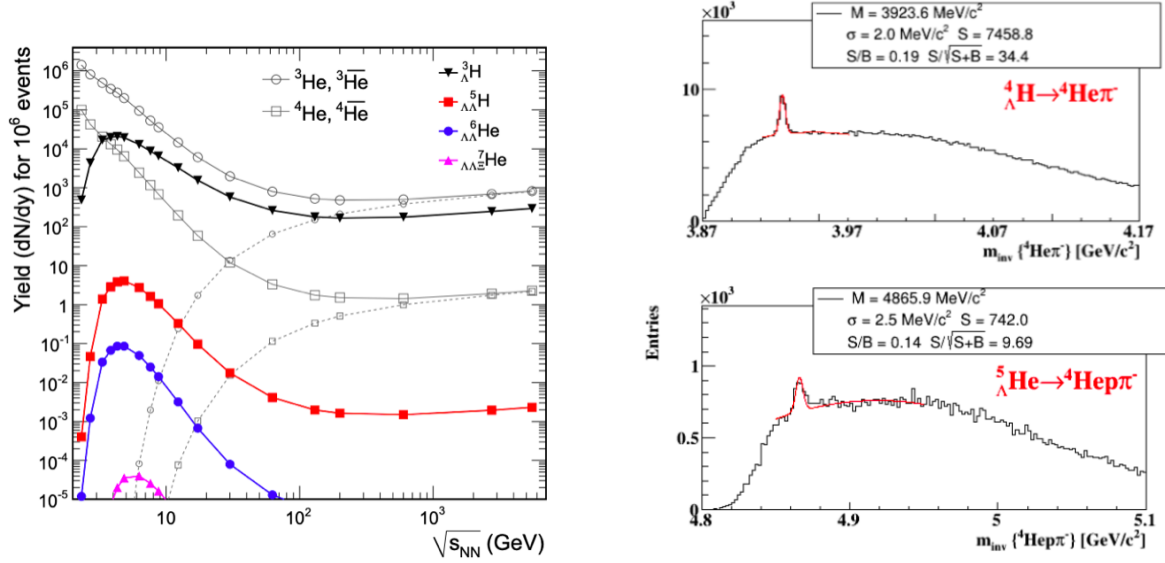


Figure 37: (Left) Thermal model predictions of various light nuclei and hypernuclei production yield at midrapidity in central heavy-ion collisions as a function of collision energy [134]. (Right) Invariant mass distribution of ${}^4\text{He}\pi^-$ (top) ${}^4\text{He}\pi\pi^-$ (bottom) from 2018 FXT data at $\sqrt{s_{\text{NN}}}=3.0$ GeV. The ${}^4_{\Lambda}\text{H}$ and ${}^5_{\Lambda}\text{He}$ hypernuclei signal is clearly visible on top of background.

1274 region from $\sqrt{s_{\text{NN}}} = 3.0 - 7.7$ GeV sits nicely in the maximum mid-rapidity production yield
 1275 of various hypernuclei while STAR detector layout has the best midrapidity acceptance cov-
 1276 erage at 3.0 GeV. Figure 37 right panel shows the reconstructed ${}^4_{\Lambda}\text{H}$ and ${}^5_{\Lambda}\text{He}$ signal from the
 1277 2018 FXT dataset at $\sqrt{s_{\text{NN}}} = 3.0$ GeV. These are so far the most unprecedented statistics
 1278 on these light nuclei that will allow us to systematically investigate their lifetimes, binding
 1279 energies as well as their production yield and collective flow behavior in heavy-ion collisions.

1280 2.1.3 Au+Au Collisions in FXT Mode at $\sqrt{s_{\text{NN}}} = 9.2, 11.5, \text{ and } 13.7$ GeV

1281 The BES-II program aims to study the nature of QCD matter by varying the temperature
 1282 and baryon chemical potential. High baryon chemical potentials are achieved by ‘stopping’
 1283 the baryons which made up the two colliding nuclei. To better understand the development
 1284 of the baryon chemical potential and its profile through the interaction region, it is necessary
 1285 to study the rapidity density distribution of the protons across a broad range in rapidity. It
 1286 is important that the rapidity range covered includes the peak of the participant distribution
 1287 which have been accelerated during the collision process. For all collider energies available
 1288 at RHIC (7.7 GeV and above), the peak of the rapidity distribution of the stopped protons
 1289 is outside or at the edge of the acceptance of the STAR TPC (which only extends 0.6 units
 1290 beyond mid-rapidity with particle identification via dE/dx , this is extended to 1.0 units
 1291 of rapidity using eTOF particle ID); for $\sqrt{s_{\text{NN}}} = 9.2, 11.5, \text{ and } 13.7$ GeV, the shifted 0.9,
 1292 1.0, and 1.1 units away from mid-rapidity respectively. However, in fixed-target mode the
 1293 STAR detector is excellent for studies of stopping as the acceptance extends 1.7 units from

1294 target rapidity (see figure 38) toward mid-rapidity; for $\sqrt{s_{\text{NN}}} = 9.2, 11.5, \text{ and } 13.7$ GeV,
 1295 $y_{\text{CM}} = 2.28, 2.50, \text{ and } 2.68$ respectively. Combining collider and fixed-target measurements
 1296 at each energy will provide full coverage from target rapidity to center-of-mass rapidity. The
 1297 stopping of the incident protons is the key to changing the baryon chemical potential in the
 1298 interaction region and the changing baryon chemical potential is the key to mapping out the
 1299 phase diagram of QCD matter.

1300 Complete rapidity density distribution for identified particles will provide important con-
 1301 straints for models. It has been noted by Shen [135] that the high rapidity tails of the dN/dy
 1302 distributions are very important and that high rapidity data are rare. In the energy range
 1303 from $\sqrt{s_{\text{NN}}} = 5.0$ to 200 GeV, the only available proton rapidity density distribution mea-
 1304 surements are from NA49 at 8.77 and 17.3 GeV [136] and from BRAHMS at 62.4 and 200
 1305 GeV [137]. Shen used these data to constrain his 3-D models of the collisions to better un-
 1306 derstand the elliptic flow measurements in heavy-ion collisions. In the BES-II energy range,
 1307 around 10 GeV, these models can set strong constraints on the dependence of Quark-Gluon
 1308 Plasma shear viscosity on temperature and net baryon chemical, however, in order to do so,
 1309 it is necessary to have knowledge of the rapidity distributions of net-protons and produced
 1310 particles.

1311 It has been proposed that the trend of the rapidity shift of the stopped protons with
 1312 collision energy will provide a signature of the softening of the equation of state at the phase
 1313 transition [138]. Specifically, the model which has a two phase equation of state shows that
 1314 the increase in the rapidity shift with collision energy stalls in the $\sqrt{s_{\text{NN}}} = 8$ to 12 GeV
 1315 range.

1316 We proposed to extend the studies to proton stopping through the BES-II energy regime.
 1317 Specifically we propose to add three more energies to the high end of the FXT energy range.
 1318 These energies are chosen to provide three more overlap energies with the collider program.
 1319 Single beam energies of 44.5, 70, and 100 GeV will provide interactions at $\sqrt{s_{\text{NN}}} = 9.2,$
 1320 $11.5, \text{ and } 13.7$ GeV (the top energy is not quite an overlap energy with the 14.6 GeV
 1321 collider system). Combining the midrapidity coverage from the collider mode and the target
 1322 rapidity coverage from the fixed-target mode will provide full rapidity coverage for inclusive
 1323 observables. Since the focus for program will be inclusive observables, 50 M events will be
 1324 sufficient at each energy. We propose that at each of these three energies, twelve hours be
 1325 spent on beam development and twelve hours be spent taking data.

1326 2.2 Further Opportunities in Run-21

1327 S

1328 2.2.1 Small System Run: O+O at $\sqrt{s_{\text{NN}}} = 200$ GeV

1329 **Introduction** Collective long-range azimuthal correlations in A+A collisions have been
 1330 successfully described as a hydrodynamic response by a fluid-like system to geometric shape
 1331 fluctuations in the initial state. In recent years, observation of similar collective phenomena
 1332 in small-system collisions, such as pp and $p+A$ collisions, has attracted wide interests in

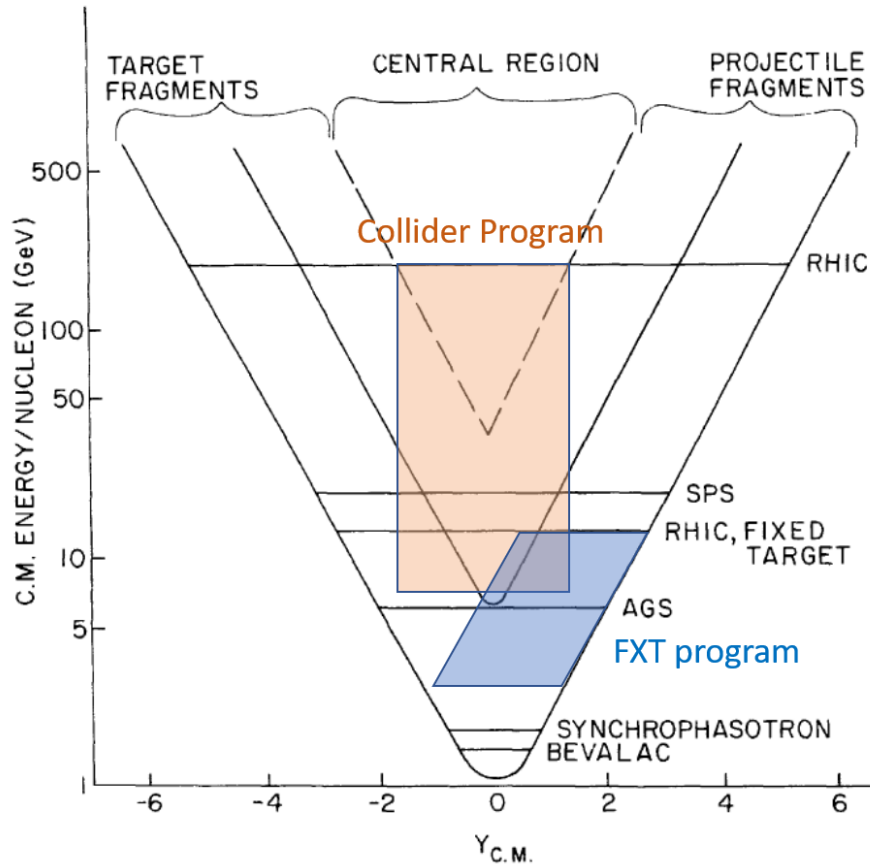


Figure 38: This figure has been modified from a figure in the introduction of the Conceptual Design Report for the RHIC facility. The black lines indicate different regions in the rapidity - center of mass energy space. The ‘V’ shaped region in the top center of the figure which is labeled at the central region have been predicted and demonstrate to be a low baryon chemical potential region characterized by a continuous phase transition between the QG and the hadron gas. The outer ‘V’ shaped region is dominated by the target fragments. Colored regions are overlaid to indicate the coverage of the STAR detector for collider (Orange) and FXT (Blue) modes. For the three higher energies currently being proposed, the FXT acceptance covers the region dominated by target fragments while the collider acceptance covers the equilibrated central region.

1333 the community. The interpretation of a fluid-like state formed there has been challenged,
 1334 as the small size and short lifetime might prevent the system from quickly thermalizing
 1335 and evolving hydrodynamically. Instead, collectivity arising either from initial momentum
 1336 correlations motivated by gluon saturation models [139] or via a few scatterings among
 1337 partons (without hydrodynamization) [140–142] has been proposed as alternative source of
 1338 collectivity that may be dominant in small systems. Lots of experimental and theoretical
 1339 efforts have been devoted to the study of collectivity in small-system collisions, with the
 1340 goal of understanding the time-scale for the emergence of collectivity and the mechanism for
 1341 early-time hydrodynamization in large collision systems.

1342 One key feature that distinguishes initial momentum correlation models (ISM) from final-
 1343 state interaction models (FSM, including hydrodynamics or a few scatterings) is the connec-
 1344 tion to the initial-state geometry [143]. In FSM, the collectivity is a geometrical response to
 1345 initial shape fluctuations, i.e., v_n is approximately proportional to the n^{th} -order initial-state
 1346 eccentricity ε_n . In ISM, such a geometrical response is expected to be absent [144]. It was
 1347 proposed that a geometry scan of various colliding systems with different spatial eccentricities
 1348 can help distinguish between contributions of these two scenarios [145].

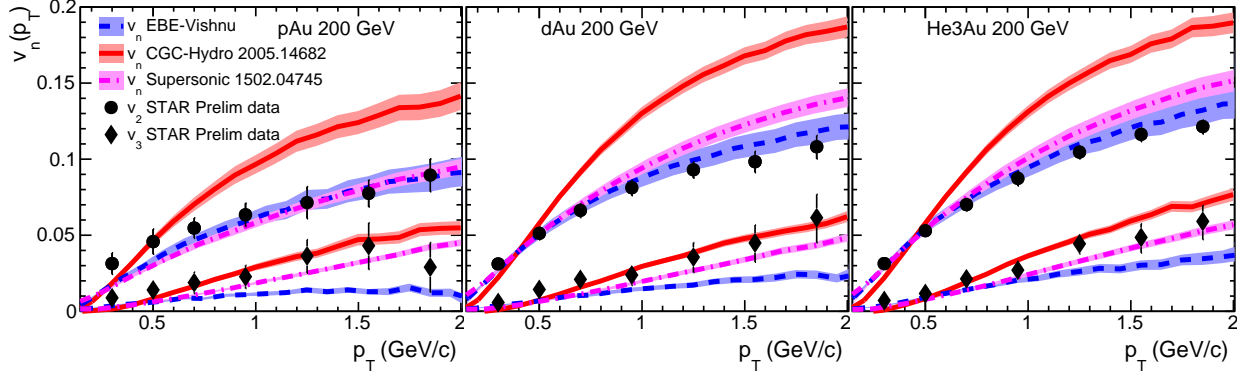


Figure 39: Comparison of v_2 and v_3 in p +Au, d +Au and ${}^3\text{He}$ +Au collisions at $\sqrt{s_{\text{NN}}} = 200$ between STAR data and various model calculations.

1349 Such a small system scan program has been recently carried out at RHIC for a few
 1350 asymmetric small systems including p +Au, d +Au and ${}^3\text{He}$ +Au, where studies of elliptic
 1351 flow (v_2) and triangular flow (v_3) have been performed [43, 146, 147]. In a Glauber model
 1352 that only considers the fluctuations of nucleon positions [145], ε_2 in d +Au and ${}^3\text{He}$ +Au is
 1353 expected to be larger than in p +Au, while ε_3 in p +Au and d +Au are expected to be smaller
 1354 than in ${}^3\text{He}$ +Au. However, once the fluctuations at subnucleonic scales are included [144],
 1355 the ε_3 are expected to be similar among all three systems. Fig. 39 compares the STAR
 1356 v_2 and v_3 results with three hydrodynamic models predictions with different assumptions
 1357 about the initial state. Calculations [148, 149] that include initial momentum anisotropy
 1358 and/or subnucleonic fluctuations indeed describe the STAR v_3 data in all three systems, but
 1359 one of the model [148] overestimates the v_2 data. On the other hand, hydrodynamic model
 1360 based on fluctuations only at nucleonic level [150] fails to describe the v_3 data. This implies
 1361 that the initial state in these asymmetric small collision systems are not well constrained, in
 1362 particular in p +Au and d +Au system (there is reasonable consensus that the flow results in
 1363 ${}^3\text{He}$ +Au is dominated by FSM). The relative importance of FSM vs. ISM for the v_n data in
 1364 small systems is an area of intense ongoing debate [151].

1365 **Physics case for a small A+A scan** So far, both RHIC and the LHC carried out col-
 1366 lisions for either relatively large (Pb+Pb, Au+Au, Xe+Xe, Cu+Cu, ...), which are well
 1367 described by hydrodynamic models, or small asymmetric systems (p +Pb, p +Au, d +Au, and
 1368 ${}^3\text{He}$ +Au), whose initial state are poorly constrained as discussed above. To quantitatively

1369 understand the initial momentum anisotropy and the role of subnucleonic fluctuations, col-
 1370 lisions of small but symmetric systems, such as O+O, Al+Al and Ar+Ar will be necessary.
 1371 They will also fill the gap between pp and Cu+Cu systems is a crucial unexplored frontier¹,
 1372 where a transition from ISM to FSM dominated collectivity may be observable. The list of
 1373 key open questions related to collectivity in small systems includes:

- 1374 • How much do initial-state correlations vs. geometry-driven final-state interactions con-
 1375 tribute to the observed collectivity? Can we unambiguously establish experimental
 1376 evidence of initial-state correlations?
- 1377 • For final-state scenarios, to what extent does the collectivity arise from a hydrodynamic
 1378 fluid-like QGP, as opposed to an off-equilibrium system with only a few scatterings per
 1379 parton?
- 1380 • What is the role of subnucleonic fluctuations in determining the initial-state geometry?
- 1381 • Can we observe jet quenching in small systems?

1382 A new comprehensive scan of colliding ion species at RHIC by systematically varying the
 1383 system size and geometry between pp and Cu+Cu collisions, will provide a unique lever-
 1384 arm to dial contributions from various mechanisms and impose strong constraints on both
 1385 ISM and FSM. Since the last RHIC $p/d/\text{He}+\text{Au}$ scan, the STAR experiment has completed
 1386 several detector upgrades that extend p_T and particle identification to $|\eta| < 1.5$, and provide
 1387 centrality and event plane determination in $2 < |\eta| < 5$ [17, 152, 153]. An ongoing forward
 1388 upgrade to instrument the $2.5 < \eta < 4$ region with tracking detectors and calorimeters
 1389 will be completed prior to 2021 run [154]. The extended detector capability will allow a
 1390 full exploration of collectivity using all the observables and methods developed for large
 1391 systems at RHIC/LHC. We will have better control of the non-flow systematics, leading to
 1392 a better understanding of the multi-particle nature of the collectivity and the longitudinal
 1393 correlations to constrain the full 3D initial conditions. As an illustration, model studies of
 1394 v_2 and v_3 in a series of small systems including symmetric (C+C, O+O, Al+Al, Ar+Ar) and
 1395 asymmetric ($p+\text{Au}$, $d+\text{Au}$, $^4\text{He}+\text{Au}$) collisions using the AMPT model are shown in Fig. 40.
 1396 AMPT belongs to the category of final-state interaction models, where v_n is largely driven by
 1397 the geometry of initial nucleon distributions. The v_2 values from asymmetric systems follow
 1398 different trends: the v_2 in $d/{}^4\text{He}+\text{Au}$ increases with N_{ch} , while it is relatively constant in
 1399 $p+\text{Au}$. The v_3 values show a similar N_{ch} dependence as symmetric systems, except for $d+\text{Au}$
 1400 which deviates from the common trend at large N_{ch} . This study demonstrates that, in a
 1401 scenario driven by final-state interactions, a clear difference is expected between $d/{}^4\text{He}+\text{Au}$
 1402 and A+A for v_2 , while a relatively similar behavior should be observed for v_3 . Contributions
 1403 from other sources, especially ISM, are expected to follow a drastically different behavior;
 1404 as the system size increases, the ISM contribution will gradually become subdominant.

¹RHIC has no limitation on small A+A systems, based on private communication with Wolfram Fischer

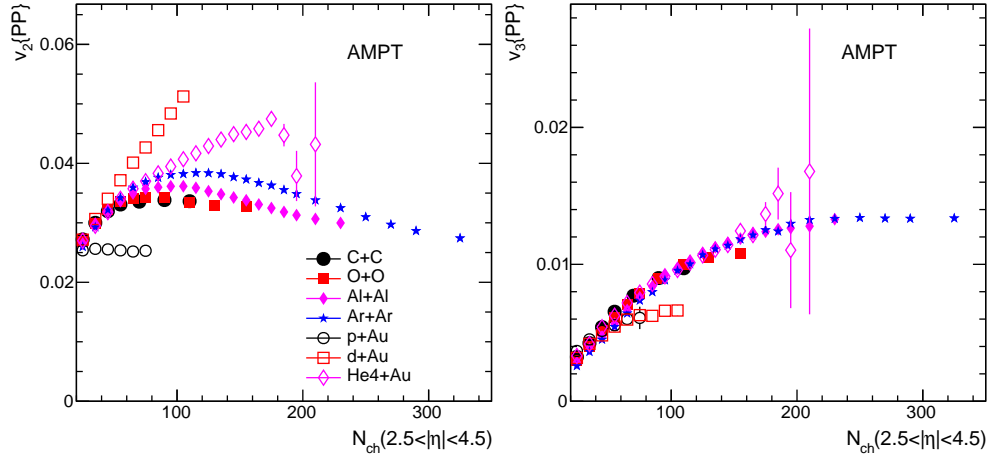
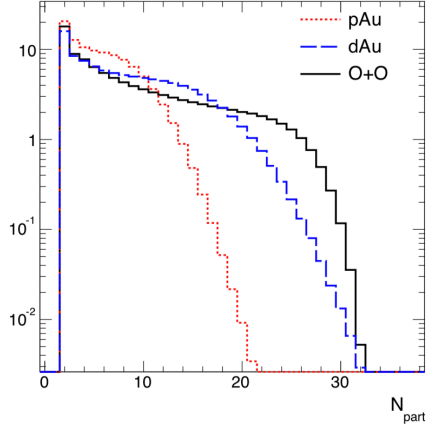


Figure 40: (Left) AMPT predictions for v_2 and (Right) v_3 as a function of N_{ch} in four symmetric and three asymmetric small collision systems.

1405 **Arguments for a short O+O run in 2021** In this BUR, we propose a O+O run at $\sqrt{s_{\text{NN}}} = 200$ GeV towards the end of the BES-II in 2021, to be followed up with a comprehensive scan
 1406 of symmetric and asymmetric small collision systems using the STAR forward upgrade after
 1407 2021, possibly in collaboration with sPHENIX. The choice of O+O collisions as the starting
 1408 point is motivated by the following reasons: 1) O+O has an N_{part} coverage comparable to
 1409 p +Au and d +Au but with a much flatter distribution (see Fig 41), which allows much better
 1410 control of initial geometry and centrality bias, 2) the Oxygen is a reasonably sized system
 1411 for which the both the nucleonic and subnucleonic DOF are important, which together
 1412 with p/dAu data can be used disentangle these contributions, 3) a strong synergy with the
 1413 proposed higher-energy O+O run at the LHC around around 2023–2024 to enable a direct
 1414 comparison of the same small-system collision species at drastically different energies. More
 1415 details, including hydrodynamic model predictions, are presented and discussed below.
 1416

1417 The recent yellow report on the future LHC heavy-ion physics program discusses the
 1418 possibility for smaller A+A collisions [155]. This includes a proposal of an O+O run at
 1419 $\sqrt{s_{\text{NN}}} = 2.76\text{--}7$ TeV in 2022², and other light-ion species such as Ar+Ar beyond 2028. As
 1420 mentioned earlier, one big advantage of the O+O system is that it allows a better control
 1421 of N_{part} and ε_n , compared to peripheral Pb+Pb collisions [155]. An O+O run at RHIC
 1422 right after the BES-II would provide a timely comparison of the same small system at very
 1423 different collision energies (0.2 TeV vs. 2.76–7 TeV). This “RHIC-LHC energy scan” provides
 1424 a unique opportunity to study systems with nearly identical initial nucleon geometry but
 1425 very different subnucleon fluctuations and different saturation scales. The large lever-arm
 1426 in collision energy should provide new insights on the onset behavior of collectivity, jet
 1427 quenching, or any other final-state effects in small systems: any model has to describe
 1428 results at both energies, which naturally leads to a better understanding of results at each
 1429 energy.

²According the latest schedule of the LHC run 3, O+O run will most likely be scheduled in 2023.



| | pAu | dAu | $^{16}\text{O}+^{16}\text{O}$ |
|-----------------------------------|-----|-----|-------------------------------|
| $\langle N_{\text{part}} \rangle$ | 5.8 | 8.8 | 9.5 |

Figure 41: The N_{part} distribution in O+O collisions compared with p +Au and d +Au collisions at $\sqrt{s_{\text{NN}}} = 200$ GeV estimated from Glauber model. The table to the right shows the average N_{part} values in the three systems.

1430 Figure. 42 compares the $v_n(p_T)$ data and hydrodynamic calculations for $n = 2$ and 3 at
 1431 two energies in a large A+A system (left) and in a p +A system (right). It is well-known that
 1432 $v_n(p_T)$ for charged hadrons in large systems has very little $\sqrt{s_{\text{NN}}}$ dependence from RHIC
 1433 to LHC [156], as well as from 39 to 200 GeV at RHIC [157, 158]. This is confirmed by the
 1434 left panel which compares Pb+Pb [159] with Au+Au [160] data at 30–40% centrality, as
 1435 well as calculations from the CGC-Hydro model. However, a comparison of $v_n(p_T)$ between
 1436 p +Pb [161] and p +Au [147] central data suggests a small difference in v_2 , while the v_3 data
 1437 are nearly identical. In the FSM picture, this suggests that the contributions of subnucleonic
 1438 fluctuations to the initial eccentricities are very different between the two collision energies.
 1439 In the ISM picture, it may be the result of an energy dependence of initial momentum
 1440 anisotropy. It would be exciting to see whether the $\sqrt{s_{\text{NN}}}$ dependence for v_2 and v_3 in p +A
 1441 collisions also persists in small A+A systems such as O+O collisions between RHIC and
 1442 LHC. The CGC-Hydro model calculations of v_2 and v_3 in O+O collisions at RHIC and
 1443 the LHC energies are shown in Fig. 42 (middle), where a split in both v_2 and v_3 between
 1444 two energies is predicted. These rather non-trivial \sqrt{s} dependence across different collision
 1445 systems reflects the rich physics mechanisms behind origin of collectivity.

1446 We propose a one-week O+O program in 2021 right after BES-II. Assuming a total
 1447 interaction rate of ~ 10 – 15 kHz (based on recent isobar runs), the STAR DAQ rate of 2 kHz
 1448 and the RHIC uptime of 50% (12 hour/day), tentative numbers of events we expect to
 1449 record for different triggers are summarized in Table 8 for one week, default run plan, and
 1450 two weeks as a more optimal running scenario. Note that we do not have an estimation of
 1451 minimum-bias trigger efficiency at this point, and assumed it to be $\sim 100\%$.

1452 The event statistics listed in Table 8 should allow precision measurements of many types
 1453 of two-particle correlations, including the N_{ch} dependence of integral v_n , p_T dependence of v_n
 1454 in 0-5% for identified particles (π , K, p and ϕ) to test the NCQ-scaling. The non-flow effects
 1455 for these observables can be studied in detail thanks to the large acceptance of iTPC and
 1456 EPD. Based on a Glauber model estimation, the $\langle N_{\text{part}} \rangle$ value is 9.5 and 26 for minimum-bias

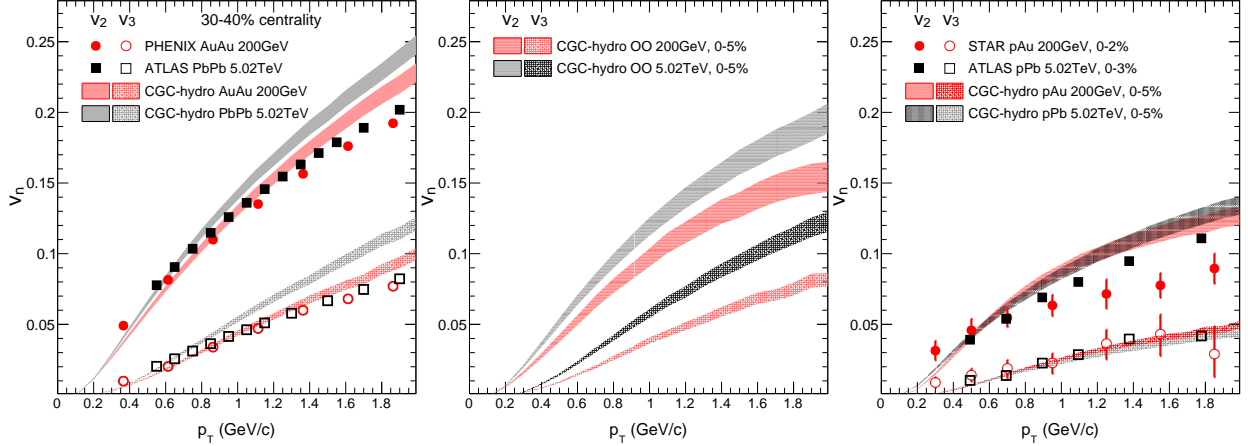


Figure 42: Comparison of measured v_2 and v_3 between Pb+Pb and Au+Au 30–40% centrality events (Left) and high-multiplicity p +Pb and p +Au data (Right) at RHIC and the LHC energies. The CGC-Hydro model calculations are also shown for Au+Au and Pb+Pb (Left), p +Au and p +Pb (Right), and O+O as a prediction (Middle) at both energies.

Table 8: Number of events (in millions) needed in an O+O run at $\sqrt{s_{NN}} = 200$ GeV for various triggers for one week (default) and two weeks (optimistic) running scenarios.

| Triggers | Minimum bias | 0–5% centrality |
|-----------------|--------------|-----------------|
| Events (1 week) | 400 M | 200 M |
| Events (2 week) | 800 M | 400 M |

1457 and 0-5% central O+O collisions, respectively.

1458 Figure 43 shows the projection of the statistical precision for the ϕ meson $v_2(p_T)$ in 0–5%
 1459 centrality O+O collisions. Under the assumption that its v_2 in O+O is similar to that of
 1460 a charged hadron in p +Au around $p_T \sim 2$ –3 GeV/ c , the estimation scales the ϕ $v_2(p_T)$ in
 1461 peripheral Au+Au collisions [162] to approximately match the charged hadron v_2 in p +Au
 1462 collisions in Fig. 42, accounting for differences in $\langle N_{part} \rangle$, event plane resolution, and event
 1463 statistics. A decent measurement of ϕ meson v_2 can be achieved with one week of running.

1464 In fact, the statistics requirement in Table 8 is mainly driven by multi-particle correla-
 1465 tions, for example four-particle cumulants for single harmonics $c_2\{4\} = \langle v_n^4 \rangle - 2 \langle v_2^2 \rangle^2$, four-
 1466 particle symmetric cumulants $SC(2, 3) = \langle v_2^2 v_3^2 \rangle - \langle v_2^2 \rangle \langle v_3^2 \rangle$ and three-particle asymmetric
 1467 cumulants $AC(2, 4) = \langle v_2^2 v_4 \cos 4(\Phi_2 - \Phi_4) \rangle$ (Φ_n is the event plane). These observables are
 1468 sensitive to event-by-event fluctuations of collectivity, and measurements of them at LHC in
 1469 pp , p +Pb and Pb+Pb collisions have led to high impact results which provide evidence for
 1470 geometry response in small systems [163–166].

1471 Figure 44 shows the projection of the statistical precision for the $c_2\{4\}$ measurement.
 1472 The projected precision should allow a measurement of $c_2\{4\}$ signal, assuming a $v_2\{4\}$ value

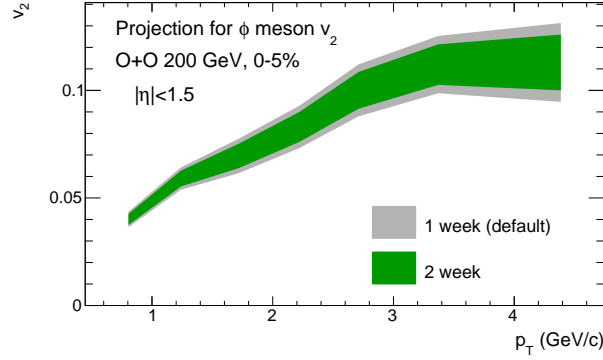


Figure 43: Projected statistical error on ϕ meson $v_2(p_T)$ in central O+O collisions within the TPC acceptance.

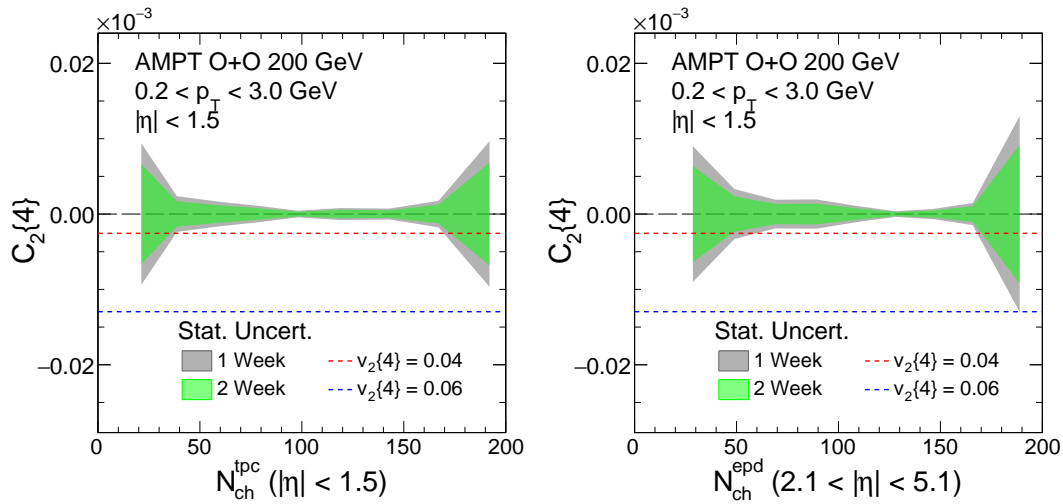


Figure 44: (Left) The projected statistical error bar on $c_2\{4\}$ in 0.2-3 GeV/c in the TPC acceptance as a function of number of charged particles in TPC acceptance and (Right) EPD acceptance.

1473 to be between 4–6%³.

1474 Figure 45 shows the projection of the statistical precision for the charged hadron R_{AA}
 1475 measurement for minimum bias O+O collisions (assume 400 Million). This calculation
 1476 includes the state-of-art knowledge of nPDF effects and jet quenching modeling of Refs.
 1477 [168, 169]. A significant suppression of $R_{AA} = 0.85 - 0.9$ is expected which should be mea-
 1478 surable with decent statistical uncertainty out to 15 GeV.

1479 **Answer to PAC questions from last year** When this proposal was presented last year,
 1480 we have received the following comments: "With regards to an O+O run, the case for this
 1481 could become persuasive if, between now and next year, theorists with expertise in hydro-
 1482 dynamics can provide some simulations that demonstrate what hydrodynamics predicts for
 1483 v2 and v3 behavior in O+O collisions, and how this compares to results from p+A, Cu+Cu,

³The p_T integrated $v_2\{4\}$ in $d+Au$ from PHENIX [167] at forward rapidity is about 4%

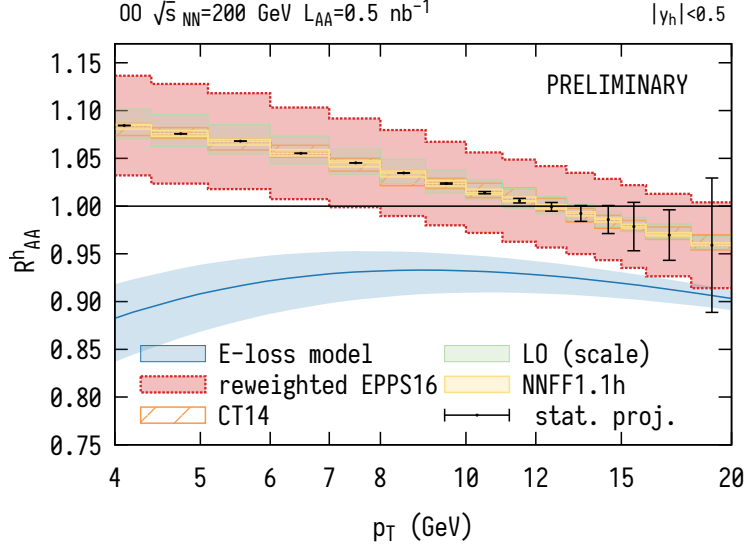


Figure 45: Prediction of minimum bias hadron nuclear modification factor for $\sqrt{s_{NN}} = 200$ GeV O+O collisions following Refs. [168, 169]. A particular parton energy loss model predictions (blue line) is overlaid with the baseline in the absence of parton rescattering. The blue band represents model uncertainty only due to experimental uncertainties in $\sqrt{s_{NN}} = 5.02$ TeV Pb+Pb collisions used to fit a free model parameter. The red band shows nPDF uncertainties reweighted with additional CMS pPb dijet data. Proton PDF (orange), leading order scale (green) and fragmentation function (yellow) uncertainties are fully correlated and cancel. Error bars illustrate statistical uncertainties for OO mock data at 100% efficiency.

1484 and Au+Au collisions. We also suggest that these calculations should be undertaken for
 1485 $\alpha + \alpha$, Be+Be, Al+Al and Ar+Ar collisions also, as well as for O+Au and other asymmetric
 1486 small+large nuclear collision options, so as to be able to make the case that O+O is the
 1487 optimal physics choice, most likely to yield new or substantially improved understanding of
 1488 questions relating to how small droplets of QGP equilibrate and what is the smallest droplet
 1489 of QGP that is possible to be formed in collisions at 200 GeV".

1490 We have prepared the following answers to these comments:

- 1491 • Why O+O? 1) O+O collisions cover similar N_{part} range as $p+\text{Au}/d+\text{Au}$ (see Fig-
 1492 ure 41) where the collectivity debate is ongoing, 2) O+O has similar N_{part} but differ-
 1493 ent nucleon/sub-nucleon fluctuations, 3) leverage similar measurement at LHC for new
 1494 insight and precision.
- 1495 • Are there theoretical calculations? Many model studies on O+O exist by now, which re-
 1496 flects the community interests: 1812.08096,1904.10415,1908.06212, 1910.09489, 2003.06747,
 1497 2005.14682. Figure 42 shows the new prediction on O+O taken from 2005.14682,
- 1498 • Why not other collision systems? Analyzing power for 2k-particle cumulants $v_n\{2k\}$
 1499 scales as $N_{\text{events}} \times N_{\text{part}}^{2k}$, system smaller than O+O, such as C+C require much longer
 1500 running time and also difficult to setup the high-multiplicity triggers due to steeply

1501
1502
1503
1504

1505
1506
1507
1508

falling N_{ch} distributions. Also these systems will not have compatible N_{part} coverage as p/d+Au systems. One may suggest to repeat the p/d+Au. But this will require long running time, since previous p+Au (d+Au) data was taken over 5 (1.5) weeks period in run15 (run16).

- **Why not larger small systems?** Larger asymmetric system we already have Cu+Au and $^3\text{He}+\text{Au}$. Results from both are consistent with final-state interpretation from both experiments and theory. Any system in between such as O+Au with $\langle N_{part} \rangle = 60$ is expected to be dominated by final state effects.

1509

2.2.2 Au+Au Collisions at $\sqrt{s_{NN}} = 17.1$ GeV

1510
1511
1512
1513
1514
1515
1516
1517
1518

Net-proton kurtosis and light nuclei yield ratio from RHIC BES-I One of the main goals of the RHIC Beam Energy Scan (BES) program is the search for the QCD critical point (CP), which is a distinct singular feature of the QCD phase diagram. The experimental confirmation of the existence of the CP would become a landmark in the exploration of the phase structure of hot dense nuclear matter. The characteristic feature of the CP is the divergence of the correlation length and density fluctuations. These critical phenomena can be probed by measuring event-by-event fluctuations of conserved quantities, such as baryon, electric charge, and strangeness numbers. The effect of the CP could show as a non-monotonic energy dependence of higher order moments of these conserved quantities in close proximity of the critical point during a beam energy scan [122].

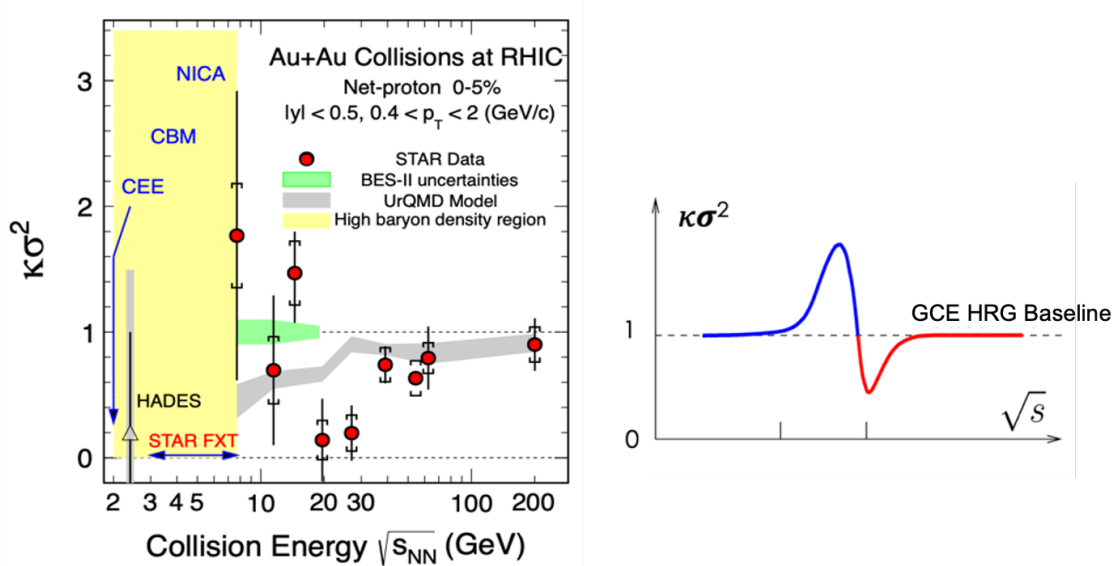


Figure 46: (Left) The fourth order net-proton fluctuations $\kappa\sigma^2$ in most central (0-5%) Au+Au collisions as a function of collision energy from STAR BES-I measurements [123]. (Right) The characteristic signature predicted by the theoretical model for energy dependence of the fourth order fluctuations when the system passes through the critical region [122].

1519

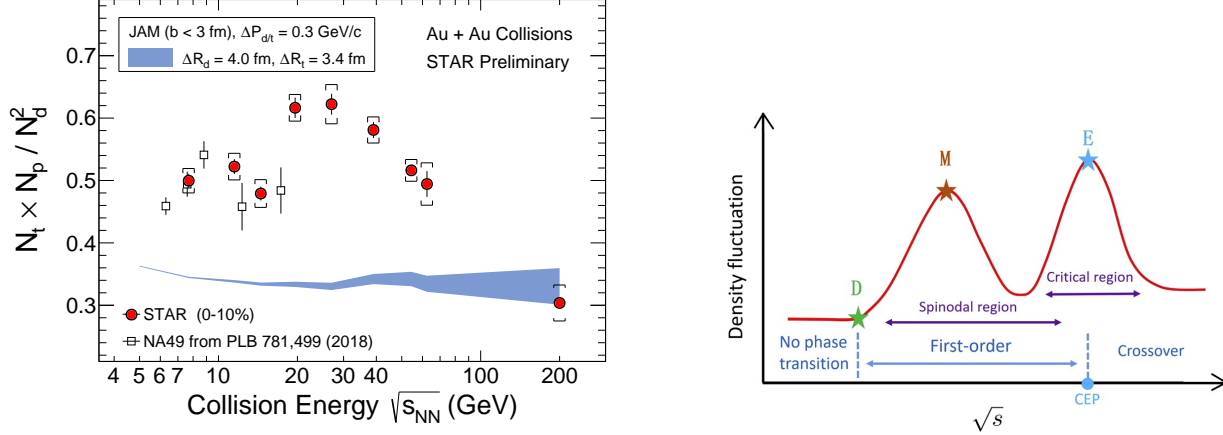


Figure 47: (Left) Collision energy dependence of the light nuclei yield ratio ($N_t \times N_p / N_d^2$) in central Au+Au collisions. The open square data based on NA49 results in central Pb+Pb collisions at $\sqrt{s_{NN}}=6.3$ (0-7%), 7.6 (0-7%), 8.8 (0-7%), 12.3 (0-7%), and 17.3 (0-12%) energies. (Right) Illustration of the density fluctuation as a function of collision energy in the critical region and the spinodal region [170].

1520 In the years 2010-2017 RHIC finished the first phase of the Beam Energy Scan (BES) and
 1521 took data in Au+Au collisions at $\sqrt{s_{NN}} = 7.7, 11.5, 14.5, 19.6, 27, 39, 54.4, 62.4,$ and 200 GeV.
 1522 With these experimental data STAR measured the higher order fluctuations of net-proton,
 1523 net-charge, and net-kaon multiplicity distributions [123, 171–175]. One striking observation
 1524 is the behavior of the fourth-order cumulants, or kurtosis, of the net-proton fluctuation $\kappa\sigma^2$
 1525 in most central (0-5%) Au+Au collisions as a function of beam energy. As shown on the
 1526 left of Fig. 46, the fourth order net-proton fluctuation is close to unity above 39 GeV but
 1527 deviates significantly below unity at 19.6 and 27 GeV, then approaches or turns above unity
 1528 at lower energies. This behavior may suggest that the created system skims close by the CP,
 1529 and receive positive and/or negative contributions from critical fluctuations. The right of
 1530 Fig. 46 shows the characteristic signature of the critical point for energy dependence of the
 1531 fourth order fluctuations when the system passes through the critical region [122]. Along
 1532 this argument, a peak structure above unity for net-proton kurtosis measurement at lower
 1533 energies could be the signature of the CP. However, it is worth to point out that a first
 1534 order phase transition could also cause a large increase of net-proton kurtosis [176]. When
 1535 entering into the spinodal region (mixed phase), the double peak structure of σ field may
 1536 cause the increase of the fourth order cumulants (C_4).

In addition, STAR has measured light nuclei (deuteron and triton) production in Au+Au collisions at RHIC BES energies. The ratio of these yields are predicted to be sensitive to the neutron relative density fluctuations at kinetic freeze-out, which is expected to increase near the critical point and/or a first order phase transition [170]. The neutron density fluctuation

is defined as $\Delta n = \langle(\delta n)^2\rangle/\langle n\rangle^2$, which can be approximated from:

$$\Delta n = \frac{1}{g} \frac{N_t \times N_p}{N_d^2} - 1,$$

1537 where N_p , N_d and N_t are the proton, deuteron and triton yields, respectively and g is a
 1538 constant factor of 0.29 [170]. In the left panel of Fig. 47, we show the yield ratio $N_t \times$
 1539 N_p/N_d^2 in central Au+Au collisions as a function of collision energy. These light nuclei yield
 1540 ratios are obtained by using the feed-down corrected proton yields, deuteron yield [177], and
 1541 preliminary triton results [178]. The ratio as a function of energy exhibits a non-monotonic
 1542 energy dependence with a peak around 19.6 GeV. The blue band showing a flat energy
 1543 dependence represents the calculation of the light nuclei yield ratio in Au+Au collisions
 1544 ($b < 3$ fm) from a transport JAM model [179]. Furthermore, the yield ratio shown in Fig. 47
 1545 seems to show a drop between 14.5 and 19.6 GeV. The experimental observation of non-
 1546 monotonic energy dependence in yield ratio may suggest a double peak structure of the
 1547 neutron density fluctuation, indicating that the system goes through the critical region and
 1548 the first order spinodal region, as displayed in Fig. 47 right.

1549 In RHIC 2021 run, we propose to take one more energy point in Au+Au collisions at
 1550 17.1 GeV based on the following two observations presented in Figs. 46 and 47, aiming at
 1551 the QCD critical point search with net-proton kurtosis and light nuclei yield ratio:

- 1552 1. Net-p kurtosis and light nuclei yield ratio, which are both sensitive to the critical
 1553 fluctuation, show dip and peak structures around 19.6 GeV. These may suggest that
 1554 the system passed through the critical region around 19.6 GeV.
- 1555 2. We observe sudden changes between 19.6 and 14.5 GeV in the energy dependence of
 1556 net-p kurtosis and light nuclei ratio measurements in the BES-I data measured by the
 1557 STAR experiment. The neutron density fluctuations at low energies below 14.5 GeV
 1558 are consistent with the results from NA49 experiment [170].

1559 These two observations indicate that the critical point may be close to 19.6 GeV. Since
 1560 there are sudden changes in both observables between 19.6 (chemical freeze-out $\mu_B = 205$ MeV)
 1561 and 14.5 GeV ($\mu_B = 266$ MeV), it is important to conduct a finer beam energy scan between
 1562 these two energies. Therefore, we request a run with Au+Au collisions at $\sqrt{s_{NN}}=17.1$ GeV
 1563 ($\mu_B = 235$ MeV), which is just between 19.6 and 14.5 GeV with equal μ_B gap, about 30 MeV,
 1564 on each side.

1565 **Answer to PAC questions from last year** When this proposal was presented last year,
 1566 we have received the following comments: "To make the case for a $\sqrt{s_{NN}} = 17.1$ GeV run, the
 1567 key input will be results from measurements of fluctuation observables from Run-19 data
 1568 taken at $\sqrt{s_{NN}} = 19.6$ and 14.6 GeV. If these measurements, with the smaller error bars
 1569 that are anticipated, show evidence for a possible two-peaked structure in the plot of net
 1570 proton kurtosis or other fluctuation observables as a function of $\sqrt{s_{NN}}$, this could at that
 1571 time become a strong argument for a run at $\sqrt{s_{NN}} = 17.1$ GeV."

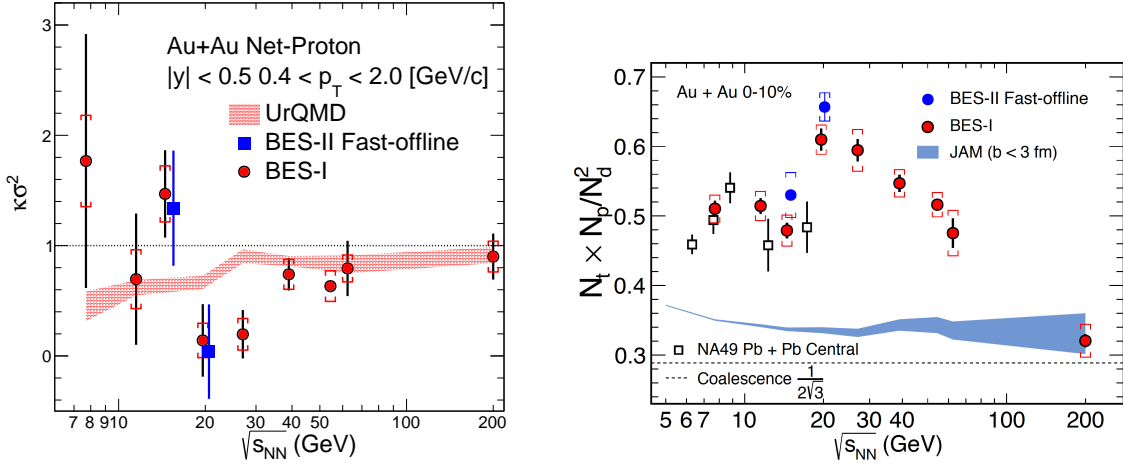


Figure 48: The red solid markers are the results from RHIC BES-I and the blue square represents the results of Run19 fast-offline data. (Left) The fourth order net-proton fluctuations $\kappa\sigma^2$ in most central (0-5%) Au+Au collisions as a function of collision energy. (Right) Collision energy dependence of the light nuclei yield ratio ($N_t \times N_p / N_d^2$) in central Au+Au collisions. The open square data based on NA49 results in central Pb+Pb collisions at $\sqrt{s_{NN}}=6.3$ (0-7%), 7.6 (0-7%), 8.8 (0-7%), 12.3 (0-7%), and 17.3 (0-12%) energies.

1572 To reply the comments from PAC last year, we have analyzed the net-proton fluctuation
 1573 and light nuclei production from the Run-19 fast-offline data of Au+Au collisions at $\sqrt{s_{NN}}$
 1574 = 14.6 and 19.6 GeV. The statistics of the Run-19 fast-offline data of 0-5% Au+Au collisions
 1575 shown in Fig. 48 are about 580k and 750k events for 14.6 and 19.6 GeV, respectively, which
 1576 are roughly about 5% of the full min.-bias statistics of these two data sets. It is found
 1577 that both net-proton fluctuation and light nuclei yield ratios in 0-5% most central Au+Au
 1578 collisions from BES-I are consistent with the results from Run 19 fast-offline data of 14.6 and
 1579 19.6 GeV. For clarity in Fig. 48, the X-axis positions of Run 19 fast-offline data are slightly
 1580 shifted.

Table 9: Event statistics (in millions) needed in a Au+Au run at $\sqrt{s_{NN}} = 17.1$ GeV for fourth order net-proton fluctuations ($\kappa\sigma^2$) and light nuclei yield ratio ($N_t \times N_p / N_d^2$) measurements.

| Triggers | Minimum Bias | net-p $\kappa\sigma^2$ (0-5%) | $N_t \times N_p / N_d^2$ (0-10%) |
|------------------|--------------|-------------------------------|----------------------------------|
| Number of events | 250 M | 6% error level | 3.6% error level |

1581 **Required number of minimum bias events and statistical uncertainty level** Ac-
 1582 cording to the previous estimation of the required event statistics for BES-II energies pre-
 1583 sented in Table 6, we need about 250 million minimum-bias events for the net-proton kurtosis
 1584 measurement at 17.1 GeV, which requires 2.5 weeks data taking. It gives us about 12.5 million

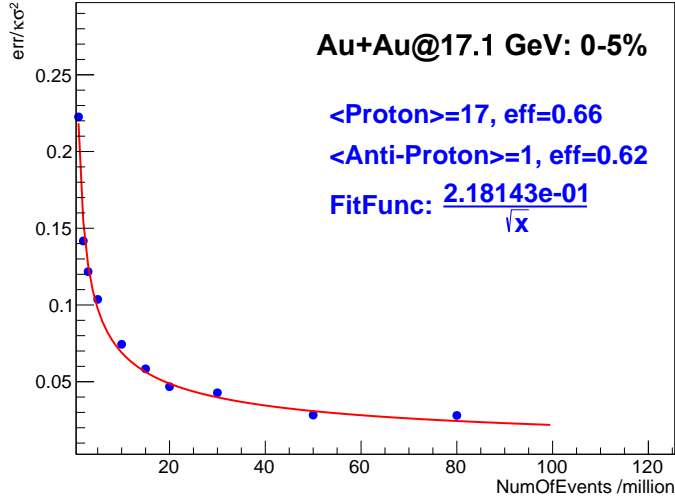


Figure 49: Monte Carlo simulation for the relative statistical errors of net-proton $\kappa\sigma^2$ in 0-5% most central Au+Au collisions at 17.1 GeV. A Skellam distribution for net-proton is assumed; the mean value for protons and anti-protons are 17 and 1, respectively. The average efficiencies for proton and anti-proton are 0.66 and 0.62, respectively.

1585 events (250/20) in 0-5% most central collisions. This will ensure that the relative statistical
 1586 error of net-proton $\kappa\sigma^2$ in 0-5% most central Au+Au collisions will reach the 6% level (shown
 1587 in Fig. 49). This event statistics will also ensure that the relative statistical error of light nu-
 1588 clei ratio will reach about 3.6% level in 0-10% central Au+Au collisions. In addition to the
 1589 improved statistics, utilizing the iTPC will enable the measurement of lower p_T light nuclei
 1590 and will reduce the systematic uncertainties associated with the low p_T yield extrapolation.

1591 If nature puts the critical point in the QCD phase diagram between 14.5 and 19.6 GeV
 1592 (with μ_B around 200–270 MeV), RHIC has the best chance to discover it !

1593 **2.2.3 Au+Au Collisions in FXT Mode at $\sqrt{s_{NN}} = 3.0$ GeV - II: 2 Billion Goal**

1594 In the previous section, we have discussed the great physics interests for low energy heavy-ion
 1595 collisions utilizing the FXT setup at the STAR experiment. We have made our arguments
 1596 of taking a minimum of 300 million Au+Au FXT events at $\sqrt{s_{NN}} = 3.0$ GeV. With further
 1597 available beam time, we would like to request to collect up to 2 billion events with the same
 1598 setup for the following physics measurements.

1599 Proton correlations higher than 4-th order are useful to study the possible contributions
 1600 of protons from hadronic phase or QGP phase [176]. The requested 2 billion events statistics
 1601 will enable us to perform the analyses of proton moments and cumulants up to 5-th and
 1602 6-th orders. The measurements of 5-th and 6-th order moments and cumulants has been
 1603 proposed to be sensitive to the search for the phase boundary in the high baryon density
 1604 region [176].

1605 A much larger data sample (2 billion events) will enable us to further investigate the
 1606 centrality dependence of ϕ meson production. The 2018 data analysis in 40-60% centrality
 1607 bin yields $\sim 13\%$ relative uncertainty in the ϕ production yield. A two-billion dataset will
 1608 reduce the statistical uncertainty to be $< 5\%$. This will allow us to study system size
 1609 dependence of ϕ meson production to quantitatively understand the canonical suppression
 1610 for strangeness. The large statistics will also offer the opportunity to further measure ϕ
 1611 meson directed and elliptic flow behavior in these collisions.

1612 While there have been tens of hypernuclei measured so far, there are only very few double-
 1613 Λ hypernuclei candidates reported from emulsion experiments [180–184]. Their properties
 1614 are directly related to the $\Lambda\Lambda$ interaction. Low energy heavy-ion collisions can be a unique
 1615 environment to copiously produce these light double- Λ hypernuclei. For instance, according
 1616 to the thermal model prediction, the ${}^5_{\Lambda\Lambda}\text{H}$ production yield increases by more than 3 orders
 1617 of magnitude at the low energies compared to that at top RHIC and LHC energies [134].

1618 We performed a Monte Carlo simulation study for the decay chain ${}^5_{\Lambda\Lambda}\text{H} \rightarrow {}^5_{\Lambda}\text{He} + \pi^-$, and
 1619 ${}^5_{\Lambda}\text{He} \rightarrow {}^4\text{He} + p + \pi^-$ within the STAR detector acceptance. Assuming the production yield
 1620 based on the thermal model prediction [134], with 2 billion Au+Au FXT data at $\sqrt{s_{\text{NN}}} =$
 1621 3.0 GeV and with the iTPC and eTOF detector, we will have a chance to observe ~ 27 signal
 1622 counts. This will be an unprecedented sample that allows us to study double- Λ hypernu-
 1623 clei properties and their production mechanism, therefore to offer new insights towards the
 1624 understanding of the $\Lambda\Lambda$ interaction.

1625 2.3 Future Possibilities

1626 2.3.1 Exploring the Nuclear Equation-of-State (EoS) with Heavy Ion Collisions

1627 In the interior of the fireball created in HI collisions, nuclear densities of up to $10 \rho_0$ can be
 1628 achieved depending on the energy of the colliding nuclei [185]. Similar densities are predicted
 1629 to be present in the core of neutron stars (NS). However, the composition and maximal mass
 1630 of NS is highly dependent on the nuclear equation-of-state (EoS) which is close related to
 1631 the compressibility of nuclear matter. Therefor HI collisions are considered as a ideal tool
 1632 to study the EoS at high nuclear densities and establish a bridge between astrophysics and
 1633 nuclear physics.

1634 Already in the early 80s several observables probing the EoS (i.e. which are sensitive
 1635 on the density and pressure of the system) like particle production [186, 187], transverse
 1636 momentum analysis [188], directed and elliptic flow [189, 190] were proposed. At low energies
 1637 and densities up to about $2.5 \rho_0$ elliptic flow analysis favour a soft EoS [191] while at AGS
 1638 energies (between 2.5 and $4.5 \rho_0$) no clear picture could be established yet. Transverse flow
 1639 measurements hint to a soft ($K \leq 210$) EoS while elliptic flow measurements indicate a stiff
 1640 ($K \approx 300$) EoS [190]. Another method to probe the equation-of-state of nuclear matter was
 1641 proposed already 1985 by Aichelin and Ko [192] by measuring the sub-threshold production
 1642 of strange particles which are created in the dense medium early in the reaction. Especially
 1643 the multi-strange particle production at sub-threshold energies should be highly sensitive to
 1644 the density of the medium since multiple-collision processes are required. So the information

1645 on the EoS is stored in the yield and slope of the excitation function of the sub-threshold
 1646 produced particles which can be compared to various theoretical models. It is also clear
 1647 that the abundance of produced particles is highest at heavy systems like $Au + Au$ since
 1648 the reaction volume is big. Therefor comparison measurements with light system like $C + C$
 1649 can be used as a reference where the influence of the EoS is small. In addition, systematic
 1650 errors both in experiment and theory cancel out to a large extent by taking the yield ratio
 1651 of produced (multi-) strange particles at both systems.

1652 Figure 50 shows the normalized yield ratio $((M_{K^+}/A)_{Au+Au}/(M_{K^+}/A)_{C+C})$ of sub-threshold
 1653 produced K^+ as a function of 4 different beam energies [193]. A comparison to different mod-
 1654 els [194, 195] predict a soft EoS at low bombarding energies around $E_{beam} \approx 1.5 GeV$. On
 1655 the other hand the finding of neutron stars with masses above 2 solar masses can only be ex-
 1656 plained by a stiff EoS [196] which should be measurable in flow observable at higher incident
 energies.

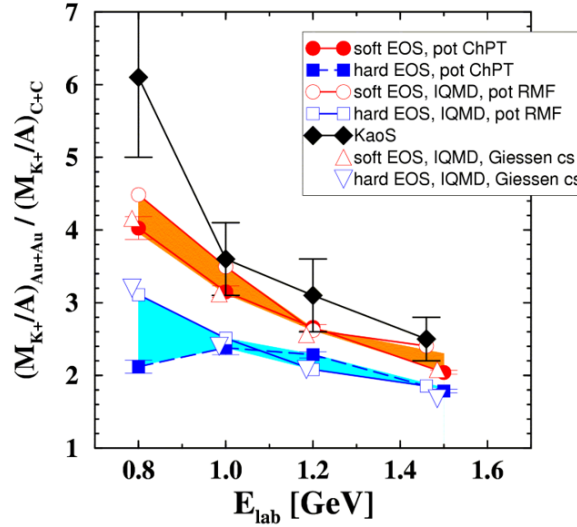


Figure 50: Excitation function of the ratio of K^+ multiplicity obtained in $Au + Au$ over $C + C$ reactions [193] together with model calculations [194, 195] indicating a soft EoS at this bombarding energies.

1657 An independent observable at these higher energies are the production rates of multi-
 1658 strange baryons, of which several have their NN production threshold in the reach of BES II:
 1659 Ξ^- (production threshold $\sqrt{s_{NN}}=3.247 GeV$), Ω^- (production threshold $\sqrt{s_{NN}}=4.092 GeV$),
 1660 Ξ^+ (over $\Xi^+\Xi^-$ -channel, production threshold $\sqrt{s_{NN}}=4.520 GeV$) and Ω^+ (over $\Omega^+\Omega^-$ -channel,
 1661 production threshold $\sqrt{s_{NN}}=5.222 GeV$). A beam energy scan in small steps (with 3 to 4
 1662 points with distance of about 200 to 300 MeV) below the production threshold energy for
 1663 the various particles species for $Au + Au$ collisions could give access to the properties of the
 1664 EoS as function of colliding energy and density. In fact a big fraction of the measurements
 1665 were already finished during the BESII campaign and only a few additional fixed target
 1666

1667 points have to be performed which depends on the number of investigated particles used as
 1668 probes. The measurement of the pressure as function of energy in small steps could even
 1669 allow for the discovery of a 1st order phase transition in the covered energy range [197]. The
 1670 measurements at the heavy system could be accompanied by a reference measurement of a
 1671 light system (for example $C + C$) for at least one particle species and extrapolated to the
 1672 others. However, since the production yield scales with the number of participants the time
 1673 needed for the light system is significantly longer (few weeks) as for the heavy system which
 1674 needs typically btw. 12 h and a day.

1675 Nevertheless the proposed measurements have a high discovery potential and could be
 1676 an opportunity for a future fixed target HI program at STAR.

1677 2.4 Exploring the Microstructure of the QGP (Run-23 and Run-25 1678 Au+Au)

1679 The completion of the RHIC's scientific mission involves the two central goals [198] of (i)
 1680 mapping out the phase diagram of the QCD, and (ii) probing the inner workings of the QGP
 1681 by resolving its properties at short length scales. The complementarity of the RHIC and LHC
 1682 facilities to study the latter is scientifically as essential as having more than one experiment
 1683 independently study the microstructure of the QGP. With several years of operating the
 1684 recently installed iTPC upgrade and the soon-to-be installation and operation of STAR's
 1685 forward detectors, the STAR collaboration will be in an excellent position to take advantage
 1686 of its vastly improved detection capabilities. Combine this with the prospect of a substantial
 1687 increase in beam luminosities and RHIC will be uniquely positioned to fully engage in a
 1688 detailed exploration of the QGP's microstructure. Through careful discussions in its physics
 1689 working groups, the STAR collaboration has identified a number of topics that together
 1690 make a compelling case to take data during Runs 23-25 alongside sPHENIX, and successfully
 1691 complete RHIC's scientific mission. In this section, we present a selection of those topics
 1692 that will take full advantage of both STAR and RHIC's unique capabilities and address the
 1693 following important questions about the inner workings of the QGP.

- 1694 • What is the precise temperature dependence of the shear η/s , and bulk ζ/s viscosity?
- 1695 • What is the nature of the 3-dimensional initial state at RHIC energies? How does
 1696 a twist of the event shape break longitudinal boost invariance and decorrelate the
 1697 direction of an event plane?
- 1698 • How is global vorticity transferred to the spin angular momentum of particles on such
 1699 short time scales? And, how can the global polarization of hyperons be reconciled with
 1700 the spin alignment of vector mesons?
- 1701 • What is the precise nature of the transition near $\mu_B = 0$, and where does the sign-
 1702 change of the susceptibility ratio χ_6^B/χ_2^B take place?
- 1703 • What is the electrical conductivity, and what are the chiral properties of the medium?

- 1704 • What can we learn about confinement and thermalization in a QGP from charmonium
1705 measurements?
- 1706 • What are the underlying mechanisms of jet quenching at RHIC energies? What do jet
1707 probes tell us about the microscopic structure of the QGP as a function of resolution
1708 scale?

1709 The event statistics projections that are used in this section will rely on the CAD's re-
1710 cently update 2023E and 2025E Au+Au luminosities [199] and are listed in Table 10. For
1711 each year we presume 24 weeks of RHIC operations, and based on past run operations an
1712 overall average of 85% \times 60% (STAR \times RHIC) uptime, respectively. The minimum-bias rates
1713 assume a conservative 1.5 kHz DAQ rates which will allow sufficient bandwidth for spe-
1714 cialized triggers which are listed as integral luminosities. In order to achieve the projected
1715 luminosities, the collaboration will look into optimizing the interaction rates at STAR by al-
1716 locating low and high luminosities periods within fills. Such periods, in which low interaction
1717 rates are sampled in the early part of a fill and high interaction rates typically in the later
1718 part, will allow us to collect clean, low pile-up, minimum bias events, while at the same time
1719 not burn beam luminosities that could affect interaction rates for sPHENIX. Clean mini-
1720 mium bias events will improve tracking efficiencies which in turn is expected to benefit many
1721 of the proposed correlation analyses. Optimization of the available bandwidth for high- p_T
1722 triggers would allow us to push for lower p_T thresholds, thus further reducing biases. The
1723 impact of such an optimization will lead to some reduction in the projected rates, while still
1724 enabling a significant improvement in the precision and kinematic reach of current STAR
1725 measurements, and making important measurements that are yet more differential possible.

| year | minimum bias [$\times 10^9$ events] | high- p_T int. luminosity [nb $^{-1}$] | | |
|------|---|---|----------|----------|
| | | all vz | vz <70cm | vz <30cm |
| 2014 | 2 | 26.5 | 19.1 | 15.7 |
| 2016 | | | | |
| 2023 | 10 | 43 | 38 | 32 |
| 2025 | 10 | 58 | 52 | 43 |

Table 10: STAR minimum bias event statistics and high- p_T luminosity projections for the 2023 and 2025 Au+Au runs. For comparison the 2014/2016 event statistics and luminosities are listed as well.

1726 At RHIC it is possible to build detectors that can span from mid-rapidity to beam rapidity
1727 – with the two recent upgrades STAR is able to achieve this unique capability. STAR's BES-
1728 II upgrade sub-systems comprised of the inner Time Projection Chamber (iTPC, $1.0 < |\eta| <$
1729 1.5), endcap Time Of Flight (eTOF, $1 < \eta < 1.5$) and Event Plane Detector (EPDs, $2.1 <$
1730 $|\eta| < 5.1$), that are all commissioned and fully operational since the beginning of 2019 [16–18].
1731 As will be discussed in Sect. 4, the STAR collaboration is constructing a forward rapidity (2.5
1732 $< \eta < 4$) upgrade that will include charged particle tracking and electromagnetic/hadronic
1733 calorimetry [200]. For charge particle tracking the aim is to construct a combination of

1734 silicon detectors and small strip thin gap chamber detectors. The combination of these two
 1735 tracking detectors will be referred to as the forward tracking system (FTS). The FTS will
 1736 be capable of discriminating the hadron charge sign. It should be able to measure transverse
 1737 momentum of charged particles in the range of $0.2 < p_T < 2$ GeV/ c with 20–30% momentum
 1738 resolution. In what follows, we will refer to the combination of the existing TPC ($|\eta| < 1$)
 1739 and the iTPC upgrade as iTPC ($|\eta| < 1.5$) for simplicity.

1740 The impetus for running STAR during the year of 2023-2025 in terms of bulk correlation
 1741 measurements in Au+Au 200 GeV collisions comes from the gain in : i) extended accep-
 1742 tance and ii) enhanced statistics. In the first subsections, we briefly describe how these two
 1743 opportunities can be exploited to perform correlations measurements that are unique to the
 1744 physics goals of the RHIC heavy ion program.

1745 Next, thanks to a reduced material budget between the beam and the iTPC, STAR will be
 1746 uniquely positioned to perform dielectron measurements which we propose to probe degrees
 1747 of freedom of the medium and its transport properties. For that we will use high precision
 1748 dilepton excess yield, i.e. l^+l^- invariant mass distribution after subtraction of dilepton
 1749 sources produced after freeze-out, and contributions from the initial collisions such as Drell-
 1750 Yan and correlated charm-anticharm pairs. Furthermore, we propose to study the virtuality,
 1751 Wigner function and final-state magnetic field in QGP. For the latter the photon-photon
 1752 collisions in ultra-peripheral, peripheral, and midcentral reactions and p+A (all centralities)
 1753 in both channels e^+e^- , $\mu^+\mu^-$ will be measured with high accuracy.

1754 In the last subsections, we address our proposed charmonium measurements and motivate
 1755 the importance of STAR's proposed program of precise jet measurements to explore the
 1756 micro-structure of the QGP.

1757 **2.4.1 Correlation Measurements Utilizing Extended Acceptance**

1758 Figure 51 demonstrates how STAR with the BES-II and forward upgrades will extend the
 1759 two-particle phase-space (in terms of η_1 and η_2 with respect to beam rapidity) many times
 1760 enabling us to perform correlation measurements over a wide window of relative pseudorapid-
 1761 ity. Since many of the important correlation measures are based on two-particle correlations,
 1762 this enhanced phase-space will provide STAR with many advantages: 1) increase the number
 1763 of pairs to bring better precision, 2) reduction in different sources of the non-flow background
 1764 by increasing pseudorapidity separation. Many multi-particle correlations will also get bene-
 1765 fited due to increase in triplets, quadruplets and so on due to overall increase in acceptance.
 1766 With this unique extended pseudorapidity reach offered by the BES-II and forward upgrade
 1767 of the STAR detector, our goal is to perform correlation measurements aimed towards a
 1768 deeper understanding of the largely unexplored three-dimensional structure of the initial
 1769 state and temperature dependent transport properties of the subsequent fluid-like medium
 1770 produced in heavy ion and small system collisions at RHIC.

1771 Two key sets of measurements are of interests: 1) pseudorapidity dependence of azimuthal
 1772 correlations, 2) pseudorapidity dependence of global hyperon polarization.

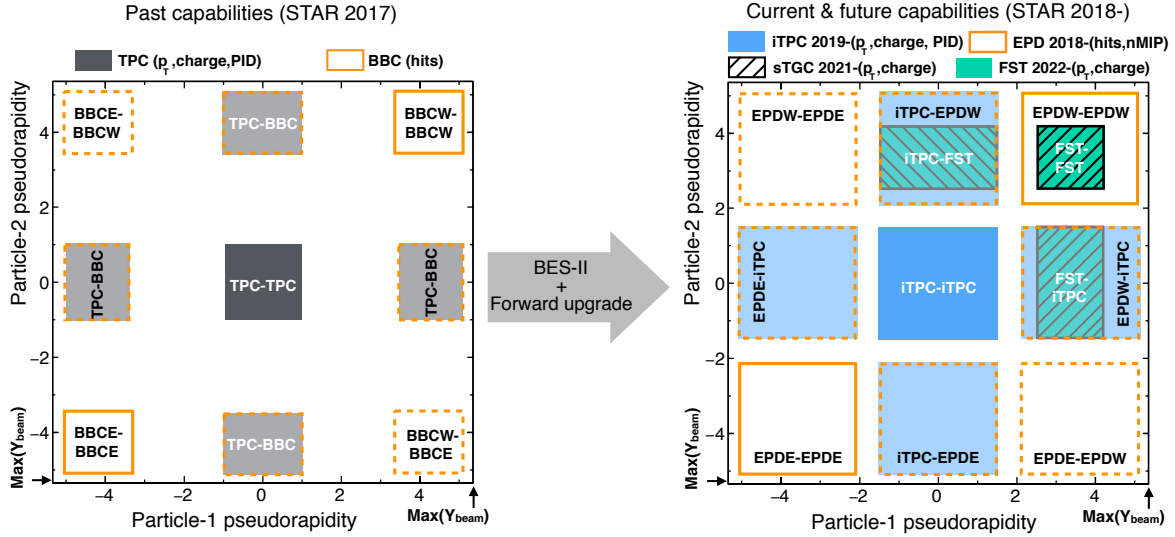


Figure 51: A visual representation of two-particle phase space in pseudorapidity covered by STAR detectors with respect to the region allowed by maximum beam rapidity ($Y_{beam}=5.36$ at 200 GeV Au+Au collisions) of RHIC. Left and right panels show the capabilities before and after BES-II and forward upgrade of the STAR detector, respectively. Note that in addition to a larger pair acceptance, the EPD granularity is over an order of magnitude larger than that of the BBC, and individual EPD tiles are shown to be separable into 1, 2, 3 MIP responses.

1773 **Pseudorapidity-dependent azimuthal correlation to tightly constrain tempera-**
 1774 **ture dependence of viscosity**

1775 The idea of tightly constraining the temperature viscosity of the QGP was envisioned in
 1776 the 2015 Long Range Plan for Nuclear Science [198]. The QCD matter formed at RHIC
 1777 shows nearly perfect fluidity characterized by the smallest viscosity to entropy ratio η/s
 1778 known in nature. The temperature dependence of η/s and other transport parameters has
 1779 not been fully constrained. One major aim is to perform precision measurements to contain
 1780 the temperature dependence of shear η/s (T) and bulk ζ/s (T) viscosity. Hydrodynamic
 1781 simulations have demonstrated that since the temperature of the produced fireball in HICs
 1782 vary with the rapidity, the measurement of the rapidity dependence of flow harmonics has
 1783 the potential to constrain η/s (T) and ζ/s (T) [201]. For this, RHIC measurements have
 1784 advantage over LHC since smaller beam rapidity at RHIC provides stronger variations of the
 1785 temperature with rapidity. The beam energy scan at RHIC provides an additional handle
 1786 on temperature to map η/s (T), and ζ/s (T) over a wide range of temperature. Indeed, the
 1787 hydrodynamic simulation of Ref [201] indicates that η/s (T) at lower temperatures, near
 1788 its possible minimum ($T = T_c$), can be better constrained by RHIC measurements. Results
 1789 from such simulations are shown in Fig. 52. In this simulation, a number of QCD-motivated
 1790 parameterizations of the temperature dependence of the shear viscosity was assumed, as
 1791 shown in Fig. 52 (left). Existing data from the PHOBOS collaboration suffer from large un-

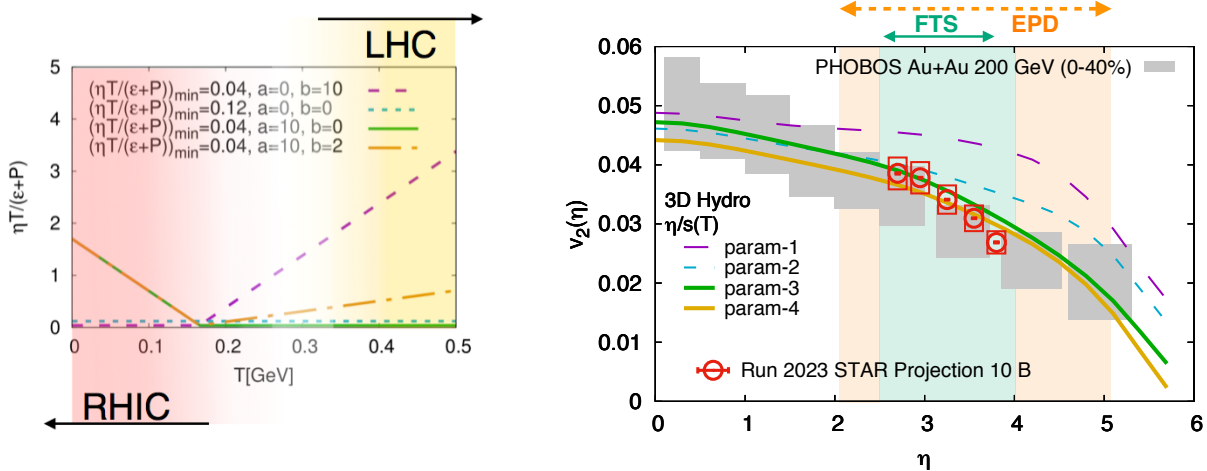


Figure 52: (Left) Different parameterizations of temperature dependence of shear viscosity to entropy η/s (T) (at zero chemical potential) used in the hydrodynamical simulation of Ref [201]. Interestingly, it has been demonstrated in Ref [202] that the region of lowest η/s is the one that can be probed at RHIC. (Right) Effects on the elliptic flow co-efficient v_2 due to the different parameterizations of the viscosity parameter indicating better constraints on η/s (T) can only be performed by measurements at forward rapidities at RHIC. The interpretation of the existing PHOBOS data is limited by the large uncertainties. The projection for STAR measurements are shown on the same plot.

1792 certainties, therefore only limited constrain on the temperature dependence of the transport
 1793 parameters can be achieved. The BES-II and the forward upgrade of STAR will provide pre-
 1794 cise estimations of different azimuthal correlation observables: $v_n(\eta)$ and other higher-order
 1795 ($n > 2$) flow coefficients $v_n(\eta)$, its fluctuations $\sigma(v_n)/v_n$ that have never been measured at
 1796 forward rapidity and are essential in terms of constraining η/s (T) near its possible minimum.
 1797 While transverse momentum integrated quantities can already constrain the shear viscosity,
 1798 additional information of transverse momentum is essential to constrain the bulk viscosity
 1799 ζ/s . With the forward tracking systems it will be possible to measure the p_T dependence of
 1800 v_n – in particular the information of $\langle p_T \rangle$ is essential to constrain the bulk viscosity $\zeta/s(T)$.
 1801 This can be done with a possible $A + A$ collisions with the forward upgrade and running of
 1802 STAR during the year 2023.

1803 Pseudorapidity-dependent azimuthal correlation to constrain the longitudinal 1804 structure of the initial state

1805 Initial-state longitudinal fluctuations and fluid dynamical response of the medium formed
 1806 in heavy ion collisions can lead to de-correlations of the direction of the reaction planes
 1807 Ψ_n (which determines the orientation of the harmonic anisotropies) with pseudorapidity (see
 1808 Fig. 53). Such effects are often referred to as torque or twist of the event shape [205–207] that
 1809 eventually leads to a breaking of longitudinal/boost/rapidity invariance. The magnitude of
 1810 the de-correlation is determined by the details of the dynamics of initial state, the distribution

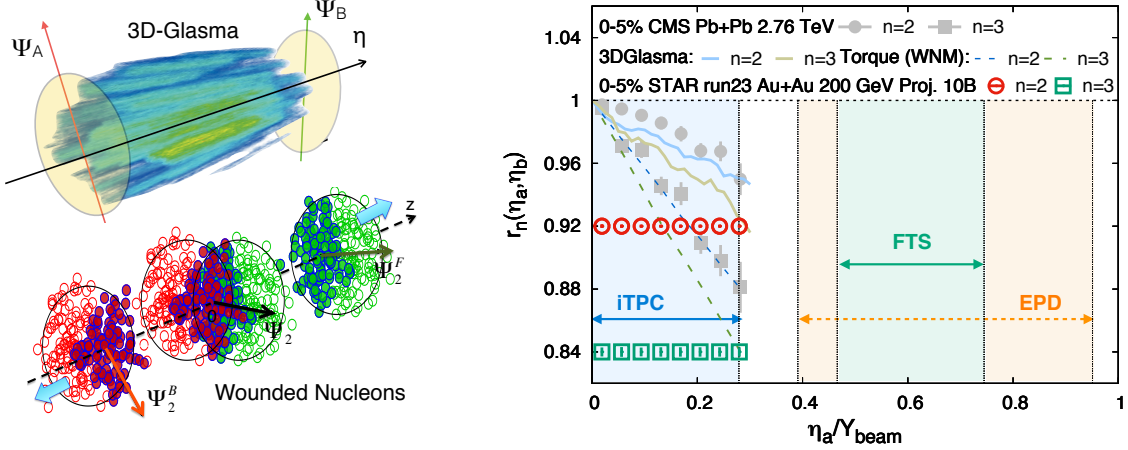


Figure 53: (Left) Cartoon to demonstrate the de-correlation of event planes in the longitudinal direction of collision from gluon saturation based 3D-Glasma model [203] and wounded nucleon model (WNM) [204, 205]. (Right) The longitudinal de-correlation of elliptic anisotropy plane as a function of the pseudorapidity in units of beam rapidity. CMS results are compared predictions from two models in the left with STAR projection for Run 2023 (using preliminary Run 19 results) for anticipated 10 B min-bias events. The colored regions show that the current and future capabilities at STAR (with iTPC+EPD+FTS) can extend such measurements with good precision by covering a large fraction of the beam rapidity at 200 GeV – this demonstrates the unique strength to STAR to study the physics of 3D initial state.

1811 of nucleons and partons inside the colliding nuclei. Several promising observables have been
 1812 proposed to study this effect, Fig. 53 shows one which can be expressed as $r_n(\eta_a, \eta_b) =$
 1813 $V_{n\Delta}(-\eta_a, \eta_b)/V_{n\Delta}(\eta_a, \eta_b)$, where $V_{n\Delta}(\eta_a, \eta_b)$ is the Fourier coefficient calculated with pairs of
 1814 particles taken from three different pseudorapidity regions $-\eta_a, \eta_a$ and η_b . The observable
 1815 $r_n(\eta_a, \eta_b)$ was originally introduced and measured by CMS collaboration in Ref [208] and also
 1816 been measured by the ATLAS collaboration in [209]. An observable using three-particle
 1817 correlations that is sensitive to this effect is [210] the relative pseudorapidity dependence of
 1818 the three-particle correlator $C_{m,n,m+n}(\eta_a, \eta_b, \eta_c) = \langle \cos(m\phi_1(\eta_a) + n\phi_2(\eta_b) - (m+n)\phi_3(\eta_c)) \rangle$.
 1819 Also, another one very similar to r_n in term of design but involves four-particle correlations
 1820 is: $R_{n,n|n,n}(\eta_a, \eta_b)$ is also very useful to study this effect [211]. As shown in Fig. 53 CMS
 1821 measurements of r_n show a strongest de-correlation ($\sim 16\%$ for $n=3$, $\sim 8\%$ for $n=2$) in central
 1822 events within the range of their acceptance. Initial state, described by gluon saturation, as
 1823 simulated by the 3D-Glasma model, the breaking of boost invariance is determined by the
 1824 QCD equations which predict the evolution of gluons in saturation regime with Bjorken-
 1825 x . At the LHC such models predict weaker de-correlation as compared to initial state
 1826 described by wounded nucleon models and does a good job in explaining the r_2 data from
 1827 CMS collaboration [203] but over-predicts r_3 results. One expect the nature of the initial
 1828 state to change from LHC to RHIC, in particular the region of Bjorken- x probed is very
 1829 different at RHIC. It is therefore extremely important to utilize the enhanced acceptance
 1830 of the STAR detector with the Au+Au 200 GeV run to study this effect. In Fig.53 STAR

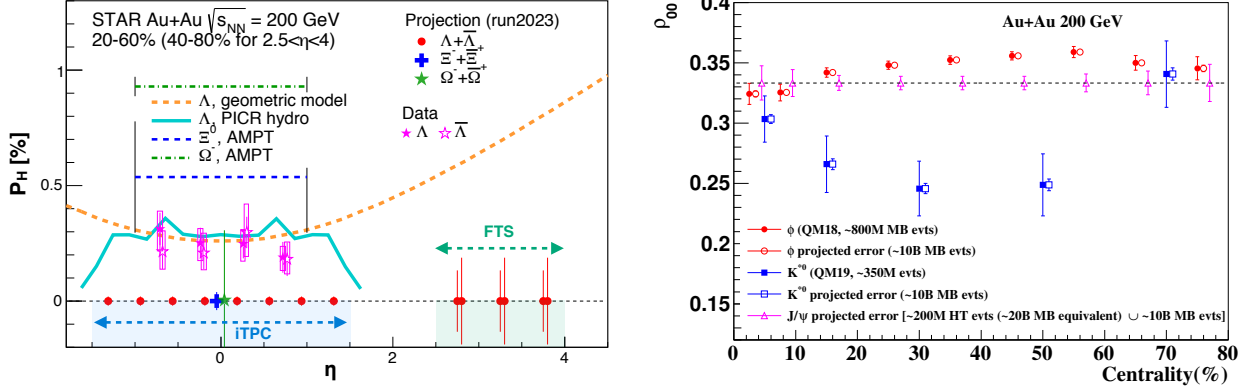


Figure 54: (Left) Projections (along with preliminary data) for differential measurement of $\Lambda(\bar{\Lambda})$ polarization over the extend range of pseudorapidity with the iTPC and FTS detectors of STAR that will help resolve tension between different theoretical model predictions (shown by curves) of polarization with η . In addition, projections for the measurements of spin-1/2 Ξ and spin-3/2 Ω particles is also shown. (Right) Spin alignment co-efficient ρ_{00} as a function of centrality, with projected errors based on ~ 10 billion events. The enhanced statistics run 2023 combined with excellent dilepton capability of STAR will enable us to measure J/ψ alignment along with increasing the significance of ϕ and K^{*0} measurements.

1831 projection using preliminary Run 19 results for 10 B events is shown for the measurement
 1832 of r_n within the acceptance $|\eta| < 1.5$. The colored regions show that the current and
 1833 future capabilities at STAR (with iTPC+EPD+FTS) can extend such measurements using
 1834 observables $r_n, C_{m,n,m+n}, R_{n,n|n,n}$ with good precision by covering either equal (iTPC only) or
 1835 larger (iTPC+FTS+EPDs) fraction of the beam rapidity at 200 GeV compared to the LHC
 1836 measurements. This unique measurement capability will help pin down the nature of the
 1837 3-dimensional initial state of heavy ion collisions. It will also help constrain different models
 1838 of QCD that predict the rapidity (or Bjorken-x) dependence of valance quark and gluon
 1839 distribution inside colliding nuclei that has been demonstrated by theoretical calculations in
 1840 Ref. [203, 212].

1841 Pseudorapidity dependence of global hyperon polarization

1842 The global polarization of hyperons produced in Au+Au collisions has been observed by
 1843 the STAR collaboration [20]. The origin of such a phenomenon has hitherto been not fully
 1844 understood. Several outstanding questions remain. How exactly the global vorticity is dy-
 1845 namically transferred to the fluid like medium on the rapid time scales of collisions? Then,
 1846 how does the local thermal vorticity of the fluid gets transferred to the spin angular momen-
 1847 tum of the produced particles during the process of hadronization and decays? In order to
 1848 address some of these questions one may consider measurement of the polarization of differ-
 1849 ent particles that are produced in different spatial parts of the system, or at different times.
 1850 A concrete proposal is to: 1) measure the $\Lambda(\bar{\Lambda})$ polarization with pseudorapidity and 2) mea-
 1851 sure it for different particles such as Ω and Ξ . Both are limited by the current acceptance and

1852 statistics available to the STAR collaboration. However, as shown in Fig.54 with the addition
 1853 of iTPC, FTS and with high statistics data from run 2023 it will be possible to perform such
 1854 measurements with a reasonable significance. iTPC (+TPC) has excellent PID capability to
 1855 measure all these hyperons. Although FTS has no PID capability we can do combinatorial
 1856 reconstruction of $\Lambda(\bar{\Lambda})$ candidates via displaced vertices. A similar analysis was performed
 1857 and published by the STAR collaboration using the FTTPC detector of STAR in Ref [213]. In
 1858 order to make a conservative projection we assume similar momentum resolution of 10 – 20%
 1859 for single charged tracks, similar overall tracking efficiency, charge state identification capa-
 1860 bility for FTS and FTTPC (see forward upgrade section for exact numbers). We also assume
 1861 the FTS with its novel-tracking framework will be able to measure a minimum separation
 1862 of 20 cm between the all pairs of one positive and one negative track (a possible decay ver-
 1863 tex) from the main vertex of the event. This will give rise to about 5% efficiency of $\Lambda(\bar{\Lambda})$
 1864 reconstruction with about 15 – 20% background contribution from $K_S^0 \rightarrow \pi^+ + \pi^-$ [213] for
 1865 which we can make projections for polarization measurement in Au+Au 200 GeV 40 – 80%
 1866 assuming 10 Billion minimum-bias events as shown in Fig. 54. Currently theoretical models
 1867 predict contradictory trends for the pseudorapidity dependence Λ polarization. If the initial
 1868 local orbital angular momentum driven by collision geometry [214] play dominant role it will
 1869 lead to increases of polarization with pseudorapidity. On the other hand if the local thermal
 1870 vorticity and hydrodynamic evolution [215] play a dominant role it will predict decreasing
 1871 trend or weak dependence with pseudorapidity. Such tensions can be easily resolved with
 1872 the future proposed measurement during the run 2023.

1873 2.4.2 Correlation Measurements Utilizing the Enhanced Statistics

1874 Over the past years the STAR collaboration has pursued dedicated measurements at Au+Au
 1875 collisions at $\sqrt{s_{NN}} = 200$ GeV that have major discovery potential but are intrinsically statis-
 1876 tics hungry. In the past, attempts have been made to combine datasets from several years to
 1877 increase the significance of such measurements. This results in additional uncorrectable sys-
 1878 tematic uncertainties in the measurements, mostly due to run-to-run variation of detector
 1879 response and collision conditions. A single stable long run with similar detector condi-
 1880 tions, as anticipated during Run-23 will not only reduce the statistical uncertainty but will
 1881 also bring the systematics under control. In the following section and also in section 1.2.6
 1882 we propose correlation measurements that will utilize the enhanced statistics from Run-
 1883 23 and that can lead to high-impact results. To start with we can assume STAR DAQ
 1884 to collect data at the rate of 1.5 kHz and a combined RHIC×STAR uptime of 50% (12
 1885 hour/day) for 24 weeks of running during Run-23. This will lead to the accumulation of
 1886 about $24 \times 7 \times 86400 \times 0.5 \times 1500 \approx 10$ billion events.

1887 Global spin alignment of J/ψ

1888 Surprisingly large signals of global spin alignment of vector mesons such as $\phi(1020)$ and
 1889 $K^{*0}(892)$ have been measured via the angular distribution of one of their decay products.
 1890 By far the experimental observation of vector meson spin alignment have not been inter-
 1891 preted satisfactorily by theory calculations. It has been realized that the mechanism driving

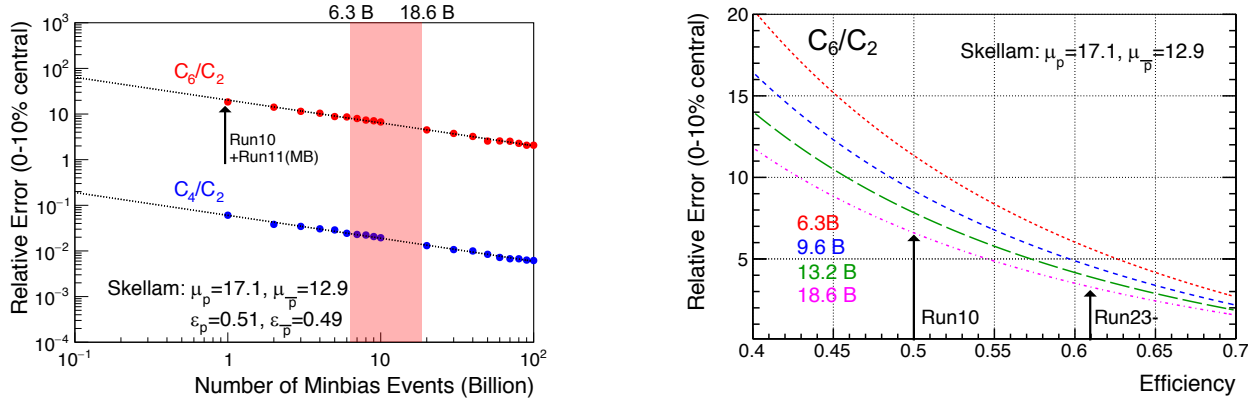


Figure 55: Projection for measurement of ratio of sixth order over second order cumulants of net-proton distribution.

1892 the global polarization of hyperons can have its imprint on vector mesons spin alignment
1893 albeit the observed strength of signals for the two measurements cannot be reconciled. In
1894 fact the large quantitative difference between the measurements of $\phi(1020)$ and $K^{*0}(892)$
1895 spin alignment as shown in Fig. 54 (right) cannot be simultaneously explained by conven-
1896 tional mechanisms of spin-orbit coupling, driven by angular momentum, without invoking
1897 the strong force fields. It is argued that the strong force field makes a dominant contribution
1898 to the spin-alignment coefficient ρ_{00} of ϕ , while for K^{*0} , the contribution is diminished due
1899 to the mixing of quark flavors (averaging-out of different meson fields) [216,217]. Therefore,
1900 the current preliminary experimental data from STAR (Fig. 54, showing $\rho_{00}(\phi) > \rho_{00}(K^{*0})$)
1901 support the role of strong force field as a key mechanism that leads to global spin align-
1902 ment. However, a stringent test of such a prediction can be performed by measuring the
1903 spin alignment of J/ψ . This is because the similar argument applies for both ϕ and J/ψ ,
1904 i.e. like s and \bar{s} , the strong field component also couples to c and \bar{c} quarks leading to larger
1905 ρ_{00} for J/ψ . In Fig. 54(right) we present the projected errors for ρ_{00} of J/ψ estimated for
1906 various centralities assuming 200 million events (24 weeks running) anticipated in Run-23
1907 by implementing High Tower (HT) triggers with the Barrel Electromagnetic Calorimeter.
1908 It is worth to mention that apart from J/ψ spin alignment, such a large statistics data set
1909 will also allow addition differential study of global spin alignment of ϕ and K^{*0} and help to
1910 further elucidate the mechanism behind vector meson spin alignment.

1911 Sixth order cumulant of net-proton distributions

1912 LQCD calculations [218,219] predict a sign change of the susceptibility ratio χ_6^B/χ_2^B with
1913 temperature (T at $\mu_B = 0$) taking place in the range of 145-165 MeV. The observation of
1914 this ratio going from positive to negative values is considered to be a signature of crossover
1915 transition. As described in the previous section, the cumulants of net-proton distribution
1916 are sensitive to the chiral crossover transition at vanishing baryon chemical potential. Inter-
1917 estingly, as reported in the last BUR and in the recent Quark Matter 2019, the preliminary
1918 results from STAR [220] observed $C_6/C_2 > 0$ in 54.4 GeV while $C_6/C_2 < 0$ in 200 GeV in

1919 central Au+Au collisions. The observation of positive C_6/C_2 at lower energies can be further
1920 confirmed by higher statistics data sets from the BES-II program over the energy range of
1921 7.7-19.6 GeV, which also include the increased acceptance iTPC. The observation of negative
1922 C_6/C_2 is intriguing and by far only seen at 200 GeV and based on the current STAR data
1923 has less than 2.5σ significance in terms of statistical uncertainties. The currently systematic
1924 uncertainty is of similar order as statistical uncertainty mainly due to combining data sets
1925 from Runs 10 and 11. As shown in the projection plot of Fig. 55 it is possible to establish
1926 definitive observation of negative C_6/C_2 at 200 GeV with nearly 10 billion minimum-bias
1927 events collected during the Run-23 with 15% increase in the reconstruction efficiency and
1928 enhanced acceptance of the iTPC detector upgrade. A similar measurement can be per-
1929 formed at the LHC however only STAR measurements can pinpoint the region of T and
1930 μ_B where this phenomenon occurs. In other words it can establish if that the sign change
1931 occurs somewhere between 54.4 GeV and 200 GeV. Such measurement has the potential to
1932 establish the first experimental observation of QCD chiral crossover transition.

1933 2.4.3 Electromagnetic Probes

1934 Probing the degrees of freedom of the medium and its transport properties

1935 As discussed in Sect. 1.1.3, at $\mu_B \sim 0$ Lattice QCD works and can be directly tested against
1936 experimental results. This will help to disentangle the ρ melting from other explanations
1937 such as collision broadening. In case the measured in-medium spectral function merges into
1938 QGP description this would indicate a transition from hadrons into a structure-less quark-
1939 antiquark continuum and thus providing the manifestation of chiral symmetry restoration.
1940 To study this, we will continue to search for a direct signature for chiral symmetry restoration
1941 via chiral ρ - a_1 mixing. The signal is predicted to be detectable in the dilepton intermediate
1942 mass range. Difficulties are related to the fact that correlated charm-anticharm and QGP
1943 saturate invariant mass region of 1.1 — 1.3 GeV/ c^2 . Therefore an accurate measurement
1944 of the excess dilepton yield, i.e. dilepton yield after subtraction of the cocktail of contribu-
1945 tions from final-state decays, Drell-Yan and those from correlated heavy-flavor decays, up
1946 to invariant mass of 2.5 GeV/ c^2 is required. The challenging analysis on charmed-decayed
1947 dielectron is ongoing from the data sets taken with the Heavy Flavor Tracker at STAR [221].
1948 Thus deeper understanding of origin of thermal radiation in Au+Au collisions at $\sqrt{s_{NN}} =$
1949 200 GeV from \sim zero mass up to 2.5 GeV/ c^2 will become possible with rigorous theoretical
1950 efforts and improved dielectron measurements. Figure 56 shows the expected statistical and
1951 systematic uncertainties of dielectron excess mass spectrum with all the detector upgrades
1952 and for the anticipated total Run-23/Run-25 statistics of 20×10^9 events.

1953 Another application of dileptons is to use them to measure transport coefficients. The
1954 electrical conductivity can be directly obtained as the low-energy limit of the EM spectral
1955 function. We aim to extract such information by studying excess dielectron yield at the
1956 low-energy regime of dilepton spectra and the conductivity peak at small invariant masses,
1957 i.e. at low invariant mass and low p_T^{ee} . Low field run could be profitable, however already
1958 now dileptons with pair p_T^{ee} down to 60 MeV/ c could be measured. Measurement of Drell-
1959 Yan in p+A collisions at low p_T would provide an important reference to constrain dilepton

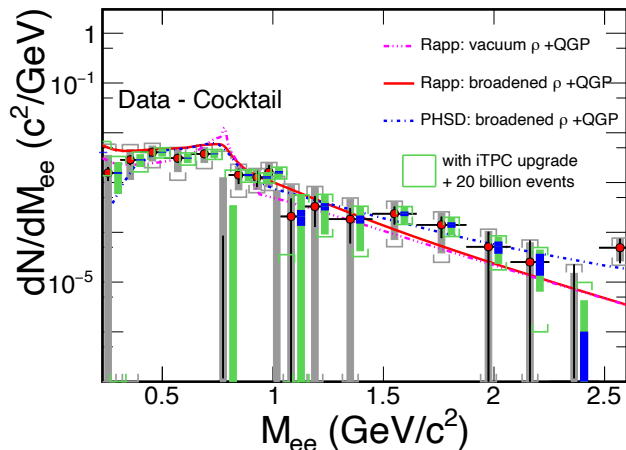


Figure 56: The expected statistical and systematic uncertainties of dielectron excess mass spectrum with the iTPC upgrade compared to the current TPC case. The data are from our measurements in $\sqrt{s_{NN}} = 200$ GeV Au+Au collisions [58]. Model comparisons are also shown. The boxes represent systematic uncertainties from data and the brackets represent the total systematic uncertainties including those from cocktails. The grey ones are for the current case while the green ones are for the expected case. The blue bands represent statistical uncertainties from 20 billion minimum-bias events with the iTPC upgrade.

1960 cocktail.

1961 To gain deeper understanding of the microscopic origin of the excess radiation, we will

- 1962 • separate early from later time radiation by measuring dilepton elliptic flow (v_2) as a
- 1963 function of dilepton mass;
- 1964 • identify the source of dilepton radiation by studying dilepton polarization versus in-
- 1965 variant mass (helicity angle);
- 1966 • measure precisely the lifetime of the interacting fireball. As an observable we will use
- 1967 integrated low-mass yield but also compare explicit model calculations with various
- 1968 $\tau_{fireball}$;
- 1969 • extract an average radiating source temperature from the fit of Boltzmann distribution
- 1970 to the invariant mass slope in the range 1.1 - 2.5 GeV/c^2 spectrum. The higher the
- 1971 invariant mass, the stronger the QGP contribution to the spectrum, the higher the
- 1972 chance to measure temperature of QGP.

1973 Last, but not least, concerning direct-photon emission, the existing difference, on the

1974 order of a factor of two, between the low momentum spectra from PHENIX and STAR in

1975 200 GeV Au+Au collisions, has to be resolved. In order to clarify the direct photon puzzle

1976 we will measure direct virtual photon yield as well as its elliptic flow coefficient. We will

1977 particularly focus on low p_T η measurement which might be instrumental in clarifying this

1978 long standing question.

1979
1980
1981
1982
1983
1984
1985
1986
1987
1988
1989
1990
1991
1992
1993
1994
1995
1996

Studying the photon Wigner function and final-state magnetic fields in the QGP

The unsuccessful description of STAR data by the STARLight model led to the attribution of the broadening to the possible residual magnetic field trapped in an electrically conducting QGP, which is the key information to study the chiral magnetic effect. Similarly, the ATLAS collaboration qualified the effect via the acoplanarity of lepton pairs in contrast to the measurements in UPC and explained the additional broadening by the multiple electromagnetic scatterings in the hot and dense medium, which is analogous to the medium P_{\perp} -broadening effects for jet quenching. These descriptions of the broadening effect in hadronic collisions are based on the assumption that there is no impact parameter dependence of the transverse momentum distribution for the electromagnetic production. Recent lowest-order QED calculation, in which the impact parameter dependence is recovered, could reasonably describe the broadening observed by STAR and ATLAS without any in-medium effect. To solve the puzzle, we propose to precisely study the initial P_{\perp} -broadening for the dilepton pair in ultra-peripheral collisions. Different neutron emission tag serve as the centrality definition, and will allow us to explore the broadening baseline variation with impact parameter. Furthermore, the differential spectrum as a function of pair P_{\perp} , rapidity, and mass enable us to study the Wigner function of the initial electromagnetic field, which provide the information to extract the momentum and space correlation of EM field.

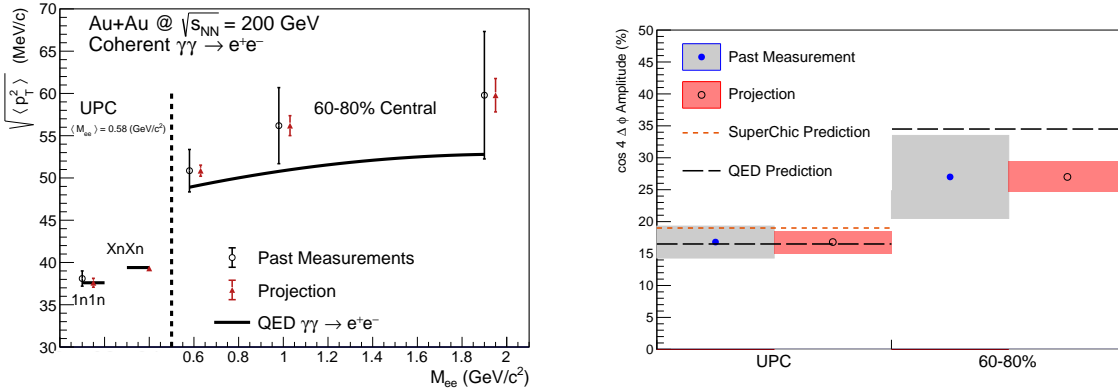


Figure 57: (Color online) Projections for measurements of the $\gamma\gamma \rightarrow e^+e^-$ process in peripheral and ultra-peripheral collisions. Left: The $\sqrt{\langle p_T^2 \rangle}$ of di-electron pairs within the fiducial acceptance as a function of pair mass, M_{ee} , for 60 – 80% central and ultra-peripheral Au+Au collisions at $\sqrt{s_{NN}} = 200$ GeV. Right: The projection of the $\cos 4\Delta\phi$ measurement for both peripheral (60–80%) and ultra-peripheral collisions.

1997
1998
1999
2000
2001
2002

As shown in Fig. 57, comparing with the latest QED calculation, there still exists additional broadening in peripheral collisions, although the significance is about 1σ , which still leave room for the medium effect. In Runs 23/25, as projected in the figure, we could judge the existence of additional broadening with much higher precision and further constrain the strength of final-state magnetic field in QGP.

Precision measurement of the amplitude of the recently observed $\cos 4\Delta\phi$ modulation of

2003 the $\gamma\gamma \rightarrow e^+e^-$ process will allow precision mapping of the photon Wigner function and
 2004 provide additional constraints on possible final-state effects, thereby complementing the P_\perp
 2005 broadening measurement. Fig 57 right panel shows the projected precision for a measurement
 2006 of the $\cos 4\Delta\phi$ modulation in Run 23/25. The modulation is a direct result of the mismatch
 2007 in initial and final spin configuration of the $\gamma\gamma \rightarrow e^+e^-$ process. Any final-state effect that
 2008 modifies the P_\perp will necessarily reduce the amplitude of the modulation. Assuming the same
 2009 central value as previously measured, evidence for suppression of the $\cos 4\Delta\phi$ modulation
 2010 will be visible at the $> 3\sigma$ level (stat. & syst. uncertainty). Precision measurement of the
 2011 $\cos 4\Delta\phi$ modulation in Run 23/25 may also allow a first direct experimental measurement
 2012 of impact parameter dependence of this new observable (by comparing UPC and 60 – 80%).
 2013 Assuming the same central values as previously measured, the improved precision will provide
 2014 evidence for impact parameter dependence at the $> 3\sigma$ level (stat. & syst. uncertainty).
 2015 Assuming the central value predicted by QED would lead to a $> 5\sigma$ difference between the
 2016 UPC case and the 60 – 80% case.

2017 **Ultra-peripheral Au+Au collisions: probe gluon distribution inside nucleus**

2018 STAR recently observed a significant $\cos 2\Delta\phi$ azimuthal modulation in $\pi^+\pi^-$ pairs from
 2019 photonuclear ρ^0 and continuum production. The structure of the observed modulation as
 2020 a function of the $\pi^+\pi^-$ pair transverse momentum, P_\perp , appears related to the diffractive
 2021 pattern. Recent theoretical calculations [222], which implemented linearly polarized pho-
 2022 tons interacting with the saturated gluons inside a nucleus, have successfully described the
 2023 qualitative features of the observed modulation (see Fig. 58), and indicate that the detailed
 2024 structure of the $\cos 2\Delta\phi$ modulation vs. P_\perp is sensitive to the nuclear geometry and gluon
 2025 distribution. Data from Run 23/25 would allow the additional statistical reach needed to
 2026 perform multi-differential analysis, proving stronger theoretical constraints. Specifically,
 2027 multi-differential analysis of the $\cos 2\Delta\phi$ modulation with respect to pair rapidity and pair
 2028 mass are needed. Multi-differential analysis with respect pair mass is needed to separate
 2029 the ρ^0 production from the continuum Drell-Soding production. Multi-differential analysis
 2030 with respect to the pair rapidity is needed to quantitatively investigate how the double-slit
 2031 interference mechanism effects the structure of the observed azimuthal modulation. Addi-
 2032 tional statistical precision is also needed for measurement of the higher harmonics. Similar
 2033 measurements with $J/\Psi \rightarrow e^+e^-$ can be performed and such measurements at higher mass
 2034 provide better comparison with more reliable QCD calculation.

2035 Ultraperipheral $A + A$ collisions, where photons generated by the Lorentz-boosted elec-
 2036 tromagnetic field of one nucleus interact with the gluons inside the other nucleus, can provide
 2037 certain 3D gluonic tomography measurements of heavy ions, even before the operation of the
 2038 future EIC. STAR has performed the experimental measurements of the photoproduction of
 2039 J/ψ at low transverse momentum in non-UPC heavy-ion collisions [223], accompanying the
 2040 violent hadronic collisions. A detailed study with pt distribution has shown that the $|t|$ dis-
 2041 tribution in peripheral collisions is more consistent with the coherent diffractive process than
 2042 the incoherent process. Although models [224, 225] incorporating different partial coherent
 2043 photon and nuclear interactions could explain the yields, it remains unclear how the coherent

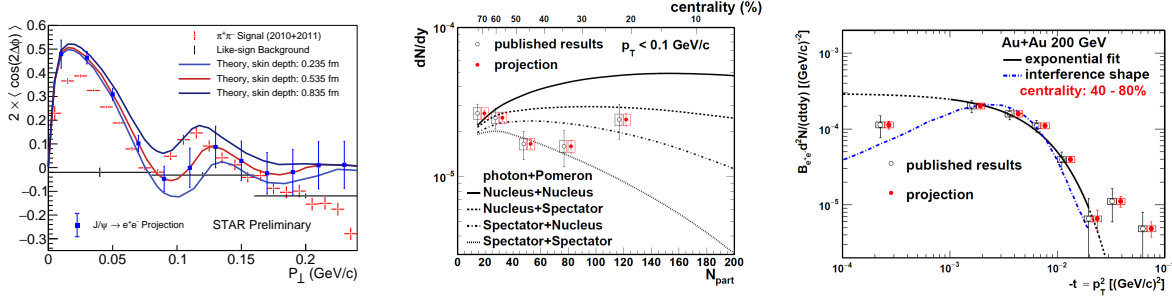


Figure 58: Left: Measurement of the $\cos 2\Delta\phi$ modulation of $\pi^+\pi^-$ pairs from photonuclear ρ^0 and continuum production compared to theoretical predictions [222]. Projections are shown for a similar measurement of the azimuthal modulation of e^+e^- pairs from photonuclear production of the J/ψ . Center: Projection of the dN/dy of photoproduced J/ψ in non-UPC events vs. the event centrality (N_{part}) compared to various theoretical production scenarios. Right: Projection of the t spectra of photoproduced J/ψ in 40 – 80% central collisions.

2044 process happens and whether final-state effects play any role [226]. Resolving this puzzle
 2045 with high statistical data and detailed $|t|$ distributions at different centralities at RHIC as
 2046 projected for 2023-2025 runs in Fig. 58 may be important for understanding what defines
 2047 the coherentsness of the photoproduction, how vector mesons are formed in the process and
 2048 how exclusive the similar process has to be in future EIC experiment with forward neutron
 2049 veto/tagging.

2050 2.4.4 Deconfinement and Thermalization With Charmonia Measurements

2051 Measurements of charmonia in heavy-ion collisions provide important information about
 2052 the thermodynamic properties of the created medium. Production of J/ψ mesons in Au+Au
 2053 collisions at RHIC was found to be suppressed compared to the production in proton+proton
 2054 collisions. The suppression of charmonium states is due to a screening of the $c\bar{c}$ potential by
 2055 the medium color charges. In addition, the J/ψ production can be affected by recombination
 2056 of charm quarks in a later stage of the collision evolution. The regeneration mechanism is
 2057 expected to contribute mostly at the low J/ψ transverse momentum range.

2058 In particular, STAR proposes to utilize the Run-23/25 RHIC heavy-ion runs to measure:
 2059 (i) low transverse momentum J/ψ elliptic flow (v_2) in order to study in more details the
 2060 recombination mechanism (ii) J/ψ directed flow (v_1) that will allow us to study the initial
 2061 tilt of the bulk medium (iii) suppression of the loosely bounded $\psi(2S)$ state to explore the
 2062 temperature profile of the medium.

2063 An important observable for studying the properties of the deconfined medium is the
 2064 second order flow harmonic of the Fourier expansion of the azimuthal distribution of the
 2065 produced hadrons, the elliptic flow coefficient v_2 . Similarly as in the case of light hadrons,
 2066 a positive v_2 of D -mesons and electrons from heavy-flavor hadron decays was observed at
 2067 RHIC energies of 54.4 and 200 GeV. Which suggests that the charm quarks may (partially)
 2068 thermalize and participate in the bulk medium collective evolution. On the other hand, the

2069 v_2 of heavier J/ψ reported by STAR based on the 2010 Au+Au 200 GeV data sample was
 2070 found to be consistent with zero, albeit within large statistical uncertainties and systematic
 2071 uncertainties due to non-flow effects. The precision of the measurement was also not enough
 2072 to distinguish between theoretical model calculations that assume only primordial J/ψ pro-
 2073 duction and the ones that include additional J/ψ production via the recombination. This
 2074 calls for a larger sample of heavy-ion data at 200 GeV, as will be provided by RHIC in 2023
 2075 and 2025, in order to observe a possible non-zero J/ψ v_2 at RHIC energies and put more
 2076 constraints on the J/ψ production models especially regarding its regeneration. Particularly
 2077 important for these studies will be the STAR potential to measure low transverse momentum
 2078 J/ψ with a very good precision. This excellent low- p_T performance at STAR can be achieved
 2079 thanks to its low material budget and great particle identification capabilities.

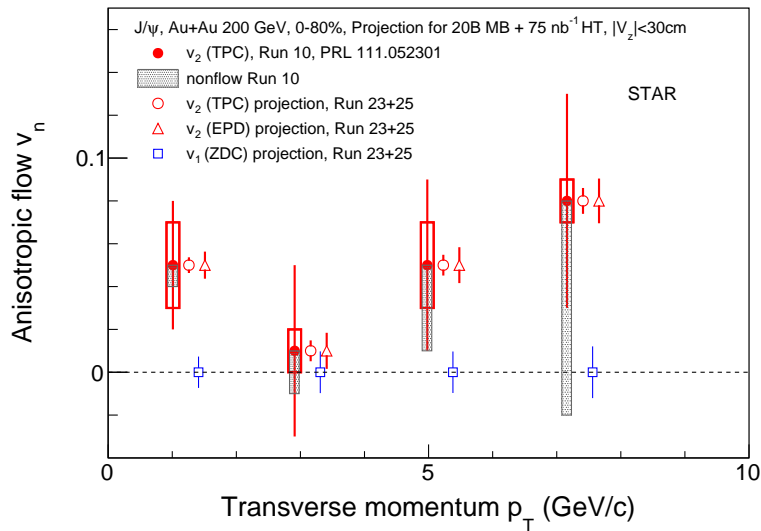


Figure 59: Projections for the J/ψ ($J/\psi \rightarrow e^+e^-$) directed (v_1) and elliptic (v_2) flow vs J/ψ p_T in 0-80% Au+Au collisions at 200 GeV, assuming 20B MB events and HT triggered events corresponding to an integrated luminosity of 75 nb^{-1} with $|V_z| < 30 \text{ cm}$.

2080 Moreover, the second order Event Plane (EP) can be reconstructed using the new Event
 2081 Plane Detectors (EPD) installed before the 2018 run. It is expected that using the EPD,
 2082 that are forward detectors, will significantly decrease the contribution from the non-flow
 2083 effects and consequently the measurement systematic uncertainties. Also, an inverse of the
 2084 EP resolution enters directly the J/ψ v_2 uncertainty calculation. Thanks to EPD, the res-
 2085 olution of the EP reconstruction at forward rapidity for the J/ψ v_2 measurement at STAR
 2086 will improve. Figure 59 presents statistical projections for the J/ψ v_2 measurement in 0-80%
 2087 central Au+Au collisions assuming 20B MB events and HT triggered events corresponding
 2088 to an integrated luminosity of 75 nb^{-1} . Both cases of the second order EP reconstruction,
 2089 using forward EPD and mid-rapidity TPC detectors, are considered and shown. However,
 2090 measurements for which the TPC is utilized for the EP reconstruction suffer from a sub-
 2091 stantial non-flow contribution which would be greatly reduced by reconstructing the second

2092 order Event Plane with the EPD. A clear significant improvement in the precision of the
 2093 J/ψ v_2 can be seen across the whole experimentally accessible J/ψ p_T coverage of the previ-
 2094 ous measurement. In addition, the new larger dataset would allow to extend the measured
 2095 p_T range beyond 10 GeV/ c .

2096 Studies of the directed flow v_1 as a function of rapidity provide crucial information to
 2097 understand the initial tilt of the medium produced in heavy-ion collision. The heavy quarks
 2098 are produced in the early stage of a heavy-ion collision and thus are of a particular interest
 2099 for the medium initial asymmetry studies. STAR recently reported the first measurement of
 2100 D-meson v_1 in Au+Au collisions at 200 GeV where the magnitude of the heavy-flavor meson
 2101 v_1 is about 25 times larger than the v_1 for charged kaons. With the 2023-2025 data, STAR
 2102 would have a unique opportunity to also study the v_1 of a bound $c\bar{c}$ state, the J/ψ mesons,
 2103 for which even larger directed flow can be expected [227]. In addition to the STAR excellent
 2104 capability to reconstruct low- p_T J/ψ , as discussed above, the iTPC detector completed in
 2105 2018 will improve the momentum resolution and extend the STAR pseudorapidity coverage
 2106 around the mid-rapidity. This will provide a better precision for the slope extraction of the
 2107 v_1 vs y measurement, that quantifies the strength of directed flow. The expected precision
 2108 of a J/ψ v_1 measurement vs p_T at STAR in 2023-2025, assuming 20B MB events and HT
 2109 triggered events corresponding to an integrated luminosity of 75 nb^{-1} , in 0-80% central
 2110 Au+Au collisions at 200 GeV is shown in Fig. 59. Together with the J/ψ v_2 measurements,
 2111 v_1 would provide a more complete picture of the J/ψ production mechanism as well as the
 2112 medium properties in heavy-ion collisions at RHIC.

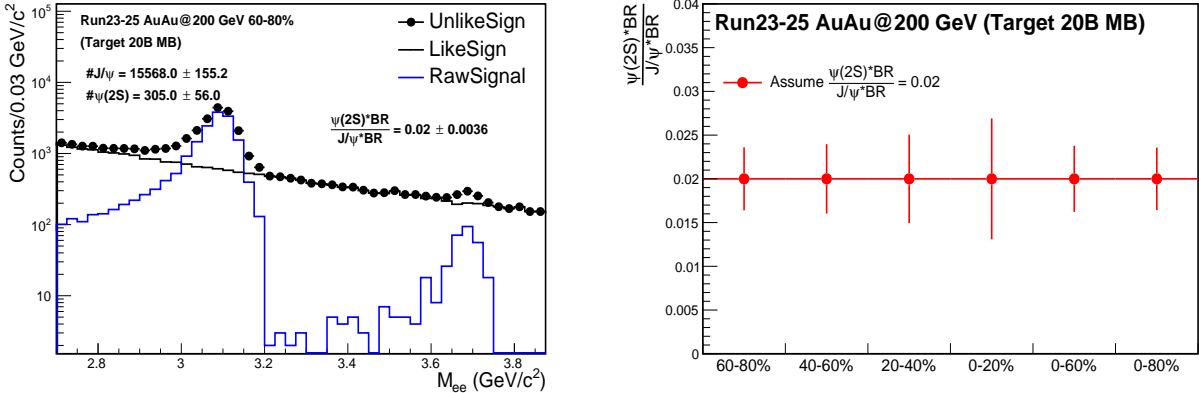


Figure 60: Projections for the J/ψ and $\psi(2S)$ signals in 60-80% Au+Au collisions at 200 GeV and the yield ratio in various centrality bins. The improvement of momentum and dE/dx resolution thanks to the STAR iTPC upgrade have not been taken into account.

2113 $\psi(2S)$ is the most loosely bounded quarkonium state accessible in the heavy-ion collision
 2114 experiments. Its dissociation temperature is predicted to be around or below the critical
 2115 temperature and is much less than that of J/ψ and Υ states. It is more likely to be dis-
 2116 sociated in the early stage and in the core of the fireball and the $\psi(2S)$ survived may have
 2117 significant contribution from the regeneration at later stage in the evolution of the fireball.

2118 The relative suppression of $\psi(2S)$ and J/ψ is sensitive to the the temperature profile of the
 2119 fireball produced in heavy-ion collisions and its space-time evolution. It is also argued that
 2120 the charmonium formation process from a $c\bar{c}$ pair may be affected by the QGP or the ini-
 2121 tial strong external magnetic field, altering the relative yields among different charmonium
 2122 states [228, 229]. The measurement of $\psi(2S)$ is much more difficult than that of J/ψ due to
 2123 a much smaller production cross-section and dilepton decay branching ratio, resulting in a
 2124 very low signal-to-background ratio. The ALICE Collaboration successfully measured the
 2125 relative suppression of $\psi(2S)$ and J/ψ in Pb+Pb collisions at forward rapidity [230], and the
 2126 ATLAS and CMS Collaboration published the relative suppression in Pb+Pb collisions at
 2127 mid-rapidity and high p_T [231, 232]. The attempt of measuring $\psi(2S)$ suppression in heavy-
 2128 ion collisions at RHIC has no success as to date. The low material budget and excellent
 2129 particle identification capability of the STAR detector together with the large data sample
 2130 in 2023 and 2025 will provide a unique opportunity to measure the suppression of $\psi(2S)$ at
 2131 low p_T and mid-rapidity in heavy-ion collisions. Figure 60 shows the projections of $\psi(2S)$
 2132 signal and the yield ratio of $\psi(2S)$ and J/ψ in Au+Au collisions assuming 20B MB events.
 2133 The improvement of momentum and dE/dx resolution thanks to the STAR iTPC upgrade
 2134 will further enhance the signal-to-background ratio and the significance of $\psi(2S)$ signal.

2135 2.4.5 Jet Probes

2136 Precise jet quenching measurements with reconstructed jets over a broad kinematic range
 2137 at RHIC are essential to meet the goal of the NSAC 2015 Long Range Plan, to “probe the
 2138 inner workings of the QGP” [198]. For example, the dependence of jet energy loss on the jet
 2139 p_T and the resolution or angular scale tagged by jet substructure observables are key tools
 2140 to discriminate jet quenching mechanisms [233–236]. In addition, the measurement of jet
 2141 acoplanarity as a probe of in-medium jet scattering is most sensitive at low jet p_T to a given
 2142 momentum transfer and to medium-induced radiative effects [237], and is least affected by
 2143 background due to vacuum Sudakov radiation [238].

2144 The highest-statistics STAR Au+Au collision datasets currently available were recorded
 2145 in 2014 and 2016, with the integrated luminosity sampled by STAR BEMC triggers shown
 2146 in Table 10. Preliminary jet analyses using the 2014 dataset are discussed in section 1.1.1
 2147 and are moving towards publication. STAR will continue to exploit these rich datasets to
 2148 carry out high-precision measurements with fully reconstructed jets over the full RHIC phase
 2149 space.

2150 The 2023 and 2025 runs will generate another significant increase in sampled integrated
 2151 luminosity, enabling a third generation of STAR heavy-ion jet measurements that are yet
 2152 more differential and precise. STAR’s open geometry near the beam pipe allows it to utilize
 2153 a wide range in the vertex position along the beam direction (vz) for jet analyses, thereby
 2154 utilizing the RHIC luminosity efficiently. Optimization of the vz range used in an analysis
 2155 entails a balance between statistical precision and complexity of corrections, with the latter
 2156 influencing the systematic uncertainty of the measurement. Recent STAR jet measurements
 2157 in Au+Au collisions have employ two different z-vertex cuts: the inclusive charged-particle
 2158 jet analysis [7] utilizes $|vz| < 30$ cm, whereas the $\gamma_{\text{dir}} + \text{jet}$ analysis [10] utilizes $|vz| < 70$

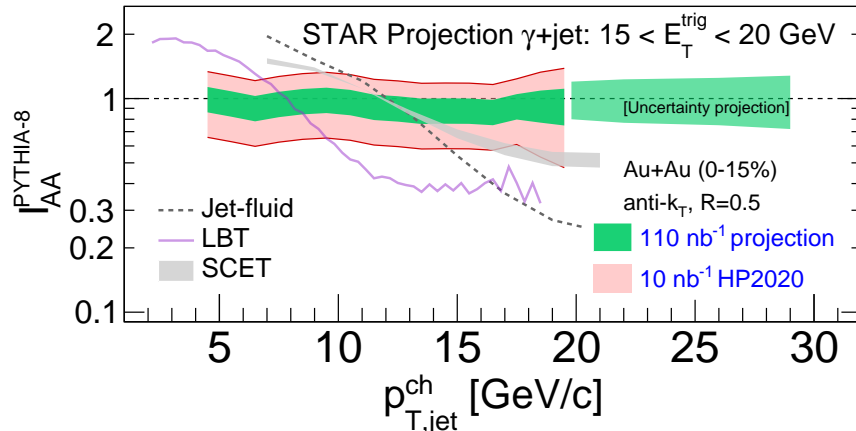


Figure 61: Ratio of semi-inclusive distributions of charged-particle jets (anti- k_T , $R = 0.5$) recoiling from a direct-photon trigger with $15 < E_T < 20$ GeV for central Au+Au collisions at $\sqrt{s_{NN}} = 200$ GeV measured by STAR (numerator) and p+p collisions simulated by PYTHIA (denominator). The pink band shows the cumulative uncertainty for the current analysis based on 10 nb^{-1} [10], while the green band shows the projected uncertainty for 110 nb^{-1} . Theory calculations are discussed in [10].

2159 cm. With the success of the $\gamma_{\text{dir}} + \text{jet}$ analysis in analyzing this broad v_z range with good
 2160 systematic precision, we will re-examine this cut for future jet measurements, including the
 2161 inclusive jet analysis. In section 2.4 we present the sampled integrated luminosity in 2023 and
 2162 2025 for both the 30 cm and 70 cm v_z cuts. The following physics performance projections
 2163 are based on the 70 cm cut, using the cumulative sampled integrated luminosity for Runs
 2164 2014, 2016, 2023 and 2025 together. For $|v_z| < 70$ cm, this total is 110 nb^{-1} , which is a
 2165 factor 11 increase in trigger statistics relative to the current analyses based on Run 14 data.

2166 To quantify the effect of this marked increase in integrated luminosity, we utilize two
 2167 mature jet measurements currently in progress and discuss their expected improvement
 2168 with enhanced integrated luminosity. These analyses are the semi-inclusive distribution
 2169 of charged-particle jets recoiling from a high- E_T direct-photon trigger ($\gamma_{\text{dir}} + \text{jet}$); and the
 2170 differential measurement of energy loss for jet populations selected by varying a substructure
 2171 metric. Since these analyses are mature, their analysis methodologies and correction schemes
 2172 are optimized, so that their projections based on increased statistics are meaningful. We do
 2173 not imply that these will be the only flagship measurements that STAR will make with the
 2174 ‘23/‘25 datasets; in addition we will focus for instance on fully reconstructed jets and uti-
 2175 lize additional substructure observables, including those not yet developed. However, these
 2176 analyses are most mature at present, and therefore provide the most accurate projections of
 2177 gain in precision.

2178 Semi-inclusive $\gamma_{\text{dir}} + \text{jet}$ measurement

2179 Figure 61 shows I_{AA} for fully-corrected semi-inclusive distributions of charged-particle jets
 2180 (anti- k_T , $R = 0.5$) recoiling from a direct-photon trigger with $15 < E_T < 20$ GeV in central

2181 Au+Au collisions at $\sqrt{s_{\text{NN}}} = 200$ GeV, for the current analysis based on 10 nb^{-1} [10] within
 2182 $|v_z| < 70$ cm, and projected for 110 nb^{-1} . Significant reduction in the uncertainty band is
 2183 seen to result from the increase in integrated luminosity, together with significant increase
 2184 in kinematic reach.

2185 Note that the projection to 110 nb^{-1} only takes into account the increase in statistical
 2186 precision, and assumes that the systematic uncertainty remains the same. The reduction in
 2187 width of the uncertainty band is therefore less than the factor $1/\sqrt{11}$ expected from statistical
 2188 considerations alone, indicating the magnitude of the systematic component. Experience
 2189 shows that systematic uncertainty can also be improved by an increase in statistical precision,
 2190 since additional and more differential systematic studies can be carried out. However, it is
 2191 not possible to project that improvement with confidence at present; thus Fig. 61 should
 2192 therefore be regarded as a conservative estimate of the improvement in precision of this
 2193 measurement channel with the projected integrated luminosity increase.

2194 Broadening of the back-to-back di-jet angular distribution due to jet scattering from con-
 2195 stituents of the QGP (medium-induced acoplanarity) was proposed over three decades ago
 2196 as a diagnostic probe of the QGP [239, 240]. While the physical picture of this process is
 2197 intuitive and compelling, such measurements are extremely challenging, because of both the
 2198 large jet backgrounds in heavy ion collisions, and the large contribution of vacuum QCD pro-
 2199 cesses (Sudakov radiation) to the di-jet angular distribution [238]. In addition, minimization
 2200 of these two effects nominally drives the experimentalist in opposite directions: minimization
 2201 of background effects prefers larger $p_{\text{T,jet}}$, whereas minimization of Sudakov broadening and
 2202 higher sensitivity to medium-induced momentum transfer prefers lower $p_{\text{T,jet}}$ [238]. These
 2203 contradictory requirements were resolved only with the development of absolutely normalized
 2204 semi-inclusive jet measurements in heavy-ion collisions, with statistically-based background
 2205 corrections that enable measurements at low $p_{\text{T,jet}}$ and large R [1, 241].

2206 The first generation searches for medium-induced acoplanarity using this approach did
 2207 not exhibit a significant signal above background [1, 241], though with limited statistical
 2208 precision. Higher-precision measurements of medium-induced acoplanarity over a broad $p_{\text{T,jet}}$
 2209 range – including low $p_{\text{T,jet}}$ – are clearly of great interest at both RHIC and the LHC. Such
 2210 measurements may provide a direct probe of \hat{q} [238], or evidence of large-angle jet scattering
 2211 off of quasi-particles in the QGP [242]. Consideration of higher-order processes suggests that
 2212 the contribution of radiative corrections to this distribution may be negative [237], thereby
 2213 narrowing rather than broadening the recoil jet azimuthal distribution; a recent preliminary
 2214 measurement by the ALICE Collaboration at the LHC may indeed have observed such an
 2215 effect [243]. Complementary measurements of medium-induced acoplanarity over wide phase
 2216 space by STAR at RHIC and ALICE at the LHC, using similar instrumentation and similar
 2217 analysis techniques, promise to provide strong constraints on theoretical descriptions of this
 2218 fundamental process, providing new insight into the inner workings of the QGP [198].

2219 Figure 62 shows the semi-inclusive distribution of the azimuthal separation between a
 2220 direct-photon trigger with $15 < E_T < 20$ GeV and a charged-particle jet (anti- k_T , $R = 0.5$)
 2221 with $10 < p_{\text{T,jet}}^{\text{ch}} < 15$ GeV/ c , in central Au+Au collisions at $\sqrt{s_{\text{NN}}} = 200$ GeV with only
 2222 statistical error bars, based on the analysis described in [10]. Azimuthal smearing of this

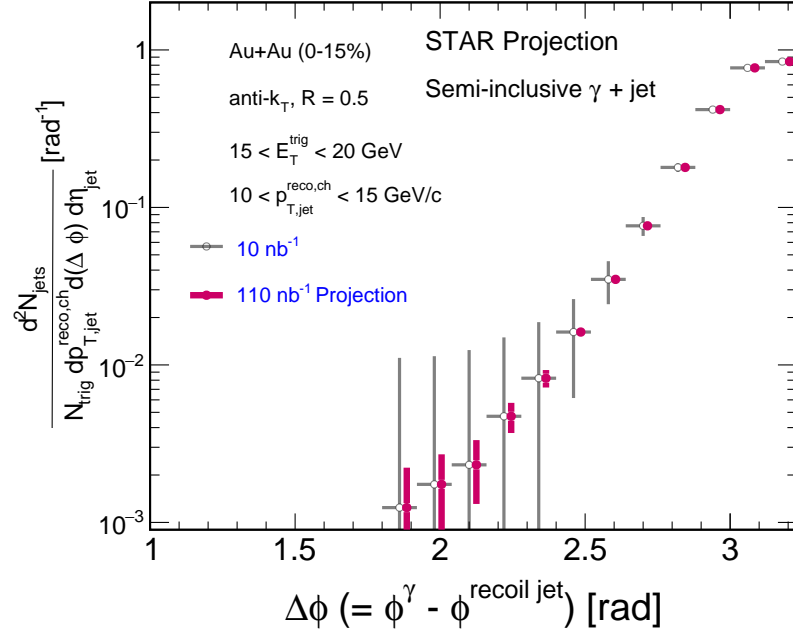


Figure 62: Semi-inclusive azimuthal distribution of charged jets (anti- k_T , $R=0.5$) with $10 < p_{T,\text{jet}}^{\text{ch}} < 15$ GeV/ c recoiling from a direct photon trigger with $15 < E_T^{\text{trig}} < 20$ GeV, in central Au+Au collisions at $\sqrt{s_{\text{NN}}} = 200$ GeV. Grey points: current analysis with 10 nb^{-1} [10]; red points: projection for 110 nb^{-1} . Error bars are statistical only.

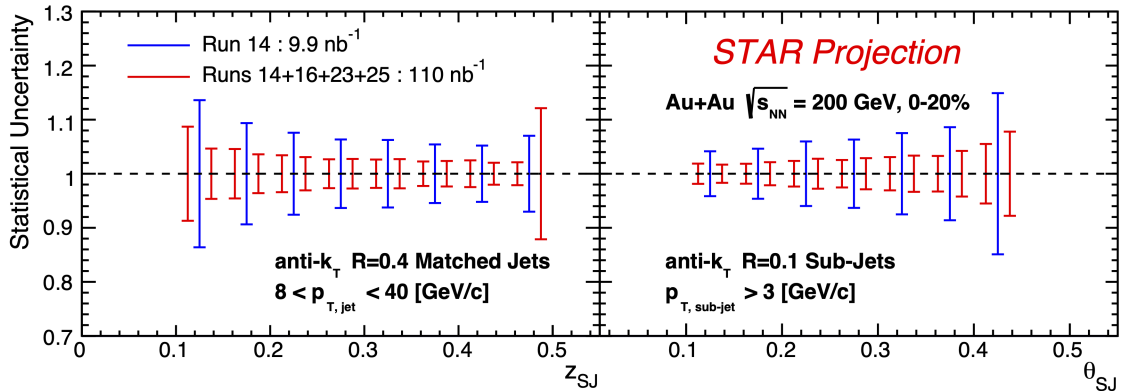


Figure 63: Two-panel figure showing statistical uncertainty for the two-subject observables in 0-20% central Au+Au collisions for 10 nb^{-1} in blue and projection for 110 nb^{-1} in red.

2223 observable due to uncorrelated background is small, and such acoplanarity measurements
 2224 are therefore strongly statistics-dominated [1, 241]. The grey points are from the current
 2225 analysis based on 10 nb^{-1} [10], whereas the red points correspond to 110 nb^{-1} . A marked
 2226 increase in measurement precision is projected, with corresponding qualitative increase in
 2227 physics impact. Similar improvements in precision for this observable are expected at the
 2228 LHC in Run 3, due to detector upgrades and enhanced machine luminosity [155].

2229 Jet measurement with a varying substructure metric

2230 An important facet of the third generation of STAR jet measurements is a systematic
 2231 exploration of parton energy loss based on controlled variation of the jet shower topology.
 2232 Jet evolution produces a unique pattern of radiation in both angle and momentum, and
 2233 jet substructure observables are a broad class of measurements of combinations of the jet
 2234 constituents' angle and/or momentum via algorithms or correlations. As the jet undergoes
 2235 interactions with the medium, jet substructure modification for a given jet energy (e.g. com-
 2236 paring the heavy-ion results to those in p+p collisions) has been used as a way to access the
 2237 microscopic properties of the medium. By selecting on jets based on their substructure, we
 2238 can study how a particular class of jets interacts with the medium to determine the effects
 2239 of e.g. color coherence, dead cone, etc. on parton-medium interactions. In other words, the
 2240 STAR jet program for Runs 23–25 will focus on jet substructure as a jet-tagger.

2241 Recent theory calculations have shown significant differences between energy loss signa-
 2242 tures for jets that are perceived by the medium as a single or multiple color charges [235].
 2243 Algorithms such as SoftDrop and sub-jets [244, 245] provide observables that correspond
 2244 to the splitting within jets via momentum fractions and an inherent angular scale which
 2245 then serve as a proxy for the resolution scale in the medium. This is often referred to as
 2246 coherent vs. de-coherent energy loss where the coherent length of the medium is related to
 2247 its temperature and \hat{q} [246]. By isolating population of jets based on their substructure,
 2248 one can directly probe energy loss for varying resolution scales. The integrated luminosity

2249 from Runs ‘23/‘25 datasets will not only provide a substantial increase in statistics in the
2250 current measurements of jet substructure, they also make the phase space available for rare
2251 processes such as wide angle emissions from high- p_T jets. This enables STAR to extend our
2252 current measurements of differential energy loss [2] to fine binning in the opening angles and
2253 momentum fractions, as shown in Fig. 63. The current resolution of $\delta\theta_{SJ} = 0.1$ [2] is predom-
2254 inantly due to statistical limitations in our older dataset sample. The significant increase in
2255 integrated luminosity for Runs 23-25, coupled with excellent tracking resolution of the STAR
2256 TPC will reduce the opening angles resolution to 0.025 and have significant population of
2257 jets where we can further identify and select jet topologies in both z and θ and study energy
2258 loss in a three-dimensional fashion. By extending to high energy splittings within jets, at
2259 varied opening angles, we can probe earlier formation times whereby vacuum-like emissions
2260 and medium induced radiations are expected to occur.

2261 STAR is uniquely situated to perform high impact differential measurements of parton
2262 energy loss starting from the unbiased, semi-inclusive jet population, to a topologically spe-
2263 cial population of jets, selected via jet substructure observables.

2264 Given the unique nature of jet-medium interactions at RHIC, with the jet and sub-jet
2265 scales sufficiently closer to the medium scale, the aforementioned measurements bolster the
2266 importance of the STAR jet program with the goal of extracting the microscopic properties
2267 of the QGP as outlined in the 2015 LRP.

3 Cold QCD Physics with $p^\uparrow p^\uparrow$ and $p^\uparrow + A$ Collisions at 510 and 200 GeV

The exploration of the fundamental structure of strongly interacting matter has always thrived on the complementarity of lepton scattering and purely hadronic probes. As the community eagerly anticipates the future Electron Ion Collider, an outstanding scientific opportunity remains to complete “must-do” measurements in p+p and $p+A$ physics during the final years of RHIC. These measurements will be essential if we are fully to realize the scientific promise of the EIC, by providing a comprehensive set of measurements in hadronic collisions that, when combined with future data from the EIC, will establish the validity and limits of factorization and universality. The Run-22 and Run-24 program outlined here will, on the one hand, lay the groundwork for the EIC, both scientifically and in terms of refining the experimental requirements of the physics program at the EIC, and thus are the natural next steps on the path to the EIC. On the other hand, while much of the physics in this program is unique to proton-proton and proton-nucleus collisions and offers discovery potential on its own, when combined with data from the EIC it will provide a broad foundation to a deeper understanding of fundamental QCD.

The separation between the intrinsic properties of hadrons and interaction-dependent dynamics, formalized by the concept of factorization, is a cornerstone of QCD and largely responsible for the predictive power of the theory in many contexts. While this concept and the associated notion of universality of the quantities that describe hadron structure have been successfully tested for unpolarized and, to a lesser extent, longitudinally polarized parton densities, its experimental validation remains an unfinished task for much of what the EIC is designed to study – the three-dimensional structure of the proton and the physics of dense partonic systems in heavy nuclei. To establish the validity and limits of factorization and universality, it is essential to have data from *both* lepton-ion and proton-ion collisions, with experimental accuracy that makes quantitative comparisons meaningful.

Beginning in Run-22, STAR will be in a unique position to provide this essential p+p and $p + A$ data. A full suite of forward detectors will be installed, providing excellent charged-particle tracking at high pseudorapidity ($2.5 < \eta < 4$) for the first time, coupled with both electromagnetic and hadronic calorimetry. This will enable STAR to explore the interesting regimes of high- x (largely valence quark) and low- x (primarily gluon) partonic physics with unparalleled precision. In addition, mid-rapidity detector upgrades motivated primarily by the BES-II program – the iTPC, eTOF, and EPD systems – will substantially extend STAR’s already excellent kinematic reach and particle identification capabilities beyond those that existed during previous p+p and $p + A$ runs.

For the case of p+p spin physics, it’s important to recognize the complementary roles that will be played by Run-22 at 510 GeV and Run-24 at 200 GeV. The combination of 510 GeV p+p collisions and the STAR Forward Upgrade will provide access to forward jet physics at perturbative scales, thereby enabling measurements at the highest and lowest x values. In parallel, mid-rapidity measurements at 510 and, especially, 200 GeV will interpolate between the high and low x values, with significant overlaps to probe evolution effects

2309 and provide cross-checks. Together, the two runs will allow STAR to measure fundamental
2310 proton properties, such as the Sivers and transversity distributions, over nearly the entire
2311 range $0.005 < x < 0.5$.

2312 Run-24 will also provide outstanding opportunities to probe fundamental questions re-
2313 garding QCD in cold nuclear matter. The STAR Forward Upgrade will enable an extensive
2314 suite of measurements probing the quark-gluon structure of heavy nuclei and the regime of
2315 low- x non-linear gluon dynamics, as predicted by saturation models. STAR will also ex-
2316 plore how a nucleus, serving as a color filter, modifies the propagation, attenuation, and
2317 hadronization of colored quarks and gluons.

2318 For these reasons, STAR requests at least 16 weeks of polarized $p+p$ data-taking at $\sqrt{s} =$
2319 510 GeV in Run-22. All data taking will involve proton beams polarized transversely relative
2320 to their momentum direction in order to focus on those observables where factorization,
2321 universality, and/or evolution remain open questions, with spins aligned either vertically or
2322 radially at the STAR IR (still to be determined through more detailed simulation studies).
2323 Based on the latest guidance from CAD, and mindful of ‘lessons learned’ in previous $p + p$
2324 runs at full energy, we will ask for luminosity-leveling of the collision rate to maximize the
2325 efficiency of our main tracking detectors. Assuming we will have running conditions similar to
2326 those achieved in Run-17, we expect to sample at least 400 pb^{-1} for our rare / non-prescaled
2327 triggers.

2328 STAR also requests at least 11 weeks of polarized $p + p$ data-taking at $\sqrt{s} = 200 \text{ GeV}$
2329 and 11 weeks of polarized $p+\text{Au}$ data-taking at $\sqrt{s_{NN}} = 200 \text{ GeV}$ during Run-24. Similar
2330 to Run-22, all of the running will involve transversely polarized protons, with the choice
2331 between vertical or radial polarization to be determined during the coming year. Based on
2332 recent (08-21-20) C-AD guidance, we expect to sample at least 235 pb^{-1} of $p+p$ collisions
2333 and 1.3 pb^{-1} of $p+\text{Au}$ collisions. These totals represent 4.5 times the luminosity that STAR
2334 sampled during transversely polarized $p + p$ collisions in Run-15, and 3 times the luminosity
2335 that STAR sampled during transversely polarized $p+\text{Au}$ collisions in Run-15.

2336 3.1 Run-22 Request for $p^\uparrow p^\uparrow$ Collisions at 510 GeV

2337 3.1.1 Inclusive transverse spin asymmetries at forward rapidities

2338 The experimental study of spin phenomena in nuclear and particle physics has a long history
2339 of producing important, and often surprising, results. Attempts to understand such data
2340 have pushed the field forward, forcing the development of both new theoretical frameworks
2341 and new experimental techniques. Recent and ongoing detector upgrades at STAR, at mid-
2342 and forward-rapidity, coupled with the versatility of RHIC, will allow us to gain new insights
2343 into long-standing puzzles, and to probe more deeply the complexities of emergent behavior
2344 in QCD.

2345 Results from PHENIX and STAR have shown that large transverse single-spin asym-
2346 metries (TSSA) for inclusive hadron production, first seen in $p+p$ collisions at fixed-target
2347 energies and modest p_T , extend to the highest RHIC center-of-mass energies, $\sqrt{s} = 500 \text{ GeV}$,
2348 and surprisingly large p_T . Figure 64 summarizes the world data for the inclusive pion asym-

2349 metries A_N as a function of Feynman- x . The asymmetries are seen to be nearly independent
 2350 of \sqrt{s} over the very wide range of roughly 5 to 500 GeV.

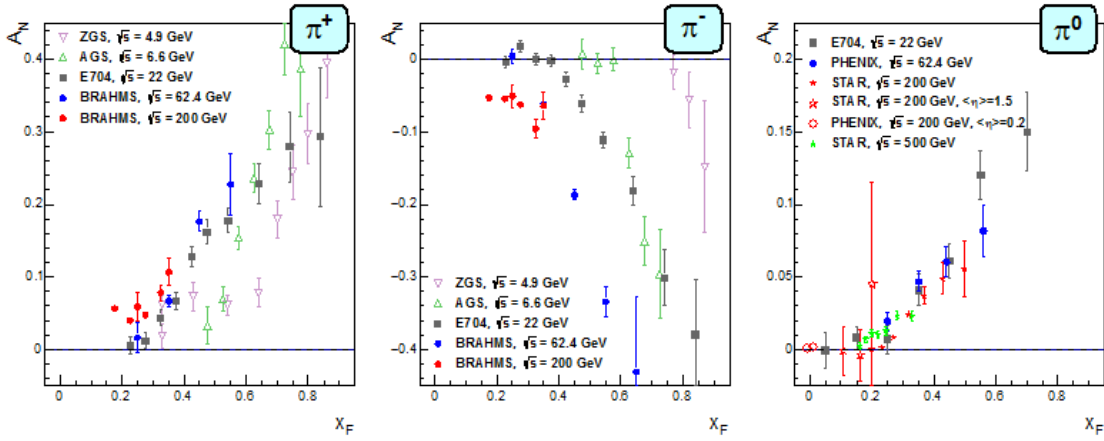


Figure 64: Transverse single-spin asymmetry A_N measurements for charged and neutral pions at different center-of-mass energies as a function of Feynman- x .

2351 To understand the observed TSSAs, one needs to go beyond the conventional leading-
 2352 twist (twist-2) collinear parton picture for the hard-scattering processes. Two theoretical
 2353 formalisms have been developed to try to explain these sizable asymmetries in the QCD
 2354 framework: transverse-momentum-dependent (TMD) parton distribution and fragmentation
 2355 functions, such as the Sivers and Collins functions; and transverse-momentum-integrated
 2356 (collinear) quark-gluon-quark correlations, which are twist-3 distributions in the initial state
 2357 proton or in the fragmentation process. For many of the experimentally accessible spin
 2358 asymmetries, several of these functions can contribute, and need to be disentangled in order
 2359 to understand the experimental data in detail, in particular the observed p_T dependence.
 2360 These functions manifest their spin dependence either in the initial state—for example, the
 2361 Sivers distribution and its twist-3 analog, the Efremov-Teryaev-Qiu-Sterman (ETQS) func-
 2362 tion [247]—or in the final state via the fragmentation of polarized quarks, such as in the
 2363 Collins function and related twist three function $\hat{H}_{FU}(z, z_z)$.

2364 Incorporating the fragmentation term within the collinear twist-3 approach demonstrated
 2365 the ability of this formalism to describe the large values of A_N for π^0 production observed at
 2366 RHIC [248]. In this work, the relevant (non-pole) 3-parton collinear fragmentation function
 2367 $\hat{H}_{FU}(z, z_z)$ was fit to the RHIC data. The so-called soft-gluon pole term, involving the ETQS
 2368 function $T_{q,F}(x_1, x_2)$, was also included by fixing $T_{q,F}$ through its well-known relation to the
 2369 TMD Sivers function f_{1T}^\perp . The authors obtained a very good description of the data due to
 2370 the inclusion of the non-pole fragmentation function and based on this work they were able
 2371 to make predictions for π^+ and π^- production asymmetries A_N at the forward rapidities
 2372 covered by the STAR upgrades, $2.5 < \eta < 4$. The results are shown in Fig. 65 for $\sqrt{s} = 200$
 2373 and 500 GeV for two rapidity ranges, $2 < \eta < 3$ and $3 < \eta < 4$.

2374 In Run-22, with the full suite of forward tracking detectors and calorimetry installed,
 2375 STAR will for the first time be able to map out inclusive charged-hadron asymmetries up to

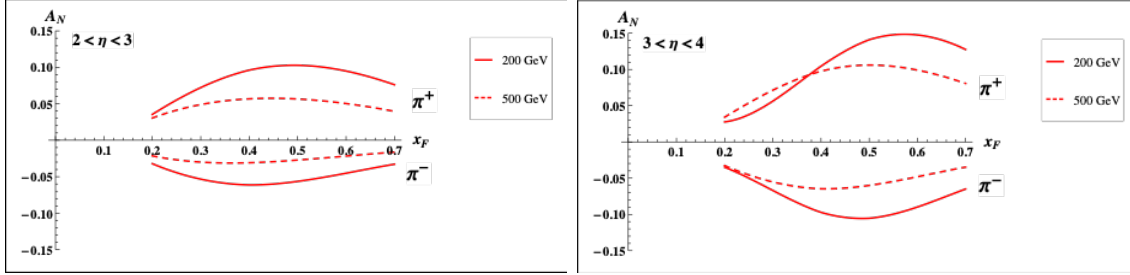


Figure 65: Predictions for A_N for π^+ and π^- production over the ranges $2 < \eta < 3$ (left) and $3 < \eta < 4$ (right) at $\sqrt{s} = 200$ GeV (solid lines) and 500 GeV (dashed lines). The $\sqrt{s} = 200$ GeV BRAHMS A_N data for charged pions cover up to x_F of 0.3.

2376 the highest energies achievable at RHIC and at these forward rapidities. It would be very
 2377 interesting to confirm that these asymmetries are indeed largely independent of center-of-
 2378 mass energy. The measurements of A_N for charged hadrons, together with analogous data
 2379 (from Run-22 as well as previous STAR runs) on A_N for direct photons and neutral pions,
 2380 should provide the best data set in the world to constrain the evolution and flavor dependence
 2381 of the twist-3 ETQS distributions and to determine if the 3-parton collinear fragmentation
 2382 function H_{FU} is the main driver of the large forward inclusive asymmetries.

2383 3.1.2 Sivers and Efremov-Teryaev-Qiu-Sterman Function

2384 There is great theoretical interest in testing the relation between the ETQS correlation
 2385 functions and the Sivers function. As discussed above, both the Sivers and the ETQS
 2386 functions encapsulate partonic spin correlations within the proton, but they are formally
 2387 defined in different frameworks. While the Sivers function is a TMD quantity that depends
 2388 explicitly on spin-dependent transverse partonic motion k_T , the ETQS function is a twist-3
 2389 collinear distribution, in which SSAs are generated through soft collinear gluon radiation

2390 Measurements of forward jet production from the ANDY collaboration [249] indicated
 2391 rather small asymmetries. This was argued to be consistent with the idea that the twist-3
 2392 parton correlation functions for up and down valence quarks should cancel, because their
 2393 behavior reflects the Sivers functions extracted from fits to the SIDIS data that demonstrate
 2394 opposite sign, but equal magnitude, up and down quark Sivers functions. Preliminary STAR
 2395 results on charge-tagged dijets at mid-rapidity (see Fig. 29) support this interpretation, with
 2396 the caveat that the measured observable (a spin-dependent $\langle k_T \rangle$) is defined in the TMD, and
 2397 not the twist-3, framework.

2398 To better test quantitatively the relation between the two regimes, one can measure spin
 2399 asymmetries for jets which are *intentionally* biased towards up or down quark jets via detec-
 2400 tion of a high- z charged hadron within the jet. Higher-twist calculations of jet asymmetries
 2401 based on the Sivers function predict sizeable effects for these flavor-enhanced jets. With the
 2402 suite of new forward detectors installed at STAR, full jet reconstruction, along with iden-
 2403 tification of a high- z hadron of known charge sign, will be possible at high pseudorapidity.
 2404 Using realistic jet smearing in a forward calorimeter and tracking system, and requiring a

2405 charged hadron with $z > 0.5$, the asymmetries can be separated and compared to the pre-
 2406 dictions for the Sivers function based on current SIDIS data. The expected uncertainties,
 2407 plotted at the predicted values, can be seen in Fig. 66. Dilutions by underlying event and
 2408 beam remnants were taken into account. The simulations have assumed only an integrated
 2409 luminosity of 100 pb^{-1} at $\sqrt{s} = 200 \text{ GeV}$, which is significantly lower than what is currently
 2410 expected for a 200 GeV polarized p+p run in 2024. The same measurement is possible at
 2411 500 GeV.

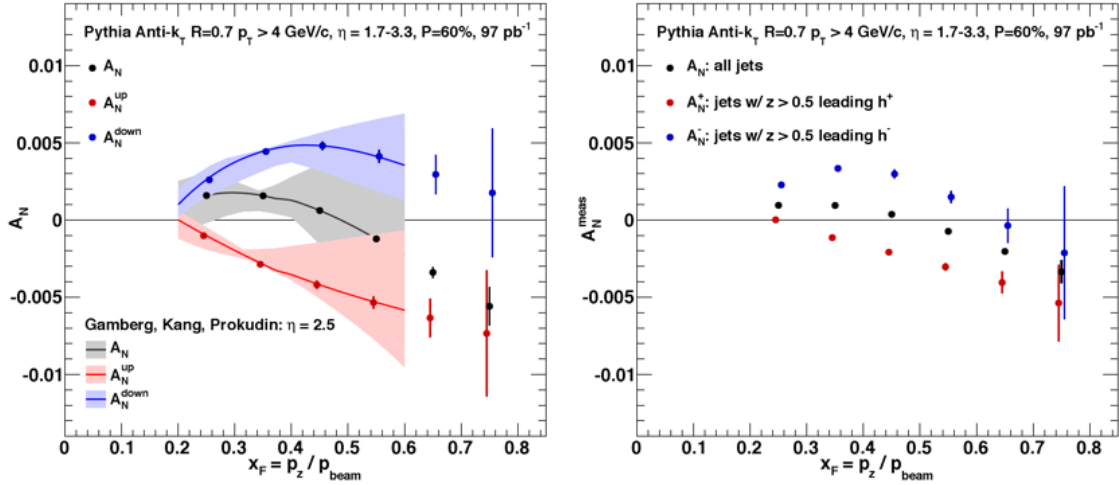


Figure 66: Left: up quark (red points), down quark (blue points) and all jet (black points) single spin asymmetries as a function of x_F as calculated by the ETQS based on the SIDIS Sivers functions. Right: Expected experimental sensitivities for jet asymmetries tagging in addition a positive hadron with z above 0.5 (red points), a negative hadron with z above 0.5 (blue points) or all jets (black) as a function of x_F . Note: these figures are for 200 GeV center-of-mass energy proton collisions – the 500 GeV results are expected to be qualitatively similar.

2412 In a TMD framework, the Sivers effect manifests itself as a correlation (a triple product)
 2413 between the transverse momentum of a parton (\vec{k}_T) with momentum fraction x , and the
 2414 transverse spin (\vec{S}) of a polarized proton moving in the longitudinal (\vec{p}) direction. Thus,
 2415 for transversely polarized protons, the Sivers effect probes whether the k_T of the constituent
 2416 quarks is preferentially oriented in a direction perpendicular to both the proton momentum
 2417 and its spin. Momentum conservation then implies that the two jets in the final state will
 2418 not emerge back-to-back on average, but instead will ‘tilt’ in the direction of the summed
 2419 k_T of the initial state partons. Moreover, the (average) tilt of interest will reverse direction
 2420 under a ‘flip’ of the proton spin; a spin-dependent $\langle k_T \rangle$ can then be extracted by associating
 2421 the azimuthal opening angle of the jet pair with this tilt.

2422 STAR carried out an earlier measurement of this transverse single-spin asymmetry using
 2423 a dijet dataset with $\sim 1 \text{ pb}^{-1}$ of integrated luminosity [113], and found it to be consistent with
 2424 zero within 2σ . An ongoing and much improved analysis has been described in Sect. 1.3.3.
 2425 Perhaps most significantly, the jets were sorted according to their net charge Q , calculated
 2426 by summing the signed momentum of all particle tracks with $p > 0.8 \text{ GeV}$, to minimize

2427 underlying event contributions, yielding jet samples with enhanced contributions from u
 2428 quarks (positive Q) and d quarks (negative Q), with a large set near $Q = 0$ dominated by
 2429 gluons. Simple kinematics allow for conversion from the spin-dependent ‘tilt’ of the dijet
 2430 pair to a value of k_T on an event-by-event basis; these are then sorted by the Q of the jet
 2431 and binned by the summed pseudorapidities of the outgoing jets, $\eta^{\text{total}} \equiv \eta_3 + \eta_4$. Because
 2432 the contributions of different partons (u , d , all else) to $\langle k_T \rangle$ vary with both Q and also η^{total} ,
 2433 in a way that can be estimated robustly using simulation, the data can be inverted to yield
 2434 values of $\langle k_T \rangle$ for the individual partons, though with coarser binning in η^{total} .

2435 With the new forward detectors in place, along with the enhanced reach in η afforded by
 2436 the iTPC, this technique can be expanded in Run-22 to cover pseudorapidities at STAR from
 2437 roughly -1 to +4, though with a gap at $1.5 < \eta < 2.5$. Despite this gap, values of $\langle k_T \rangle$ can be
 2438 extracted for u and d quarks for η^{total} ranging from ~ -1.5 to as high as 7 with reasonable
 2439 statistics. This latter regime will probe $2 \rightarrow 2$ hard scattering events in which $x_1 \gg x_2$,
 2440 *i.e.*, a sample enriched in valence quarks interacting with low- x gluons. Such measurements,
 2441 exploiting the full kinematic reach of STAR, will not only allow precise determinations of
 2442 the average transverse partonic motion, $\langle k_T \rangle$, exhibited by individual partonic species in
 2443 the initial state, but will provide important information on the x dependence of the proton
 2444 Sivers functions.

2445 Collisions at $\sqrt{s} = 510$ GeV will also allow STAR to continue our successful program
 2446 to study the evolution and sign change of the Sivers function. By focusing on interactions
 2447 in which the final state involves only weakly interacting particles, and hence the transverse
 2448 partonic motion (in a TMD framework) or the collinear gluon radiation (in twist-3) must be
 2449 in the initial state, one can test for the predicted sign change in A_N relative to interactions
 2450 in which these terms must appear in the final state, such as SIDIS measurements. The
 2451 improved tracking capabilities provided by the iTPC upgrade will allow us to push our mid-
 2452 rapidity W^\pm and Z^0 measurements to larger rapidity $y_{W/Z}$, a regime where the asymmetries
 2453 are expected to increase in magnitude and the anti-quark Sivers’ functions remain largely
 2454 unconstrained. Figure 67 demonstrates the expected precision of asymmetry measurements
 2455 after data from the 2017 run has been fully analyzed. In addition to the noted extension
 2456 of our kinematic reach, an additional 16 or more weeks of beam time at $\sqrt{s} = 510$ GeV in
 2457 Run-22 would increase our data set by more than a factor of 2. This experimental accuracy
 2458 would significantly enhance the quantitative reach of testing the limits of factorization and
 2459 universality in lepton-proton and proton-proton collisions.

2460 3.1.3 Transversity, Collins Function and Interference Fragmentation Function

2461 A complete picture of nucleon spin structure at leading twist must include contributions
 2462 from the unpolarized and helicity distributions, as well as those involving transverse po-
 2463 larization, such as the transversity distribution [252–254]. The transversity distribution
 2464 can be interpreted as the net transverse polarization of quarks within a transversely polar-
 2465 ized proton. The difference between the helicity and transversity distributions for quarks
 2466 and antiquarks provides a direct, x -dependent connection to nonzero orbital angular mo-
 2467 mentum components in the wave function of the proton [255]. Recently, the first lattice

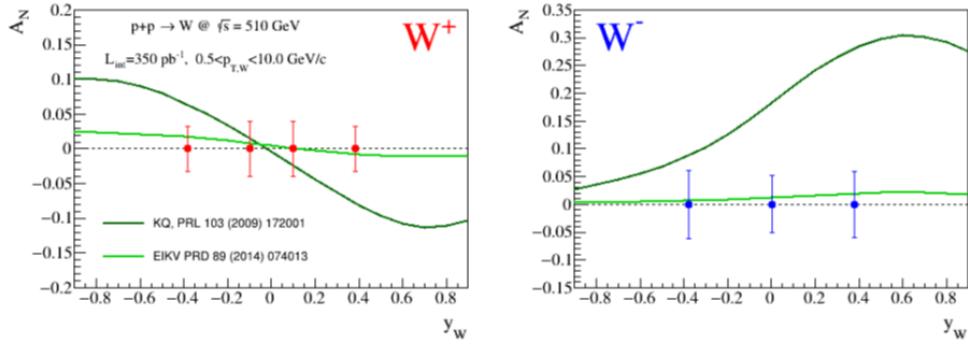


Figure 67: Projected uncertainties for transverse single-spin asymmetries of W^\pm bosons as functions of their rapidity for a delivered integrated luminosity of 350 pb^{-1} and an average beam polarization of 55%. The dark and light green lines are theoretical predictions from the KQ [250] and EIKV [251] groups, respectively, folding in data on the sea-quark Sivers functions.

2468 QCD calculation of the transversity distribution has been performed [256]. In addition,
 2469 the measurement of transversity has received substantial interest as a means to access the
 2470 tensor charge of the nucleon, defined as the integral over the valence quark transversity:
 2471 $\delta q^a = \int_0^1 [\delta q^a(x) - \delta \bar{q}^a(x)] dx$ [253, 257]. Measuring the tensor charge is very important for
 2472 several reasons. First, it is an essential and fundamental quantity to our understanding of
 2473 the spin structure of the nucleon. Also, the tensor charge can be calculated on the lattice
 2474 with comparatively high precision, due to the valence nature of transversity, and hence is
 2475 one of the few quantities that allow us to compare experimental results on the spin structure
 2476 of the nucleon directly to *ab initio* QCD calculations. Finally, the tensor charge describes
 2477 the sensitivity of observables in low-energy hadronic reactions to beyond the standard model
 2478 physics processes with tensor couplings to hadrons. Examples are experiments with ultra-
 2479 cold neutrons and nuclei.

2480 Transversity is difficult to access due to its chiral-odd nature, requiring the coupling of
 2481 this distribution to another chiral-odd distribution. Semi-inclusive deep-inelastic scattering
 2482 (SIDIS) experiments have successfully probed transversity through two channels: asym-
 2483 metric distributions of single pions, convoluting the TMD transversity distribution with
 2484 the TMD Collins fragmentation function, and azimuthally asymmetric distributions of di-
 2485 hadrons, coupling transversity to the so-called “interference fragmentation function” (IFF)
 2486 in the framework of collinear factorization. Yet in spite of a wealth of lepton-scattering
 2487 data, the kinematic reach of existing SIDIS experiments limits the precision with which the
 2488 proton’s transversity can be extracted, as the range of Bjorken- x values that can be accessed
 2489 does not extend above $x \sim 0.3$

2490 In hadronic collisions, the k_T integrated quark transversity distribution may be accessed
 2491 via two channels. The first is the single spin asymmetry of the azimuthal distribution of
 2492 hadrons in high energy jets [109]. In the jet+hadron channel, the collinear transversity
 2493 distribution couples to the TMD Collins function [109, 110]. This makes p+p collisions a
 2494 more direct probe of the Collins fragmentation function than Collins asymmetries in SIDIS

2495 [109], where a convolution with the TMD transversity distribution enters. This also makes
 2496 the Collins asymmetry in p+p collisions an ideal tool to explore the fundamental QCD
 2497 questions of TMD factorization, universality, and evolution. The second channel is the
 2498 single spin asymmetry of pion pairs, where transversity couples to the collinear interference
 2499 fragmentation function [258]. STAR mid-rapidity IFF data [259] have been included in the
 2500 first extraction of transversity from SIDIS and proton-proton IFF asymmetries [260].

2501 The universality of TMD PDFs and fragmentation functions in p+p collisions has been an
 2502 open question. General arguments [261, 262] have shown that factorization can be violated
 2503 in hadron-hadron collisions for TMD PDFs like the Sivers function, though very recent
 2504 calculations indicate the violations might be quite small [263, 264]. In contrast, while there
 2505 is no general proof that the Collins effect in p+p collisions is universal to all orders, explicit
 2506 calculations [109, 110, 265, 266] have shown that diagrams like those that violate factorization
 2507 of the Sivers function make no contribution to the Collins effect at the one- or two-gluon
 2508 exchange level, thereby preserving its universality at least to that level.

2509 Comparisons of the transversity distributions extracted from the Collins and IFF channels
 2510 will allow STAR to study the size and nature of any factorization breaking effects for TMD
 2511 observables in hadronic collisions. Likewise, comparisons with the transversity, Collins and
 2512 IFF distributions extracted from SIDIS collisions will shed light on universality and constrain
 2513 evolution effects. The measurement of evolution effects in TMD distributions is particularly
 2514 important because, unlike the collinear case, TMD evolution contains a non-perturbative
 2515 component that cannot be calculated directly. Measurements at \sqrt{s} of 200 and 510 GeV will
 2516 provide additional experimental constraints on evolution effects and provide insights into the
 2517 size and nature of TMD observables at the future Electron-Ion Collider.

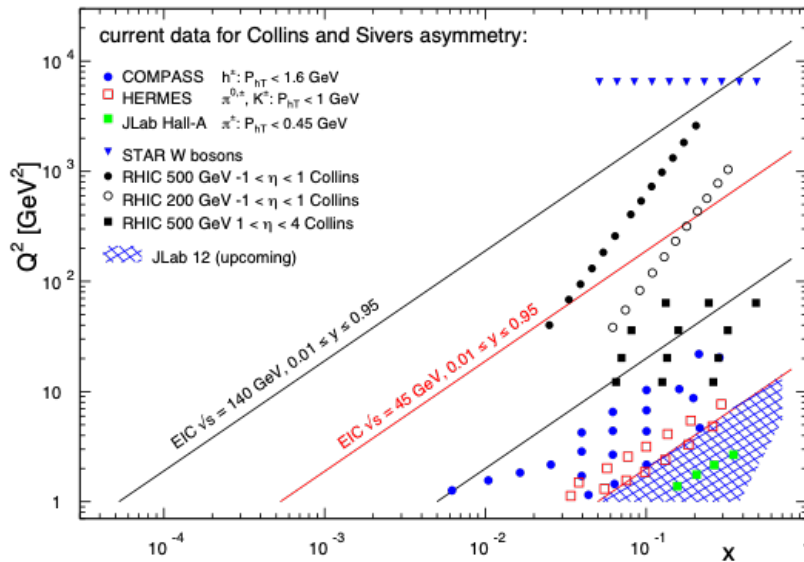


Figure 68: $x - Q^2$ coverage of RHIC measurements compared to existing Collins and Sivers effect measurements in SIDIS and the future coverage of the EIC.

2518 Extending measurements of di-hadron and Collins asymmetries to the forward direction

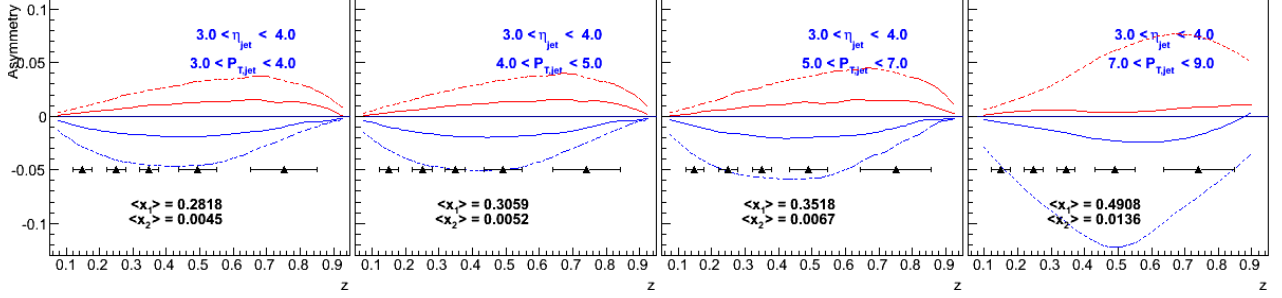


Figure 69: Expected h^- Collins asymmetry uncertainties at $3 < \eta < 4$ (black points) from a sampled luminosity of 268 pb^{-1} at $\sqrt{s} = 510 \text{ GeV}$, compared to positive (red) and negative (blue) pion asymmetries based on the Torino extraction (full lines) and the Soffer bound (dashed lines) as a function of hadron z for bins in jet p_T . Most uncertainties are smaller than the height of the triangles.

2519 during Run-22 will allow access to transversity in the region $x > 0.3$. This valence quark
 2520 region is not currently probed by any experiments and is essential for the determination of
 2521 the tensor charge, which receives 70% of its contributions from $0.1 < x < 1.0$. In addition,
 2522 probing transversity in p+p collisions also provides better access to the d -quark transversity
 2523 than is available in SIDIS, due to the fact that there is no charge weighting in the hard
 2524 scattering QCD $2 \rightarrow 2$ process in p+p collisions. This is a fundamental advantage of p+p
 2525 collisions, as any SIDIS measurement of the d -quark transversity has to be on a bound
 2526 system, *e.g.* He-3, which ultimately requires nuclear corrections to extract distributions.
 2527 The high scale we can reach in 500 GeV collisions at RHIC has allowed STAR [267] to
 2528 demonstrate, for the first time, that previous SIDIS measurements at low scales are in fact
 2529 accessing the nucleon at leading twist. Figure 68 shows the $x - Q^2$ coverage spanned by
 2530 the RHIC measurements compared to the future EIC, JLab-12, and the current SIDIS world
 2531 data.

2532 Another fundamental advantage of p+p collisions is the ability to access gluons di-
 2533 rectly. While gluons cannot be transversely polarized in a transversely polarized spin 1/2
 2534 hadron, they can be linearly polarized. Similarly, there exists an equivalent of the Collins
 2535 fragmentation function for the fragmentation of linearly polarized gluons into unpolarized
 2536 hadrons [268]. The linear polarization of gluons is a largely unexplored phenomenon, but it
 2537 has been a focus of recent theoretical work, in particular due to the relevance of linearly po-
 2538 larized gluons in unpolarized hadrons for the p_T spectrum of the Higgs boson measured at the
 2539 LHC. Polarized proton collisions with $\sqrt{s} = 510 \text{ GeV}$ at RHIC, in particular for asymmetric
 2540 parton scattering if jets are detected in the backward direction, are an ideal place to study
 2541 the linearly polarized gluon distribution in polarized protons. (Note that the distributions of
 2542 linearly polarized gluons inside an unpolarized and a polarized proton provide independent
 2543 information). A first measurement of the ‘‘Collins-like’’ effect for linearly polarized gluons
 2544 has been done by STAR with data from Run-11 [267], providing constraints on this function
 2545 for the first time.

2546 Figure 69 shows projected uncertainties for Collins asymmetries at 510 GeV with the

2547 Forward Upgrade during Run-22. As indicated on the figure, jets with $3 < \eta < 4$ and
 2548 $3 < p_T < 9$ GeV/ c will explore transversity in the important region $0.3 < x < 0.5$ that
 2549 has not yet been probed in SIDIS. A realistic momentum smearing of final state hadrons as
 2550 well as jets in this rapidity range was assumed and dilutions due to beam remnants (which
 2551 become substantial at rapidities close to the beam) and underlying event contributions have
 2552 been taken into account. As no dedicated particle identification at forward rapidities will be
 2553 available for these measurements, only charged hadrons were considered. This mostly reduces
 2554 the expected asymmetries due to dilution by protons (10-14%) and a moderate amount of
 2555 kaons (12-13%). As anti-protons are suppressed compared to protons in the beam remnants,
 2556 especially the negative hadrons can be considered a good proxy for negative pions ($\sim 78\%$
 2557 purity according to PYTHIA6). Given their sensitivity to the down quark transversity via
 2558 favored fragmentation, they are particularly important since SIDIS measurements, due to
 2559 their electromagnetic interaction, are naturally dominated by up-quarks. We have estimated
 2560 our statistical uncertainties based on an accumulated luminosity of 268 pb^{-1} , which leaves
 2561 nearly invisible uncertainties after smearing. These expected uncertainties are compared to
 2562 the asymmetries obtained from the transversity extractions based on SIDIS and Belle data
 2563 [269] as well as from using the Soffer positivity bound for the transversity PDF [270]. More
 2564 recent global fits have slightly different central up and down quark transversity distributions.
 2565 But due to the lack of any SIDIS data for $x > 0.3$, the upper uncertainties are compatible
 2566 with the Soffer bounds. This high- x coverage will give important insights into the tensor
 2567 charge, which is essential to understand the nucleon structure at leading twist.

2568 Although the studies presented here are for the Collins asymmetries, the resulting sta-
 2569 tistical uncertainties will be similar for other measurements using azimuthal correlations of
 2570 hadrons in jets. One important example is the measurement of “Collins-like” asymmetries to
 2571 access the distribution of linearly polarized gluons. As described earlier, the best kinematic
 2572 region to access this distribution is at backward angles with respect to the polarized proton
 2573 and at small jet p_T . Figure 69 shows that a high precision measurement of the distribution
 2574 of linearly polarized gluons down to $x \sim 0.005$ will be performed concurrently.

2575 It is also important to recognize that these hadron-in-jet measurements with the STAR
 2576 Forward Upgrade will provide very valuable experience detecting jets close to beam rapidity
 2577 that will inform the planning for future jet measurements in similar kinematics at the EIC.

2578 While the STAR Forward Upgrade will provide sensitivity to transversity to the highest
 2579 x , concurrent mid-rapidity measurements (see Fig. 68) will provide the most precise informa-
 2580 tion as a function of x , z , j_T , and Q^2 to probe questions of TMD factorization, universality,
 2581 and evolution. The left panel of Fig. 70 shows published STAR measurements of the Collins
 2582 asymmetry vs. pion z in 500 GeV p+p collisions from 2011 [267]. The results, which repre-
 2583 sented the first ever observation of the Collins effect in p+p collisions, are consistent at the
 2584 2-sigma level with model predictions, with and without TMD evolution, derived from fits to
 2585 e^+e^- and SIDIS data [109,271]. However, greater precision is clearly necessary for a detailed
 2586 universality test, as well as to set the stage for the EIC.

2587 In 2017, STAR sampled about 14 times the luminosity that we recorded in 2011. In Run-
 2588 22, we propose to record another data set equivalent to 16 times the sampled luminosity from

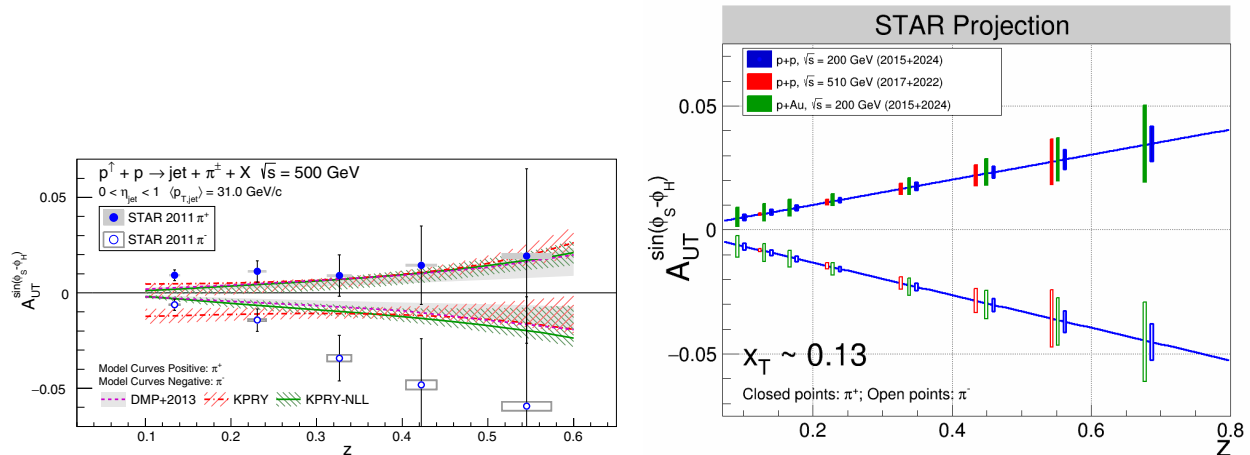


Figure 70: The left panel shows STAR measurements of the Collins asymmetry vs. pion z in 500 GeV p+p collisions from Run-11, compared to several model calculations. See [267] for details. The right panel shows projected statistical uncertainties for STAR Collins asymmetry measurements at $0 < \eta < 0.9$ in p+p at $\sqrt{s} = 200$ and 510 GeV and p+Au at $\sqrt{s_{NN}} = 200$ GeV. The points have arbitrarily been drawn on the solid lines, which represent simple linear fits to the STAR preliminary 200 GeV p+p Collins asymmetry measurements from 2015. (Note that only one bin is shown spanning $0.1 < z < 0.2$ for 510 GeV p+p, whereas three bins are shown covering the same z range for the 200 GeV measurements.)

2589 2011. Furthermore, during Run-22 the iTPC will improve the dE/dx particle identification
 2590 compared to the previous years. Studies using the dE/dx distributions seen in our 200 GeV
 2591 p+p data from 2015 and the actual dE/dx resolution improvements that have been achieved
 2592 during BES-II indicate the iTPC will yield a 20 – 25% increase in the effective figure-of-
 2593 merit for pions with $|\eta| < 0.9$. The right-hand panel of Fig. 70 shows the projected STAR
 2594 statistical uncertainties for the Collins asymmetry at $0 < \eta < 0.9$ in 510 GeV p+p collisions
 2595 once the Run-17 and Run-22 data sets are fully analyzed. It's also important to recognize
 2596 that the iTPC will also enable STAR to measure the Collins asymmetry over the region
 2597 $0.9 < \eta < 1.3$ during Run-22, in addition to the projections that are shown in Fig. 70.

2598 Statistical improvements from 2011 data [259] to 2017+'22 data comparable to those
 2599 shown for the Collins effect in Fig. 70 are also expected for mid-rapidity measurements of
 2600 transversity in 510 GeV p+p collisions using IFF asymmetries.

2601 3.1.4 Spatial Imaging of the Nucleon

2602 Diffractive and Ultra Peripheral processes at RHIC are an essential tool that can elucidate
 2603 the origin of single-spin asymmetries in polarized p+p collisions and access the orbital motion
 2604 of partons inside the proton. Also at an EIC diffractive processes have been identified as the
 2605 golden tool to study several key physics programs

- 2606 • What is the spatial distribution of quarks and gluons inside the nucleon?

2607 • What is the role of orbital motion of sea quarks and gluons in building the nucleon
2608 spin?

2609 • Saturation in nuclei.

2610 **Diffraction:** The essential characteristics of diffraction in QCD are summarized by two
2611 facts:

2612 • The event is still called diffractive if there is a rapidity gap. Due to the presence
2613 of a rapidity gap, the diffractive cross-section can be thought of as arising from an
2614 exchange of several partons with zero net color between the target and the projectile.
2615 In high-energy scattering, which is dominated by gluons, this color neutral exchange
2616 (at the lowest order) consists of at least two exchanged gluons. This color singlet
2617 exchange has historically been called the pomeron, which had a specific interpretation
2618 in Regge theory. A crucial question in diffraction is the nature of the color neutral
2619 exchange between the protons. This interaction probes, in a novel fashion, the nature
2620 of confining interactions within hadrons.

2621 • The proton/nuclear target is not always an opaque “black disk” obstacle of geometric
2622 optics. A projectile that interacts more weakly due to color-screening and asymptotic
2623 freedom is likely to produce a different diffractive pattern from a larger, more strongly
2624 interacting, projectile.

2625 HERA discovered that 15% of the total ep cross-section is given by diffractive events
2626 (for details see [272] and references therein), basically independent of kinematics. At RHIC
2627 center-of-mass energies diffractive scattering events constitute $\sim 25\%$ of the total inelastic
2628 p+p cross-section [273]. As described above diffraction is defined as an interaction that
2629 is mediated by the exchange of the quantum numbers of the vacuum, as shown in Fig. 71.
2630 Experimentally these events can be characterized by the detection of a very forward scattered
2631 proton and jet (singly diffractive) or two jets (doubly diffractive) separated by a large rapidity
2632 gap. Central diffraction, where two protons, separated by rapidity gaps, are reconstructed
2633 along with a jet at mid-rapidity, is also present, but suppressed compared to singly and
2634 doubly diffractive events. To date, there have been no data in p+p collisions studying spin
2635 effects in diffractive events at high \sqrt{s} apart from measuring single spin asymmetries in
2636 elastic p+p scattering [274–277].

2637 A discovery of large transverse single spin asymmetries in diffractive processes would
2638 open a new avenue to study the properties and understand the nature of the diffractive
2639 exchange in p+p collisions. One of the primary observables of STAR to access transverse
2640 spin phenomena has been forward neutral pion production in transversely polarized p+p
2641 collisions at both $\sqrt{s} = 200$ and 500 GeV. Figure 31 shows the isolated and non-isolated
2642 transverse single spin asymmetries A_N for π^0 detected in the STAR FMS at $2.5 < \eta < 4.0$
2643 as a function of x_F .

2644 All these observations might indicate that the underlying subprocess causing a significant
2645 fraction of the large transverse single spin asymmetries in the forward direction are not

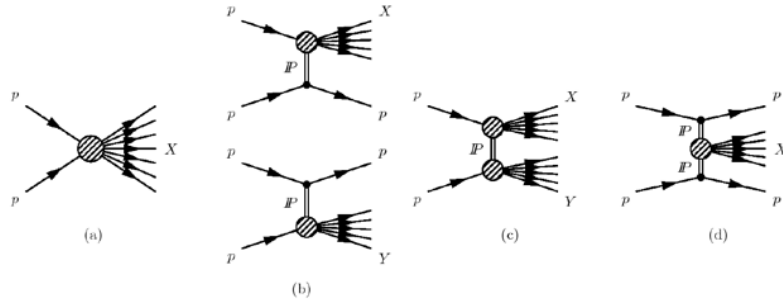


Figure 71: Schematic diagrams of (a) nondiffractive, $pp \rightarrow X$, (b) singly diffractive, $pp \rightarrow Xp$ or $pp \rightarrow pY$, (c) doubly diffractive, $pp \rightarrow XY$, and (d) centrally diffracted, $pp \rightarrow pXp$, events.

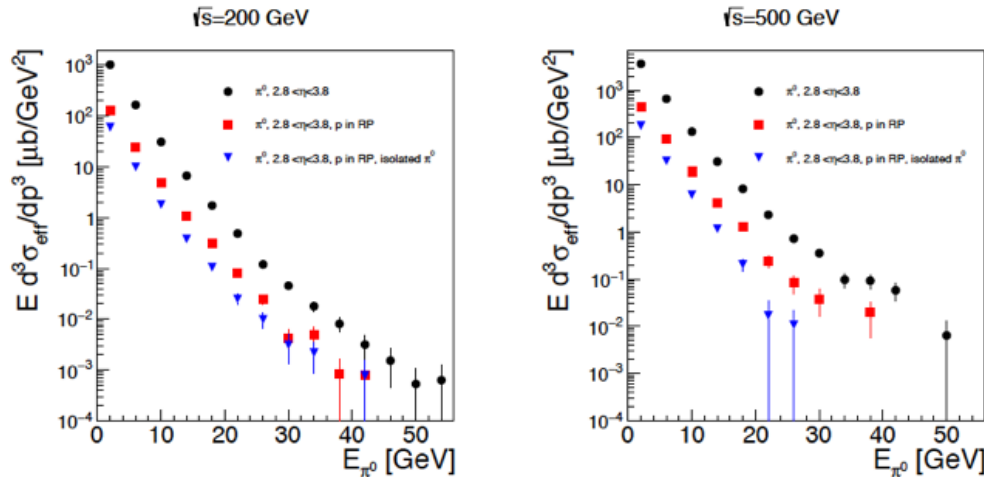


Figure 72: Estimate of the cross-section for hard diffractive processes at $\sqrt{s}=200$ GeV and 500 GeV using Pythia 8. The different points reflect different analysis cuts applied: π^0 in rapidity $2.8 < \eta < 3.8$ (black), one proton is required to be detected in the STAR Roman Pot acceptance (red) and an isolation cut of 35 mrad around the π^0 (blue).

2646 of $2 \rightarrow 2$ parton scattering processes but of diffractive nature. PYTHIA-8 [11] was used
 2647 to evaluate the fraction of hard diffractive events [278] contributing to the inclusive π^0
 2648 cross-section at forward rapidities. Figure 72 shows the hard diffractive cross-section for
 2649 π^0 production at $\sqrt{s}=200$ GeV and 500 GeV for a rapidity range of $2.5 < \eta < 4.0$ with
 2650 and without applying several experimental cuts, i.e. the proton in the STAR Roman Pot
 2651 acceptance. The prediction from this PYTHIA-8 simulation is that 20% of the total inclusive
 2652 cross-section at forward rapidities is of diffractive nature. This result is in agreement with
 2653 measurements done over a wide range of \sqrt{s} (see Fig. 12 in Ref. [272]).

2654 In 2015 STAR collected data in $\sqrt{s} = 200$ GeV transversely polarized p+p collisions,
 2655 where an isolated π^0 is detected in the forward pseudorapidity range along with the forward-
 2656 going proton p, which scatters with a near-beam forward pseudorapidity into Roman Pot
 2657 detectors. The sum of the π^0 and the scattered proton energies is consistent with the incident
 2658 proton energy of 100 GeV, indicating that no further particles are produced in this direction.
 2659 Correlations between the π^0 and scattered proton have been presented [279], along with
 2660 single-spin asymmetries which depend on the azimuthal angles of both the pion and the

2661 proton. This is the first time that spin asymmetries have been explored for this process, and
2662 a model to explain their azimuthal dependence is needed.

2663 The STAR Forward Upgrade will be a game changer for diffractive measurements at
2664 RHIC. It will allow the reconstruction of full jets both at $\sqrt{s}=200$ GeV and 500 GeV. As
2665 at HERA we will be able to reconstruct jets produced with the scattered proton tagged
2666 in Roman Pots and/or requiring rapidity gaps. Measuring spin asymmetries for diffractive
2667 events as function of \sqrt{s} might reveal surprises, which will inspire new physics opportunities
2668 for EIC, i.e SSA in polarized eA collisions.

2669 **3.2 Run-24 Request for Polarized p+p and p+A Collisions at 200** 2670 **GeV**

2671 Run-24, with polarized p+p and p+Au collisions at $\sqrt{s_{NN}} = 200$ GeV, will likely be the last
2672 RHIC spin/cold QCD run. This run will provide STAR with the unique opportunity to in-
2673 vestigate these 200 GeV collision systems with the Forward Upgrade providing full tracking
2674 and calorimetry coverage over the region $2.5 < \eta < 4$ and the iTPC providing enhanced
2675 particle identification and expanded pseudorapidity coverage at mid-rapidity. These power-
2676 ful detection capabilities, when combined with substantially increased sampled luminosity
2677 compared to Run-15, will enable critical measurements to probe universality and factoriza-
2678 tion in transverse spin phenomena and nuclear PDFs and fragmentation functions, as well as
2679 low- x non-linear gluon dynamics characteristic of the onset of saturation. This will provide
2680 unique insights into fundamental QCD questions in the near term, and essential baseline
2681 information for precision universality tests when combined with measurements from the EIC
2682 in the future.

2683 We therefore request at least 11 weeks of polarized p+p data-taking at $\sqrt{s} = 200$ GeV
2684 and 11 weeks of polarized p+Au data-taking at $\sqrt{s_{NN}} = 200$ GeV during Run-24. All of
2685 the running will involve transversely polarized protons, with the choice between vertical
2686 or radial polarization to be determined during the coming year. Based on recent (08-21-
2687 20) C-AD guidance, we expect to sample at least 235 pb^{-1} of p+p collisions and 1.3 pb^{-1}
2688 of p+Au collisions. These totals represent 4.5 times the luminosity that STAR sampled
2689 during transversely polarized p+p collisions in Run-15 and 3 times the luminosity that
2690 STAR sampled during transversely polarized p+Au collisions in Run-15.

2691 **3.2.1 Spin Physics with Polarized p+p and p+Au Collisions at 200 GeV**

2692 Section 1.3.3 described several very mature STAR analyses that are based on the transversely
2693 polarized p+p and p+Au data sets that we recorded during 2015. Run-24 will enable STAR
2694 to probe these questions with a far more capable detector and much larger data sets than were
2695 available during Run-15, thereby allowing us to set the stage for related future measurements
2696 at the EIC. Here we give brief descriptions of several of the opportunities presented by Run-
2697 24.

2698 **Forward transverse spin asymmetries:** Section 1.3.3 presents a small subset of the
 2699 results that STAR will publish very soon in a pair of papers discussing forward transverse
 2700 spin asymmetries in p+p, p+Al, and p+Au collisions measured with the Forward Meson
 2701 Spectrometer (FMS). One paper focuses on the dynamics that underlie the large asymmetries
 2702 that have been seen to date. Figure 31 shows that A_N for forward π^0 production in p+p
 2703 collisions at 200 and 500 GeV is substantially larger when the π^0 is isolated than when it
 2704 is accompanied by additional nearby photons. The same analysis also shows that A_N for
 2705 inclusive electromagnetic jets (EM-jets) in 200 and 500 GeV collisions is substantially larger
 2706 than that for EM-jets that contain three or more photons and that the Collins asymmetry
 2707 for π^0 in EM-jets is very small. The other paper focuses on the nuclear dependence of A_N
 2708 for π^0 in $\sqrt{s_{NN}} = 200$ GeV collisions. It presents a detailed mapping of A_N as functions of
 2709 x_F and p_T for all three collision systems. Figure 30 shows the observed nuclear dependence
 2710 is very weak. The same analysis shows that isolated *vs.* non-isolated π^0 behave similarly in
 2711 p+Al and p+Au collisions as they do in p+p collisions.

2712 These two papers will provide a wealth of new data to inform the ongoing discussion
 2713 regarding the origin of the large inclusive hadron transverse spin asymmetries that have
 2714 been seen in p+p collisions at forward rapidity over a very broad range of collision energies.
 2715 Nonetheless, the STAR Forward Upgrade will be a game changer for such investigations. It
 2716 will enable measurements of A_N for $h^{+/-}$, in addition to π^0 . It will enable isolation criteria to
 2717 be applied to the $h^{+/-}$ and π^0 that account for nearby charged, as well as neutral, fragments.
 2718 It will enable full jet asymmetry and Collins effect measurements, again for $h^{+/-}$ in addition
 2719 to π^0 , rather than just EM-jet measurements. It will permit all of these measurements to
 2720 be performed at both 510 GeV, as discussed in Sects. 3.1.1 and 3.1.2, and at 200 GeV. And
 2721 all of these observables can be tagged by forward protons detected in the STAR Roman
 2722 pots to identify the diffractive component of the observed transverse spin asymmetries. For
 2723 p+p there will be considerable overlap between the kinematics at the two energies, but the
 2724 510 GeV measurements will access higher p_T , while the 200 GeV measurements will access
 2725 higher x_F . Meanwhile, at 200 GeV we will also perform the full suite of measurements in
 2726 p+Au to identify any nuclear effects. Figure 65 shows one set of predictions for the inclusive
 2727 $\pi^{+/-}$ A_N in 200 and 500 GeV p+p collisions, while Fig. 66 shows the estimated sensitivity
 2728 of one hadron-in-jet measurement that will help to isolate the Sivers effect contribution at
 2729 200 GeV.

2730 **Sivers effect:** Sections 1.3.3 and 3.1.2 describe the first ever observation of the Sivers
 2731 effect in dijet production. Such measurements are crucial to explore questions regarding
 2732 factorization of the Sivers function in dijet hadroproduction [261–264]. Those results were
 2733 derived from 200 GeV transverse spin data that STAR recorded in 2012 and 2015 (total
 2734 sampled luminosity ~ 75 pb $^{-1}$ for the two years combined). Nonetheless, the uncertainties
 2735 remain large, as can be seen in Fig. 29. Run-24 data will reduce the uncertainties for
 2736 $|\eta_3 + \eta_4| < 1$ by a factor of two. The increased acceptance from the iTPC will reduce the
 2737 uncertainties at $|\eta_3 + \eta_4| \approx 2.5$ by a much larger factor, while the Forward Upgrade will
 2738 enable the measurements to be extended to even larger values of $|\eta_3 + \eta_4|$. When combined

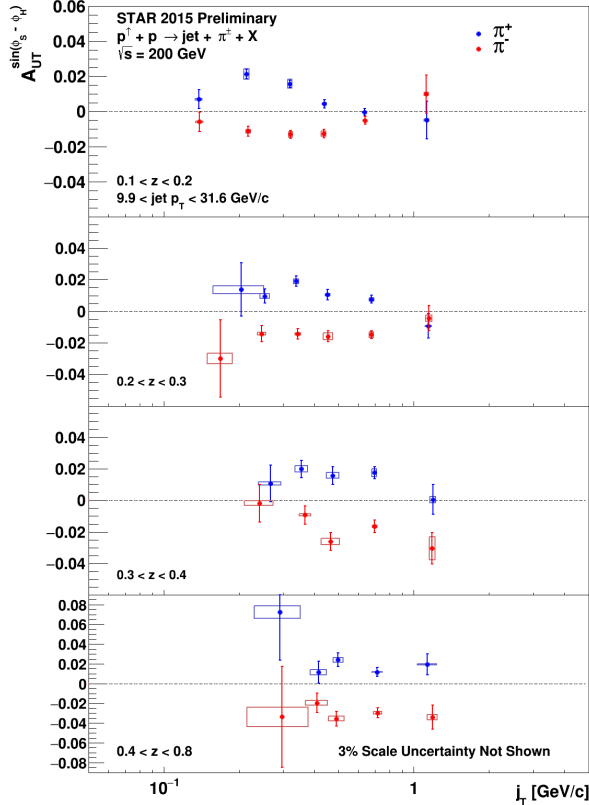


Figure 73: Preliminary 2015 results for the Collins asymmetry for charged pions in 200 GeV p+p collisions as a function of z and j_T , integrated over $9.9 < p_T < 31.6$ GeV/ c and $0 < \eta < 0.9$.

2739 with the 510 GeV data from 2017 and 2022 (see Sect. 3.1.2), the results will provide a detailed
 2740 mapping *vs.* x for comparison to results for Sivers functions extracted from SIDIS, Drell-Yan,
 2741 and vector boson production.

2742 **Transversity and related quantities:** As described in Sect. 3.1.3, measurements of the
 2743 Collins asymmetry and IFF in p+p collisions at RHIC probe fundamental questions regarding
 2744 TMD factorization, universality, and evolution. Data from 200 GeV p+p collisions will play
 2745 an essential role toward answering these questions. Figure 68 shows that 200 GeV p+p
 2746 collisions interpolate between the coverage that we will achieve during Run-22 at high- x
 2747 with the Forward Upgrade and at low- x with the STAR mid-rapidity detectors. They will
 2748 also provide a significant overlapping region of x coverage, but at Q^2 values that differ by a
 2749 factor of 6. This will provide valuable information about evolution effects, as well as cross-
 2750 checks between the two measurements. Furthermore, for most of the overlapping x region,
 2751 200 GeV p+p collisions will also provide the greatest statistical precision (see for example
 2752 Fig. 70), thereby establishing the most precise benchmark for future comparisons to ep data
 2753 from the EIC.

2754 The high statistical precision of the Run-24 data will enable detailed multi-dimensional
 2755 binning for the Collins asymmetry results. This is particularly valuable because, as empha-
 2756 sized in [109, 110], hadron-in-jet measurements in p+p collisions provide a direct probe of
 2757 the Collins fragmentation function since they combine it with the *collinear* transversity dis-

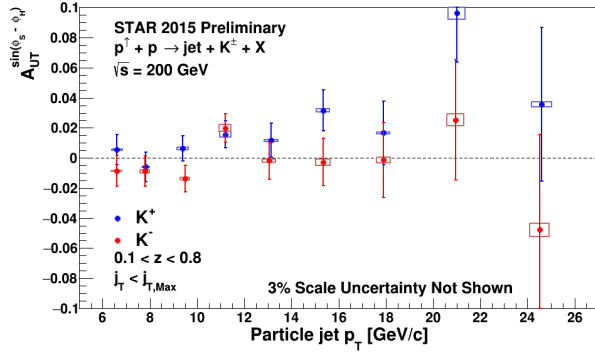


Figure 74: Preliminary 2015 results for the $K^{+/-}$ Collins asymmetries *vs.* jet p_T for $0 < \eta < 0.9$ in 200 GeV p+p collisions.

2758 tribution. In general, the observed asymmetries are functions of jet (p_T, η), hadron (z, j_T),
 2759 and Q^2 . However, the physics interpretations associated with these variables separate, with
 2760 p_T and η primarily coupling to the incident quark x and the polarization transfer in the
 2761 hard scattering, while z and j_T characterize the fragmentation kinematics. Thus, A_{UT} *vs.*
 2762 p_T , as shown in Fig. 28 for the preliminary 2015 analysis, provides information about the
 2763 transversity distribution. In parallel, the (z, j_T) dependence, integrated over a wide range of
 2764 jet p_T , as shown in Fig. 73 for the preliminary 2015 results, provides a detailed look at the
 2765 Collins fragmentation function. Note that STAR finds the maximum value of A_{UT} shifts to
 2766 higher j_T as z increases. The statistical uncertainties in Figs. 28 and 73 will be reduced by
 2767 a factor of 2.5 when Run-15 and Run-24 data are combined together.

2768 The 2015 Collins analysis has also, for the first time, measured the Collins effect for
 2769 charged kaons in p+p collisions, as shown in Fig. 74. The asymmetries for K^+ , which
 2770 like π^+ have a contribution from favored fragmentation of u quarks, are about 1.5-sigma
 2771 larger than those for π^+ in Fig. 28, while those for K^- , which can only come from unfavored
 2772 fragmentation, are consistent with zero at the 1-sigma level. These trends are similar to those
 2773 found in SIDIS by HERMES [280] and COMPASS [281], and provide additional insight into
 2774 the Collins fragmentation function. This same analysis with Run-24 data will yield statistical
 2775 uncertainties a factor of 3 smaller than those in Fig. 74. This is a much greater improvement
 2776 than would be expected from the increase in sampled luminosity thanks to the improved
 2777 dE/dx resolution provided by the iTPC. In addition, the iTPC will enable the measurements
 2778 in Figs. 28, 73, and 74 to be extended to an additional higher η bin ($0.9 < \eta < 1.3$).

2779 RHIC has the unique opportunity to extend the Collins effect measurements to nuclei.
 2780 This will provide an alternative look at the universality of the Collins effect in hadroproduc-
 2781 tion by dramatically increasing the color flow options of the sort that have been predicted
 2782 to break factorization for TMD PDFs like the Sivers effect [261, 262]. This will also explore
 2783 the spin dependence of the hadronization process in cold nuclear matter. STAR collected a
 2784 proof-of-principle data set during the 2015 p+Au run that is currently under analysis. Those
 2785 data will provide a first estimate of medium-induced effects. However, the small nuclear ef-
 2786 fects seen by STAR for forward inclusive $\pi^0 A_N$ (see Fig. 30) indicate that greater precision
 2787 will likely be needed. Figure 70 shows the projected 2015+'24 statistical uncertainties for
 2788 the p+Au Collins asymmetry measurement at $\sqrt{s_{NN}} = 200$ GeV, compared to those for the

2789 p+p at the same energy.

2790 **Ultra-peripheral collisions:** The formalism of generalized parton distributions (GPDs)
 2791 provides a theoretical framework which addresses some of the above questions [282–285].
 2792 Constraints on GPDs have mainly been provided by exclusive reactions in DIS, e.g. deeply
 2793 virtual Compton scattering. RHIC, with its unique capability to collide transversely polar-
 2794 ized protons at high energies, has the opportunity to measure A_N for exclusive J/Ψ produc-
 2795 tion in ultra-peripheral collisions (UPCs) [286]. In such a UPC process, a photon emitted by
 2796 the opposing beam particle (p or A) collides with the polarized proton. The measurement is
 2797 at a fixed $Q^2 \sim M_{J/\psi}^2 \approx 10 \text{ GeV}^2$ and $10^{-4} < x < 10^{-1}$. A nonzero asymmetry would be the
 2798 first signature of a nonzero GPD E_g for gluons, which is sensitive to spin-orbit correlations
 2799 and is intimately connected with the orbital angular momentum carried by partons in the
 2800 nucleon and thus with the proton spin puzzle.

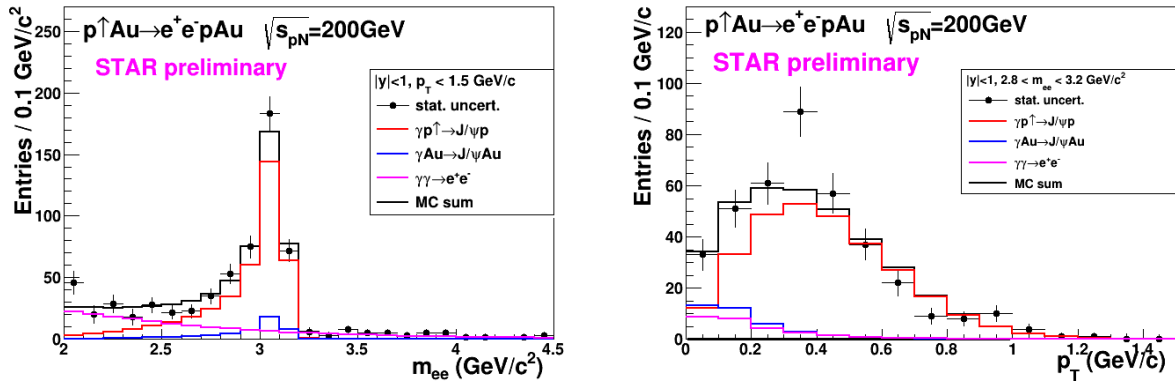


Figure 75: Mass distribution of selected e^+e^- pairs (left), and p_T distribution of the J/ψ mass peak (right). The colored histograms are the indicated processes modelled by STARlight and the sum fit to the data.

2801 The 2015 p⁺Au data allowed a proof-of-principle of such a measurement. A trigger
 2802 requiring back-to-back energy deposits in the Barrel Electromagnetic Calorimeter selected
 2803 J/Ψ candidates. The e^+e^- mass distribution after selection cuts is shown in the left of
 2804 Fig. 75, and the pair p_T distribution of the J/ψ mass peak is shown on the right of the
 2805 figure. The data are well described by the STARlight model [287] (colored histograms in
 2806 the figure), including the dominant $\gamma+p^+\rightarrow J/\psi$ signal process and the $\gamma+Au\rightarrow J/\psi$ and
 2807 $\gamma+\gamma\rightarrow e^+e^-$ background processes. The left of Fig. 76 shows the transverse asymmetry A_N^γ
 2808 for the signal J/ψ , which have a mean photon-proton center-of-mass energy $W_{\gamma p} \approx 24 \text{ GeV}$.
 2809 The result is consistent with zero. Also shown is a prediction based on a parameterization
 2810 of E_g [288]; the present data provide no discrimination of this prediction.

2811 This measurement can be greatly improved with a high statistics transversely polarized
 2812 p⁺Au run in 2024. The integrated luminosity for the 2015 measurement was 140 nb^{-1} ; the
 2813 2024 run will provide 1.3 pb^{-1} , allowing a sizeable reduction of statistical uncertainty in the

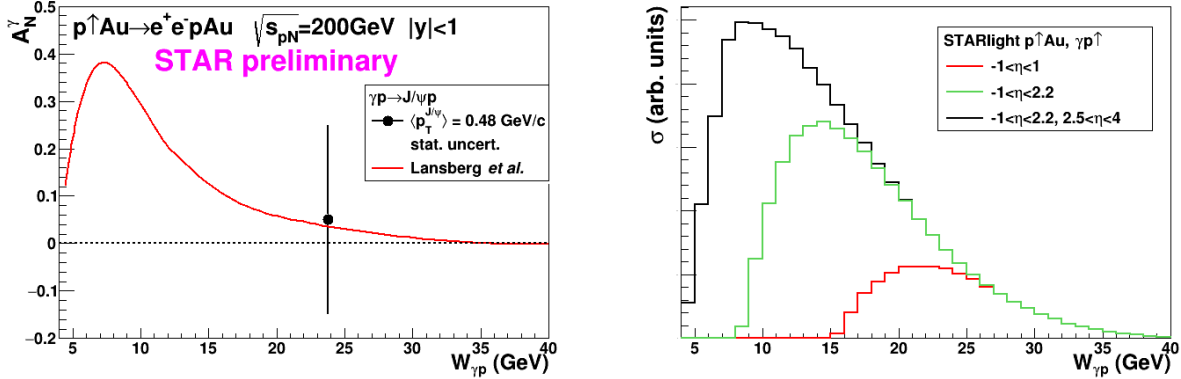


Figure 76: Left: The measured J/ψ transverse asymmetry A_N^γ and a prediction based on a parameterization of E_g . Right: The accepted cross section for $\gamma+p^\dagger \rightarrow J/\psi$ for various detector pseudorapidity η ranges; the black curve shows the result for the full STAR detector with the Forward Upgrade and the iTPC.

2814 same $W_{\gamma p}$ range. However, the Forward Upgrade and iTPC will also provide a significant
 2815 extension of the $W_{\gamma p}$ range of the measurement. The right panel of Fig. 76 shows the
 2816 accepted cross section for $\gamma+p^\dagger \rightarrow J/\psi$ for various detector pseudorapidity ranges. With the
 2817 full detector, the sensitive cross section is a factor of five times the central barrel alone and
 2818 the expected asymmetry is substantially larger. The statistical uncertainty on A_N^γ as shown
 2819 in the left of Fig. 76 will be ≈ 0.02 , offering a powerful test of a non-vanishing E_g . Also, the
 2820 accepted region has a lower mean $W_{\gamma p} \approx 14$ GeV. Predictions based on E_g parameterizations
 2821 such as shown in the figure have a larger asymmetry at lower $W_{\gamma p}$, with increased possibility
 2822 of a nonzero result. Alternatively, the increased statistics will allow a measurement of A_N^γ
 2823 in bins of $W_{\gamma p}$.

2824 Similar measurements are also possible with future $p^\dagger+p^\dagger$ runs at $\sqrt{s} = 200$ and 510
 2825 GeV. However, the UPC cross section scales with Z^2 of the the nucleus emitting the photon;
 2826 for protons this is $1/79^2$ relative to Au nuclei, which makes analogous measurements in p+p
 2827 collisions extremely luminosity hungry.

2828 3.2.2 Physics Opportunities with Unpolarized proton-Nucleus Collisions

2829 Our quest to understand QCD processes in Cold Nuclear Matter (CNM) centers on the
 2830 following fundamental questions:

- 2831 • Can we experimentally find evidence of a novel universal regime of non-linear QCD
 2832 dynamics in nuclei?
- 2833 • What is the role of saturated strong gluon fields, and what are the degrees of freedom
 2834 in this high gluon density regime?
- 2835 • What is the fundamental quark-gluon structure of light and heavy nuclei?

- Can a nucleus, serving as a color filter, provide novel insight into the propagation, attenuation and hadronization of colored quarks and gluons?

Various aspects of these questions have been addressed by numerous experiments and facilities around the world, most of them at significantly lower center-of-mass energies and kinematic reach than RHIC. Deep inelastic scattering on nuclei addresses some of these questions with results from, for instance, HERMES at DESY [289–291], CLAS at JLab [292], and in the future at the JLab 12 GeV. This program is complemented by hadron-nucleus reactions in fixed target p+A at Fermilab (E772, E886, and E906) [293] and at the CERN-SPS.

In the following we propose a measurement program unique to RHIC to constrain the initial state effects in strong interactions in the nuclear environment. We also highlight the complementarity to the LHC p+Pb program and stress why RHIC data are essential and unique in the quest to further our understanding of nuclei. The uniqueness of the RHIC program is based on the flexibility of the RHIC accelerator to run collisions of different particle species at very different center-of-mass energies. This in combination with the enhanced STAR detector capabilities in Run-24 allows to disentangle nuclear effects in the initial and final state as well as leading twist shadowing from saturation effects in a kinematic regime where all these effects are predicted to be large. Most of the discussed measurements critically rely on the Forward Upgrade.

The initial state of nuclear collisions:

Nuclear parton distribution functions: A main emphasis of the 2015 and later p+A runs is to determine the initial conditions of the heavy ion nucleus before the collision to support the theoretical understanding of the A+A program both at RHIC and the LHC. In the following, the current status of nPDFs will be discussed, including where the unique contributions of RHIC lie, in comparison to the LHC and the future EIC.

Our current understanding of nuclear parton distribution functions (nPDFs) is still very limited, in particular, when compared with the rather precise knowledge of PDFs for free protons collected over the past 30 years. Figure 77 shows an extraction of nPDFs from available data, along with estimates of uncertainties. All results are shown in terms of the nuclear modification ratios, i.e., scaled by the respective PDF of the free proton. The yellow bands indicate regions in x where the fits are not constrained by data [294] and merely reflect the freedom in the functional form *assumed* in the different fits. Clearly, high precision data at small x and for various different values of Q^2 are urgently needed better to constrain the magnitude of suppression in the x region where non-linear effects in the scale evolution are expected. In addition, such data are needed for several different nuclei, as the A-dependence of nPDFs cannot be predicted from first principles in pQCD and, again, currently relies on assumptions. Note that the difference between DSSZ [295] and EPS09 for the gluon modification arise from the different treatment of the PHENIX midrapidity $\pi^0 R_{dAu}$ data [296], which in the EPS09 [297] fit are included with an extra weight of 20. The $\pi^0 R_{dAu}$ data are the only data, which can probe the gluon in the nucleus directly, but these

2876 data also suffer from unknown nuclear effects in the final state (see [298]). Therefore, it is
 2877 absolutely critical to have high precision data only sensitive to nuclear modification in the
 2878 initial state over a wide range in x and intermediate values of Q^2 (away from the saturation
 2879 regime) to establish the nuclear modification of gluons in this kinematic range.

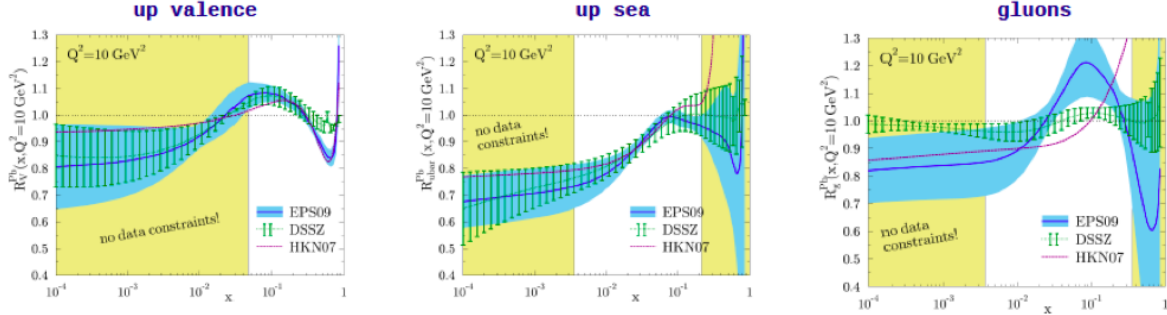


Figure 77: Summary of the most recent sets of nPDFs. The central values and their uncertainty estimates are given for the up valence quark, up sea quark, and the gluon. The yellow bands indicate regions in x where the fits are not constrained by any data (taken from Ref. [294]).

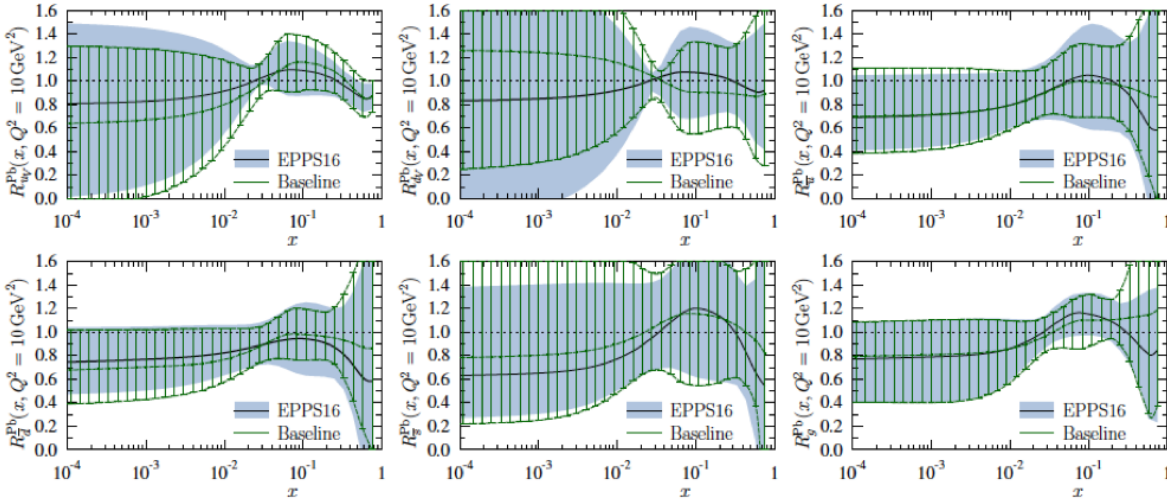


Figure 78: The nuclear modifications at $Q^2=10 \text{ GeV}^2$ from the EPPS-16 fit (black central line and light-blue bands) compared with the Baseline fit (green curves with hatching) which uses only the data included in the EPS09 fit.

2880 It is important to realize that the measurements from RHIC are compelling and essential
 2881 even when compared to what can be achieved in p+Pb collisions at the LHC. Due to the
 2882 higher center-of-mass system energy most of the LHC data have very high Q^2 , where the
 2883 nuclear effects are already reduced significantly by evolution and are therefore very difficult to
 2884 constrain. Two recent articles [299,300] assessed the impact of the available LHC Run-I p+Pb
 2885 data on determinations of nPDFs. The rather moderate impact of these data is illustrated

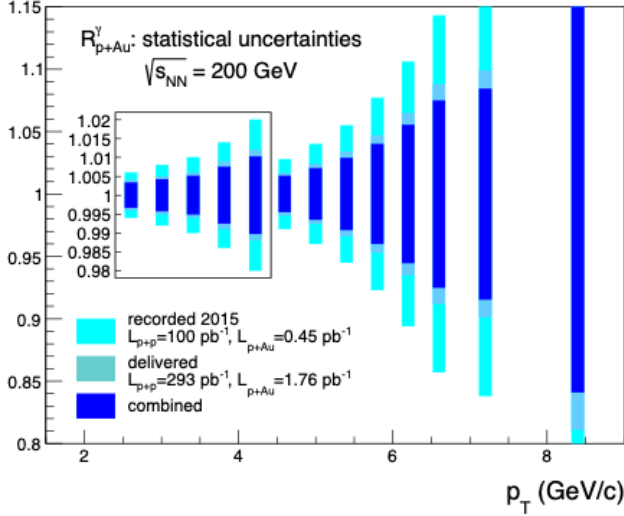


Figure 79: Projected statistical uncertainties for R_{pA} for direct photons in Run-2015 (light blue) and a run in 2024 (blue) and the sum of both (dark blue). The recorded luminosity for Run-2015 was $L_{pAu} = 450 \text{ nb}^{-1}$ and $L_{pp} = 100 \text{ pb}^{-1}$. The delivered luminosity for Run-2024 is assumed to be $L_{pAu} = 1.8 \text{ pb}^{-1}$ and $L_{pp} = 300 \text{ pb}^{-1}$.

2886 in Figure 78. Note that the extra weight factor of 20 for the PHENIX midrapidity $\pi^0 R_{dAu}$
 2887 data [296] in the original EPS09 [297] fit was removed in all of the new fits, leading to a
 2888 much smaller nuclear modification factor for gluons, especially at medium to high x .

2889 RHIC has the *unique* capability to provide data in a kinematic regime (moderate Q^2 and
 2890 medium-to-low x) where the nuclear modification of the sea quark and the gluon is expected
 2891 to be sizable and currently completely unconstrained. In addition, and unlike the LHC,
 2892 RHIC has the potential to vary the nucleus in p+A collisions and as such also constrain the
 2893 A -dependence of nPDFs.

2894 Extraction of this information is less ambiguous if one uses processes in which strong
 2895 (QCD) final-state interactions can be neglected or reduced. Such golden channels would
 2896 include: a measurement of R_{pA} for Drell-Yan production at forward pseudo-rapidities with
 2897 respect to the proton direction ($2.5 < \eta < 4.$) to constrain the nuclear modifications of sea-
 2898 quarks; and of R_{pA} for direct photon production in the same kinematic regime to constrain
 2899 the nuclear gluon distribution. Data for the first measurement of R_{pA} for direct photon
 2900 production have already been taken during the p+Au and p+Al runs in 2015, with recorded
 2901 luminosities by STAR of $L_{pAu} = 0.45 \text{ pb}^{-1}$ and $L_{pAl} = 1 \text{ pb}^{-1}$, respectively. The anticipated
 2902 statistical precision for pA runs in 2015 and projections for the run in 2024 are shown in
 2903 Fig. 79. The Forward Upgrade with its tracking at forward rapidities will also provide the
 2904 possibility to measure R_{pA} for positive and negatively charged hadrons.

2905 Figure 80(left) shows the significant impact of the Run-2015 and 2024 R_{pA} for direct
 2906 photon production on the corresponding theoretical expectations and their uncertainties
 2907 obtained with the EPPS-16 set of nPDFs. The uncertainty bands are obtained through a
 2908 re-weighting procedure [301] by using the projected data shown in Fig. 79 and randomizing
 2909 them according to their expected statistical uncertainties around the central values obtained
 2910 with the current set of EPPS-16 nPDFs. Figure 80(right) shows how these measurements
 2911 will help significantly in further constraining the nuclear gluon distribution in a broad range
 2912 of x that is roughly correlated with accessible transverse momenta of the photon, i.e., few

2913 times $10^{-3} < x < \text{few times } 10^{-2}$. The relevant scale Q^2 is set be $\sim p_T^2$ and ranges from 6
 2914 GeV^2 to about 40 GeV^2 . Like all other inclusive probes in p+p and pA collisions, e.g., jets,
 2915 no access to the exact parton kinematics can be provided event-by-event but global QCD
 2916 analyses easily account for that. After the p+Au run in 2024, the statistical precision of the
 2917 prompt photon data will be sufficient to contribute to a stringent test of the universality
 2918 of nuclear PDFs when combined with the expected data from the EIC (see Figure 2.22 and
 2919 2.23 in Ref [302]).

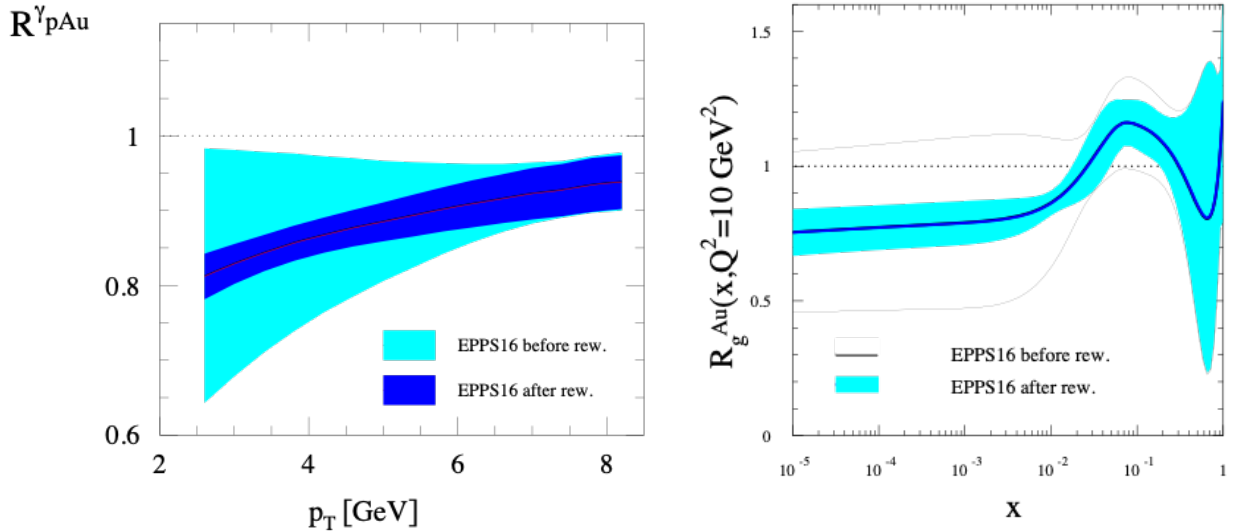


Figure 80: (left) The impact of the direct photon R_{pA} data measured in Run-2015 (blue band) and for the anticipated statistics for the future p+Au run in 2024 (dark blue band) compared with the current uncertainties (cyan band) from EPPS-16. (right) The impact of the direct photon R_{pA} data measured in Run-2015 and for the anticipated statistics for the future p+Au run in 2024 on EPPS-16. The impact is shown on the nuclear suppression factor R_g of nPDF to the proton PDF, the grey bands represent the uncertainties before including the RHIC pseudo data.

2920 Figure 81 shows the kinematic coverage in $x-Q^2$ of past, present, and future experiments
 2921 capable of constraining nuclear parton distribution functions. The experiments shown pro-
 2922 vide measurements that access the initial state parton kinematics on an event-by event basis
 2923 (in a leading order approximation) while remaining insensitive to any nuclear effects in the
 2924 final state. Some of the LHC experiments cover the same x -range as DY at forward pseudo-
 2925 rapidities at RHIC but at a much higher scale Q^2 , where nuclear modifications are already
 2926 significantly reduced [300, 303, 304]. At intermediate Q^2 , DY at RHIC will extend the low- x
 2927 reach by nearly one decade compared to EIC.

2928 The biggest challenge of a DY measurement is to suppress the overwhelming hadronic
 2929 background: the total DY cross-section is about 10^{-5} to 10^{-6} smaller than the corresponding
 2930 hadron production cross-sections. Therefore, the probability of misidentifying a hadron
 2931 track as a lepton has to be suppressed to the order of 0.1% while maintaining reasonable
 2932 electron detection efficiencies. To that end, we have studied the combined electron/hadron

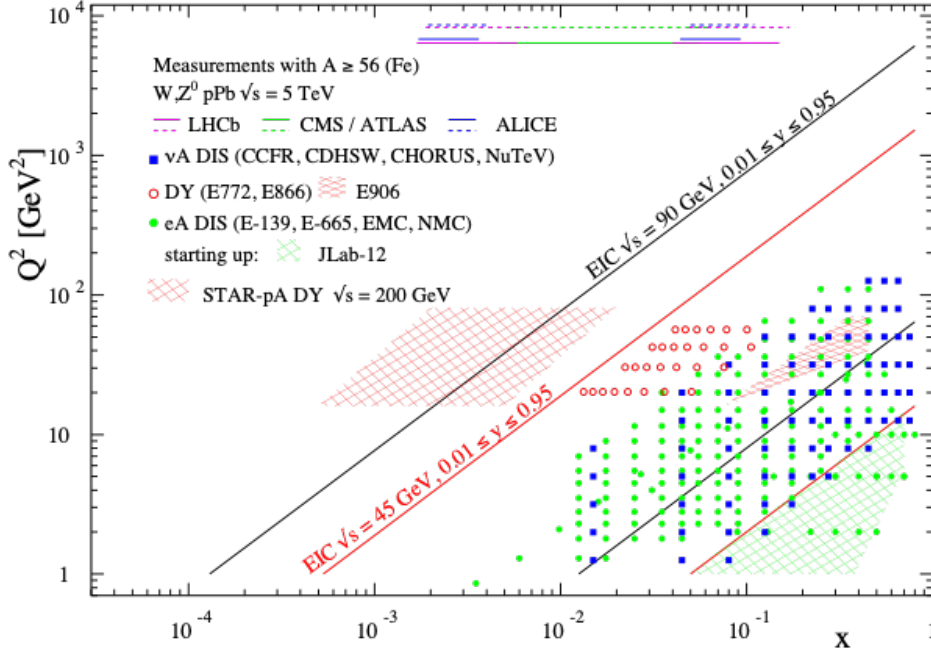


Figure 81: The kinematic coverage in $x \sqrt{Q^2}$ of past, present and future experiments constraining nPDFs with access to the exact parton kinematics event-by-event and no fragmentation in the final state.

2933 discriminating power of the Forward Upgrade. It was found that by applying multivariate
 2934 analysis techniques to the features of EM/hadronic shower development and momentum
 2935 measurements we can achieve hadron rejection powers of 200 to 2000 for hadrons of 15 GeV
 2936 to 50 GeV with 80% electron detection efficiency.

2937 The same procedure as for the direct photon R_{pA} was used to study the potential impact
 2938 of the DY R_{pA} data for the EPPS-19 sets of nPDFs. We expect again a significant impact
 2939 on the uncertainties of R_{pA} DY upon including the projected and properly randomized data.
 2940 Clearly, the DY data from RHIC will be instrumental in reducing present uncertainties in
 2941 nuclear modifications of sea quarks. Again, these data will prove to be essential in testing the
 2942 fundamental universality property of nPDFs in the future when EIC data become available.

2943 STAR's unique detector capabilities will provide the first data on J/Ψ -production in
 2944 ultra-peripheral collisions. This measurement provides access to the spatial gluon distri-
 2945 bution by measuring the t -dependence of $d\sigma/dt$. As follows from the optical analogy, the
 2946 Fourier-transform of the square root of this distribution yields the source distribution of the
 2947 object probed. To study the gluon distribution in the gold nucleus, events need to be tagged
 2948 where the photon is emitted from the proton. For both observables a measurement with
 2949 different nuclei is required to pin down the A -dependence of nPDFs. The J/Ψ -production
 2950 in ultra-peripheral collisions requires significantly more statistics than accumulated to date.

2951 **Gluon saturation:** Our understanding of the proton structure and of the nuclear
 2952 interactions at high energy would be advanced significantly with the definitive discovery
 2953 of the saturation regime [305–311]. Saturation physics would provide an infrared cutoff for
 2954 perturbative calculations, the saturation scale Q_s , which grows with the atomic number of the
 2955 nucleus A and with decreasing value of x . If Q_s is large it makes the strong coupling constant

2956 small, $\alpha_s(Q_s^2) \ll 1$ allowing for perturbative QCD calculations to be under theoretical
 2957 control.

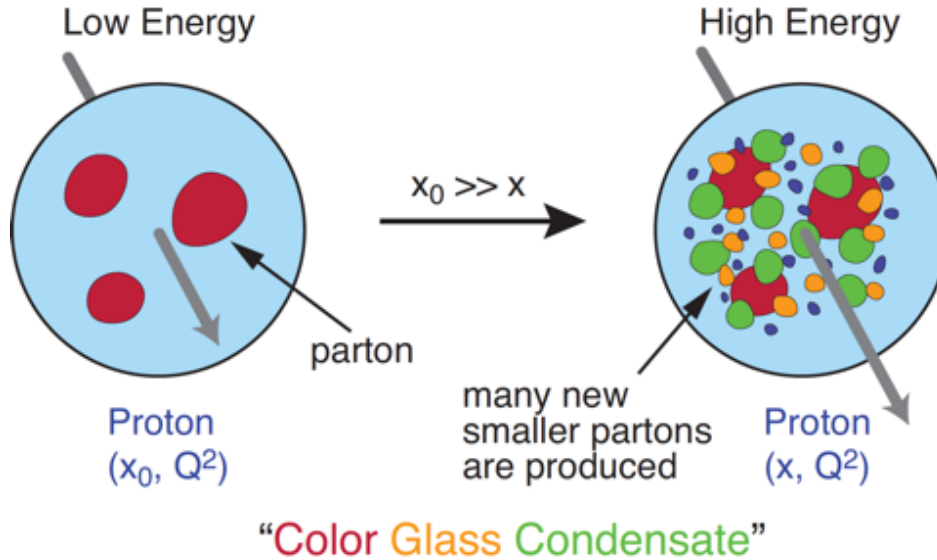


Figure 82: Proton wave function evolution towards small- x

2958 It is well known that PDFs grow at small- x . If one imagines how such a high number of
 2959 small- x partons would fit in the (almost) unchanged proton radius, one arrives at the picture
 2960 presented in Figure 82: the gluons and quarks are packed very tightly in the transverse plane.
 2961 The typical distance between the partons decreases as the number of partons increases, and
 2962 can get small at low- x (or for a large nucleus instead of the proton). One can define the
 2963 saturation scale as the inverse of this typical transverse inter-parton distance. Hence Q_s
 2964 indeed grows with A and decreasing x .

2965 The actual calculations in saturation physics start with the classical gluon fields (as gluons
 2966 dominate quarks at small- x) [312–318], which are then evolved using the nonlinear small- x
 2967 BK/JIMWLK evolution equations [319, 320, 320–328]. The saturation region can be well-
 2968 approximated by the following formula: $Q_s^2 \sim (A/x)^{1/3}$. Note again that at small enough
 2969 x the saturation scale provides an IR cutoff, justifying the use of perturbative calculations.
 2970 This is important beyond saturation physics, and may help us better understand small- x
 2971 evolution of the TMDs.

2972 While the evidence in favor of saturation physics has been gleaned from the data col-
 2973 lected at HERA, RHIC and the LHC, the case for saturation is not sealed and alternative
 2974 explanations of these data exist. The EIC is slated to provide more definitive evidence for
 2975 saturation physics [329]. To help the EIC complete the case for saturation, it is mandatory to
 2976 generate higher-precision measurements in p+A collisions at RHIC. These higher-precision
 2977 measurements would significantly enhance the discovery potential of the EIC as they would
 2978 enable a stringent test of universality of the CGC. We stress again that a lot of theoretical
 2979 predictions and results in the earlier Sections of this document would greatly benefit from

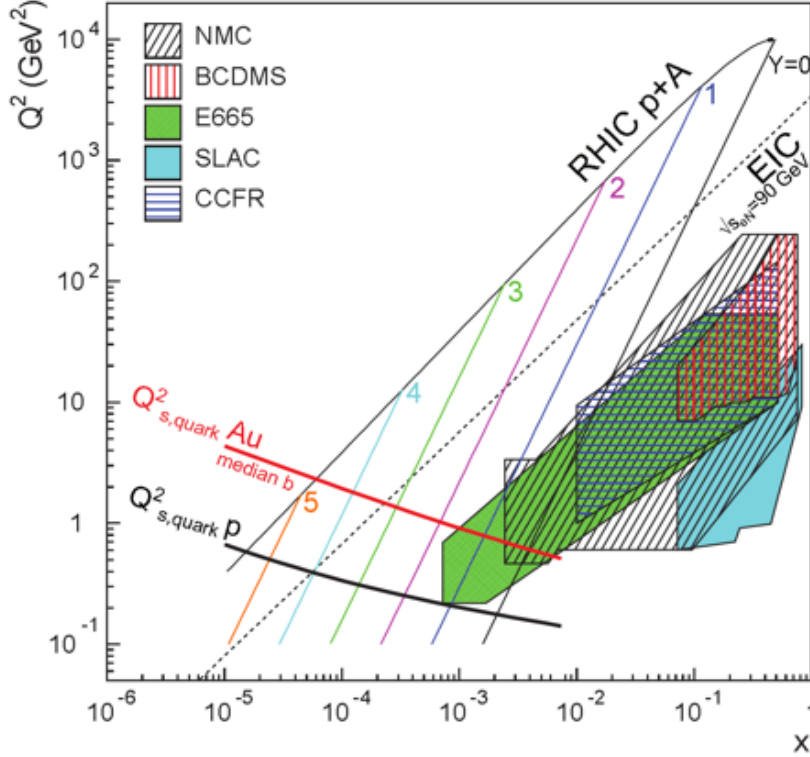


Figure 83: Kinematic coverage in the $x - Q^2$ plane for p+A collisions at RHIC, along with previous e+A measurements, the kinematic reach of an electron-ion collider, and estimates for the saturation scale Q_s in Au nuclei and protons. Lines are illustrative of the range in x and Q^2 covered with hadrons at various rapidities.

2980 saturation physics: the small- x evolution of TMDs in a longitudinally or transversely polarized proton, or in an unpolarized proton, can all be derived in the saturation framework [330]
 2981 in a theoretically better-controlled way due to the presence of Q_s . Hence saturation physics
 2982 may help us understand both the quark and gluon helicity PDFs as well as the Siverts and
 2983 Boer-Mulders functions.
 2984

2985 The saturation momentum is predicted to grow approximately like a power of energy,
 2986 $Q_s^2 \sim E^{\lambda/2}$ with $\lambda \sim 0.2-0.3$, as phase space for small- x (quantum) evolution opens up. The
 2987 saturation scale is also expected to grow in proportion to the valence charge density at the
 2988 onset of small- x quantum evolution. Hence, the saturation scale of a large nucleus should
 2989 exceed that of a nucleon by a factor of $A^{1/3} \sim 5$ (on average over impact parameters). RHIC
 2990 is capable of running p+A collisions for different nuclei to check this dependence on the mass
 2991 number. This avoids potential issues with dividing say p+Pb collisions in N_{part} classes [331].
 2992 Figure 83 shows the kinematic coverage in the $x-Q^2$ plane for p+A collisions at RHIC, along
 2993 with previous e+A measurements and the kinematic reach of an EIC. The saturation scale for
 2994 a Au nucleus and the proton is also shown. To access at RHIC a kinematic regime sensitive
 2995 to saturation with $Q^2 > 1 \text{ GeV}^2$ requires measurements at forward rapidities. For these
 2996 kinematics the saturation scale is moderate, on the order of a few GeV^2 , so measurements
 2997 sensitive to the saturation scale are by necessity limited to semi-hard processes.

2998 Until today the golden channel at RHIC to observe strong hints of saturation has been
 2999 the angular dependence of two-particle correlations, because it is an essential tool for testing
 3000 the underlying QCD dynamics [331]. In forward-forward correlations facing the $p(d)$ beam

3001 direction one selects a large- x parton in the p(d) interacting with a low- x parton in the
 3002 nucleus. For $x < 0.01$ the low- x parton will be back-scattered in the direction of the large-
 3003 x parton. Due to the abundance of gluons at small x , the backwards-scattered partons
 3004 are dominantly gluons, while the large- x partons from the p(d) are dominantly quarks.
 3005 The measurements of di-hadron correlations by STAR and PHENIX [332, 333], have been
 3006 compared with theoretical expectations using the CGC framework based on a fixed saturation
 3007 scale Q_s and considering valence quarks in the deuteron scattering off low- x gluons in the
 3008 nucleus with impact parameter $b = 0$ [334, 335]. Alternative calculations [336] based on both
 3009 initial and final state multiple scattering, which determine the strength of this transverse
 3010 momentum imbalance, in which the suppression of the cross-section in d+Au collisions arises
 3011 from cold nuclear matter energy loss and coherent power corrections have also been very
 3012 successful to describe the data.

3013 The 2015 p +Au run at RHIC has provided unique opportunities to study this channel in
 3014 more detail at STAR. The high delivered integrated luminosities allow one to vary the trigger
 3015 and associated particle p_T from low to high values and thus crossing the saturation boundary
 3016 as shown in Figure 83 and reinstate the correlations for central p +A collisions for forward-
 3017 forward π^0 's. Studying di-hadron correlations in p +A collisions instead of d+Au collisions has
 3018 a further advantage. In reference [337], the authors point out that the contributions from
 3019 double-parton interactions to the cross-sections for $dA \rightarrow \pi^0\pi^0 X$ are not negligible. They
 3020 find that such contributions become important at large forward rapidities, and especially in
 3021 the case of d+Au scattering. Figure 84 shows the results for the di-hadron correlations for π^0
 3022 from the 2015 p +p and p +A run. Shown is the ratio of the area, the width and the level of
 3023 pedestal of the backward peak for p +Au and p +p as function of the p_T of the trigger and
 the associated π^0 and the activity in the collision as measured by the BBC. The results show

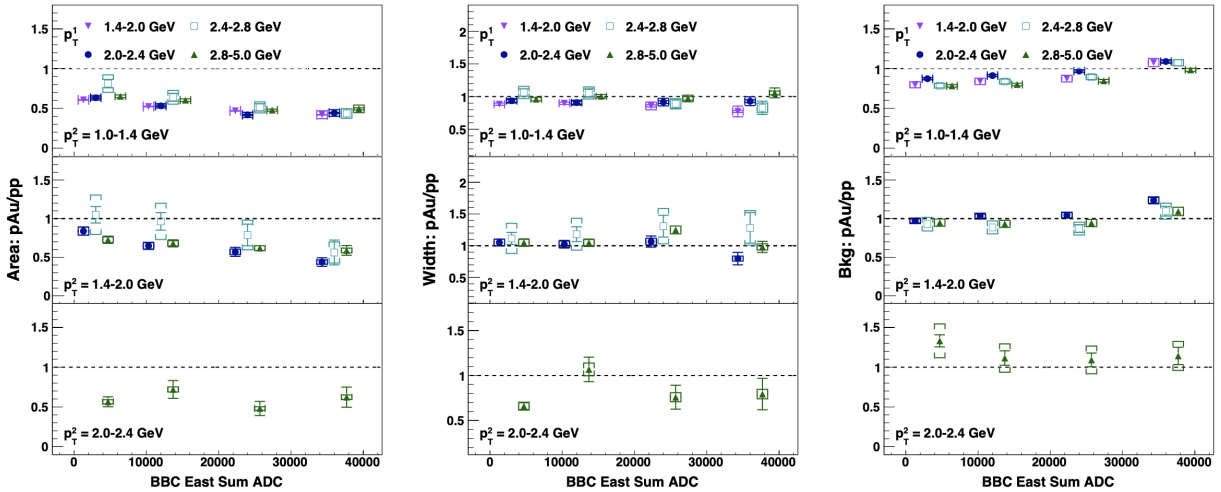


Figure 84: The results for the di-hadron correlations for π^0 from the 2015 p +p and p +A run.

3024 basically no change in the width of the backward peak and the background/pedestal the peak
 3025 is sitting on shows only up to a 20% increase in p +Au to p +p. But the area of the of the
 3026

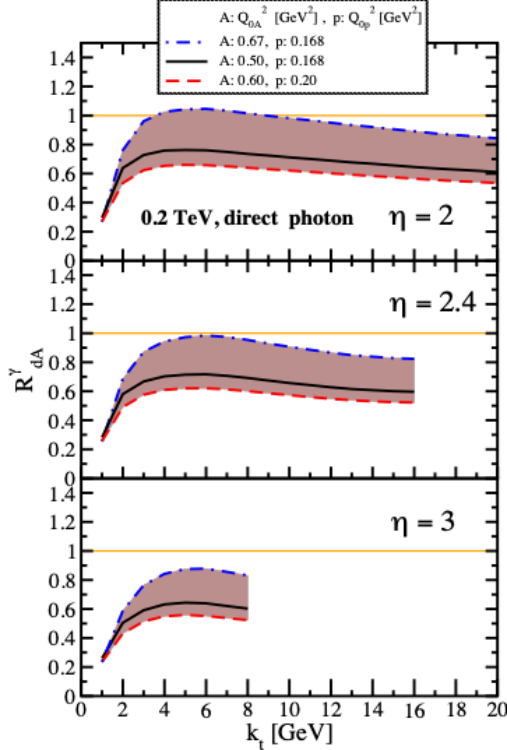


Figure 85: Nuclear modification factor for direct photon production in p(d)A collisions at various rapidities at RHIC $\sqrt{s} = 0.2$ TeV. The curves are the results obtained from Eq. (12) in Ref. [338] and the solution to rcBK equation using different initial saturation scales for a proton Q_{op} and a nucleus Q_{oA} . The band shows our theoretical uncertainties arising from allowing a variation of the initial saturation scale of the nucleus in a range consistent with previous studies of DIS structure functions as well as particle production in minimum-bias p+p, p+A and A+A collisions in the CGC formalism, see Ref. [338] for details.

3027 backward peak shows a large suppression with increasing activity in the collision. For fixed
 3028 activity the biggest suppression is observed for the smallest trigger p_T in combination with
 3029 the smallest p_T for the associated π^0 . This behaviour is consistent with different calculations
 3030 based on the CGC formalism. This result is the first clean observable, which cannot yet
 3031 be explained in a different framework than CGC and as such a clear hint for non-linear
 3032 effects. With the Forward Upgrade several other channels, i.e charged di-hadron and di-jets
 3033 correlations, will also be available, which will allow a rigorous test of the calculation in the
 3034 CGC formalism. It is noted that these results are crucial for the equivalent measurements at
 3035 an EIC, which are planned at close to identical kinematics, because only if non-linear effects
 3036 are seen with different complementary probes, i.e., ep and pA, one can claim a discovery of
 3037 saturation effects and their universality.

3038 It is important to note that for the measurements to date in p(d)+A collisions both
 3039 initial and final states interact strongly, leading to severe complications in the theoretical
 3040 treatment (see [339, 340], and references therein). As described in detail in the Section
 3041 above in p+A collisions, these complications can be ameliorated by removing the strong
 3042 interaction from the final state, by using photons and Drell-Yan electrons. The Run-2015
 3043 p+A run will for the first time provide data on R_{pA} for direct photons and therefore allow
 3044 one to test CGC based predictions on this observable as depicted in Figure 85 (taken from
 3045 Ref. [338]). The higher delivered integrated luminosity for the upcoming p+Au run in
 3046 2024 together with the Forward Upgrade will enable one to study more luminosity hungry
 3047 processes and/or complementary probes to the di- π^0 correlations, i.e. di-hadron correlations
 3048 for charged hadrons, photon-jet, photon-hadron and di-jet correlations.

3049 We use direct photon plus jet (direct γ +jet) events as an example channel to indicate
 3050 what can be done in 2024. These events are dominantly produced through the gluon Compton
 3051 scattering process, $g+q \rightarrow \gamma+q$, and are sensitive to the gluon densities of the nucleon
 3052 and nuclei in p+p and p+A collisions. Through measurements of the azimuthal correlations
 3053 in p+A collisions for direct γ +jet production, one can study gluon saturation phenomena
 3054 at small-x. Unlike di-jet production that is governed by both the Weizsäcker-Williams and
 3055 dipole gluon densities, direct γ +jet production only accesses the dipole gluon density, which
 3056 is better understood theoretically [338, 341]. On the other hand, direct γ +jet production
 3057 is experimentally more challenging due to its small cross-section and large background con-
 3058 tribution from di-jet events in which photons from fragmentation or hadron decay could be
 3059 misidentified as direct photons. The feasibility to perform direct γ +jet measurements with
 3060 the Forward Upgrade in unpolarized p+p and p+Au collisions at $\sqrt{s_{NN}} = 200$ GeV has been
 3061 studied. PYTHIA-8.189 [342] was used to produce direct γ +jet and di-jet events. In order
 3062 to suppress the di-jet background, the leading photon and jet are required to be balanced
 3063 in transverse momentum, $|\phi^\gamma - \phi^{jet}| > 2\pi/3$ and $0.5 < \frac{p_T^\gamma}{p_T^{jet}} < 2$. Both the photon and jet
 3064 have to be in the forward acceptance $1.3 < \eta < 4.0$ with $p_T > 3.2$ GeV/ c in 200 GeV p+p
 3065 collisions. The photon needs to be isolated from other particle activities by requiring the
 3066 fraction of electromagnetic energy deposition in the cone of $\Delta R=0.1$ around the photon is
 3067 more than 95% of that in the cone of $\Delta R=0.5$. Jets are reconstructed by an anti- k_T algo-
 3068 rithm with $\Delta R=0.5$. After applying these selection cuts, the signal-to-background ratio is
 3069 around 3:1 [343]. The expected number of selected direct γ +jet events is around 1.0M/0.9M
 3070 at $\sqrt{s_{NN}} = 200$ GeV in p+Au collisions for the proposed run in 2024. We conclude that a
 3071 measurement of direct photon-hadron correlation from p+A collisions is feasible, which is
 3072 sensitive to the gluon density in $0.001 < x < 0.005$ in the Au nucleus where parton saturation
 3073 is expected.

3074 **The final state:**

3075 **Nuclear fragmentation functions:** In spite of the remarkable phenomenological suc-
 3076 cesses of QCD, a quantitative understanding of the hadronization process is still one of the
 3077 great challenges for the theory. Hadronization describes the transition of a quark or gluon
 3078 into a final state hadron. It is a poorly understood process even in elementary collisions.
 3079 RHIC's unique versatility will make it possible to study hadronization in vacuum and in the
 3080 nuclear medium, and additionally with polarized beams (see Sect. 3.2.1 for the latter).

3081 It has long been recognized that the hadron distributions within jets produced in p+p
 3082 collisions are closely related to the fragmentation functions that have typically been measured
 3083 in e^+e^- collisions and SIDIS. The key feature of this type of observable is the possibility to
 3084 determine the relevant momentum fraction z experimentally as the ratio of the hadron to the
 3085 jet transverse momentum. Recently [344] a quantitative relationship has been derived in a
 3086 form that enables measurements of identified hadrons in jets in p+p collisions to be included
 3087 in fragmentation function fits on an equal footing with e^+e^- and SIDIS data. Furthermore,
 3088 hadrons in p+p jets provide unique access to the gluon fragmentation function, which is

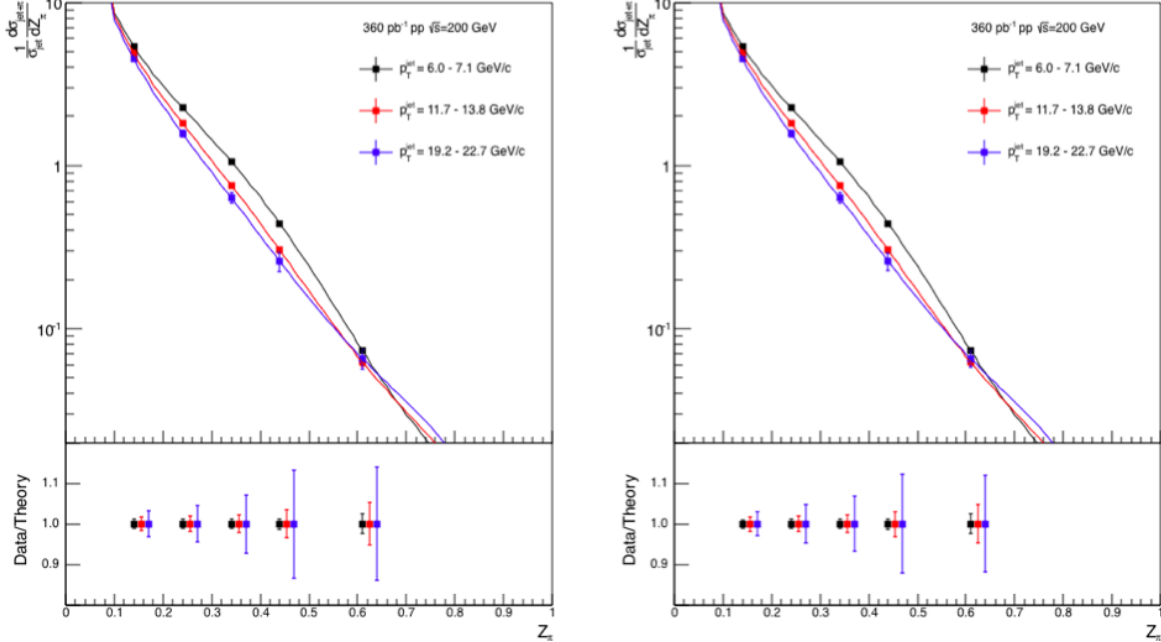


Figure 86: Anticipated precision for identified π^+ (left) and π^- (right) within jets at $|\eta| < 0.4$ in 200 GeV p+p collisions for three representative jet p_T bins. The data points are plotted on theoretical predictions based on the DSS14 pion fragmentation functions [344, 345]. Kaons and (anti)protons will also be measured, over the range from $z < 0.5$ at low jet p_T to $z < 0.2$ at high jet p_T , with uncertainties a factor of ~ 3 larger than those for pions.

3089 poorly determined in current fits [345], in part due to some tension found in the inclusive
 3090 high p_T pion yields measured by the PHENIX and ALICE collaborations. Here, the proposed
 3091 measurements can provide valuable new insight into the nature of this discrepancy.

3092 This development motivated STAR to initiate a program of identified particle fragmen-
 3093 tation function measurements using p+p jet data at 200 and 500 GeV from 2011, 2012, and
 3094 2015. Figure 86 shows the precision that is anticipated for identified π^+ and π^- in 200 GeV
 3095 p+p collisions for three representative jet p_T bins after the existing data from 2012 and 2015
 3096 are combined with future 200 GeV p+p data from 2024. Identified kaon and (anti)proton
 3097 yields will also be obtained, with somewhat less precision, over a more limited range of hadron
 3098 z . Once the 2017 data are fully analyzed, the uncertainties for 510 GeV p+p collisions will
 3099 be comparable to that shown in Fig. 86 at high jet p_T , and a factor of ~ 2 larger than shown
 3100 in Fig. 86 at low jet p_T . Identified hadron yields will also be measured multi-dimensionally
 3101 vs. j_T , z , and jet p_T , which will provide important input for unpolarized TMD fits.

3102 Data from the HERMES experiment [289, 291, 346] have shown that production rates of
 3103 identified hadrons in semi-inclusive deep inelastic $e+A$ scattering differ from those in $e+p$
 3104 scattering. These differences cannot be explained by nuclear PDFs, as nuclear effects of
 3105 strong interactions in the initial state should cancel in this observable. Only the inclusion of
 3106 nuclear effects in the hadronization process allows theory to reproduce all of the dependencies
 3107 (z , x , and Q^2) of R_{eA} seen in SIDIS, as shown in Fig. 87.

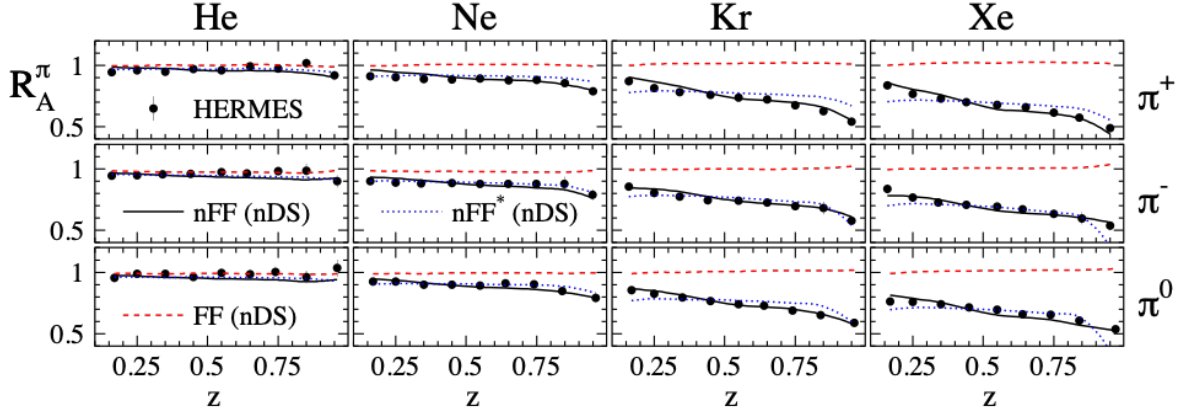


Figure 87: R_{eA} in SIDIS for different nuclei in bins of z as measured by HERMES [289, 291, 346]. The solid lines correspond to the results using effective nuclear FF [298] and the nDS medium modified parton densities [347]. The red dashed lines are estimates assuming the nDS medium modified PDFs but standard DSS vacuum FFs [348, 349] and indicate that nPDFs are insufficient to explain the data

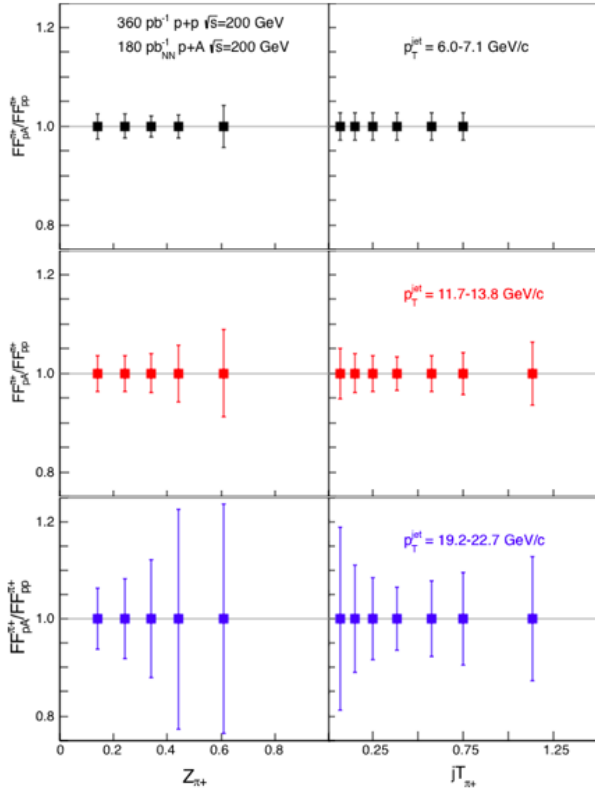


Figure 88: Anticipated precision for measurements of π^+ fragmentation functions in p+A/p+p at $|\eta| < 0.4$ vs. z and j_T in 2024 for three representative jet p_T bins. Uncertainties for π^- will be similar to those shown here for π^+ , while those for kaons and (anti)protons will be a factor of ~ 3 larger. Note that, to be species independent, the nucleon-nucleon equivalent luminosity is specified for p+A.

3108 It is critical to see if these hadronization effects in cold nuclear matter persist at the
3109 higher \sqrt{s} and Q^2 accessed at RHIC and EIC – both to probe the underlying mechanism,
3110 which is not understood currently, and to explore its possible universality. The combination
3111 of p+p jet data from RHIC and future SIDIS data from EIC will also provide a much clearer
3112 picture of modified gluon hadronization than will be possible with EIC data alone. Using
3113 the 200 GeV p+Au data collected in 2015, STAR will be able to make a first opportunistic
3114 measurement of these hadron-jet fragmentation functions in nuclei, but the precision will
3115 be limited. Additional data will be needed in 2024 in order to provide a sensitive test for
3116 universality, as shown in Figure 88.

3117 4 Detector Updates, Operations, and Opportunities

3118 In this section we discuss the performance of the endcap Time of Flight (eTOF) in Run-20
3119 and progress of the construction of the Forward upgrades. The iTPC and EPD were fully
3120 integrated for Run-19.

3121 4.1 Status and Performance of the eTOF

3122 The full eTOF hardware installation was completed in Nov. 2018 followed by the first
3123 data taking started in Feb. 2019 by recording about 580 M Au+Au events at $\sqrt{s_{NN}} =$
3124 19.6 GeV with an eTOF participation of 85%. However, due to several beam loss events
3125 causing instantaneous high currents on the readout strips all eTOF preamplifier boards got
3126 damaged and no further useful operation was possible during that year. It was decided to
3127 replace all preamplifier boards with an improved version using ESD protections diodes on
3128 the input. Beside minor issues eTOF showed an excellence performance during Run-20. A
3129 reliable start-up procedure and control interface was implemented that allows the full system
3130 to be controlled via only 2 commands issued by the shift crew. For Run-20 an improved
3131 clock distribution method was installed offering a system synchronization in the order of 35
3132 ps over the full wheel. Figure 89 shows the width of the time distribution (red corresponds
3133 to the Gaussian sigma and blue to the RMS) obtained by measuring the arrival time of
3134 injected pulser signals on every TDC board. The stability of the system is demonstrated on
3135 the right plot of Fig. 89. Here the mean of time distribution width from all pulser channels
3136 is plotted vs. the run number. The range of 130 runs reflects a time period of several days.

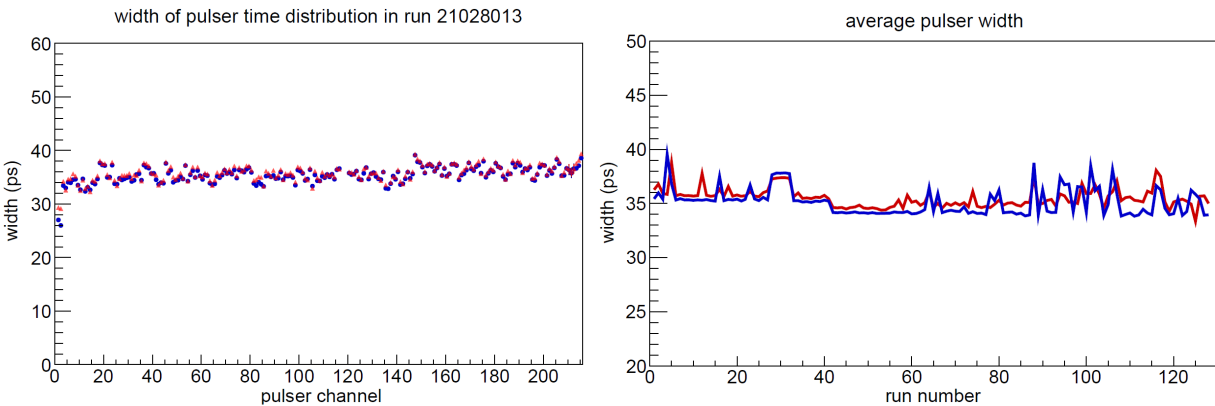


Figure 89: Left: Width of the time distribution obtained by measuring the arrival time of injected pulser signals on every GET4 board. Right: Mean of the time distribution width vs. the run number.

3137 All fixed target runs in 2020 were successfully completed and about 100 M events with
3138 eTOF data were collected for each energy. For the $\sqrt{s_{NN}} = 11.5$ GeV collider run 235 M
3139 events with eTOF data were recorded. The eTOF performance remained stable also during
3140 the Run-20b after the break due to COVID-19.

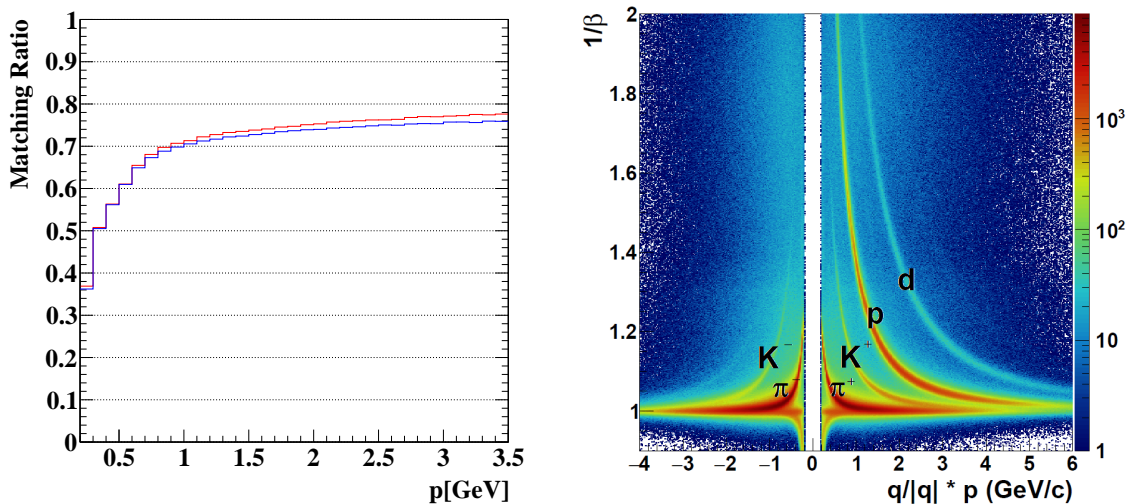


Figure 90: Left: Matching efficiency of MRPC hits in respect to the extrapolated TPC tracks as function of the particle momentum. Right: $1/\beta$ as function of particle momentum. The separation of kaons from pions up to a momenta of 2.5 GeV/c demonstrates the PID capability of eTOF.

3141 In order to demonstrate the eTOF performance fixed target data at $\sqrt{s_{NN}} = 7.7$ GeV were
 3142 calibrated and the matching efficiency with the TPC has been deduced as function of the
 3143 particle momentum (see left Fig.90). At a momentum of 1 GeV/c a matching efficiency of
 3144 70% is obtained for both MRPC types (red and blue are different MRPC types with different
 3145 electrode materials). Beyond 1 GeV/c the curve levels off at 75%. The time resolution (not
 3146 shown here) was determined to be in the order of 80 ps. The good time resolution is
 3147 reflected in the $1/\beta$ versus the particle momenta plot shown in the right Fig. 90. The narrow
 3148 particle bands allow for a kaon to pion separation of up to a momentum of 2.5 GeV/c which
 3149 demonstrates the excellent PID capability of eTOF.

3150 For the upcoming period no major hardware changes for eTOF are foreseen. During Run-
 3151 20 one MRPC counter developed a high dark current and noise and will be replaced at the
 3152 next shutdown. Due to COVID-19 travel restrictions it is planed to ship a fully assembled
 3153 module (3 MRPC counters) to BNL as a replacement for the module housing the broken
 3154 counter. On a different module it is planned to replace one GBTx readout card, which is
 3155 currently not working. A substantial eTOF upgrade will be performed on the firmware side
 3156 of the readout FPGAs which can be done remotely from outside BNL. This implies also
 3157 small adaptations in the control software. With this upgrade an improved startup reliability
 3158 and a more stable operation is intended.

3159 4.2 Forward Upgrade

3160 STAR is constructing a forward detector system, realized by combining tracking with elec-
 3161 tromagnetic and hadronic calorimeters for the years beyond 2021. It will have superior
 3162 detection capability for neutral pions, photons, electrons, jets and leading hadrons covering

3163 a region of $2.5 < \eta < 4$. The design of the Forward Calorimeter System (FCS) is driven by
3164 consideration of detector performance, integration into STAR and cost optimization. For
3165 the electromagnetic calorimeter the refurbished PHENIX sampling EMCal is used, and the
3166 hadronic calorimeter will be newly constructed as a sandwich iron scintillator plate sampling
3167 type, based on the extensive STAR Forward Upgrade and EIC Calorimeter Consortium R&D.
3168 The existing EPD will be used as a trigger detector especially for a 2 electron trigger. Both
3169 calorimeters share the same cost-effective readout electronics, with SiPMs as photo-sensors.
3170 This FCS system will have very good ($\sim 10\%/\sqrt{E}$) electromagnetic and ($\sim 50\%/\sqrt{E} + 10\%$)
3171 hadronic energy resolutions. In addition, a Forward Tracking System (FTS) is being con-
3172 structed. The FTS will be capable of discriminating hadron charge sign for transverse
3173 asymmetry and Drell-Yan measurements in $p+A$. In heavy ion collisions, measurements of
3174 charged particle transverse momenta of $0.2 < p_T < 2$ GeV/ c with 20-30% momentum res-
3175 olution are required. To keep multiple scattering and photon conversion background under
3176 control, the material budget of the FTS must be small. Hence, the FTS design is based on
3177 three Silicon mini-strip detectors that consist of disks with a wedge-shaped design to cover
3178 the full azimuth and $2.5 < \eta < 4.0$; they are read out radially from the outside to minimize
3179 the material. The Si-disks are combined with four small-strip Thin Gap Chamber (sTGC)
3180 wheels following the ATLAS design [350, 351]. The Si mini-strip disks will be placed in the
3181 region $z = 146.6 - 173.7$ cm. The 4 sTGC wheels would be placed 30 cm apart starting from
3182 $z = 273$ cm. The Si-Disks readout is based on APV chips, which will reuse the readout chain
3183 of the IST, which was part of the STAR HFT. For the sTGC the readout will be based on
3184 the ATLAS VMM3 chip [352].

3185 4.2.1 Status

3186 Following the successful directors review in November 2018, the project submitted a proposal
3187 for a NSF MRI for construction of EMCAL and HCAL and the associated electronics. The
3188 NSF MRI was approved in Summer 2019 and work has been ongoing on all aspects of the
3189 upgrade.

3190 4.2.2 Forward Calorimetry System

3191 The platform that supports the HCAL and EMCAL was installed in 2019, followed by the
3192 installation of the refurbished PHENIX EMCAL blocks. The installed EMCAL blocks are
3193 depicted in Fig. 91. The HCAL absorber blocks are under production at Chapman Lake
3194 Instrumentation and Getto Industrial Plating. The first sets of blocks have arrived at BNL.
3195 The scintillating tiles have been produced and all 18200 are in hand. About 10,000 of these
3196 have been polished at ACU and Valpo and are ready for installation. Other parts are being
3197 fabricated at Rutgers, Temple and Ohio State. Front-end electronics cards with the SiPM
3198 and readout for both EMCAL and HCAL are in production and testing is underway. The
3199 front end cards will be readout by 78 DEP/ADC boards and 3 trigger processor boards
3200 housed in 5 crates. About half have been delivered and are undergoing testing at BNL.
3201 All DAQ PCs and receiver cards have been installed. The installation will commence once

3202 the Run-20b is completed by mid September, and key personnel has come to BNL. The
3203 commissioning of the FCS will be continue during Run-21, and will be ready for Run-22.



Figure 91: A view of the installed forward ECal detector halves, left and right from the beam pipe.

3204 4.2.3 Forward Silicon Tracking

3205 The procedures for the Si-detector module fabrication has been developed and documented.
3206 Several prototype mechanical structures with hybrids mounted have been produced and
3207 two wedges were assembled with Si-sensors. Performance of two fully assembled prototype
3208 wedges have been evaluated with cosmic ray data and show that all channels can be read out,
3209 the signal-to-noise meets requirements, and the efficiency is higher than 90%. The design

3210 of the support structures and the interface to the detector modules is nearly complete. If
3211 time allows in the upcoming shutdown a test installation of the support frame into STAR
3212 is planned. The cooling system, which was used previously for the HFT IST sub-system,
3213 has been revived and verification of its performance is on-going. An internal production
3214 readiness review with external reviewers was held on August 3, and the initial steps of the
3215 mass production have started. The review recommendations, which were useful, will be
3216 implemented. Currently there is only limited schedule float for the installation in August
3217 2021.

3218 4.2.4 sTGC Tracking

3219 A full prototype module of the sTGC was designed and produced at Shandong University
3220 and tested. This module is now at BNL to undergo testing with the n-pentane gas system
3221 that is being built at BNL. Due to space constraints around the beam pipe the final detector
3222 will have pentagon shaped modules. The design is complete and production has started
3223 of the final pre-production module; mass production is expected to start in October. The
3224 read-out electronics are based on the ATLAS VMM3 chip [352] developed for the same kind
3225 of detector. The strips of each sTGC layer can be handled by 24 Front-End Boards (FEB).
3226 In total 96 FEBs are needed for 4 sTGC layers. The FEBs are vertically inserted in the
3227 sTGC chamber. The signals are sent to Readout Boards (ROD) placed in standard VME
3228 crates and interfaced to the STAR DAQ. The electronics design and fabrication is done at
3229 USTC, Hefei. The FEB prototype boards have been tested, the prototype RDO is under
3230 construction, and the VMM3 chips are being procured. The design of the installation and
3231 mounting frames need to be finished. The n-pentane gas system and Interlocks have been
3232 designed and have been approved.

3233 4.2.5 Software

3234 The trigger algorithms for the FCS have been well defined and simulated, the FPGA codes
3235 are currently under development.

3236 The forward tracking utilizing hits from the 4 sTGC planes and 3 Si-layers has been de-
3237 veloped and good performance has been demonstrated. As forward tracking is very different
3238 than mid-rapidity tracking new tools had to be developed. The tracking algorithm is based
3239 on modern techniques and depends on GENFIT, a general purpose tracking toolkit and in
3240 addition the iLCSoft KiTrack a Cellular Automata library are used to seed track finding.

3241 References

- 3242 [1] STAR, L. Adamczyk *et al.*, Phys. Rev. C **96**, 024905 (2017), 1702.01108.
- 3243 [2] STAR, R. Kunnawalkam Elayavalli, PoS **HardProbes2018**, 090 (2018), 1903.12115.
- 3244 [3] STAR, J. Adam *et al.*, Phys. Rev. D **101**, 052004 (2020), 1912.08187.
- 3245 [4] STAR, J. Adam *et al.*, Phys. Rev. C **102**, 014905 (2020), 1911.12168.
- 3246 [5] STAR, J. Adam *et al.*, (2019), 1906.09363.
- 3247 [6] STAR, J. Adam *et al.*, (2020), 2003.02114.
- 3248 [7] STAR, J. Adam *et al.*, (2020), 2006.00582.
- 3249 [8] STAR, J. Adam *et al.*, Phys. Rev. D **100**, 052005 (2019), 1906.02740.
- 3250 [9] STAR, R. Licenik, Measurement of inclusive jet production in Au+Au collisions at
3251 $\sqrt{s_{NN}} = 200$ GeV by the STAR experiment, 2020, 2008.10006.
- 3252 [10] STAR, N. R. Sahoo, Measurement of γ +jet and π^0 +jet in central Au+Au collisions
3253 at $\sqrt{s_{NN}} = 200$ GeV with the STAR experiment, 2020, 2008.08789.
- 3254 [11] T. Sjöstrand *et al.*, Comput. Phys. Commun. **191**, 159 (2015), 1410.3012.
- 3255 [12] ATLAS, M. Aaboud *et al.*, Phys. Rev. Lett. **123**, 042001 (2019), 1902.10007.
- 3256 [13] CMS, S. Chatrchyan *et al.*, Phys. Rev. C **90**, 024908 (2014), 1406.0932.
- 3257 [14] STAR, S. Oh, Measurement of semi-inclusive jet fragmentation functions in Au+Au
3258 collisions at $\sqrt{s_{NN}} = 200$ GeV in STAR, 2020, 2008.08631.
- 3259 [15] STAR, L. Adamczyk *et al.*, Phys. Rev. Lett. **119**, 062301 (2017), 1609.03878.
- 3260 [16] SN0619 : A Proposal for STAR Inner TPC Sector Upgrade (iTTPC) [https://drupal.](https://drupal.star.bnl.gov/STAR/starnotes/public/sn0619)
3261 [star.bnl.gov/STAR/starnotes/public/sn0619](https://drupal.star.bnl.gov/STAR/starnotes/public/sn0619).
- 3262 [17] STAR, CBM eTOF Group, The CBM Collaboration eTOF Group, (2016), 1609.05102.
- 3263 [18] J. Adams *et al.*, Nucl. Instrum. Meth. A **968**, 163970 (2020), 1912.05243.
- 3264 [19] STAR, J. Adam *et al.*, Phys. Rev. C **98**, 014910 (2018), 1805.04400.
- 3265 [20] STAR, L. Adamczyk *et al.*, Nature **548**, 62 (2017), 1701.06657.
- 3266 [21] W.-T. Deng and X.-G. Huang, Phys. Rev. C **93**, 064907 (2016), 1603.06117.

- 3267 [22] STAR, J. Adams, Differential measurements of Λ polarization in Au+Au
3268 collisions and a search for the magnetic field by STAR, in *the XXVII-*
3269 *Ith International Conference on Ultra-relativistic Nucleus-Nucleus Collisions*, 2019,
3270 <https://indico.cern.ch/event/792436/contributions/3535689/>.
- 3271 [23] I. Karpenko and F. Becattini, *Eur. Phys. J. C* **77**, 213 (2017), 1610.04717.
- 3272 [24] Y. Jiang, Z.-W. Lin, and J. Liao, *Phys. Rev. C* **94**, 044910 (2016), 1602.06580, [Erra-
3273 tum: *Phys.Rev.C* 95, 049904 (2017)].
- 3274 [25] K. Schilling, P. Seyboth, and G. E. Wolf, *Nucl. Phys. B* **15**, 397 (1970), [Erratum:
3275 *Nucl.Phys.B* 18, 332 (1970)].
- 3276 [26] STAR, S. Singha, Measurement of global spin alignment of k^*0 , $k^*\pm$
3277 and ϕ vector mesons using the STAR detector at RHIC, in *the XXVII-*
3278 *Ith International Conference on Ultra-relativistic Nucleus-Nucleus Collisions*, 2019,
3279 <https://indico.cern.ch/event/792436/contributions/3535685/>.
- 3280 [27] R. Bryan and B. Scott, *Phys. Rev.* **177**, 1435 (1969).
- 3281 [28] M. Nagels, T. Rijken, and J. de Swart, *Phys. Rev. D* **17**, 768 (1978).
- 3282 [29] STAR, L. Adamczyk *et al.*, *Phys. Rev. Lett.* **115**, 222301 (2015), 1505.07812.
- 3283 [30] STAR, S. Huang, Explore the nuclei deformation with a expanding
3284 QGP fireball, in *The 36th Winter Workshop on Nuclear Dynamics*, 2020,
3285 <https://indico.cern.ch/event/841247/contributions/3740391/>.
- 3286 [31] G. Giacalone, *Phys. Rev. Lett.* **124**, 202301 (2020), 1910.04673.
- 3287 [32] U. Heinz and R. Snellings, *Ann. Rev. Nucl. Part. Sci.* **63**, 123 (2013), 1301.2826.
- 3288 [33] STAR, J. Adam *et al.*, (2020), 2006.13537.
- 3289 [34] ALICE, S. Acharya *et al.*, *Phys. Lett.* **B773**, 68 (2017), 1705.04377.
- 3290 [35] P. Alba *et al.*, (2017), 1711.05207.
- 3291 [36] B. Schenke, C. Shen, and P. Tribedy, *Phys. Rev.* **C99**, 044908 (2019), 1901.04378.
- 3292 [37] H. Song, S. A. Bass, U. Heinz, T. Hirano, and C. Shen, *Phys. Rev. Lett.* **106**, 192301
3293 (2011), 1011.2783, [Erratum: *Phys.Rev.Lett.* 109, 139904 (2012)].
- 3294 [38] D. Teaney and L. Yan, *Phys. Rev.* **C83**, 064904 (2011), 1010.1876.
- 3295 [39] Z. Qiu and U. W. Heinz, *Phys.Rev.* **C84**, 024911 (2011), 1104.0650.
- 3296 [40] G. Denicol, H. Niemi, E. Molnar, and D. Rischke, *Phys. Rev. D* **85**, 114047 (2012),
3297 1202.4551, [Erratum: *Phys.Rev.D* 91, 039902 (2015)].

- 3298 [41] W. Florkowski, R. Ryblewski, and M. Spaliński, Phys. Rev. D **94**, 114025 (2016),
3299 1608.07558.
- 3300 [42] K. Dusling and R. Venugopalan, Phys. Rev. Lett. **108**, 262001 (2012), 1201.2658.
- 3301 [43] PHENIX, C. Aidala *et al.*, Nature Phys. **15**, 214 (2019), 1805.02973.
- 3302 [44] CMS, S. Chatrchyan *et al.*, Phys. Lett. B **724**, 213 (2013), 1305.0609.
- 3303 [45] STAR, R. A. Lacey, Long-range collectivity in small collision-systems with two- and
3304 four-particle correlations @ STAR, in *28th International Conference on Ultrarelativistic*
3305 *Nucleus-Nucleus Collisions*, 2020, 2002.11889.
- 3306 [46] L. D. McLerran and T. Toimela, Phys. Rev. D **31**, 545 (1985).
- 3307 [47] H. Weldon, Phys. Rev. D **42**, 2384 (1990).
- 3308 [48] R. Rapp and J. Wambach, Eur. Phys. J. A **6**, 415 (1999), hep-ph/9907502.
- 3309 [49] P. M. Hohler and R. Rapp, Phys. Lett. B **731**, 103 (2014), 1311.2921.
- 3310 [50] C. Jung and L. von Smekal, Phys. Rev. D **100**, 116009 (2019), 1909.13712.
- 3311 [51] H.-T. Ding *et al.*, Phys. Rev. D **83**, 034504 (2011), 1012.4963.
- 3312 [52] J. Atchison and R. Rapp, J. Phys. Conf. Ser. **832**, 012057 (2017).
- 3313 [53] R. Rapp and H. van Hees, Phys. Lett. B **753**, 586 (2016), 1411.4612.
- 3314 [54] R. Chatterjee, D. K. Srivastava, U. W. Heinz, and C. Gale, Phys. Rev. C **75**, 054909
3315 (2007), nucl-th/0702039.
- 3316 [55] J. Deng, Q. Wang, N. Xu, and P. Zhuang, Phys. Lett. B **701**, 581 (2011), 1009.3091.
- 3317 [56] P. Mohanty *et al.*, Phys. Rev. C **85**, 031903 (2012), 1111.2159.
- 3318 [57] E. Speranza, A. Jaiswal, and B. Friman, Phys. Lett. B **782**, 395 (2018), 1802.02479.
- 3319 [58] STAR, L. Adamczyk *et al.*, Phys. Rev. Lett. **113**, 022301 (2014), 1312.7397, [Adden-
3320 dum: Phys.Rev.Lett. 113, 049903 (2014)].
- 3321 [59] STAR, L. Adamczyk *et al.*, Phys. Rev. C **92**, 024912 (2015), 1504.01317.
- 3322 [60] STAR, L. Adamczyk *et al.*, Phys. Lett. B **750**, 64 (2015), 1501.05341.
- 3323 [61] STAR, J. Adam *et al.*, (2018), 1810.10159.
- 3324 [62] B. B. Brandt, A. Francis, H. B. Meyer, and H. Wittig, JHEP **03**, 100 (2013), 1212.4200.
- 3325 [63] STAR, J. Adam *et al.*, (2019), 1910.12400.

- 3326 [64] G. Baur, Nucl. Phys. Proc. Suppl. **184**, 143 (2008), 0711.2882.
- 3327 [65] C. Li, J. Zhou, and Y.-J. Zhou, Phys. Rev. D **101**, 034015 (2020), 1911.00237.
- 3328 [66] S. Klein, A. Mueller, B.-W. Xiao, and F. Yuan, (2020), 2003.02947.
- 3329 [67] STAR Collaboration, J. Adam *et al.*, Phys. Rev. Lett. **124**, 172301 (2020).
- 3330 [68] J. Adam *et al.*, Physics Letters B **797**, 134917 (2019).
- 3331 [69] STAR Collaboration, J. Adam *et al.*, Phys. Rev. Lett. **123**, 162301 (2019).
- 3332 [70] STAR Collaboration, J. Adam *et al.*, Phys. Rev. C **99**, 034908 (2019).
- 3333 [71] M. Djordjevic, Phys. Rev. Lett. **112**, 042302 (2014).
- 3334 [72] H. van Hees, M. Mannarelli, V. Greco, and R. Rapp, Phys. Rev. Lett. **100**, 192301
3335 (2008).
- 3336 [73] S. Cao, G.-Y. Qin, and S. A. Bass, Phys. Rev. C **92**, 024907 (2015).
- 3337 [74] P. B. Gossiaux and J. Aichelin, Phys. Rev. C **78**, 014904 (2008).
- 3338 [75] M. Djordjevic and M. Djordjevic, Phys. Rev. C **90**, 034910 (2014).
- 3339 [76] STAR Collaboration, L. Adamczyk *et al.*, Phys. Rev. Lett. **118**, 212301 (2017).
- 3340 [77] STAR Collaboration, L. Adamczyk *et al.*, Phys. Rev. C **95**, 034907 (2017).
- 3341 [78] D. Kharzeev and R. D. Pisarski, Phys.Rev. **D61**, 111901 (2000), hep-ph/9906401.
- 3342 [79] D. Kharzeev, Phys.Lett. **B633**, 260 (2006), hep-ph/0406125.
- 3343 [80] S. A. Voloshin, Phys. Rev. Lett. **105**, 172301 (2010), 1006.1020.
- 3344 [81] W.-T. Deng, X.-G. Huang, G.-L. Ma, and G. Wang, Phys. Rev. C **97**, 044901 (2018),
3345 1802.02292.
- 3346 [82] H.-J. Xu *et al.*, Phys. Rev. Lett. **121**, 022301 (2018), 1710.03086.
- 3347 [83] J. Hammelmann, A. Soto-Ontoso, M. Alvioli, H. Elfner, and M. Strikman, (2019),
3348 1908.10231.
- 3349 [84] STAR 2017 BUR [https://drupal.star.bnl.gov/STAR/system/files/STAR_BUR_](https://drupal.star.bnl.gov/STAR/system/files/STAR_BUR_Run1718_v22_0.pdf)
3350 [Run1718_v22_0.pdf](https://drupal.star.bnl.gov/STAR/system/files/STAR_BUR_Run1718_v22_0.pdf).
- 3351 [85] STAR, J. Adam *et al.*, (2019), 1911.00596.
- 3352 [86] STAR, J. Zhao, (2020), 2002.09410.

- 3353 [87] CMS, A. M. Sirunyan *et al.*, Phys. Rev. **C97**, 044912 (2018), 1708.01602.
- 3354 [88] H.-j. Xu *et al.*, Chin. Phys. **C42**, 084103 (2018), 1710.07265.
- 3355 [89] S. A. Voloshin, Phys. Rev. **C98**, 054911 (2018), 1805.05300.
- 3356 [90] J. Zhao, H. Li, and F. Wang, Eur. Phys. J. C **79**, 168 (2019), 1705.05410.
- 3357 [91] STAR, J. Adam *et al.*, (2020), arXiv:2006.05035.
- 3358 [92] STAR, P. Tribedy, Nucl. Phys. A **967**, 740 (2017), 1704.03845.
- 3359 [93] STAR, J. Adam *et al.*, (2020), arXiv:2006.04251.
- 3360 [94] STAR, Y. Lin, (2020), 2002.11446.
- 3361 [95] N. Magdy, S. Shi, J. Liao, N. Ajitanand, and R. A. Lacey, Phys. Rev. C **97**, 061901
3362 (2018), 1710.01717.
- 3363 [96] A. Tang, Chin. Phys. C **44**, 054101 (2020), 1903.04622.
- 3364 [97] L. Finch and S. Murray, Phys. Rev. C **96**, 044911 (2017), 1801.06476.
- 3365 [98] STAR, M. Zurek, Longitudinal double-spin asymmetries for inclusive jets produced
3366 in $\sqrt{s} = 200$ GeV proton-proton collisions at STAR, in *Nuclear Physics Seminar,*
3367 *Brookhaven National Laboratory*, 2020, <https://indico.bnl.gov/event/8632/>.
- 3368 [99] STAR, N. Lukow, Longitudinal double-spin asymmetries for dijets pro-
3369 duced in $\sqrt{s} = 200$ GeV proton-proton collisions at STAR, 2020,
3370 <https://drupal.star.bnl.gov/STAR/blog/nlukow/dijet-all-2015-preliminary>.
- 3371 [100] STAR, L. Adamczyk *et al.*, Phys. Rev. Lett. **115**, 092002 (2015), 1405.5134.
- 3372 [101] STAR, L. Adamczyk *et al.*, Phys. Rev. **D95**, 071103 (2017), 1610.06616.
- 3373 [102] D. de Florian, R. Sassot, M. Stratmann, and W. Vogelsang, Phys. Rev. Lett. **113**,
3374 012001 (2014), 1404.4293.
- 3375 [103] NNPDF, E. R. Nocera, R. D. Ball, S. Forte, G. Ridolfi, and J. Rojo, Nucl. Phys.
3376 **B887**, 276 (2014), 1406.5539.
- 3377 [104] J. Adam *et al.*, Physical Review D **100** (2019).
- 3378 [105] STAR, T. Lin, Azimuthal Transverse Single-Spin Asymmetries of Charged Pions
3379 Within Jets from Polarized pp Collisions at $\sqrt{s} = 200$ GeV, in *Nuclear Physics Semi-*
3380 *nar, Brookhaven National Laboratory*, 2020, <https://indico.bnl.gov/event/8633/>.

- 3381 [106] STAR, H. Liu, Measurement of transverse single-spin asymmetries for dijet production
3382 in polarized p+p collisions at $\sqrt{s} = 200$ GeV at STAR, in *Nuclear Physics Seminar,*
3383 *Brookhaven National Laboratory*, 2020, <https://indico.bnl.gov/event/8633/>.
- 3384 [107] STAR, S. Heppelmann, Preview from RHIC Run 15 pp and pAu Forward Neutral
3385 Pion Production from Transversely Polarized Protons, in *7th International Workshop*
3386 *on Multiple Partonic Interactions at the LHC*, pp. 228–231, 2016.
- 3387 [108] STAR, Z. Zhu, Measurement of transverse single spin asymmetries at forward rapidities
3388 by the STAR experiment at $\sqrt{s} = 200$ and 500 GeV at STAR, in *Nuclear Physics*
3389 *Seminar, Brookhaven National Laboratory*, 2020, <https://indico.bnl.gov/event/8632/>.
- 3390 [109] Z.-B. Kang, X. Liu, F. Ringer, and H. Xing, *JHEP* **11**, 068 (2017), 1705.08443.
- 3391 [110] Z.-B. Kang, A. Prokudin, F. Ringer, and F. Yuan, *Phys. Lett. B* **774**, 635 (2017),
3392 1707.00913.
- 3393 [111] U. D’Alesio, F. Murgia, and C. Pisano, *Phys. Rev. D* **83**, 034021 (2011), 1011.2692.
- 3394 [112] J. K. Adkins, *Studying Transverse Momentum Dependent Distributions in Polarized*
3395 *Proton Collisions via Azimuthal Single Spin Asymmetries of Charged Pions in Jets*,
3396 PhD thesis, University of Kentucky, 2015, 1907.11233.
- 3397 [113] STAR, B. Abelev *et al.*, *Phys. Rev. Lett.* **99**, 142003 (2007), 0705.4629.
- 3398 [114] J. Cammarota *et al.*, (2020), 2002.08384.
- 3399 [115] STAR, E. Braidot, Suppression of Forward Pion Correlations in d+Au Interactions
3400 at STAR, in *45th Rencontres de Moriond on QCD and High Energy Interactions*, pp.
3401 355–338, 2010, 1005.2378.
- 3402 [116] STAR, M. Posik, *PoS DIS2019*, 028 (2019), 1908.08490.
- 3403 [117] NuSea, R. S. Towell *et al.*, *Phys. Rev.* **D64**, 052002 (2001), hep-ex/0103030.
- 3404 [118] SeaQuest, K. Nagai, *PoS DIS2018*, 033 (2018).
- 3405 [119] STAR, S. Fazio, Measurements of weak boson production with the STAR detector,
3406 in *QCD Spin Physics: A Symposium to Honor Jacques Soffer, Brookhaven National*
3407 *Laboratory*, 2019, <https://indico.bnl.gov/event/6274/>.
- 3408 [120] V. Bertone, I. Scimemi, and A. Vladimirov, *JHEP* **06**, 028 (2019), 1902.08474.
- 3409 [121] M. A. Stephanov, K. Rajagopal, and E. V. Shuryak, *Phys. Rev. D* **60**, 114028 (1999),
3410 hep-ph/9903292.
- 3411 [122] M. Stephanov, *Phys. Rev. Lett.* **107**, 052301 (2011), 1104.1627.

- 3412 [123] STAR, J. Adam *et al.*, (2020), 2001.02852.
- 3413 [124] HADES, J. Adamczewski-Musch *et al.*, (2020), 2002.08701.
- 3414 [125] B. Ling and M. A. Stephanov, Phys. Rev. C **93**, 034915 (2016), 1512.09125.
- 3415 [126] STAR, L. Adamczyk *et al.*, Phys. Rev. **C96**, 044904 (2017), 1701.07065.
- 3416 [127] F. Becattini, J. Manninen, and M. Gazdzicki, Phys. Rev. C **73**, 044905 (2006), hep-
3417 ph/0511092.
- 3418 [128] A. Andronic, P. Braun-Munzinger, and J. Stachel, Phys. Lett. B **673**, 142 (2009),
3419 0812.1186, [Erratum: Phys.Lett.B 678, 516 (2009)].
- 3420 [129] J. Cleymans, D. Elliott, A. Keranen, and E. Suhonen, Phys. Rev. C **57**, 3319 (1998),
3421 nucl-th/9711066.
- 3422 [130] J. Cleymans, A. Forster, H. Oeschler, K. Redlich, and F. Uhlig, Phys. Lett. B **603**,
3423 146 (2004), hep-ph/0406108.
- 3424 [131] I. Kraus, J. Cleymans, H. Oeschler, K. Redlich, and S. Wheaton, Phys. Rev. C **76**,
3425 064903 (2007), 0707.3879.
- 3426 [132] HADES, J. Adamczewski-Musch *et al.*, Phys. Lett. B **778**, 403 (2018), 1703.08418.
- 3427 [133] FOPI, K. Piasecki *et al.*, Phys. Rev. C **94**, 014901 (2016), 1602.04378.
- 3428 [134] A. Andronic, P. Braun-Munzinger, J. Stachel, and H. Stocker, Phys. Lett. B **697**, 203
3429 (2011), 1010.2995.
- 3430 [135] C. Shen and S. Alzhrani, Phys. Rev. C **102**, 014909 (2020), 2003.05852.
- 3431 [136] NA49, T. Anticic *et al.*, Phys. Rev. **C83**, 014901 (2011), 1009.1747.
- 3432 [137] BRAHMS, I. Arsene *et al.*, Phys. Rev. Lett. **93**, 242303 (2004), nucl-ex/0403005.
- 3433 [138] Yu. B. Ivanov, Phys. Rev. **C87**, 064905 (2013), 1304.1638.
- 3434 [139] K. Dusling, W. Li, and B. Schenke, Int. J. Mod. Phys. **E25**, 1630002 (2016),
3435 1509.07939.
- 3436 [140] L. He *et al.*, Phys. Lett. **B753**, 506 (2016), 1502.05572.
- 3437 [141] A. Kurkela, U. A. Wiedemann, and B. Wu, Kinetic transport is needed to reliably ex-
3438 tract shear viscosity from pA and AA data, in Vol. arXiv:1805.04081, 2018, 1805.04081.
- 3439 [142] P. Romatschke, Eur. Phys. J. **C78**, 636 (2018), 1802.06804.
- 3440 [143] J. L. Nagle and W. A. Zajc, Ann. Rev. Nucl. Part. Sci. **68**, 211 (2018), 1801.03477.

- 3441 [144] B. Schenke, S. Schlichting, and R. Venugopalan, Phys. Lett. **B747**, 76 (2015),
3442 1502.01331.
- 3443 [145] J. L. Nagle *et al.*, Phys. Rev. Lett. **113**, 112301 (2014), 1312.4565.
- 3444 [146] PHENIX, A. Adare *et al.*, Phys. Rev. Lett. **111**, 212301 (2013), 1303.1794.
- 3445 [147] STAR, S. Huang, Nucl. Phys. A **982**, 475 (2019).
- 3446 [148] B. Schenke, C. Shen, and P. Tribedy, (2020), 2005.14682.
- 3447 [149] P. Romatschke, Eur. Phys. J. C **75**, 305 (2015), 1502.04745.
- 3448 [150] C. Shen, J.-F. Paquet, G. S. Denicol, S. Jeon, and C. Gale, Phys. Rev. C **95**, 014906
3449 (2017), 1609.02590.
- 3450 [151] Workshop on collectivity of small systems in high-energy collisions, 14-16 march 2019,
3451 <https://indico.cern.ch/event/771998/>, Accessed May 2019.
- 3452 [152] STAR, STAR Public Note SN0644 - Technical Design Report for the iTPC Upgrade,
3453 <https://drupal.star.bnl.gov/STAR/starnotes/public/sn0644>.
- 3454 [153] STAR, STAR Public Note SN0666 - An Event Plane Detector for STAR, <https://drupal.star.bnl.gov/STAR/starnotes/public/sn0666>.
3455
- 3456 [154] STAR, STAR Public Note SN0648 - The STAR Forward Calorimeter System and
3457 Forward Tracking System beyond BES-II, <https://drupal.star.bnl.gov/STAR/starnotes/public/sn0648>.
3458
- 3459 [155] Z. Citron *et al.* *Report from Working Group 5: Future physics opportunities for high-*
3460 *density QCD at the LHC with heavy-ion and proton beams* Vol. 7 (, 2019), pp. 1159–
3461 1410, 1812.06772.
- 3462 [156] ALICE, K. Aamodt *et al.*, Phys. Rev. Lett. **105**, 252302 (2010), 1011.3914.
- 3463 [157] PHENIX, S. S. Adler *et al.*, Phys. Rev. Lett. **94**, 232302 (2005), nucl-ex/0411040.
- 3464 [158] STAR, J. Adam *et al.*, Phys. Lett. **B784**, 26 (2018), 1804.08647.
- 3465 [159] ATLAS, M. Aaboud *et al.*, Eur. Phys. J. **C78**, 997 (2018), 1808.03951.
- 3466 [160] PHENIX, A. Adare *et al.*, Phys. Rev. Lett. **107**, 252301 (2011), 1105.3928.
- 3467 [161] ATLAS, G. Aad *et al.*, Phys. Rev. C **90**, 044906 (2014), 1409.1792.
- 3468 [162] STAR, B. I. Abelev *et al.*, Phys. Rev. Lett. **99**, 112301 (2007), nucl-ex/0703033.
- 3469 [163] CMS Collaboration, Phys. Lett. B **765**, 193 (2017), 1606.06198.

- 3470 [164] CMS Collaboration, Phys. Rev. Lett. **115**, 012301 (2015), 1502.05382.
- 3471 [165] ATLAS, M. Aaboud *et al.*, Phys. Lett. **B789**, 444 (2019), 1807.02012.
- 3472 [166] ALICE, S. Acharya *et al.*, Investigations of anisotropic flow using multi-particle
3473 azimuthal correlations in pp, p-Pb, Xe-Xe, and Pb-Pb collisions at the LHC,
3474 arXiv:1903.01790, 2019, 1903.01790.
- 3475 [167] PHENIX, C. Aidala *et al.*, Phys. Rev. Lett. **120**, 062302 (2018), 1707.06108.
- 3476 [168] A. Huss *et al.*, (2020), 2007.13758.
- 3477 [169] A. Huss *et al.*, (2020), 2007.13754.
- 3478 [170] K. J. Sun, L.-W. Chen, C. M. Ko, J. Pu, and Z. Xu, Phys. Lett. **B781**, 499 (2018),
3479 1801.09382.
- 3480 [171] STAR, L. Adamczyk *et al.*, Phys. Rev. Lett. **112**, 032302 (2014), 1309.5681.
- 3481 [172] STAR, L. Adamczyk *et al.*, Phys. Rev. Lett. **113**, 092301 (2014), 1402.1558.
- 3482 [173] STAR, L. Adamczyk *et al.*, Phys. Lett. **B785**, 551 (2018), 1709.00773.
- 3483 [174] STAR, X. Luo, PoS **CPOD2014**, 019 (2015), 1503.02558.
- 3484 [175] X. Luo, Nucl. Phys. **A956**, 75 (2016), 1512.09215.
- 3485 [176] A. Bzdak, V. Koch, D. Oliinychenko, and J. Steinheimer, Phys. Rev. **C98**, 054901
3486 (2018), 1804.04463.
- 3487 [177] STAR, J. Adam *et al.*, accepted by PRC **arXiv:1903.11778** (2019), 1903.11778.
- 3488 [178] STAR, D. Zhang, Light Nuclei (*d*, *t*) Production in Au + Au Collisions at $\sqrt{s_{NN}} =$
3489 7.7 - 200 GeV, in *28th International Conference on Ultrarelativistic Nucleus-Nucleus*
3490 *Collisions*, 2020, 2002.10677.
- 3491 [179] H. Liu *et al.*, Phys. Lett. B **805**, 135452 (2020), 1909.09304.
- 3492 [180] M. Danysz *et al.*, Phys. Rev. Lett. **11**, 29 (1963).
- 3493 [181] D. Prowse, Phys. Rev. Lett. **17**, 782 (1966).
- 3494 [182] S. Aoki *et al.*, Prog. Theor. Phys. **85**, 1287 (1991).
- 3495 [183] H. Takahashi *et al.*, Nucl. Phys. A **721**, 951 (2003).
- 3496 [184] T. A. Rijken, M. Nagels, and Y. Yamamoto, Prog. Theor. Phys. Suppl. **185**, 14 (2010).
- 3497 [185] I. Arsene *et al.*, Phys. Rev. C **75**, 034902 (2007), nucl-th/0609042.

- 3498 [186] J. Harris *et al.*, Phys. Lett. B **153**, 377 (1985).
- 3499 [187] R. Stock, Phys. Rept. **135**, 259 (1986).
- 3500 [188] J. Molitoris and H. Stoecker, Phys. Rev. C **32**, 346 (1985).
- 3501 [189] H. Kruse, B. Jacak, and H. Stoecker, Phys. Rev. Lett. **54**, 289 (1985).
- 3502 [190] P. Danielewicz, R. Lacey, and W. G. Lynch, Science **298**, 1592 (2002), nucl-th/0208016.
- 3503 [191] W. Reisdorf, Heavy ion collisions in the 1A GeV regime: how well do we join up to
3504 astrophysics?, in *International Workshop on Nuclear Symmetry Energy and Reaction*
3505 *Mechanisms*, 2013, 1307.4210.
- 3506 [192] J. Aichelin and C. M. Ko, Phys. Rev. Lett. **55**, 2661 (1985).
- 3507 [193] KAOS, C. T. Sturm *et al.*, Phys. Rev. Lett. **86**, 39 (2001), nucl-ex/0011001.
- 3508 [194] C. Hartnack and J. Aichelin, J. Phys. G **28**, 1649 (2002).
- 3509 [195] C. Fuchs *et al.*, J. Phys. G **28**, 1615 (2002), nucl-th/0103036.
- 3510 [196] T. Klahn *et al.*, Phys. Rev. C **74**, 035802 (2006), nucl-th/0602038.
- 3511 [197] T. Fischer *et al.*, Nature Astron. **2**, 980 (2018), 1712.08788.
- 3512 [198] A. Aprahamian *et al.*, Reaching for the horizon: The 2015 long range plan for
3513 nuclear science, 2015, The 2015 Long Range Plan for Nuclear Science “Reach-
3514 ing for the Horizon” [http://science.energy.gov/~media/np/nsac/pdf/2015LRP/](http://science.energy.gov/~media/np/nsac/pdf/2015LRP/2015_LRPNS_091815.pdf)
3515 [2015_LRPNS_091815.pdf](http://science.energy.gov/~media/np/nsac/pdf/2015LRP/2015_LRPNS_091815.pdf).
- 3516 [199] RHIC luminosity projection [https://www.rhichome.bnl.gov//RHIC/Runs/](https://www.rhichome.bnl.gov//RHIC/Runs/RhicProjections.pdf)
3517 [RhicProjections.pdf](https://www.rhichome.bnl.gov//RHIC/Runs/RhicProjections.pdf).
- 3518 [200] The STAR Forward Calorimeter System and Forward Tracking System beyond
3519 BES-II [https://drupal.star.bnl.gov/STAR/files/Proposal.ForwardUpgrade.](https://drupal.star.bnl.gov/STAR/files/Proposal.ForwardUpgrade.Nov_.2018.Review.pdf)
3520 [Nov_.2018.Review.pdf](https://drupal.star.bnl.gov/STAR/files/Proposal.ForwardUpgrade.Nov_.2018.Review.pdf).
- 3521 [201] G. Denicol, A. Monnai, and B. Schenke, Phys. Rev. Lett. **116**, 212301 (2016),
3522 1512.01538.
- 3523 [202] H. Niemi, G. S. Denicol, P. Huovinen, E. Molnar, and D. H. Rischke, Phys. Rev. **C86**,
3524 014909 (2012), 1203.2452.
- 3525 [203] B. Schenke and S. Schlichting, Phys. Rev. **C94**, 044907 (2016), 1605.07158.
- 3526 [204] W. Li, Nucl. Phys. A **967**, 59 (2017), 1704.03576.
- 3527 [205] P. Bozek, W. Broniowski, and J. Moreira, Phys. Rev. **C83**, 034911 (2011), 1011.3354.

- 3528 [206] J. Jia and P. Huo, Phys. Rev. **C90**, 034915 (2014), 1403.6077.
- 3529 [207] L.-G. Pang, H. Petersen, G.-Y. Qin, V. Roy, and X.-N. Wang, Eur. Phys. J. **A52**, 97
3530 (2016), 1511.04131.
- 3531 [208] CMS, V. Khachatryan *et al.*, Phys. Rev. C **92**, 034911 (2015), 1503.01692.
- 3532 [209] ATLAS, M. Aaboud *et al.*, Eur. Phys. J. C **78**, 142 (2018), 1709.02301.
- 3533 [210] STAR Collaboration, L. Adamczyk *et al.*, Manuscript under preparation (2016).
- 3534 [211] A. Behera, M. Nie, and J. Jia, Phys. Rev. Res. **2**, 023362 (2020), 2003.04340.
- 3535 [212] C. Shen and B. Schenke, Phys. Rev. **C97**, 024907 (2018), 1710.00881.
- 3536 [213] STAR, B. Abelev *et al.*, Phys. Rev. C **76**, 064904 (2007), 0706.0472.
- 3537 [214] Z.-T. Liang, J. Song, I. Upsal, Q. Wang, and Z.-B. Xu, (2019), 1912.10223.
- 3538 [215] Y. Xie, D. Wang, and L. P. Csernai, Eur. Phys. J. C **80**, 39 (2020), 1907.00773.
- 3539 [216] X.-L. Sheng, L. Oliva, and Q. Wang, Phys. Rev. D **101**, 096005 (2020), 1910.13684.
- 3540 [217] X.-L. Sheng, Q. Wang, and X.-N. Wang, (2020), 2007.05106.
- 3541 [218] A. Bazavov *et al.*, Phys. Rev. D **95**, 054504 (2017), 1701.04325.
- 3542 [219] S. Borsanyi *et al.*, JHEP **10**, 205 (2018), 1805.04445.
- 3543 [220] STAR, A. Pandav, (2020), 2003.12503.
- 3544 [221] STAR, F. Seck, Measurements of dielectron production in Au+Au collisions at $\sqrt{s_{NN}}$
3545 = 27, 54.4 and 200 GeV with the STAR experiment, in *28th International Conference*
3546 *on Ultrarelativistic Nucleus-Nucleus Collisions (Quark Matter 2019)*, 2019.
- 3547 [222] H. Xing, C. Zhang, J. Zhou, and Y.-J. Zhou, The $\cos 2$ azimuthal asymmetry in 0
3548 meson production in ultraperipheral heavy ion collisions, 2020, 2006.06206.
- 3549 [223] STAR, J. the STAR Collaboration, Adam *et al.*, Phys. Rev. Lett. **123**, 132302 (2019),
3550 1904.11658.
- 3551 [224] W. Zha *et al.*, Phys. Rev. C **97**, 044910 (2018).
- 3552 [225] M. B. G. Ducati and S. Martins, Phys. Rev. D **97**, 116013 (2018).
- 3553 [226] W. Shi, W. Zha, and B. Chen, Phys. Lett. B **777**, 399 (2018), 1710.00332.
- 3554 [227] B. Chen, M. Hu, H. Zhang, and J. Zhao, Phys. Lett. B **802**, 135271 (2020), 1910.08275.

- 3555 [228] X. Guo, S. Shi, N. Xu, Z. Xu, and P. Zhuang, Phys. Lett. B **751**, 215 (2015),
3556 1502.04407.
- 3557 [229] B. Chen, X. Du, and R. Rapp, Nucl. Part. Phys. Proc. **289-290**, 475 (2017),
3558 1612.02089.
- 3559 [230] ALICE, J. Adam *et al.*, JHEP **05**, 179 (2016), 1506.08804.
- 3560 [231] ATLAS, M. Aaboud *et al.*, Eur. Phys. J. C **78**, 762 (2018), 1805.04077.
- 3561 [232] CMS, A. M. Sirunyan *et al.*, Phys. Rev. Lett. **118**, 162301 (2017), 1611.01438.
- 3562 [233] JETSCAPE, S. Cao *et al.*, Phys. Rev. C **96**, 024909 (2017), 1705.00050.
- 3563 [234] JETSCAPE, A. Kumar *et al.*, Jet quenching in a multi-stage Monte Carlo approach,
3564 in *28th International Conference on Ultrarelativistic Nucleus-Nucleus Collisions*, 2020,
3565 2002.07124.
- 3566 [235] Y. Mehtar-Tani and K. Tywoniuk, Phys. Rev. D **98**, 051501 (2018), 1707.07361.
- 3567 [236] Y. Mehtar-Tani and K. Tywoniuk, Nucl. Phys. A **979**, 165 (2018), 1706.06047.
- 3568 [237] B. Zakharov, (2020), 2003.10182.
- 3569 [238] L. Chen, G.-Y. Qin, S.-Y. Wei, B.-W. Xiao, and H.-Z. Zhang, Phys. Lett. B **773**, 672
3570 (2017), 1607.01932.
- 3571 [239] D. A. Appel, Phys. Rev. D **33**, 717 (1986).
- 3572 [240] J. Blaizot and L. D. McLerran, Phys. Rev. D **34**, 2739 (1986).
- 3573 [241] ALICE, J. Adam *et al.*, JHEP **09**, 170 (2015), 1506.03984.
- 3574 [242] F. D’Eramo, K. Rajagopal, and Y. Yin, JHEP **01**, 172 (2019), 1808.03250.
- 3575 [243] ALICE, J. Norman.
- 3576 [244] A. J. Larkoski, S. Marzani, G. Soyez, and J. Thaler, JHEP **05**, 146 (2014), 1402.2657.
- 3577 [245] Y.-T. Chien and R. Kunnawalkam Elayavalli, (2018), 1803.03589.
- 3578 [246] J. Blaizot and Y. Mehtar-Tani, p. 217 (2016).
- 3579 [247] J.-w. Qiu and G. F. Sterman, Phys. Rev. D **59**, 014004 (1999), hep-ph/9806356.
- 3580 [248] K. Kanazawa, Y. Koike, A. Metz, and D. Pitonyak, Phys. Rev. D **89**, 111501 (2014).
- 3581 [249] L. Bland *et al.*, Physics Letters B **750**, 660 (2015).
- 3582 [250] Z.-B. Kang and J.-W. Qiu, Phys. Rev. Lett. **103**, 172001 (2009).

- 3583 [251] P. Sun, J. Isaacson, C. P. Yuan, and F. Yuan, Universal non-perturbative functions
3584 for sidis and drell-yan processes, 2014, 1406.3073.
- 3585 [252] J. P. Ralston and D. E. Soper, Nuclear Physics B **152**, 109 (1979).
- 3586 [253] R. Jaffe and X.-D. Ji, Nucl. Phys. B **375**, 527 (1992).
- 3587 [254] P. Mulders and R. Tangerman, Nucl. Phys. B **461**, 197 (1996), hep-ph/9510301,
3588 [Erratum: Nucl.Phys.B 484, 538–540 (1997)].
- 3589 [255] D. Sivers, Nuovo Cim. C **035N2**, 171 (2012), 1109.2521.
- 3590 [256] C. Alexandrou *et al.*, Phys. Rev. D **98**, 091503 (2018).
- 3591 [257] R. Jaffe and X.-D. Ji, Phys. Rev. Lett. **67**, 552 (1991).
- 3592 [258] J. C. Collins, S. F. Heppelmann, and G. A. Ladinsky, Nucl. Phys. B **420**, 565 (1994),
3593 hep-ph/9305309.
- 3594 [259] L. Adamczyk *et al.*, Phys. Lett. B **780**, 332–339 (2018).
- 3595 [260] M. Radici and A. Bacchetta, Phys. Rev. Lett. **120**, 192001 (2018), 1802.05212.
- 3596 [261] J. Collins and J.-W. Qiu, Phys. Rev. D **75**, 114014 (2007).
- 3597 [262] T. C. Rogers and P. J. Mulders, Phys. Rev. D **81**, 094006 (2010).
- 3598 [263] X. Liu, F. Ringer, W. Vogelsang, and F. Yuan, Factorization and its breaking in dijet
3599 single transverse spin asymmetries in pp collisions, 2020, 2008.03666.
- 3600 [264] Z.-B. Kang, K. Lee, D. Y. Shao, and J. Terry, The sivers asymmetry in hadronic dijet
3601 production, 2020, 2008.05470.
- 3602 [265] F. Yuan, Phys. Rev. Lett. **100**, 032003 (2008).
- 3603 [266] F. Yuan, Phys. Rev. D **77**, 074019 (2008).
- 3604 [267] STAR, L. Adamczyk *et al.*, Phys. Rev. D **97**, 032004 (2018), 1708.07080.
- 3605 [268] M. Anselmino *et al.*, Phys. Rev. D **73**, 014020 (2006), hep-ph/0509035.
- 3606 [269] M. Anselmino *et al.*, Phys. Rev. D **75**, 054032 (2007).
- 3607 [270] J. Soffer, Phys. Rev. Lett. **74**, 1292 (1995).
- 3608 [271] U. D’Alesio, F. Murgia, and C. Pisano, Phys. Lett. B **773**, 300–306 (2017).
- 3609 [272] H1, ZEUS, F. Aaron *et al.*, Eur. Phys. J. C **72**, 2175 (2012), 1207.4864.
- 3610 [273] CMS, V. Khachatryan *et al.*, Phys. Rev. D **92**, 012003 (2015), 1503.08689.

- 3611 [274] S. L. Bultmann *et al.*, Phys. Lett. B **579**, 245 (2004), nucl-ex/0305012.
- 3612 [275] S. Bultmann *et al.*, Phys. Lett. B **632**, 167 (2006), nucl-ex/0507030.
- 3613 [276] pp2pp, S. Bultmann *et al.*, Phys. Lett. B **647**, 98 (2007), nucl-ex/0610022.
- 3614 [277] STAR, L. Adamczyk *et al.*, Phys. Lett. B **719**, 62 (2013), 1206.1928.
- 3615 [278] I. Helenius, in *Talk at 7th International Work-*
 3616 *shop on Multiple Partonic Interactions at the LHC*,
 3617 <http://indico.ictp.it/event/a14280/session/266/contribution/1042/material/slides/0.pdf>.
- 3618 [279] STAR, C. Dilks, PoS **DIS2016**, 212 (2016), 1805.08875.
- 3619 [280] A. Airapetian *et al.*, Phys. Lett. B **693**, 11–16 (2010).
- 3620 [281] C. Adolph *et al.*, Phys. Lett. B **744**, 250–259 (2015).
- 3621 [282] D. Müller, D. Robaschik, B. Geyer, F.-M. Dittes, and J. Hořejší, Fortsch. Phys. **42**,
 3622 101 (1994), hep-ph/9812448.
- 3623 [283] X.-D. Ji, Phys. Rev. Lett. **78**, 610 (1997), hep-ph/9603249.
- 3624 [284] A. Radyushkin, Phys. Lett. B **380**, 417 (1996), hep-ph/9604317.
- 3625 [285] M. Burkardt, Phys. Rev. D **62**, 071503 (2000), hep-ph/0005108, [Erratum: Phys.Rev.D
 3626 66, 119903 (2002)].
- 3627 [286] S. Klein and J. Nystrand, Photoproduction of J / psi and Upsilon in pp and anti-p p
 3628 collisions, in *5th Workshop on Small x and Diffractive Physics*, 2003, hep-ph/0310223.
- 3629 [287] S. R. Klein, J. Nystrand, J. Seger, Y. Gorbunov, and J. Butterworth, Comput. Phys.
 3630 Commun. **212**, 258 (2017), 1607.03838.
- 3631 [288] J. Lansberg, L. Massacrier, L. Szymanowski, and J. Wagner, Phys. Lett. B **793**, 33
 3632 (2019), 1812.04553.
- 3633 [289] HERMES, A. Airapetian *et al.*, Phys. Lett. B **577**, 37 (2003), hep-ex/0307023.
- 3634 [290] HERMES, A. Airapetian *et al.*, Nucl. Phys. B **780**, 1 (2007), 0704.3270.
- 3635 [291] HERMES, A. Airapetian *et al.*, Phys. Lett. B **684**, 114 (2010), 0906.2478.
- 3636 [292] W. Brooks and H. Hakobyan, Nucl. Phys. A **830**, 361C (2009), 0907.4606.
- 3637 [293] NuSea, M. Vasilev *et al.*, Phys. Rev. Lett. **83**, 2304 (1999), hep-ex/9906010.
- 3638 [294] DIS–2014 [https://indico.cern.ch/event/258017/contributions/1588381/
 3639 attachments/453934/629277/pA_DIS2014_Paukkunen.pdf](https://indico.cern.ch/event/258017/contributions/1588381/attachments/453934/629277/pA_DIS2014_Paukkunen.pdf).

- 3640 [295] D. de Florian, R. Sassot, P. Zurita, and M. Stratmann, Phys. Rev. D **85**, 074028
3641 (2012), 1112.6324.
- 3642 [296] PHENIX, S. Adler *et al.*, Phys. Rev. Lett. **98**, 172302 (2007), nucl-ex/0610036.
- 3643 [297] K. Eskola, H. Paukkunen, and C. Salgado, Nucl. Phys. A **855**, 150 (2011), 1011.6534.
- 3644 [298] R. Sassot, M. Stratmann, and P. Zurita, Phys. Rev. D **81**, 054001 (2010), 0912.1311.
- 3645 [299] K. J. Eskola, P. Paakkinen, H. Paukkunen, and C. A. Salgado, Eur. Phys. J. C **77**,
3646 163 (2017), 1612.05741.
- 3647 [300] N. Armesto, H. Paukkunen, J. M. Penín, C. A. Salgado, and P. Zurita, Eur. Phys. J.
3648 C **76**, 218 (2016), 1512.01528.
- 3649 [301] H. Paukkunen and P. Zurita, JHEP **12**, 100 (2014), 1402.6623.
- 3650 [302] E. Aschenauer *et al.*, (2014), 1409.1633.
- 3651 [303] H. Paukkunen, K. J. Eskola, and C. Salgado, Nucl. Phys. A **931**, 331 (2014), 1408.4563.
- 3652 [304] K. J. Eskola, H. Paukkunen, and C. A. Salgado, JHEP **10**, 213 (2013), 1308.6733.
- 3653 [305] L. Gribov, E. Levin, and M. Ryskin, Phys. Rept. **100**, 1 (1983).
- 3654 [306] E. Iancu and R. Venugopalan, The Color glass condensate and high-energy scattering
3655 in QCD, in *In *Hwa, R.C. (ed.) et al.: Quark gluon plasma* 249-3363*, 2003, hep-
3656 ph/0303204.
- 3657 [307] H. Weigert, Prog. Part. Nucl. Phys. **55**, 461 (2005), hep-ph/0501087.
- 3658 [308] J. Jalilian-Marian and Y. V. Kovchegov, Prog. Part. Nucl. Phys. **56**, 104 (2006),
3659 hep-ph/0505052.
- 3660 [309] F. Gelis, E. Iancu, J. Jalilian-Marian, and R. Venugopalan, Ann. Rev. Nucl. Part. Sci.
3661 **60**, 463 (2010), 1002.0333.
- 3662 [310] G. Giuliani, H. Zheng, and A. Bonasera, Prog. Part. Nucl. Phys. **76**, 116 (2014),
3663 1311.1811.
- 3664 [311] Y. V. Kovchegov and E. Levin *Quantum chromodynamics at high energy* Vol. 33 (Cam-
3665 bridge University Press, 2012).
- 3666 [312] A. H. Mueller and J.-w. Qiu, Nucl. Phys. B **268**, 427 (1986).
- 3667 [313] L. McLerran and R. Venugopalan, Phys. Rev. D **49**, 2233 (1994).
- 3668 [314] L. McLerran and R. Venugopalan, Phys. Rev. D **49**, 3352 (1994).

- 3669 [315] L. McLerran and R. Venugopalan, Phys. Rev. D **50**, 2225 (1994).
- 3670 [316] Y. V. Kovchegov, Phys. Rev. D **54**, 5463 (1996).
- 3671 [317] Y. V. Kovchegov, Phys. Rev. D **55**, 5445 (1997).
- 3672 [318] J. Jalilian-Marian, A. Kovner, L. McLerran, and H. Weigert, Phys. Rev. D **55**, 5414
3673 (1997).
- 3674 [319] A. H. Mueller, Nucl. Phys. **B415**, 373 (1994).
- 3675 [320] A. H. Mueller and B. Patel, Nucl. Phys. B **425**, 471 (1994), hep-ph/9403256.
- 3676 [321] I. Balitsky, Nucl. Phys. **B463**, 99 (1996), hep-ph/9509348.
- 3677 [322] I. Balitsky, Phys. Rev. D **60**, 014020 (1999), hep-ph/9812311.
- 3678 [323] Y. V. Kovchegov, Phys. Rev. **D60**, 034008 (1999), hep-ph/9901281.
- 3679 [324] Y. V. Kovchegov, Phys. Rev. D **61**, 074018 (2000), hep-ph/9905214.
- 3680 [325] J. Jalilian-Marian, A. Kovner, and H. Weigert, Phys. Rev. D **59**, 014015 (1998),
3681 hep-ph/9709432.
- 3682 [326] J. Jalilian-Marian, A. Kovner, A. Leonidov, and H. Weigert, Phys. Rev. D **59**, 014014
3683 (1998), hep-ph/9706377.
- 3684 [327] E. Iancu, A. Leonidov, and L. D. McLerran, Phys. Lett. B **510**, 133 (2001), hep-
3685 ph/0102009.
- 3686 [328] E. Iancu, A. Leonidov, and L. D. McLerran, Nucl. Phys. **A692**, 583 (2001), hep-
3687 ph/0011241.
- 3688 [329] A. Accardi *et al.*, Eur. Phys. J. A **52**, 268 (2016), 1212.1701.
- 3689 [330] Y. V. Kovchegov and M. D. Sievert, Nucl. Phys. B **903**, 164 (2016), 1505.01176.
- 3690 [331] CMS, S. Chatrchyan *et al.*, Eur. Phys. J. C **74**, 2951 (2014), 1401.4433.
- 3691 [332] STAR, E. Braidot, Nucl. Phys. A **854**, 168 (2011), 1008.3989.
- 3692 [333] PHENIX, A. Adare *et al.*, Phys. Rev. Lett. **107**, 172301 (2011), 1105.5112.
- 3693 [334] C. Marquet, Nucl. Phys. A **796**, 41 (2007), 0708.0231.
- 3694 [335] J. L. Albacete and C. Marquet, Phys. Rev. Lett. **105**, 162301 (2010), 1005.4065.
- 3695 [336] Z.-B. Kang, I. Vitev, and H. Xing, Phys. Rev. D **85**, 054024 (2012), 1112.6021.
- 3696 [337] M. Strikman and W. Vogelsang, Phys. Rev. D **83**, 034029 (2011), 1009.6123.

- 3697 [338] J. Jalilian-Marian and A. H. Rezaeian, Phys. Rev. D **86**, 034016 (2012), 1204.1319.
- 3698 [339] J. L. Albacete and C. Marquet, Nucl. Phys. A **854**, 154 (2011), 1009.3215.
- 3699 [340] K. J. Eskola, H. Paukkunen, and C. A. Salgado, JHEP **07**, 102 (2008), 0802.0139.
- 3700 [341] A. H. Rezaeian, Phys. Rev. D **86**, 094016 (2012), 1209.0478.
- 3701 [342] T. Sjostrand, S. Mrenna, and P. Z. Skands, Comput. Phys. Commun. **178**, 852 (2008),
3702 0710.3820.
- 3703 [343] Di-jet production from pythia8.189 is scaled down due to its overestimation of inclusive
3704 π_0 yields compared to those reported by BRAHMS in phys. rev. lett. 98 (2007) 252001
3705 and STAR in phys. rev. lett. 97 (2006) 152302.
- 3706 [344] T. Kaufmann, A. Mukherjee, and W. Vogelsang, Phys. Rev. D **92**, 054015 (2015),
3707 1506.01415, [Erratum: Phys.Rev.D 101, 079901 (2020)].
- 3708 [345] D. de Florian, R. Sassot, M. Epele, R. J. Hernández-Pinto, and M. Stratmann, Phys.
3709 Rev. D **91**, 014035 (2015), 1410.6027.
- 3710 [346] A. Khouaja *et al.*, Nucl. Phys. A **780**, 1 (2006).
- 3711 [347] D. de Florian and R. Sassot, Phys. Rev. D **69**, 074028 (2004), hep-ph/0311227.
- 3712 [348] D. de Florian, R. Sassot, and M. Stratmann, Phys. Rev. D **75**, 114010 (2007), hep-
3713 ph/0703242.
- 3714 [349] D. de Florian, R. Sassot, and M. Stratmann, Phys. Rev. D **76**, 074033 (2007),
3715 0707.1506.
- 3716 [350] V. Smakhtin *et al.*, Nucl. Instrum. Meth. **A598**, 196 (2009).
- 3717 [351] A. Abusleme *et al.*, Nucl. Instrum. Meth. **A817**, 85 (2016), 1509.06329.
- 3718 [352] Iakovidis, George, EPJ Web Conf. **174**, 07001 (2018).